NASA/CP-2001-210827

Microgravity Materials Science Conference 2000

Edited by
Narayanan Ramachandran
Universities Space Research Association
Huntsville AL

Nancy Bennett
Universities Space Research Association
Huntsville AL

Dannah McCauley
University of Alabama in Huntsville
Huntsville AL

Karen Murphy
Morgan Research Corporation
Marshall Space Flight Center
Huntsville AL

Samantha Poindexter
Universities Space Research Association
Huntsville AL

Proceedings of a conference sponsored by the
Microgravity Research Division, NASA Headquarters
and held at Huntsville, Alabama, June 6-8, 2000

March 2001

Main Menu

The NASA STI Program Office...in Profile

Since its founding, NASA has been dedicated to the advancement of aeronautics and space science. The NASA Scientific and Technical Information (STI) Program Office plays a key part in helping NASA maintain this important role.

The NASA STI Program Office is operated by Langley Research Center, the lead center for NASA's scientific and technical information. The NASA STI Program Office provides access to the NASA STI Database, the largest collection of aeronautical and space science STI in the world. The Program Office is also NASA's institutional mechanism for disseminating the results of its research and development activities. These results are published by NASA in the NASA STI Report Series, which includes the following report types:

- TECHNICAL PUBLICATION. Reports of completed research or a major significant phase of research that present the results of NASA programs and include extensive data or theoretical analysis. Includes compilations of significant scientific and technical data and information deemed to be of continuing reference value. NASA's counterpart of peer-reviewed formal professional papers but has less stringent limitations on manuscript length and extent of graphic presentations.

- TECHNICAL MEMORANDUM. Scientific and technical findings that are preliminary or of specialized interest, e.g., quick release reports, working papers, and bibliographies that contain minimal annotation. Does not contain extensive analysis.

- CONTRACTOR REPORT. Scientific and technical findings by NASA-sponsored contractors and grantees.

- CONFERENCE PUBLICATION. Collected papers from scientific and technical conferences, symposia, seminars, or other meetings sponsored or cosponsored by NASA.

- SPECIAL PUBLICATION. Scientific, technical, or historical information from NASA programs, projects, and mission, often concerned with subjects having substantial public interest.

- TECHNICAL TRANSLATION. English-language translations of foreign scientific and technical material pertinent to NASA's mission.

Specialized services that complement the STI Program Office's diverse offerings include creating custom thesauri, building customized databases, organizing and publishing research results...even providing videos.

For more information about the NASA STI Program Office, see the following:

- Access the NASA STI Program Home Page at ***http://www.sti.nasa.gov***

- E-mail your question via the Internet to help@sti.nasa.gov

- Fax your question to the NASA Access Help Desk at (301) 621–0134

- Telephone the NASA Access Help Desk at (301) 621–0390

- Write to:
  NASA Access Help Desk
  NASA Center for AeroSpace Information
  7121 Standard Drive
  Hanover, MD 21076–1320
  (301)621–0390

Available from:

NASA Center for AeroSpace Information
7121 Standard Drive
Hanover, MD 21076–1320
(301) 621–0390

National Technical Information Service
5285 Port Royal Road
Springfield, VA 22161
(703) 487–4650

Microgravity Materials Science Conference

Von Braun Center, Huntsville, Alabama

June 6 - 8, 2000

Organized by

Microgravity Materials Science Discipline Working Group

Sponsored by

Microgravity Research Division, NASA Headquarters, Washington, D. C.

Hosted by

NASA Marshall Space Flight Center, Huntsville, Alabama

Foreword

The 2000 Microgravity Materials Science Conference was held June 6-8 at the Von Braun Center, Huntsville, Alabama. It was organized by the Microgravity Materials Science Discipline Working Group, sponsored by the Microgravity Research Division (MRD) at NASA Headquarters, and hosted by NASA Marshall Space Flight Center and the Alliance for Microgravity Materials Science and Applications (AMMSA). It was the fourth NASA conference of this type in the microgravity materials science discipline. The microgravity science program sponsored approximately two hundred investigations, all of whom made oral or poster presentations at this conference. In addition, posters and exhibits covering NASA microgravity facilities, Advanced Technology Development projects sponsored by the NASA Microgravity Research Division at NASA Headquarters, and commercial interests were exhibited. The purpose of the conference was to inform the materials science community of research opportunities in reduced gravity and to highlight the spring 2001 release of the NASA Research Announcement (NRA) to solicit proposals for future investigations. It also served to review the current research and activities in materials science, to discuss the envisioned long-term goals, and to highlight new crosscutting research areas of particular interest to MRD. The conference was aimed at materials science researchers from academia, industry, and government. A workshop on In Situ Resource Utilization (ISRU) was held in conjunction with the conference with the goal of evaluating and prioritizing processing issues in Lunar and Martian-type environments. The workshop participation included invited speakers and investigators currently funded in the material science program under the Human Exploration and Development of Space (HEDS) initiative. The conference featured a plenary session every day with an invited speaker that was followed by three parallel breakout sessions in sub-disciplines. Attendance was close to three hundred and fifty people. Posters were available for viewing during the conference and a dedicated poster session was held on the second day. Nanotechnology, Radiation shielding materials, Space Station science opportunities, Biomaterials research and Outreach and Educational aspects of the program were featured in the plenary talks. This volume, the first to be released on CD-Rom for materials science, is comprised of the research reports submitted by the Principal Investigators at the conference.

Table of Contents

*Dr. Frans Spaepen is the Co-Principal Investigator on this project.

Main Menu

Appendix A: Author Index

M

N

O

P

R

S

T

U

V

W

Y

Z

AADSF	Advanced Automated Directional Solidification Furnace
AAL	Aero-Acoustic Levitation
AAS	Atomic Absorption Spectroscopy
ACCESS	Advanced Cosmic Ray Composition Experiment
ACRT	Accelerated Crucible Rotation Technique
AGHF	Advanced Gradient Heating Facility
AHP	Axial Heat Processing
ALICE	Heavy ion experiment being built for the Large Hadron Collider (LHC) project at CERN, Geneva, Switzerland
ALN	Aluminum Nitride
AOTF	Acousto-Optic Tunable Filter
AP	Ammonium persulfate
ASD	Accelerated Stokesian Dynamics
ATD	Advanced Technology Development
ATLAS	Atmospheric Laboratory for Applications and Science
BCC	Body Centered Cubit
BEI	Backscatter Electron Images
BG	Bioactive Glass
BMG	Bulk Metallic Glasses
BODIPY	A fluorescein derivative
BRYNTRN	Radiation transport code
BUU	Boltzmann-Uehling-Uhlenbeck
CA	Cellular Automata
CAM	CO_2 Acquisition Membrane
CCD	Charge-Coupled Device
CDC	Container-Less Directional Solidification
CERN	European Laboratory for Particle Physics (Geneva, Switzerland)
CFD	Computational Fluid Dynamics
CFX	Commercial Flow Code
CGB	Crystal Growth with a Baffle
CGH	Coupled Growth in Hypermonotectics
CMDS	Center for Materials Development in Space (at the University of Alabama in Huntsville, AL)
CMMR	Center for Microgravity Materials Research (at the University of Alabama in Huntsville, AL)
CNES	Centre National d'Etudes Spatiales (France)
CNES	Centre Nationale d'Études Spatiales ("National Center for Space Studies," French Space Agency)
CRI	Containerless Research Incorporated
CSLM	Coarsening in Solid-Liquid Mixtures
CSM	Colorado School of Mines
CT	Computed Tomography
CTE	Coefficient of Thermal Expansion
CVS	Coupled Vibrational Stirring
DCC	Diffusion Cloud Chamber

DCVA	N,N-dimethyl-p-(2,2-dicyanovinyl) aniline
DDC	Dynamic Decompression and Cooling
DECLIC	Dispositif pour l'Etude de la Croissance et des Liquides Critiques (DECLIC) (Facility for the Study of the Growth and the Fluids near Critical Point)
DIT	Diffusion Interface Theory
DLS	Dynamic Light Scattering
DLVO	Derjaguin, Landau, Verwey, Overbeek
DMSO	High temperature solvent
DNS	Direct Numerical Simulations
DODMAC	Dimethyldioctylammonium chloride
DOE	Department of Energy
DPIMS	Diffusion Processes in Molten Semiconductors
DSC	Differential Scanning Calorimetry
DTA	Differential Thermal Analysis
EBW	Electron-Beam Welding
ED	Electron Diffraction
EDG	Electro Dynamic Gradient
EDGE	Equiaxed Dendritic Solidification Experiment
EDS	Energy Dispersion Spectroscopy
EDS	Energy Dispersive X-ray Spectroscopy
EIS	Electrochemical Impedance Spectroscopy
EIT	Effective Interfacial Tension
EITIC	Effective Interfacial Tension Induced Convection
EKTAPRO	A Kodak camera
ELMS	Evolution of Local Microstructures
ELT	Electrodynamic Levitator Trap
EML	Electromagnetic Levitator
EPD	Etch Pit Density
EPMA	Electron Probe Micro-Analyzer
ESL	Electrostatic Levitation/Levitator
EXPRESS	(Expedite the Processing of Experiments to Space Station)
FCC	Face Centered Cubit
FDLB	Finite Difference Lattice Boltzmann
Fe-MAS	Fe-bearing Magnesium Aluminosulphate
FLUENT	Computational fluid dynamics software
FLUKA	A Monte-Carlo simulation code for radiation transport
FTIR	Fourier Transform Infrared Spectrometry
FZ	Float/floating Zone
GCR	Galactic Cosmic Ray
GDMS	Glow Discharge Mass Spectroscopy
GEANT	A Monte-Carlo simulation code for radiation transport
GF-AA	Graphite Furnace- Atomic Absorption Spectroscopy
GFL	Gas Film Levitation
GOSAMR	Gelation of Sols; Applied Microgravity Research
GTAW	Gas-Tungsten Arc Welding
GUI	Graphical User Interface
HAD	High-density Amorphous

HARV	High Aspect Ratio Vessel
HBT	High Performance Transistors
HD	Hoop Direction
HDDA	hexane diol diacrylate
HDIV	Holographic Diffraction Image Velocimetry
HDPE	High-Density Polyethylenes
HECT	High Energy Transport Code
HEDS	Human Exploration and Development of Space
HEMA	hydroxyethyl methancrylate
HETC	A Monte-Carlo simulation code for radiation transport
HPCVD	High Pressure Chemical Vapor Deposition
HPMS	High Pressure Mass Spectrometry
HRTXD	High Resolution Triple Crystal X-ray Diffractometry/Diffraction
HTESL	High Temperature Electrostatic Levitator
HTSC	High Temperature Superconductor
HZETRN	Radiation transport code
ICP-AES	Inductively Coupled Plasma-Atomic Emission Spectroscopy
ICP-MS	Inductively Coupled Plasma-Mass Spectrometry
IDGE	Isothermal Dendritic Growth Experiment
IML	International Microgravity Laboratory
INFN	Instituto Nazionale di Fisica Nucleare (Italian National Nuclear Physics funding agency)
IR	Infra Red
ISCP	*In-Situ* Consumables Production
ISPP	*In-Situ* Propellent Production
ISRU	*In-Situ* Resource Utilization
ISS	International Space Station
ITO	Indium-Tin-Oxide
JPL	Jet Propulsion Laboratory (Pasadena, CA, managed by the California Institute of Technology)
JSC	NASA Johnson Space Center (Houston, TX)
KC-135	A NASA aircraft that performs parabolic maneuvers to produce short durations (20 seconds) of reduced gravity (0.01 g) environment.
KDP	Potassium Dihydrogen Phosphate
KSC	NASA Kennedy Space Center (Cape Canaveral, FL)
LAHET	A Monte-Carlo simulation code for radiation transport
LaRC	NASA Langley Research Center (Hampton, VA)
LB	Langmuir-Blodgett
LB	Lattice Boltzmann
LBNL	Lawrence Berkeley National Laboratory
LBW	Laser Beam Welding
LC	Liquid Crystal
LCP	Liquid Crystalline Polymeric
LDA	Low-density Amorphous
LDPE	Low-Density Polyethylenes
LED	Light Emitting Diode
LEO	Low Earth Orbit

LET	Linear Energy Transfer
LF	Low Frequency
LIF	Laser-Induced Fluorescence
LM	Lockheed Martin
LMS	Life and Microgravity Spacelab
LPS	Liquid Phase Sintering
MCA	Membrane Casting Apparatus
MCA	Multi-Channel Analyzer
MD	Molecular Dynamics
MDO	Multidisciplinary Optimization
MEPHISTO	Matérial pour l'Étude des Phenomènes Intéressants de la Solidification sur Terre et en Orbite ("Apparatus for the Study of Interesting Phenomena of Solidification on Earth and in Orbit")
MeV	One million electron volts
MGB	Materials Science Glovebox
MI	Melt Indices
MIT	Massachusetts Institute of Technology
MITH	Millikelvin Thermostat
MNR	Nuclear Magnetic Resonance
MOCVD	Metal Organic Chemical Vapor Deposition
MOR	Modulus of Rupture
MRD	Microgravity Research Division
MSAD	Microgravity Science and Applications Department
MSFC	NASA Marshall Space Flight Center (Huntsville, AL)
MSL	Microgravity Sciences Laboratory
MSL-1R	Materials Sciences Laboratory (R represents the reflight)
MST	Microscopic Solvability Theory
MST	Minimum Spanning Tree
MTF	Membrane Test Facility
MTF	Moderate Temperature Facility
MTV	Molecular Tagging Velocimetry
MV	Macrovoids
MVPD	Macrovoid Penetration Depth
NAA	Neutron Activation Analysis
NCS	Nucleation of Crystals from Solution
NCSL	Nanocrystal Superlattices
ND	Normal Direction
NIST	National Institute of Standards and Technology
NLO	Nonlinear Optical
NMR	Nuclear Magnetic Resonance
NRA	NASA Research Announcement
NSF	National Science Foundation
NUCFRG	A radiation transport code
OB	Oberbeck-Boussinesq
OMCVD	Organometallic Chemical Vapor Deposition
OO	Object Oriented
ORBITEC	Orbital Technologies Corporation

OSD	Office of the Secretary of Defense
PAW	Physics Analysis Workstation
PB	Polybutadiene
PBT	Polybutylene terephthalate
PC	Personal Computer
PD	Penetration Depth
PDLC	Polymer Dispersed Liquid Crystals
PDM	Power Distribution Module
PE	Polyethylene
PEE	Polyethylethylene
PEO	Polyethylene Oxide
PEP	Particle Engulfment and Pushing
PI	Principal Investigator
PID	Proportional Integral Derivative
PIPS	Polymerization Induced Phase Separation
PIV	Particle Image Velocimetry
PL	Photoluminescence
PMMA	polymethylmethacrylate
POCC	Payload Operations Control Center (NASA MSFC)
Pr	Prandtl Number
PS	polystyrene
PVA	Pivalic Acid
PVT	Physical Vapor Transport
QMSFRG	Quantum Multiple Scattering Fragmentation Model, a radiation transport code
QMST	Quantum Multiple Scattering Theories
R2PI	Resonant-Two-Photon-Ionization
RDF	Radial Distribution Function
RDR	Requirements Definition Review
RE	Rare Earth
Re	Reynolds Number
REMPI	Resonance Enhanced Multiphoton Ionization
RIDGE	Rensellaer Isothermal Dendritic Growth Experiment
RMF	Rotating Magnetic Field
ROMP	Ring Opening Metathesis Polymerization
ROOT	An object-oriented physics analysis infrastructure
RQC	Rotating Quench Cell
RWV	Rotating Wall Bioreactor Vessel
SAMS	Space Acceleration Measurement System
SAXS	Small-Angle X-ray Scattering
Sc	Schmidt Number
SCN	Succinonitrile
SCN-ACE	Succinonitrile-acetone
SCN-E	Succinonitrile-ethanol
SCN-GLY	Succinonitrile-glycerol
SCN-W	Succinonitrile-water
SCR	Science Concepts Review
SD	Standard Deviations

SD	Stokesian Dynamics
SEM	Scanning Electron Microscopy
SEP	Société Européene de Propulsion
Sh	Sherwood Number
SHG	Second Harmonig Generation
SHIVA	Spaceflight Holography Investigation in a Virtual Apparatus
SHS	Self-propagating High-temperature Synthesis
SIMS	Secondary Ion Mass Spectrometry
SIPS	Solvent Induced Phase Separation
SIV	Stereoscopic Imaging Velocimetry
SLI	Solid-liquid Interface
SOPC	Stearoyl, Oleoyl Phosphatidylcholine
SPE	Solar Particle Event
STM	Scanning Tunneling Microscopcy
STS	Space Transportation System (Shuttle/external tank/solid rocket booster system, also a Shuttle mission designation)
SUBSA	Solidification Using the Baffle in Sealed Ampoules
SWBXT	Synchrotron White Beam X-ray Topography
TDSE	Transient Dendritic Solidification Experiment
TEM	Transmission Electron Microscopy
TEM	Tunneling Electron Microscope
TEMC	Thermoelectromagnetic Convection
TEMPUS	Tiegelfreies Elektromagnetisches Prozessieren Unter Schwerelosigkeit (German Electromagnetic Containerless Processing Facility)
TEOS	Tetraethylorthosilicate
TEPC	Tissue Equivalent Proportional Counter
THM	Traveling Heater Method
TIPS	Thermally Induced Phase Separation
TLS	Two Level System
TMF	Traveling Magnetic Field
TRL	Technology Readiness Level
TRR	Time-Resolved Relativity
TSL Theory	Classical Theory of Phase Coarsening by Todes, Lifshitz, and Slyozov
TTT	Time-Temperature-Transformation
UAH	University of Alabama in Huntsville
UF	Utilization Flight
USAXS	Ultra-Small Angle X-ray Scattering
USML	United States Microgravity Laboratory
USMP	United States Microgravity Payload
UV	Ultra Violet
UW	University of Wisconsin
VB	Vertical Bridgman
VFMV	Flow-Visualized Microvoid
WAXS	Wide Angle X-Ray Scattering
WCI	Wetting Characteristics of Immiscibles
XCAP	Image analysis software
XRD	X-ray Diffraction

XRF	X-ray Fluorescence
YAG	Yttria Aluminum Garnet
YSV	Yttria Stabilized Zirconia
YSZ	Yttria-stabilized zirconia
ZBLAN	A glass which contains the fluorides of zirconium, barium, lanthanum, aluminum, and sodium

Prof. Reza Abbaschian
University of Florida
Department of Materials Science and Engineering
P.O. Box 116400
132 Rhines Hall
Gainesville, FL 32611-2066
T 352-846-3300; F 352-392-7219
rabba@mse.ufl.edu

Dr. M. Abid
University of Southern California
Department of Aerospace and Mechanical Engineering
Los Angeles, CA 90089-1453

Prof. James H. Adair
Pennsylvania State University
Materials Science and Engineering
217 Materials Research Laboratory
University Park, PA 16802
T 814-863-6047; F 814-863-9704
JAdair@mrl.psu.edu

Dr. J. D. Adam
Northrop Grumman Corporation
Science and Technology Center
ESSS MS-3D14, ATL
1212 Winterson Road
Linthicum, MD 21090
F 410-765-7652

Prof. Rigoberto Castillo Advincula
University of Alabama, Birmingham
Department of Chemistry
CHEM Building, Room 201
901 14th Street South
Birmingham, AL 35294-1240
T 205-934-8286; F 205-934-2543
gobet@uab.edu

Dr. N. I. Agladze
Cornell University
Laboratory of Atomic and Solid State Physics
517 Clark Hall
Ithaca, NY 14853-2501
F 607-255-6428

Mr. William Ainsworth
University of Southern Mississippi
Department of Chemistry and Biochemistry
P. O. Box 5043
Hattiesburg, MS 39406-5053
F 601-266-6045

Prof. Ali Reza Alemozafar
Stanford University
Laboratory for Advanced Materials
McCullough Building
476 Lomita Mall
Stanford, CA 94305-4045

Prof. Iwan Alexander
Case Western Reserve University
Department of Mechanical and Aerospace Engineering
416 Glennan Building
10900 Euclid Avenue
Cleveland, OH 44106
T 216-368-6045; F 216-368-6445
ida2@po.cwru.edu

Dr. Andreas Alexandrou
Worcester Polytechnic Institute
Mechanical Engineering Department
100 Institute Road
Worcester, MA 01609-2280
T 508-831-5147; F 508-831-5680
andalexa@wpi.wpi.edu

Prof. Jens Alkemper
Northwestern University
Department of Materials Science and Engineering
2225 North Campus Drive
Evanston, IL 60208-3108
T 847-491-5943; F 847-491-7820
j-alkemper@nwu.edu

Prof. M. Cengiz Altan
University of Oklahoma
School of Aerospace and Mechanical Engineering
865 Asp Avenue, Room 212
Norman, OK 73019
T 405-325-1737; F 405-325-1088
altan@ou.edu

Mr. Alex Altgilbers
Vanderbilt University
5527 Kenadall Drive
Nashville, TN 37209
T 615-322-2756; F 615-343-8645
asa@vuse.vanderbilt.edu

Prof. D. M. Anderson
George Mason University
Department of Mathematical Sciences
Fairfax, CA 27599

Prof. Timothy J. Anderson
University of Florida
Department of Chemical Engineering
P.O. Box 116005
Gainesville, FL 32611
T 352-392-0881; F 352-392-9513
tim@nersp.nerdc.ufl.edu

Prof. J. Barry Andrews
University of Alabama, Birmingham
Department of Materials and
Mechanical Engineering, BEC 254
1150 10th Avenue Southwest
Birmingham, AL 35294
T 205-934-8452; F 205-934-8485
bandrews@Engr.uab.edu

Prof. A. V. Anilkumar
Vanderbilt University
1743 Station B
Nashville, TN 37235
T 615-343-7293; F 615-343-8730
nil@vuse.vanderbilt.edu

Prof. Robert E. Apfel
Yale University
Department of Mechanical Engineering
Room M-1
9 Hillhouse Avenue
P.O. Box 208286
New Haven, CT 06520-8286
T 203-432-4346; F 203-432-7654
robert.apfel@yale.edu

Dr. Neer Asherie
Massachusetts Institute of Technology
Department of Physics
Center for Materials Science and Engineering
Material Processing Center
77 Massachusetts Avenue
Cambridge, MA 02139

Dr. Michael R. Ayers
Lawrence Berkeley National Laboratory
1 Cyclotron Road
MS 70-110A
Berkeley, CA 94720
T 510-486-4292; F 510-486-7303
mrayers@inreach.com

Prof. Portonovo S. Ayyaswamy
University of Pennsylvania
Department of Mechanical Engineering and
Applied Mechanics
Philadelphia, PA 19104-6315
T 215-898-8362; F 215-573-6334
ayya@eniac.seas.upenn.edu

Prof. Michael J. Aziz
Harvard University
Division of Engineering and Applied Sciences
29 Oxford Street
Cambridge, MA 02138-2901
T 617-495-9884; F 617-495-9837
maziz@harvard.edu

Prof. Klaus J. Bachmann
North Carolina State University
Department of Materials Science and Engineering
Research Bldg.-1, Room 219
Box 7919, Centennial Campus
100 Capability Drive
Raleigh, NC 27695-7919
T 919-513-1926; F 919-515-3419
k_bachmann@ncsu.edu

Prof. Renal Backov
University of Florida
Department of Chemistry
P.O. Box 117200
Gainesville, FL 32611-7200
F 352-392-3255

Prof. F. F. Badavi
Christopher Newport University
1 University Place
Newport News, VA 23606

Dr. Gautam D. Badhwar
NASA JSC
Solar System Division
Mail Code SN
2101 NASA Road One
Houston, TX 77058-3696
T 281-483-5065; F 281-483-5276
gautam.d.badhwar1@jsc.nasa.gov

Dr. S. Baker
University of Massachusetts
Polymer Science and Engineering Department
Amhurst, MA 01003-4530

Prof. R. Michael Banish
University of Alabama, Huntsville
CMMR, VBRH, D-11
301 Sparkman Drive
Huntsville, AL 35899
T 256-824-6969; F 256-824-6944
banishm@email.uah.edu

Prof. Frank S. Bates
University of Minnesota
Department of Chemical Engineering and
Materials Science
Amundson Hall
421 Washington Avenue, S.E.
Minneapolis, MN 55455-0132

Prof. R. H. Baughman
New Jersey Institute of Technology
University Heights
Newark, NJ 07102-1982

Prof. Robert J. Bayuzick
Vanderbilt University
Department of Chemical Engineering
303A Olim Hall
Nashville, TN 37235
T 615-322-7047; F 615-343-8645
bayuzick@vuse.vanderbilt.edu

Prof. Christoph Beckermann
University of Iowa
Department of Mechanical Engineering
2412 SC Engineering Building
Iowa City, IA 52242-1527
T 319-335-5681; F 319-335-5669
becker@Engr.uiowa.edu

Mr. Giulio Bellizia
University of Illinois, Chicago
2828 North Pine Grove, Apt. 317
Chicago, IL 60657
T 312-413-7601; F 312-413-0447

Prof. Andre Benard
Michigan State University
Department of Mechanical Engineering
2555 Engineering Building
East Lansing, MI 48824
T 517-432-1522; F 517-353-1750
benard@egr.msu.edu

Prof. George B. Benedek
Massachusetts Institute of Technology
Department of Physics
Room 13-2005
77 Massachusetts Avenue
Cambridge, MA 02139-4307
T 617-253-4828; F 617-225-2585
gbb@mit.edu

Dr. K. W. Benz
Kristallographisches Inst.
Der Universitat
Hebelstrasse 25 D-7800
Freiberg, Germany

Prof. H. Bermudez
University of Pennsylvania
120 Hayden Hall
3320 Smith Walk
Philadelphia, PA 19104

Prof. Jerry Bernholc
North Carolina State University
Department of Physics
Box 8202
Raleigh, NC 27695-8202
T 919-515-3126; F 919-515-7331
bernholc@ncsu.edu

Dr. David Berns
Tufts University
Department of Physics and Astronomy
Science and Technology Center, Room 208
4 Colby Street
Medford, MA 02155
F 617-627-3744

Dr. J. Bhowmick
Vanderbilt University
1743 Station B
Nashville, TN 37235
F 615-343-8730

Dr. Konstantinos Boboridis
National Institute of Standards and Technology
100 Bureau Drive
MS 8555
Gaithersburg, MD 20899-8555

Dr. William J. Boettinger
National Institute of Standards and Technology
Metallurgy Division
Materials Science and Engineering Lab.
Bldg. 223, Room A153
Gaithersburg, MD 20899
T 301-975-6160; F 301-975-4553
wboettinger@nist.gov

Prof. G. Bonilla
University of Massachusetts, Amherst
Department of Chemical Engineering
Goessmann Laboratory
Amherst, MA 01003

Prof. Nicholas Booth
University of Alabama in Huntsville
CMMR, VBRH, D-29
Huntsville, AL 35899
T 256-824-6019; F 256-824-6499
boothn@email.uah.edu

Prof. Christopher Bowman
University of Colorado, Boulder
Department of Chemical Engineering
Campus Box 424
Boulder, CO 80309-0424
T 303-492-3247; F 303-492-4341
bowmanc@colorado.edu

Prof. John F. Brady
California Institute of Technology
Division of Chemistry and Chemical Engineering
210-41
Pasadena, CA 91125
T 626-395-4183; F 626-568-8743
jfbrady@caltech.edu

Prof. A. Brannan
University of Minnesota
Department of Chemical Engineering and Materials Science
Amundson Hall
421 Washington Avenue S.E.
Minneapolis, MN 55455-0132

Prof. Robert F. Brebrick
Marquette University
Department of Mechanical and Industrial Engineering
P.O. Box 1881
Milwaukee, WI 53201-1881
robert.brebrick@marquette.edu

Prof. Kenneth Brezinsky
University of Illinois, Chicago
Department of Chemical Engineering
810 South Clinton Street
Chicago, IL 60607-7000
kenbrez@uic.edu

Prof. M. E. Brown
Kansas State University
Department of Chemistry
311 CHEM-BIOCHEM
Manhattan, KS 66506
mpeterso@ksu.edu

Dr. R. Brun
CERN
EP/AIP
Bat. 12 1-013
CH-1221 Geneva 23, Switzerland
F 41 22 767 9480

Prof. Arnold Burger
Fisk University
Center for Photonic Materials and Devices
Department of Physics
1000 17th Avenue N
Nashville, TN 37208-3051
T 615-329-8516; F 615-329-8634
aburger@dubois.fisk.edu

Dr. Craig Burkhard
Clarkson University
International Center for Gravity, Materials Science and Applications
Box 5814
Potsdam, NY 13699-5814
F 315-268-3833

Dr. Federico Carminati
CERN
EP/AIP, Bat. 12 1-013
CH-1221 Geneva 23, Switzerland
T 41 22 767 4959; F 41 22 767 9480
frederico.carminati@cern.ch

Dr. William E. Carswell
University of Alabama in Huntsville
Mail Code SD47
Marshall Space Flight Center
MSFC, AL 35812
T 256-544-0829; F 256-544-8762
bill.carswell@msfc.nasa.gov

Dr. Adrian V. Catalina
Universities Space Research Assoc.
Mail Code SD47
Marshall Space Flight Center
MSFC, AL 35812
T 256-544-1326; F 256-544-2559
adrian.catalina@msfc.nasa.gov

Prof. Peggy Cebe
Tufts University
Department of Physics and Astronomy
Science and Technology Center, Room 208
4 Colby Street
Medford, MA 02155
T 617-627-3365; F 617-627-3744
peggy@cebe.phy.tufts.edu

Prof. Soyoung Stephen Cha
University of Illinois, Chicago
Department of Mechanical Engineering
M/C 251, 2039 ERF
842 West Taylor Street
Chicago, IL 60607-7022
T 312-996-9612; F 312-413-0447
sscha@uic.edu

Dr. Arnon Chait
NASA GRC
Mail Stop 105-1
21000 Brookpark Road
Cleveland, OH 44135
T 216-433-3558; F 216-433-5033
arnon.chait@grc.nasa.gov

Mr. Yuri Chekanov
University of Southern Mississippi
Department of Chemistry and Biochemistry
P. O. Box 5043
Hattiesburg, MS 39406-5053
F 601-266-6045

Prof. James R. Chelikowsky
University of Minnesota
Department of Chemical Engineering and Materials Science
151 Amundson Hall
421 Washington Avenue S.E.
Minneapolis, MN 55455-0132
T 612-625-4837; F 612-626-7246
jrc@msi.umn.edu

Dr. P. Y. P. Chen
University of New South Wales
School of Mechanical and Manufacturing Engineering
Sydney, NSW 2052, Australia
T 61-2-385-5162; F 61-2-633-1222

Prof. Weinong (Wayne) Chen
The University of Arizona
Department of Aerospace and Mechanical Engineering
1130 N. Mountain Avenue
Tucson, AZ 85721
T 520-621-6114; F 520-621-8191
wchen@allen.ame.arizona.edu

Prof. Alexander A. Chernov
Universities Space Research Assoc.
Mail Code SD47
Marshall Space Flight Center
MSFC, AL 35812
T 256-544-9196; F 256-544-8762
alex.chernov@msfc.nasa.gov

Prof. Michael Cima
Massachusetts Institute of Technology
Materials Processing Center
Bldg. 12-011
77 Massachusetts Avenue
Cambridge, MA 02139-4307
T 617-253-6877; F 617-258-6936
mjcima@mit.edu

Prof. Noel A. Clark
University of Colorado, Boulder
Department of Physics
Boulder, CO 80309-0390

Prof. Juan Pablo Claude
University of Alabama, Birmingham
Department of Chemistry
CHEM Building, Room 201
901 14th Street South
Birmingham, AL 35294-1240
T 205-975-2478; F 205-934- 2543
jpclaude@uab.edu

Dr. M. S. Clowdsley
NASA LaRC
MS 188 B
Hampton, VA 23681
F 757-864-8094

Dr. Sharon Cobb
NASA MSFC
Mail Code SD47
Marshall Space Flight Center
MSFC, AL 35812
T 256-544-7791; F 256-544-8762
sharon.cobb@msfc.nasa.gov

Prof. Carlos Coimbra
Drexel University
Philadelphia, PA 19104

Prof. Reid F. Cooper
University of Wisconsin, Madison
Department of Materials Science and Engineering
1509 University Avenue
Madison, WI 53706-1595
T 608-262-1133; F 608-262-8353
cooper@engr.wisc.edu

Dr. Sam R. Coriell
National Institute of Standards and Technology
100 Bureau Drive, MS 8555
Gaithersburg, MD 20899-8555
T 301-975-6169; F 301-975-4553
sam.coriell@nist.gov

Prof. Thomas H. Courtney
Michigan Technological University
Department of Materials Science and Engineering
1400 Townsend Drive
Houghton, MI 49931-1295
T 906-487-2036; F 906-487-2934
thc@mtu.edu

Prof. Gregory P. Crawford
Brown University
Division of Engineering
Box D
182 Hope Street
Providence, RI 02912
T 401-863-2858; F 401-863-912
Gregory_Crawford@brown.edu

Mr. Kevin Croat
Washington University
Physics Department
Box 1105
One Brookings Drive
Saint Louis, MO 63130
T 314-935-6379; F 314-935-6219
tkc@howdy.wustl.edu

Prof. Arne Croell
TU Bergakademie Freiberg
Inst. für NE-Metallurgie und Reinststoffe
Leipziger Str. 23
D-09599 Freiberg, Germany
T 49-3731-39-2017
F 49-3731-39-2268
arne.croell@inemet.tu-freiberg.de

Mr. Daniel Crunkleton
University of Florida
Department of Chemical Engineering
P.O. Box 116005
227 CHE
Gainesville, FL 32611
T 352 392-2420; F 352 392-9513
dcrunkle@che.ufl.edu

Dr. Francis A. Cucinotta
NASA JSC
Code SN
2101 NASA Road 1
Houston, TX 77058
T 281-483-0968; F 281-483-2696
fcucinot@ems.jsc.nasa.gov

Dr. Peter A. Curreri
NASA MSFC
Mail Code SD48
Marshall Space Flight Center
MSFC, AL 35812
T 256-544-7763; F 256-544-6660
peter.curreri@msfc.nasa.gov

Prof. Jonathan Dantzig
University of Illinois, Urbana
Department of Mechanical Engineering
MC-244
1206 W. Green Street
Urbana, IL 61801
T 217-333-4107; F 217-244-6534
dantzig@uiuc.edu

Prof. Delbert E. Day
University of Missouri, Rolla
Materials Research Center
1870 Miner Circle
Rolla, MO 65409-1170
T 573-341-4354; F 573-341-2071
day@umr.edu

Dr. Henry C. de Groh III
NASA GRC
Mail Stop 105-1
21000 Brookpark Road
Cleveland, OH 44135
T 216-433-5025; F 216-433-5033
henry.c.degroh@grc.nasa.gov

Prof. Graham D. de Vahl Davis
University of New South Wales
School of Mechanical and
Manufacturing Engineering
Sydney, NSW 2052, Australia
T 61-2-385-4099; F 61-2-633-1222
g.devahldavis@unsw.edu.au

Prof. Kenneth A. Debelak
Vanderbilt University
Department of Chemical Engineering
Box 1604, Station B
Nashville, TN 37235
T 615-322-2088; F 615-343-7951
kenneth.a.debelak@vanderbilt.edu

Prof. Jeffrey J. Derby
University of Minnesota
Department of Chemical Engineering and Materials Science
151 Amundson Hall
421 Washington Avenue, S.E.
Minneapolis, MN 55455-0132
T 612-625-1313; F 612-626-7246
derby@tc.umn.edu

Mr. G. Dhanaraj
State University of New York, Stony Brook
Department of Materials Science and Engineering
Stony Brook, NY 11794-2275

Prof. Alejandro R. Diaz
Michigan State University
Department of Mechanical Engineering
East Lansing, MI 48824
T 517-353-0825; F 517-353-1750
diaz@egr.msu.edu

Prof. Nikolaus Dietz
North Carolina State University
Department. of Materials Science
P.O. Box 7919
Raleigh, NC 27695-7919
T 919-515-8804; F 919-515-3419
ndietz@unity.ncsu.edu

Prof. B. Discher
University of Pennsylvania
Department of Chemical Engineering
BioEngineering and Mechanical Engineering
Philadelphia, PA 19104-6315

Prof. Dennis E. Discher
University of Pennsylvania
Department of Chemical Engineering
BioEngineering and Mechanical Engineering
Philadelphia, PA 19104-6315

Dr. Peter Dold
Universitat Freiburg
Kristallographisches Institut
Hebelstrasse 25
D-79106, Freiberg 1, Germany
T 49-761-203-6449; F 49-761-203-6434
pit@sgi3.krist.uni-freiburg.de

Dr. James Patton Downey
NASA MSFC
Mail Code SD48
Marshall Space Flight Center
MSFC, AL 35812
T 256-544-6432; F 256-544-2102
james.downey@msfc.nasa.gov

Prof. Edward L. Dreizin
New Jersey Institute of Technology
Department of Mechanical Engineering
University Heights
Newark, NJ 07102-1982
T 973-596-5751; F 973-642-4282
dreizin@njit.edu

Dr. Y. Du
Michigan Technological University
Department of Materials Science and Engineering
1400 Townsend Drive
Houghton, MI 49931-1295
F 906-487-2934

Prof. Paul Ducheyne
University of Pennsylvania
Department of BioEngineering
120 Hayden Hall, 3320 Smith Walk
Philadelphia, PA 19104-6315
T 215-898-8501; F 215-573-2071
ducheyne@seas.upenn.edu

Prof. Michael Dudley
State University of New York, Stony Brook
Department of Materials Science and Engineering
Stony Brook, NY 11794-2275
T 631-632-8500; F 631-632-8052
michael.dudley@sunysb.edu

Dr. T. Duffar
Centre d'Etudes Nuclaires Grenoble
85X Avenue des Martyrs
38041 Grenobel Cedex, France
F 33-76-88-51-18

Dr. Thierry Dumont
Université Lyon I
Laboratoire d'Analyse Numirique
Batiment 101
43 bd du 11 Novembre 1918
69622 Villeurbanne Cedex, France
F 33 4 72 44 80 53

Prof. Prabir K. Dutta
Ohio State University
Department of Chemistry
120 West Eighteenth Avenue
Columbus, OH 43210
T 614-292-4532; F 614-292-1685
dutta.1@osu.edu

Dr. Walter M. B. Duval
NASA GRC
Mail Stop 105-1
21000 Brookpark Road
Cleveland, OH 44135
T 216-433-5023; F 216-433-5033
walter.m.duval@grc.nasa.gov

Prof. M. Samy El-Shall
Virginia Commonwealth University
Department of Chemistry
1001 W. Main Street
Richmond, VA 23284-2006
T 804-828-3518; F 804-828-8599
selshall@hsc.vcu.edu

Mr. Peter Engel
Wyle Laboratories Inc., Florida Operations
Bldg. K7-569, Room 1142
Wyle-32
K7-569 Saturn Causeway
P.O. Box 21072
Kennedy Space Center, FL 32815
T 321-861-5158; F 321-861-6163
peterengle@hotmail.com

Dr. Edwin Ethridge
NASA MSFC
Mail Code SD47
Marshall Space Flight Center
MSFC, AL 35812
T 256-544-7767; F 256-544-1777
edwin.ethridge@msfc.nasa.gov

Prof. James W. Evans
University of California, Berkeley
Department of Materials Science and Engineering
Berkeley, CA 94720
T 510-642-3807; F 510-642-9164
evans@socrates.berkeley.edu

Dr. Rebecca L. A. Everman
University of Wisconsin, Madison
Department of Materials Science and Engineering
1509 University Avenue
Madison, WI 53706-1595
F 608-262-8353

Prof. Alexandre Fedoseyev
University of Alabama, Huntsville
CMMR
VBRH, Research Institute D-4
Huntsville, AL 35899
T 256-824-6889; F 256-824-6944
alex@cmmr.uah.edu

Prof. Robert S. Feigelson
Stanford University
Center for Materials Research
Press Warehouse
Stanford, CA 94305-4045
T 650-723-4007; F 650-723-3752
feigel@soe.stanford.edu

Dr. A. Ferrari
INFI
Milan, Italy

Dr. Shari Feth
University of Alabama in Huntsville
Mail Code SD47
Marshall Space Flight Center
MSFC, AL 35812
T 256-544-0519; F 256-544-8762
sheri.feth@msfc.nasa.gov

Dr. Merton C. Flemings
Massachusetts Institute of Technology
Materials Processing Center
77 Massachusetts Avenue, Rm. 8-407
Cambridge, MA 02139
T 617-253-3233; F 617-258-6886
flemings@mit.edu

Mr. David T. Frate
NASA GRC
Mail Stop 500-115
21000 Brookpark Road
Cleveland, OH 44135

Dr. Donald O. Frazier
NASA MSFC
Mail Code SD40
Marshall Space Flight Center
MSFC, AL 35812
T 256-544-7825; F 256-544-2102
don.frazier@msfc.nasa.gov

Dr. J. E. Frei
Rensselaer Polytechnic Institute
CII 9113
110 8th Street
Troy, NY 12180
F 518-276 2073

Prof. Andrienne C. Friedli
Middle Tennessee State University
Department of Chemistry
Box X076 MTSU
Murfreesboro, TN 37312
T 615-898-2071; F 615-898-5182
acfriedli@mtsu.edu

Dr. Archie Fripp Jr.
125 Little John Road
Williamsburg, VA 23185
T 757-253-2822
afripp@widomaker.com

Prof. Anup K. Gangopadhyay
Washington University, St. Louis
Department of Physics
Campus Box 1105
One Brookings Drive
St. Louis, MO 63130
T 314-935-4654; F 314-935-6379
Anup@howdy.wustl.edu

Dr. H. Gao
University of Pennsylvania
Department of Mechanical Engineering and
Applied Mechanics
Philadelphia, PA 19104-6315
F 215-573-6334

Dr. N. A. Gatsonis
Worcester Polytechnic Institute
100 Institute Road
Worcester, MA 01609-2280

Dr. Yi Ge
University of Illinois, Chicago
Department of Mechanical Engineering
M/C 251, 2039 ERF
842 West Taylor Street
Chicago, IL 60607-7022
F 312-413-0447

Dr. Georgi Georgiev
Tufts University
Department of Physics and Astronomy
Science and Technology Center
4 Colby Street, Room 208
Medford, MA 02155
F 617-627-3744

Prof. Randall M. German
The Pennsylvania State University
147 Research Bldg. West
University Park, PA 16802-6809
T 814-863-8025; F 814-863-8211
rmg4@psu.edu

Dr. Donald C. Gillies
NASA MSFC
Mail Code SD47
Marshall Space Flight Center
MSFC, AL 35812
T 256-544-9302; F 256-544-8762
donald.gillies@msfc.nasa.gov

Ms. Cindie Giummarra
Rensselaer Polytechnic Institute
CII 9113
110 8th Street
Troy, NY 12180
T 518-276 6130; F 518-276 2073
giummc@rpi.edu

Prof. Matthew Glaser
University of Colorado, Boulder
Department of Physics
Condensed Matter Lab.
Boulder, CO 80309-0390
T 303-492-3029; F 303-492-2998
glaser@bly.Colorado.edu

Prof. Martin E. Glicksman
Rensselaer Polytechnic Institute
Department of Materials Science and Engineering
Materials Research Center, Room 9111
110 8th Street
Troy, NY 12180
T 518-276-6721; F 518-276-2198
glickm@rpi.edu

Prof. Arun M. Gokhale
Georgia Institute of Technology
School of Materials Science and Engineering
778 Atlantic Drive
Atlanta, GA 30332-0245
T 404-894-2887; F 404-894-9140
arun.gokhale@mse.gatech.edu

Prof. Nigel D. Goldenfeld
University of Illinois, Urbana-Champaign
Beckman Institute
Loomis Lab, MC 704
1110 W Green
Urbana. IL 61801
T 217-333-8027
nigel@uiuc.edu
nigel@guava.physics.uiuc.edu

Dr. Vladimir D. Golyshev
All-Union Science Res. Inst. of Mineral
Raw Mat. Synthesis, VNIISIMS
Institutskaya str 1
Alexandrov-City 601600
Vladimirskaya Region; Russia
T 7-095-584-5816 or 7-(09244)92693
F 7-095-584-5816
post@thermo.vladimir.su

Dr. M. Gonik
All-Union Science Res. Inst. of Mineral
Raw Mat. Synthesis, VNIISIMS
Institutskaya str 1
Alexandrov-City 601600
Vladimirskaya Region, Russia
F 7-095-584-5816

Prof. Brian Grady
University of Oklahoma
School of Chemical Engineering and Materials Science
100 East Boyd, EC Rm. T-223
Norman, OK 73019-0628
T 405-325-4369; F 405-325-5813
bpgrady@mailhost.ecn.ou.edu

Prof. Alan R. Greenberg
University of Colorado, Boulder
Department of Mechanical Engineering
Campus Box 427
Boulder, CO 80309-0427
T 303-492-6613; F 303-492-4637
alan.greenberg@colorado.edu

Dr. Richard N. Grugel
NASA MSFC
Mail Code SD47
Marshall Space Flight Center
MSFC, AL 35812
T 256-544-9165; F 256-544-8762
richard.grugel@msfc.nasa.gov

Prof. Turgut M. Gür
Stanford University
Laboratory for Advanced Materials
McCullough Building, Room 135
476 Lomita Mall
Stanford, CA 94305-4045
T 650-723-6597; F 650-723-3044
turgut@stanford.edu

Prof. D. E. Gustafson
Vanderbilt University
Department of Chemical Engineering
P.O. Box 1604, Station B
Nashville, TN 37235

Mr. Robert J. Gustafson
Orbital Technologies Corp. (ORBITEC)
Space Center
1212 Fourier Drive
Madison, WI 53717
T 608-827-5000 Ext. 225
F 608-827-5050
gustafsonr@orbitec.com

Prof. Naomi J. Halas
Rice University
ECE Department - Mail Stop 366
6100 South Main
Houston, TX 77251
T 713-348-5611; F 713-348-5686
halas@rice.edu

Prof. Daniel A. Hammer
University of Pennsylvania
120 Hayden Hall
3320 Smith Walk
Philadelphia, PA 19104
T 215-573-6761; F 215-573-2071
hammer@seas.upenn.edu

Mr. Glen Haulenbeek
University of Alabama in Huntsville
Von Braun Research Hall, 34-M
Huntsville, AL 35899

Dr. Lawrence H. Heilbronn
Lawrence Berkeley National Laboratory
MS 74-197
One Cyclotron Road
Berkeley, CA 94720
T 510-486-4002; F 510-486-6949
LHHeilbronn@LBL.gov

Prof. John Heinbockel
Old Dominion University
Norfolk, VA 23529
jheinboc@odu.edu

Dr. J. C. Heinrich
University of Arizona
Department of Aerospace and Mechanical Engineering
Tucson, AZ 85721
T 520-621-6118
heinrich@zeus.ame.arizona.edu

Prof. William H. Hofmeister
Vanderbilt University
Department of Chemical Engineering
P.O. Box 1604, Station B
Nashville, TN 37235
T 615-322-7053; F 615-343-3202
hof@vuse.vanderbilt.edu

Dr. Dirk Holland-Moritz
Institut fur Raumsimulation
Deutsches Zentrum fur Luft -und Raumfahrt
Linder Hohe
D-51170 Cologne, Germany
T 49-0-2203-601 3292
F 49-0-2203-61768
dirk.holland-moritz@dlr.de

Prof. Mark D. Hollingsworth
Kansas State University
Chemistry Department
111 Willard Hall
Manhattan, KS 66506
T 785-532-2727; F 785-532-6666
mdholl@ksu.edu

Prof. George M. Homsy
Stanford University
Department of Chemical Engineering
Sauffer Building 3, Room113
Stanford, CA 94305
T 650-723-2419; F 650-723-9780
bud@chemeng.stanford.edu

Dr. Arlon J. Hunt
Lawrence Berkeley National Laboratory
Division of Environmental Energy Technologies
Mail Stop 70-108
One Cyclotron Road
Berkeley, CA 94720
T 510-486-5370; F 510-486-7303
ajhunt@lbl.gov

Dr. Robert W. Hyers
NASA MSFC
Mail Code SD47
Marshall Space Flight Center
MSFC, AL 358123
T 256-544-1683; F 256-544-8762
robert.hyers@msfc.nasa.gov

Dr. Ronald G. Iacocca
Pennsylvania State University
147 Research Building, West
University Park, PA 16802-6809
F 814-863-8211

Prof. Alexander F. Izmailov
Polytechnic University
Department of Chemical Engineering
Six Metrotech Center
Brooklyn, NY 11201
T 718-336-2835; F 718-336-2825
Izmailov@duke.poly.edu

Prof. Kenneth A. Jackson
University of Arizona
Arizona Materials Laboratory
Department of Materials Science and Engineering
4715 East Fort Lowell Road
Tucson, AZ 85712
T 520-322-2981; F 520-322-2993
kaj@aml.arizona.edu

Prof. Lyle Jalbert
University of Alabama, Huntsville
CMMR, Von Braun Research Hall
Huntsville, AL 35899
T 256-824-6963; F 256-824-6944
lyle.jalbert@teleionsolutions.com

Ms. Linda B. Jeter
NASA MSFC
Mail Code SD44
Marshall Space Flight Center
MSFC, AL 35812
T 256-544-7392; F 256-544-5892
linda.jeter@msfc.nasa.gov

Prof. David R. Johnson
Purdue University
School of Materials Engineering
1289 MSEE Building
West Lafayette, IN 47907-1289
T 765-494-7009; F 765-494-1204
davidjoh@ecn.purdue.edu

Dr. J. Jordan
Orbital Technologies Corp. (ORBITEC)
Space Center
1212 Fourier Drive
Madison, WI 53717
T 608-827-5000; F 608-827-5050

Dr. O. Jouravlev
Institute of Chemical Problems of Microelectronics
Vernadsky prospect 86
Moscow 117571, Russia
F 7-095-230-47-56

Dr. Frank Robert Juretzko
University of Alabama
Department of Metallurgical Engineering
Box 870202
Tuscaloosa, AL 35487-0202
T 205-348-1748; F 205-348-8574
juretzko@yahoo.com

Prof. Monica L. Kaforey
Case Western Reserve University
Department of Materials Science and Engineering
330 White Building
10900 Euclid Avenue
Cleveland, OH 44106
T 216-368-4219; F 216-368-3209
mlk14@po.cwru.edu

Ms. Natalie Kaiser
Universitat Freiburg
Kristallograph. Institute
Hebelstrasse 25
D-79104 Freiburg, Germany
T 49-761-203-6455; F 49-761-203-6434
natalie@sgi3.krist.uni-freiburg.de

Mr. Nam Hyun Kang
Pennsylvania State University
Applied Research Laboratory
150 MRI Building, Research Park
University Park, PA 16802
T 814-863-8558; F 814-863-2986
hhk105@psu.edu

Prof. David L. Kaplan
Tufts University
Department of Chemical Engineering
4 Colby Street
Medford, MA 02155
T 617-627-3251; F 617-627-3991
dkaplan1@emerald.tufts.edu

Prof. Alain S. Karma
Northeastern University
Department of Physics
111 Dana Research Center
360 Huntington Avenue
Boston, MA 02115
T 617-373-2929; F 617-373-2943
karma@neu.edu

Dr. Andrey V. Kartavykh
Institute for Chemical Problems of Microelectronics
Vernadsky prospect 86
Moscow 117571, Russia
F 7-095-230-47-56
ihpm@glas.arc.org
L22-icpm@mail.girmet.ru

Dr. Mohammad Kassemi
NTLC/NASA Glenn Research Center
Mail Stop 110-3
21000 Brookpark Road
Cleveland, OH 44135
T 216-433-5031; F 216-433-3793
mohammad.kassemi@grc.nasa.gov

Dr. Piotr Kaszynski
Middle Tennessee State University
Department of Chemistry
Box X076 MTSU
Murfreesboro. TN 37312
F 615-898-5182

Ms. Lara Keefer
Case Western Reserve University
10900 Euclid Avenue
White Building
Cleveland, OH 44106
T 216-368-0119; F 216-368-3209
lak5@po.cwru.edu

Prof. Kenneth F. Kelton
Washington University, St. Louis
Department of Physics
Campus Box 1105
One Brookings Drive
St. Louis, MO 63130
T 314-935-6228; F 314-935-6219
kfk@wuphys.wustl.edu

Prof. Tobias Kerle
University of Massachusetts
Department of Polymer Science
120 Governors Drive
Amherst, MA 01003
T 413-577-1535; F 413-577-1510
kerle@mail.pse.umass.edu

Dr. Ilyas I. Khayrullin
New Jersey Institute of Technology
Department of Electrical and Computer Engineering
University Heights
Newark, NJ 07102-1982

Dr. M.-H. Y. Kim
College of William and Mary
P.O. Box 8795
Williamsburg, VA 23187-8795

Prof. Shinwoo Kim
Hoseo University
Department of Materials Science and Engineering
Baebang Sechul-Ri Asan Chungnam
South Korea
T 82-418-540-5474
swkim@dogsur.hoseo.ac.kr

Mr. James D. Kinnison
The Johns Hopkins Applied Physics Laboratory
11100 Johns Hopkins Road
Laurel, MD 20723-6099
T 443-778-6169; F 443-778-6696
james.kinnison@jhuapl.edu

Dr. John P. Kizito
NCMR
21000 Brookpark Road
Cleveland, OH 44135
T 216-433-2275; F 216-433-3793
jpk5@po.cwru.edu

Prof. Kenneth J. Klabunde
Kansas State University
Department of Chemistry
111 Willard Hall
Manhattan, KS 66506
T 785-532-6849; F 785-532-6666
kenjk@ksu.edu

Prof. Manoochehr M. Koochesfahani
Michigan State University
Department of Mechanical Engineering
East Lansing, MI 48824
T 517-353-5311; F 517-353-7179
koochesf@egr.msu.edu

Prof. Matthew B. Koss
Rensselaer Polytechnic Institute
Materials Science and Engineering Department
CII 4225
110 8th Street
Troy, NY 12180-3590
T 518-276-2844; F 518-276-2198
kossm@rpi.edu

Prof. Sindo Kou
University of Wisconsin, Madison
Department of Materials Science and Engineering
1103 Engineering Research Building
1500 Engineering Drive
Madison, WI 53706
T 608-262-0576; F 608-262-8648
kou@engr.wisc.edu

Prof. Matthew John M. Krane
Purdue University
School of Materials Engineering
West Lafayette, IN 47907
T 765-494-4107; F 765-494-1204
krane@ecn.purdue.edu

Prof. William Krantz
University of Cincinnati
Department of Chemical Engineering
Cincinnati, OH 43221-0171
T 513-5564021 ; F 513-556-6741

Dr. Shankar Krishnan
Containerless Research, Inc.
906 University Place
Evanston, IL 60201
T 847-467-2678; F 847-467-2679
shanky@containerless.com

Prof. Anil D. Kulkarni
St. Louis University Medical Center
3635 Vista at Grand
St. Louis, MO 63110-0250
T 314-268-5274; F 314-268-5180

Mr. Jeffrey C. LaCombe
Rensselaer Polytechnic Institute
Materials Science and Engineering Department
CII Building, Room 4219
Troy, NY 12180
T 518-276-8068; F 518-276-2198
lacomj@rpi.edu

Dr. F.-C. Lai
University of Oklahoma
School of Aerospace and Mechanical Engineering
Room 212
865 Asp Avenue
Norman, OK 73019
F 405-325-1088

Prof. Ravindra B. Lal
Alabama A&M University
Department of Physics
P.O. Box 71
Normal, AL 35762
T 256-858-8148; F 256-851-5622
lal@caos.aamu.edu

Prof. David J. Larson Jr.
SUNY-SB/NASA Headquarters
Mail Code UM
Washington, DC 20546-0001
T 202-358-2237; F 202-358-2837
dlarson@hq.nasa.gov

Prof. C.-M. Lee
University of Pennsylvania
120 Hayden Hall
3320 Smith Walk
Philadelphia, PA 19104

Dr. Sandor L. Lehoczky
NASA MSFC
Mail Code SD40
Marshall Space Flight Center
MSFC, AL 35812
T 256-544-7758; F 256-544-8762
sandor.lehoczky@msfc.nasa.gov

Dr. R. A. Lemdiasov
Worcester Polytechnic Institute
100 Institute Road
Worcester, MA 01609-2280

Mr. Eddie Leonardi
University of New South Wales
School of Mechanical and Manufacturing Engineering
Sydney, NSW 2052, Australia
T 61-2-385-5162; F 61-2-633-1222
e.leonardi@unsw.edu.au

Dr. Fred W. Leslie
NASA MSFC
Mail Code SD47
Marshall Space Flight Center
MSFC, AL 35812
T 256-544-1633; F 256-544-6660
fred.leslie@msfc.nasa.gov

Prof. Jennifer A. Lewis
University of Illinois, Urbana-Champaign
Department of Materials Science and Engineering
Room 212A Ceramics Building
105 S. Goodwin Avenue
Urbana, IL 61801
T 217-244-4973; F 217-244-6917
jalewis@staff.uiuc.edu

Prof. Ben Q. Li
Washington State University
School of Mechanical and Materials Engineering
P.O. Box 642920
Pullman, WA 99164-2920
T 509-335-7386; F 509-335-4662
li@mme.wsu.edu

Prof. Fengcui Li
Clarkson University
International Center for Gravity, Materials Science and Applications
Potsdam, NY 13699-5700
F 315-268-3841

Mr. Chaowalit Limmaneevichitr
University of Wisconsin, Madison
Department of Materials Science and Engineering
1103 Engineering Research Building
1500 Engineering Drive
Madison, WI 53706
F 608-262-8648
limmanee@cae.wisc.edu

Prof. X.-M. Lin
Kansas State University
Department of Physics
111 Willard Hall
Manhattan, KS 66506

Prof. Z. Lin
University of Massachusetts
Polymer Science and Engineering Department
Amhurst, MA 01003-4530

Dr. Aleksey Lomakin
Massachusetts Institute of Technology
Room 13-2014
77 Massachusetts Avenue
Cambridge, MA 02139-4307
T 617-253-6804; F 617-225-2585
aleksey@critical.mit.edu

Dr. W. Loser
Institute of Solid State and Materials Research
Helmholtzstraße 20
D-01069 Dresden, Germany

Dr. Samuel A. Lowry
CFD Research Corporation
215 Wynn Drive
Huntsville, AL 35805-1958
T 256-726-4853; F 256-726-4806
sal@cfdrc.com

Dr. S. Z. Lu
Michigan Technological University
Department of Materials Science and Engineering
College of Enginering
1400 Townsend Drive
Houghton, MI 49931-1295
F 906-487-2934

Dr. Afina Lupulescu
Rensselaer Polytechnic Institute
Materials Science and Engineering Department
Materials Research Center
110 8th Street
Troy, NY 12180
T 518-276-2023; F 518-276-2073
lupula@rpi.edu

Mr. Paul Luz
NASA MSFC
Mail Code SD40
Marshall Space Flight Center
MSFC, AL 35812

Prof. Nancy Ma
University of Missouri, Rolla
Department of Mechanical and Aerospace
Engineering and Engineering Mechanics
1870 Miner Circle
Rolla, MO 65409-0050
T 573-341-4626; F 573-341-6899
ma@umr.edu

Dr. Allen K. MacKnight
Honeywell International Inc.
2525 W. 190th Street
M/S-36-1-93140
Torrance, CA 90504
T 310-512-3307; F 310-512-2246
al.macknight@honeywell.com

Prof. Jules Magda
University of Utah
Department of Chemical and Fuels Engineering
50 S. Central Campus Drive, Rm. 3290
Salt Lake City, UT 84112
T 801-581-7536; F 801-581-8692
jj.magda@m.cc.utah.edu

Ms. Diane C. Malarik
NASA GRC
Mail Stop 500-115
21000 Brookpark Road
Cleveland, OH 44135
T 216-433-3203; F 216-433-8660
diane.malarik@grc.nasa.gov

Dr. Jason T. Manka
Middle Tennessee State University
Department of Chemistry
Box X076 MTSU
Murfreesboro, TN 37312
F 615-898-5182

Prof. Carlos Marin
University of Alabama, Huntsville
CMMR, VBRH, D-29
Huntsville, AL 35899
T 256-824-6950; F 256-824-6944
marinc@email.uah.edu

Prof. Raquel Martin
Tufts University
Department of Chemical Engineering
4 Colby Street
Medford, MA 02155

Prof. Jonathan Masere
University of Southern Mississippi
Department of Chemistry and Biochemistry
P. O. Box 5043
Hattiesburg, MS 39406-5053
T 601-266-5899; F 601-266-6045
jonathan@wave.st.usm.edu

Mr. Larry W. Mason
Lockheed Martin
Mail Stop BO560
P.O. Box 179
Denver, CO 80201-0179
T 303-971-9067; F 303-971-0829
larry.w.mason@lmco.com

Dr. Douglas Matson
Massachusetts Institute of Technology
Materials Processing Center
77 Massachusetts Avenue, Room 8-409
Cambridge, MA 02139
T 617-253-3248; F 617-258-6886
matson@mit.edu

Prof. David H. Matthiesen
Case Western Reserve University
Department of Materials Science and Engineering
420 White Bldg., 10900 Euclid Avenue
Cleveland, OH 44106-7204
T 216-368-1366; F 216-368-3209
dhm5@po.cwru.edu

Prof. Richard J. Matyi
University of Wisconsin, Madison
Department of Materials Science and Engineering
1509 University Avenue
Madison, WI 53706
T 608-263-1716; F 608-262-8353
matyi@engr.wisc.edu

Prof. Richard H. Maurer
Johns Hopkins University
Applied Physics Laboratory
11100 Johns Hopkins Road
Laurel, MD 20723-6099
T 240-228-6482; F 240-228-6099
richard.maurer@jhuapl.edu

Prof. Jimmy W. Mays
University of Alabama at Birmingham
Department of Chemistry
Room 201
Birmingham, AL 35294
T 205-934-8101; F 205-934-8158
jmays@uab.edu

Dr. Sandip Mazumder
CFD Research Corporation
215 Wynn Drive, #501
Huntsville, AL 35805
T 256-726-4856; F 256-726-4806
sm@cfdrc.com

Dr. Konstantin Mazuruk
Universities Space Research Association
Mail Code SD47
Marshall Space Flight Center
MSFC, AL 35812
T 256-544-8633; F 256-544-8762
consty.mazuruk@msfc.nasa.gov

Ms. Sonya D. McCall
North Carolina State University
Materials Science and Engineering Department
Centennial Campus, Research Bldg. 1
Box 7919
Raleigh, NC 27695
T 919-515-8965; F 919-515-8967
sdmccall@unity.ncsu.edu

Dr. Geoffrey B. McFadden
National Institute of Standards and Technology
Computational and Mathematical
Sciences Division
Building 820, Room 365
100 Bureau Drive, Stop 8910
Gaithersburg, MD 20899-8910
T 301-975-2711; F 301-990-4127
mcfadden@nist.gov

Prof. John J. McGrath
Michigan State University
Department of Mechanical Engineering
A106 Research Complex - Engineering
East Lansing, MI 48824-1226
T 517-355-0299; F 517 355-7179
mcgrath@me.msu.edu

Prof. Michael McNallan
University of Illinois, Chicago
CME Department
M/C 246
842 W. Taylor Street
Chicago, IL 60607
T 312-996-2436; F 312-996-2426
mcnallan@uic.edu

Prof. Constantine Megaridis
University of Illinois, Chicago
Department of Mechanical Engineering
Mail Code 251
842 W. Taylor Street
Chicago, IL 60607-7022
T 312-996-3436; F 312-413-0447
cmm@uic.edu

Prof. Eckart Meiburg
University of California, Santa Barbara
Department Mechanical and Environmental Engineering
Santa Barbara, CA 93106
T 805-893-5278; F 805-893-5278
meiburg@Engr.ucsb.edu

Dr. Jack Miller
Lawrence Berkeley National Laboratory
One Cyclotron Road, MS 29-100
Berkeley, CA 94720
T 510-486-7130; F 510-486-7934
J_miller@lbl.gov

Dr. H. A. Mook
Oak Ridge National Laboratory
Neutron Scattering Group
P.O. Box 2008
Oak Ridge, TN 37831-6393
T 423-574-5242; F 423-574-6268
ham@ornl.gov

Dr. Shariar Motakef
CAPE Simulations Inc.
One Bridge Street, Suite 100
Newton, MA 02458
T 617-796-8882 x 101; F 617-796-7870
motakef@capesim.com

Mr. Sundeep Mukherjee
University of Alabama
Department of Metallurgical Engineering
Box 870202
Tuscaloosa, AL 35487-0202
T 205-348-1748; F 205-348-8574
mukhe001@bama.ua.edu

Prof. William W. Mullins
Carnegie Mellon University
Department of Materials Science and Engineering
5000 Forbes Avenue
Pittsburgh, PA 15213
T 412-268-2541; F 412-268-7696
wm06@andrew.cmu.edu

Prof. Bruce T. Murray
State University of New York, Binghampton
Mechanical Engineering Department
P.O. Box 6000
Binghampton, NY 13902-6000
T 607-777-6561; F 607-777-4620
bmurray@binghamton.edu

Dr. Allan S. Myerson
Illinois Institute of Technology
10 West 33rd Street
Chicago, IL 60616
T 718-260-3223; F 718-260-3125
myerson@iit.edu

Prof. Ralph E. Napolitano
Iowa State University
Ames Laboratory
104 Wilhelm Hall
Ames, IA 50011-3020
T 515-294-9101; F 515-294-4291
napolitano@ameslab.gov

Prof. Ranga Narayanan
University of Florida
Department of Chemical Engineering
Gainesville, FL 32611
T 352-392-9103; F 352-392-9513
ranga@che.ufl.edu

Prof. Robert J. Naumann
University of Alabama, Huntsville
Von Braun Research Institute M-43
Huntsville, AL 35899
T 256-824-6846; F 256-824-6919
naumannr@email.uah.edu

Prof. V. Nikolakis
University of Massachusetts, Amherst
Department of Chemical Engineering
Goessmann Laboratory
Amherst, MA 01003

Dr. Paul C. Nordine
Containerless Research, Inc.
910 University Place
Evanston, IL 60201
T 847-467-2678; F 846-467-2679
pnordine@containerless.com

Prof. E. A. O'Rear
University of Oklahoma
School of Chemical Engineering and Materials Science
100 East Boyd, EC Rm. T-223
Norman, OK 73019-0628
F 405-325-5813

Dr. Kinichi Ohsaka
University of Southern California
Aerospace and Mechanical Engineering
Los Angeles, CA 90089-1453
T 714 529-3544; F 714-529-3544

Dr. S. J. Oldenburg
Rice University
ECE Department and Department of Chemistry
Houston, TX 77005

Prof. Aleksandar G. Ostrogorsky
Rensselaer Polytechnic Institute
Department of Mechanical Engineering
JEC 2026
Troy, NY 12180
T 518-276-6975; F 518-276-6025
ostroa@rpi.edu

Dr. T. Peignier
University of Alabama, Huntsville
CMMR, VBRH, D-29
Huntsville, AL 35899
F 256-824-6944

Dr. Matthew R. Pekny
Intel Mask Operations
Mailstop SC2-12
3065 Bowers Avenue
Santa Clara, CA 95054-3202

Prof. John H. Perepezko
University of Wisconsin, Madison
Department of Materials Science and Engineering
1509 University Avenue
Madison, WI 53706-1595
T 608-263-1678; F 608-262-8353
perepezk@engr.wisc.edu

Prof. M. L. Peterson
Kansas State University
Department of Chemistry
311 CHEM-BIOCHEM
Manhattan, KS 66506
T 785-532-5419
mpeterso@ksu.edu

Mr. Vladimir Pines
NASA GRC
Mail Stop 105-1
21000 Brookpark Road
Cleveland, OH 44135

Prof. Lawrence S. Pinsky
University of Houston
Physics Department-5506
4800 Calhoun Blvd.
Houston, TX 77204-5506
T 713-743-3552; F 713-743-3589
pinsky@uh.edu

Dr. Y. B. Pithawalla
Virginia Commonwealth University
Department of Chemistry
1001 W. Main Street
Richmond, VA 23284-2006
F 804-828-8599

Prof. David R. Poirier
University of Arizona
Department of Materials Science and Engineering
P.O. Box 210072
Tucson, AZ 85721-0072
T 520-621-6072; F 520-621-8059
poirierd@u.arizona.edu

Prof. John A. Pojman
University of Southern Mississippi
Department of Chemistry and Biochemistry
P.O. Box 5043
Hattiesburg, MS 39406-5043
T 601-266-5035; F 601-266-6075
john.pojman@usm.edu

Prof. Dmitri Popov
Clarkson University
International Center for Gravity, Materials Science and Applications
Potsdam, NY 13699-5700
T 315-268-7672; F 315-268-3841
popovdi@craft.comp.clarkson.edu

Mr. Timothée Pourpoint
University of Alabama, Huntsville
CMMR
Von Braun Research Hall
Huntsville, AL 35899
T 256-824-6960; F 256-824-6944
pourpot@email.uah.edu

Dr. David L. Price
Argonne National Lab.
MSD-223
9700 S. Cass Ave
Argonne, IL 60439

Prof. Shula Radin
University of Pennsylvania
Department of BioEngineering
3320 Smith Walk
Philadelphia, PA 19104
T 215-898-5140; F 215-573-2071
radin@seas.upenn.edu

Prof. Leo Radzihovsky
University of Colorado, Boulder
Department of Physics
Condensed Matter Laboratory
Boulder, CO 80309-0390
T 303-492-5436; F 303-492-2998
radzihov@lulu.colorado.edu

Prof. Miriam H. Rafailovich
State University of New York, Stony Brook
Department of Materials Science and Engineering
322 Old Engineering Building
Stony Brook, NY 11794-2275
T 631-632-8483; F 631-632-5764
miriam.rafailovich@sunysb.edu

Mr. Balaji Raghothamachar
State University of New York, Stony Brook
Department of Materials Science and Engineering
Stony Brook, NY 11794-2275
T 631-632-8501; F 631-632-8052
braghoth@ic.sunysb.edu

Dr. Valery V. Rakov
Institute for Chemical Problems of Microelectronics
Vernadsky prospect 86
Moscow 117571, Russia
T 7-095-239-9953; F 7-095-233-8869
ihpm@glas.apc.org

Dr. N. Ramachandran
Universities Space Research Assoc.
Mail Code SD47
Marshall Space Flight Center
MSFC, AL 35812
T 256-544-8308; F 256-544-8891
narayanan.ramachandran@msfc.nasa.gov

Prof. Ram Ramanathan
Clarkson University
International Center for Gravity, Materials Science and Applications
Potsdam, NY 13699-5700
F 315-268-3841

Dr. Roger Rangel
University of California, Irvine
Department of Mechanical and Aerospace Engineering
Engineering Gateway 4200
Irvine, CA 92697-3975
rhrangel@uci.edu

Dr. Nasser Rashidnia
NASA GRC
Mail Stop 500-102
21000 Brookpark Road
Cleveland, OH 44135
T 216-433-3622; F 216-433-3793

Mr. Thomas J. Rathz
University of Alabama, Huntsville
Mail Code SD47
Marshall Space Flight Center
MSFC, AL 35812
T 256-544-1409; F 256-544-1374
tom.rathz@msfc.nasa.gov

Prof. Chandra S. Ray
University of Missouri, Rolla
Materials Research Center
Martin E. Straumanis Hall
Rolla, MO 65409
T 573-341-6432; F 573-341-2071
csray@umr.edu

Prof. Liya L. Regel
Clarkson University
International Center for Gravity,
Materials Science and Applications
8 Clarkson Avenue
Box 5814
Potsdam, NY 13699-5700
T 315-268-7672; F 315-268-3833
regel@agent.clarkson.edu

Dr. Won-Kyu Rhim
Jet Propulsion Lab.
M/S 183-401
4800 Oak Grove Drive
Pasadena, CA 91109
T 818-354-2925; F 818-393-5039
won-kyu.rhim@jpl.nasa.gov

Dr. Eric E. Rice
Orbital Technologies Corp.
1212 Fourier Drive
Space Center
Madison, WI 53717
T 608 827-5000 x 230 F 608 827-5050
ricee@orbitec.com

Dr. Michael B. Robinson
NASA MSFC
Mail Code SD47
Marshall Space Flight Center
MSFC, AL 35812
T 256-544-7774; F 256-544-2176
mike.robinson@msfc.nasa.gov

Dr. Jan R. Rogers
NASA MSFC
Mail Code SD47
Marshall Space Flight Center
MSFC, AL 35812
T 256-544-1081; F 256-544-2102
jan.rogers@msfc.nasa.gov

Prof. Gregory S. Rohrer
Carnegie Mellon University
Department of Materials Science and Engineering
Roberts Engineering Hall
Room 143
5000 Forbes Avenue
Pittsburgh, PA 15213
T 412-268-2696; F 412-268-7596
gr20@andrew.cmu.edu

Prof. Christopher M. Roland
North Carolina State University
Department of Physics
Box 8202
Raleigh, NC 27695-8202
T 919-515-3170; F 919-515-7331
roland@gatubela.physics.ncsu.edu

Prof. Paul D. Ronney
University of Southern California
Department of Aerospace and Mechanical
Engineering; OHE 430H
Los Angeles, CA 90089-1453
T 213-740-0490; F 213-740-8071
ronney@usc.edu

Prof. David R. Roth
The Johns Hopkins University
Applied Physics Laboratory
11100 Johns Hopkins Road
Laurel, MD 20723-6099
T 240-228-4022; F 240-228-6696
david.roth@jhuapl.edu

Prof. John A. Roth
Vanderbilt University
Department of Chemical Engineering
Box 1604 B
Nashville, TN 37235
T 615-322-3517; F 615-343-7951
jar@vuse.vanderbilt.edu

Dr. M. Rushyniak
Virginia Commonwealth University
Department of Chemistry
1001 W. Main Street
Richmond, VA 23284-2006
F 804-828-8599

Prof. Thomas P. Russell
University of Massachusetts
Polymer Science and Engineering Department
Amherst, MA 01003-4530
T 413-577-1617; F 413-545-0082
russell@iskra.pse.umass.edu

Dr. Marie-Louise Sabougi
Argonne National Laboratory
MSD-223
9700 S. Cass Ave
Argonne, IL 60439

Prof. Albert Sacco, Jr.
Northeastern University
Center for Advanced Microgravity Material Processing
342 Snell Engineering Center
360 Huntington Avenue
Boston, MA 02115
T 617-373-7910; F 617-373-2209
asacco@coe.neu.edu

Prof. Satwindar S. Sadhal
University of Southern California
Department of Aerospace and Mechanical Engineering
Olin Hall - OHE 430
Los Angeles, CA 90089-1453
T 213-740-0492; F 213-740-8071
sadhal@usc.edu

Prof. Donald R. Sadoway
Massachusetts Institute of Technology
Department of Materials Science and Engineering
77 Massachusetts Avenue, Room 8-109
Cambridge, MA 02139-4307
T 617-253-3487; F 617-253-3487
dsadoway@mit.edu

Dr. Paola Sala
INFI
Milan, Italy

Prof. Rajiv Sampath
Cornell University
Sibley School of Mechanical and Aerospace Engineering
188 Frank H.T. Rhodes Hall
Ithaca, NY 14853-3801
F 607-255-9410

Prof. Paul G. Sanders
Harvard University
Division of Engineering and Applied Sciences
29 Oxford Street
Cambridge, MA 02138-2901
F 617-495-9837

Dr. Robert J. Schaefer
National Institute of Standards and Technology
Metallurgy Division
Materials (223), Room B268, Stop 8550
100 Bureau Drive
Gaithersburg, MD 20899-8550
T 301-975-5961; F 301-926-4553
robert.schaefer@nist.gov

Dr. Marcus Schweizer
Universities Space Research Assoc.
Mail Code SD47
Marshall Space Flight Center
MSFC, AL 35812
T 256-544-4167; F 256-544-8762
marcus.schweizer@msfc.nasa.gov

Prof. Rose Scripa
University of Alabama, Birmingham
Department of Materials Science and Engineering
1075 13th Street S
Birmingham, AL 35294
T 205-934-8453; F 205-934-8437
rscripa@Engr.uab.edu

Prof. Robert F. Sekerka
Carnegie Mellon University
Department of Physics
6416 Wean Hall
Pittsburgh, PA 15213-3890
T 412-268-2362; F 412-681-0648
rs07@andrew.cmu.edu

Dr. Subhayu Sen
Universities Space Research Assoc.
Mail Code SD47
Marshall Space Flight Center
MSFC, AL 35812
T 256-544-8264; F 256-544-8762
s.sen@msfc.nasa.gov

Dr. D. Sengupta
CFD Research Corporation
215 Wynn Drive
Huntsville, AL 35805-1958

Miss Brenda Serrano
University of Florida
Department of Chemical Engineering
P.O. Box 116005
227 CHE
Gainesville, FL 32611
T 352-392-2420; F 352-392-9513
besr@grove.ufl.edu

Dr. C. Seybert
University of California, Berkeley
Department of Materials Science and Engineering
Berkeley, CA 94720
F 510-642-9164

Prof. Mark Shavers
Loma Linda University/JSC
SN3
NASA Johnson Space Center
Houston, TX 77058
T 281-483-5899; F 281-483-5276
mshavers@ems.jsc.nasa.gov

Mr. In-Seok Shin
University of Alabama, Huntsville
VBRH, M-40
Huntsville, AL 35899
T 256-824-6630; F 256-824-6791
shini@email.uah.edu

Dr. J. L. Shinn
NASA LaRC
MS 188 B
NASA Langley Research Center
Hampton, VA 23681
F 757-864-8094

Dr. Laurent Sibille
Universities Space Research Assoc.
Mail Code SD48
Marshall Space Flight Center
MSFC, AL 35812
T 256-544-5221; F 256-544-6660
laurent.sibille@msfc.nasa.gov

Prof. Albert Sievers
Cornell University
Laboratory of Atomic and Solid State Physics
517 Clark Hall
Ithaca, NY 14853-2501
T 607-255-6422; F 607-255-6428
sievers@ccmr.cornell.edu

Prof. Jogender Singh
Pennsylvania State University
Applied Research Laboratory
Engineering Science and Mechanics Department
P.O. Box 30
University Park, PA 16802
T 814-863-9898; F 814-863-2986
jxs46@psu.edu

Dr. N. B. Singh
Northrop Grumman Corporation
Science and Technology Center
ESSS MS-3D14, ATL
1212 Winterson Road
Linthicum, MD 21090
T 410-765-1590; F 410-765-7652
narsingh_b_singh@md.northgrum.com

Dr. Robert C. Singleterry, Jr.
NASA LaRC
Materials Division
Environmental Interactions Branch
Mail Stop 188B
Hampton, VA 23681
T 757-864-1437; F 757-864-8094
r.c.singleterry@larc.nasa.gov

Dr. James Singletery, Jr.
Jet Propulsion Laboratory
4800 Oak Grove Drive
Mail Stop 302-306
Pasadena, CA 91109-8099
T 818-354-5046; F 818-393-4540

Dr. James S. Slepick
University of Illinois, Chicago
Department of Mechanical Engineering
M/C 251, 2039 ERF
842 West Taylor Street
Chicago, IL 60607-7022
F 312-413-0447

Dr. David D. Smith
NASA MSFC
Mail Code SD48
Marshall Space Flight Center
MSFC, AL 35812
T 256-544-7778; F 256-544-2102
david.d.smith@msfc.nasa.gov

Prof. Grant D. Smith
University of Utah
Materials Science and Engineering Department
122 S Central Campus Drive, Rm. 304
Salt Lake City, UT 84112-0560
T 801-585-3381; F 801-581-4816
gsmith2@geoffrey.emro.utah.edu

Prof. V. A. Snyder
Northwestern University
Department of Materials Science and Engineering
2225 North Campus Drive
Evanston, IL 60208-3108
F 847-491-7820

Prof. Kwang Jin Song
Yale University
Mason Lab M15
9 Hillhouse Avenue
New Haven, CT 06520
T 203-432-4342; F 203-432-7654
kwangjin.song@yale.edu

Prof. Christopher M. Sorensen
Kansas State University
Department of Physics
Manhattan, KS 66506
T 785-532-1626
sor@phys.ksu.edu

Prof. K. R. Sridhar
University of Arizona
NASA Ames Research Center
MS 239-23
Moffett Field, CA 94035-1000
T 650-604-1649; F 650-604-1092
sridhar@ares.ame.arizona.edu

Prof. Doru M. Stefanescu
University of Alabama
Department of Metallurgy and Materials Engineering
Solidification Laboratory
Room A-129 Bevill Bldg.
P. O. Box 870202
Tuscaloosa, AL 35487-0202
T 205-348-1748; F 205-348-8574
doru@coe.Engr.ua.edu

Dr. Ingo Steinbach
ACCESS
e.V.
Intzestr. 5
52072 Aachen, Germany
T 49-241-805899; F 49-241-38578
i.steinbach@access.rwth-aachen.de

Prof. S. Stoeva
Kansas State University
Department of Chemistry
111 Willard Hall
Manhattan, KS 66506

Dr. Ching-Hua Su
NASA MSFC
Mail Code SD47
Marshall Space Flight Center
MSFC, AL 35812
T 256-544-7776; F 256-544-8762
ching.hua.su@msfc.nasa.gov

Dr. Frank R. Szofran
NASA MSFC
Mail Code SD47
Marshall Space Flight Center
MSFC, AL 35812
T 256-544-7777; F 256-544-8762
frank.szofran@msfc.nasa.gov

Prof. Daniel R. Talham
University of Florida
Department of Chemistry
P.O. Box 117200
Gainesville, FL 32611-7200
T 352-392-9016; F 352-392-3255
talham@Chemicalufl.edu

Prof. Surendra N. Tewari
Cleveland State University
Department of Chemical Engineering
S.H. 464
Cleveland, OH 44115
T 216-523-7342; F 216-687-9220
tewari@csvax.egr.csuohio.edu

Dr. Sheila Ann Thibeault
NASA LaRC
Mail Stop 188B
Hampton, VA 23681-2199
T 757 864-4250
S.A.Thibeault@larc.nasa.gov

Dr. V. Timchenko
University of New South Wales
School of Mechanical and Manufacturing
Engineering
Sydney, NSW 2052, Australia
T 61-2-385-5162; F 61-2-633-1222

Dr. Padetha Tin
NASA GRC
NCMR
21000 Brookpark Road
Cleveland, OH 44135
T 216-433-8164; F 216-433-5033
padetha.tin@grc.nasa.gov

Dr. Paul Todd
SHOT Inc.
7200 Highway 150
Greenville, IN 47124
T 812-923-9591; F 812-923-9598
ptodd@shot.com

Prof. Lawrence W. Townsend
University of Tennessee
Nuclear Engineering Department
Knoxville, TN 37996-2300
T 865-974-5048; F 865-974-0668
ltownsen@utk.edu

Dr. Ram K. Tripathi
NASA LaRC
MS 188 B
NASA Langley Research Center
Hampton, VA 23681
T 757-864-1467; F 757-864-8094
r.k.tripathi@larc.nasa.gov

Prof. Rohit Trivedi
Iowa State University
Ames Laboratory
100 Wilhelm Hall
Ames, IA 50011-3020
T 515-294-5869; F 515-294-4291
trivedi@ameslab.gov

Dr. James D. Trolinger
MetroLaser Inc.
18010 Skypark Circle, # 100
Irvine, CA 92614-6428
T 949-553-0688; F 949-553-0495
jtrolinger@metrolaserinc.com

Dr. Miroslaw Trznadel
Middle Tennessee State University
Department of Chemistry
Box X076, MTSU
Murfreesboro, TN 37312
F 615-898-5182

Prof. Michael Tsapatsis
University of Massachussets, Amherst
Department of Chemical Engineering
159 Goessmann Laboratory
Amherst, MA 01003
T 413-545-0276; F 413-545-1647
tsapatsi@ecs.umass.edu

Dr. V. Tsvetivsky
All-Union Science Research Institute of Mineral
Raw Materials Synthesis
VNIISIMS
Institutskaya str 1
Alexandrov-City 601600
Vladimirskaya Region, Russia
F 7-095-584-5816

Dr. Dennis Tucker
NASA MSFC
Mail Code SD70
Marshall Space Flight Center
MSFC, AL 35812
T 256-544-2685; F 256-544-2659
dennis.tucker@msfc.nasa.gov

Dr. V. Ufimtsev
Institute for Chemical Problems of Microelectronics
Vernadsky prospect 86
Moscow 117571, Russia
F 7-095-230-47-56

Prof. Regina Valluzzi
Tufts University
Bioengineering Center
4 Colby Street
Medford, MA 02155
T 617-627-3136; F 617-627-3991
rv@marvin.tufts.edu

Prof. Peter G. Vekilov
University of Alabama, Huntsville
CMMR, VBRH, D-29
Huntsville, AL 35899
T 256-824-6892; F 256-824-6944
peter@cmmr.uah.edu

Prof. Dionisios G. Vlachos
University of Massachusetts, Amherst
Department of Chemical Engineering
159 Goessmann Laboratory
Amherst, MA 01003
T 413-545-6143; F 413-545-1647
vlachos@snail.ecs.umass.edu

Dr. Marcus Vlasse
NASA MSFC
Mail Code SD10
Marshall Space Flight Center
MSFC, AL 35812
T 256-544-7781; F 256-544-7128
marcus.vlasse@msfc.nasa.gov

Dr. Vitaly Volpert
Université Lyon I
Laboratoire d'Analyse Numirique
Batiment 101
43 bd du 11 Novembre 1918
69622 Villeurbanne Cedex, France
T 33 4 72 44 83 17; F 33 4 72 44 80 53
VOLPERT@LAN1.UNIV-LYON1.FR

Dr. Martin P. Volz
NASA MSFC
Mail Code SD47
Marshall Space Flight Center
MSFC, AL 35812
T 256-544-5078; F 256-544-8762
martin.volz@msfc.nasa.gov

Prof. Peter W. Voorhees
Northwestern University
Department of Materials Science and Engineering
2225 North Campus Drive
Evanston, IL 60208-3108
T 847-491-7815; F 847-491-7820
p-voorhees@northwestern.edu

Dr. Ljubomir Vujisic
CAPE Simulations Inc.
One Bridge Street, Suite 100
Newton, MA 01752
T 617-796-8882 x 103
F 617-796-7870
vujisic@capesim.com

Prof. John S. Walker
University of Illinois, Urbana
Mechanical and Industrial Engineering Department
140 Mechanical Engineering Building
1206 West Green Street
Urbana, IL 61802
T 217-333-7979; F 217-244-6534
jswalker@uiuc.edu

Dr. D. B. Wallace
Microfab Technologies
1104 Summitt Avenue
Plano, TX 75074

Dr. Y. Wang
Clarkson University
International Center for Gravity, Materials
Science and Applications
Box 5814
Potsdam, NY 13699-5814
F 315-268-3833

Prof. J. Douglas Way
Colorado School of Mines
Chemical Engineering and Petroleum Refining
Department
1500 Illinois Street
Golden, CO 80401-1887
T 303-273-3519; F 303-273-3730
dway@mines.edu

Dr. Richard Weber
Containerless Research, Inc.
906 University Place
Evanston, IL 60201-3149
T 847-467-2678; F 847-467-2679
weber@containerless.com

Prof. Francis C. Wessling
University of Alabama, Huntsville
CMDS, VBRH, M-65
301 Sparkman Drive
Huntsville, AL 35899
T 256-824-6620; F 256-824-6791
wessling@email.uah.edu

Dr. A. A. Wheeler
University of Southampton
Highfield
Southampton SO17 1BJ
United Kingdom

Prof. Joe B. Whitehead Jr.
University of Southern Mississippi
Department of Physics and Astronomy
Box 5046
Hattiesburg, MS 39406
T 601-266-4934; F 601-266-5149
Joe.Whitehead@usm.edu

Ms. Michaela E. K. Wiegel
Massachusetts Institute of Technology
77 Massachusetts Avenue
13-4150
Cambridge, MA 02139
T 617-253-2381; F 617-253-5827
wiegel@mit.edu

Prof. William R. Wilcox
Clarkson University
International. Center for Gravity, Materials
Science and Applications
Box 5814
Potsdam, NY 13699-5814
T 315-268-7672; F 315-268-3833
wilcox@clarkson.edu

Dr. Hermann Wilke
Institute for Crystal Growth
Rudower Chaussee 6
D-12489 Berlin – Adlershof
Germany

Prof. Donna Wilson
Tufts University
Department of Chemical Engineering
4 Colby Street
Medford, MA 02155

Dr. John W. Wilson
NASA LaRC
Materials Division
Mail Stop 188-B
8 West Taylor Street
Hampton, VA 23681-0001
T 757-864-1414; F 757-864-7730
john.w.wilson@larc.nasa.gov

Dr. Thomas L. Wilson
NASA JSC
Mail Code SN3
Houston, TX 77058
T 281-483-2147; F 281-483-5276
thomas.l.wilson@jsc.nasa.gov

Mr. William K. Witherow
NASA MSFC
Mail Code SD48
Marshall Space Flight Center
MSFC, AL 35812
T 256-544-7811; F 256-544-2102
bill.witherow@msfc.nasa.gov

Prof. August F. Witt
Massachusetts Institute of Technology
Department of Materials Science and Engineering
77 Massachusetts Avenue, Room 13-4138
Cambridge, MA 02139-4307
T 617-253-5303; F 617-253-5728
afwitt@mit.edu

Mr. Daniel Wolfe
Rice University
ECE Department and Department of Chemistry
Houston, TX 77005

Prof. Y.-Y. Won
University of Minnesota
Department of Chemical Engineering and Materials Science
Amundson Hall
421 Washington Avenue S.E.
Minneapolis, MN 55455-0132

Prof. Andrew Yeckel
University of Minnesota
Chemical Engineering and Materials Science
421 Washington Avenue SE
Minneapolis, MN 55455
T 612-626-9455; F 612-626-7246
yeckel@cems.umn.edu

Prof. Nicholas J. Zabaras
Cornell University
Sibley School of Mechanical and Aerospace Engineering
188 Frank H.T. Rhodes Hall
Ithaca, NY 14853-3801
T 607-255-9104; F 607-255-9410
zabaras@cornell.edu

Dr. J. Zaccaro
CNES
Laboratoire de Cristallographie
BP 166 38042
Grenoble cedex 09, France

Dr. Anvar A. Zakhidov
Honeywell Inc.
Honeywell Technical Center (HTC)
101 Columbia Road
Morristown, NJ 07962-1021
T 973-455-3935; F 973-455-5991
anvar.zakhidov@honeywell.com

Dr. J. Zartman
University of Colorado, Boulder
Department of Mechanical
Engineering
Campus Box 427
Boulder, CO 80309-0427
F 303-492-4637

Dr. Cary Zeitlin
Lawrence Berkeley National Laboratory
One Cyclotron Road
Mail Stop 29-100
Berkeley, CA 94720
T 510-486-5518; F 510-486-6949
cjzeitlin@lbl.gov

Dr. H. Zhang
Northrop Grumman Corporation
Science and Technology Center
ESSS MS-3D14, ATL
1212 Winterson Road
Linthicum, MD 21090
F 410-765-7652

Prof. Hui Zhang
State University of New York, Stony Brook
Department of Mechanical Engineering
Stony Brook, NY 11794-2300
T 631-632-8492; F 631-632-8544
Hui.Zhang@sunysb.edu

Prof. Evgenii V. Zharikov
Russian Academy of Sciences
General Physics Institute
Laser Materials and Technology Research Center
Vavilov Street 38, Build. D
117942 Moscow, Russia
T 7-095-135-8352; F 7-095-135-0270
zharikov@Isk.gpi.ru

Dr. Shen Zhu
Universities Space Research Assoc.
Mail Code SD47
Marshall Space Flight Center
MSFC, AL 35812
T 256-544-2916; F 256-544-8762
shen.zhu@msfc.nasa.gov

Prof. Maria I. Zugrav
University of Alabama, Huntsville
CMDS, VBRH D-29
301 Sparkman Drive
Huntsville, AL 35899
T 256-824-6650; F 256-824-6944
zugravm@email.uah.edu

Task Checkoff List for Testing Processing Electronic Documents in IPS Date: 6/15/2001		
	IPS ID: 2001 082 994	Report Number: CP-2001-210827
Title: MICROGRAVITY MATERIALS SCIENCE CONFERENCE 2000 VOL. 2		
IPS Eval	Task (User: PNF)	Enter comments, recommendations. A ✓ means the process was satisfactory.
Start:	open IPS record / document file Internal Retieval System or DMX2000	
	What format did you view: txt, pdf, tif preference/why	
	What tasks did you have difficulty with?	
End:	copy & paste from electronic doc	
IPS Ctlg	Task (User:)	
Start:	open IPS record / document file Internal Retieval System or DMX2000	
End:	What format did you view: txt, pdf, tif preference/why	
	What tasks did you have difficulty with?	
IPS A&I	Task (User:)	
Start:	open IPS record / document file Internal Retieval System or DMX2000	
End:	What format did you view: txt, pdf, tif preference/why	
	What tasks did you have difficulty with?	
IPS QA	Task (User:)	
Start:	open IPS record / document file Internal Retieval System or DMX2000	
End:	What format did you view: txt, pdf, tif preference/why	
	What tasks did you have difficulty with?	

THE EFFECT OF MICROGRAVITY ON THE GROWTH OF SILICA NANOSTRUCTURES

D.D. Smith[1*], L. Sibille[2*], R. Cronise[1], S.J. Oldenburg[3†], D. Wolfe[3‡], and N.J. Halas[3]

[1]Microgravity Sciences and Applications Dept., NASA Marshall Space Flight Center
[2]Universities Space Research Association, NASA Marshall Space Flight Center
[3] ECE Dept. and Dept. of Chemistry, Rice University, Houston, TX 77005

The process of the formation of structures from coagulating ensembles is fundamentally important since the collective behavior of the constituents often results in dramatically improved or unusual mechanical, thermal, chemical, and optical properties. In this study we examine the effect of microgravity on the formation of silica structures, specifically particles and gels.

There is previous evidence that the formation of this "soft" matter is altered in microgravity. The first commercially available products from space (still available from NIST) were the monodisperse latex sphere standards of Vanderhoff *et al.* who demonstrated that emulsion polymerization of latexes in space resulted in better monodispersity, increased uniformity and reduced coagulation (1). In addition it has been hypothesized that in unit gravity, buoyancy driven fluid flows and sedimentation deleteriously perturb sol-gel substructures prior to gelation, and these perturbations are "frozen" into the resulting microstructure (2,3). Wessling *et al.* (4) have reported that the formation of polyurethane foams in low gravity reduced the average void size, increased the pore roundness, and narrowed the standard deviation in pore size. Leontjev *et al.* (5) observed fluid flows due to convection and sedimentation during the formation of polyacrylamide gels, and deduced from electrophoretic separations that the resulting pore size distributions were narrower for gels formed in microgravity. More recently Zhu *et al.* (6,7) have shown that colloidal crystals of polymethylmethacrylate (PMMA) formed in microgravity are an order of magnitude larger and that completely different polymorphs can result. Okubo *et al.* have studied the kinetics of the formation of colloidal silica particles (both from aqueous silicates and alkoxides) during parabolic aircraft flights using dynamic light scattering and transmission measurements and have found that their formation rate is considerably reduced in microgravity (8).

Stable silica nanoparticle dispersions may be formed either by polymerization of silicic acids or through hydrolysis and condensation of silicon alkoxides (the sol-gel or Stöber route). These two routes are distinguished from one another by the mechanism of particle formation. Comparison of nuclear magnetic resonance (NMR) spectra obtained from Ludox, a commercial aqueous silicate, with acid-catalyzed silicon alkoxides has demonstrated that solutions of the former are dominated by monomers and tetra-functionalized species, whereas di- and tri-functionalized species dominate for alkoxides (9). Moreover, comparison of small-angle x-ray scattering (SAXS) measurements of Ludox with acid- and base-catalyzed alkoxides shows that only aqueous silicate sols are uniform, whereas alkoxides generate fractal particles (10). As Brinker points out (9), these results illustrate that sols derived from aqueous silicates are fully hydrolyzed and grow by classical monomer addition resulting in uniform polymeric

*These authors should be considered of equal importance
†Present Address: Seashell Technologies, San Diego, CA 92116
‡Present Address: Department of Chemistry, Harvard University, Cambridge, MA 02138

particles, whereas sols derived from silicon alkoxides grow through cluster aggregation and retain a fractal inner morphology even while the particles coarsen through surface tension reorganization.

Two distinct regimes characterize particle growth; diffusion-limited, in which the transport of mass to the growing structure is the dominant limitation to growth; and reaction-limited, in which the efficiency of attachment limits the growth process. These two regimes are universal; the structures formed in one regime are strikingly similar even from vastly different material systems (11). In general, diffusion-limited conditions result in a reduction in the growth rate because there is a decrease in the frequency of collisions. Moreover, those species that do collide do not have the chance to do so in an energetically favorable configuration; i.e. exterior sites are favored. As a result, aggregates formed in diffusion-limited conditions are distinguished by lower fractal dimensions. Reaction-limited growth, on the other hand, is characterized by more compact structures. The sticking coefficient is small enough that species are able to sample attachment sites for energetically favorable configurations.

In this study the formation of silica Stöber particles in microgravity is examined. Microgravity allows diffusion-limited conditions to persist in recipes which typically are reaction-limited, essentially expanding the parameter space under which diffusion-limited conditions prevail, and providing us with a snapshot of the aggregation process that would not normally be accessible. In the case of silica nanostructures, microgravity provides a bias towards diffusion-limited cluster-cluster growth, altering structure formation, and generally resulting in lower fractal dimensions.

Four different recipes were developed in laboratory preparations using the Stöber method (12,13). Silica Stöber particles grown on the ground are of good quality in the range 100 - 700 nm. However, at certain precursor concentration ratios the particles are either polydisperse, bimodal, rough, or partially aggregated. Hence the recipes were carefully chosen to examine these "failure conditions," essentially spanning a large portion of the parameter space over which Stöber particles may be produced. The first recipe (R1) was a control sample chosen to produce the best possible particles in terms of monodispersity and sphericity. The second recipe (R2) was chosen to produce the smallest Stöber particles, which tend to be rough, irregular, and less monodisperse. The third recipe (R3) was chosen to produce a bimodal size distribution, while the fourth recipe (R4) was chosen to produce large irregular (nonspherical) particles. The stoichiometry of each recipe is shown in Table 1. Note that only recipes R3 and R4 contain additional water.

Table 1. Stiochiometry of silica sol-gel recipes.

Recipe	TEOS (ml)	Ethanol (ml)	Water (ml)	NH_4OH (ml)
R1	0.140	4.21	n.a.	0.654
R2	0.153	4.59	n.a.	0.245
R3	0.446	3.81	0.576	0.170
R4	0.335	3.58	0.420	0.665

For the space-flight experiment, each 5 ml recipe was divided into two parts and loaded into coupled polyurethane (Hydex) syringes separated by a breakable Parafilm seal to enable mixing of the reactants. The first part consisted of tetraethylorthosilicate (TEOS) and half the ethanol, while the second part consisted of water, ammonium hydroxide (30% NH_3), and the remaining ethanol. Each batch was also divided into ground and space samples, which were stoichiometrically identical. The designated space samples (12 total, 3 per recipe) were then placed in the Gelation of Sols; Applied Microgravity Re-

search (GOSAMR) hardware and activated aboard the space shuttle orbiter (mission STS-95) after microgravity conditions had been established. The GOSAMR hardware, built by 3M Corporation and refurbished for this experiment, essentially consists of a set of modules, each of which contains 8 coupled syringe cartridges. Upon activation a battery-powered motor-driven lead screw with a reversing actuator drives the syringe cartridges back and forth, which mixes the solutions after breaking the barrier seals between them. Upon return of the flight samples, an ultraprobe sonicator was used to obtain diluted suspensions of the samples in ethanol, and these were allowed to evaporate onto carbon coated copper tunneling electron microscope (TEM) grids.

Visual inspection revealed that each of the space-grown samples had formed marginally coherent low-density gels, and that these gels coexisted in the syringe with regions of solvent. Ground-grown samples remained in suspension. The resulting ground control particles were only slightly different in size and polydispersity from the laboratory preparations. A dramatic difference between the ground-grown silica structures and those grown in microgravity was observed. Whereas growth in unit gravity produces Stöber particles, growth in microgravity favors loose gel structures. In fact for recipes R1 and R2 it was difficult to find any Stöber particles at all in the space-grown samples. However, all space-grown samples did form gels, and these gels had a common form and scale which was nearly recipe independent. The particles making up the backbone of the gel were elongated with diameters of approximately 10 nm and lengths of about 50 nm. These gels are similar to the structures observed by Yoshida (14).

For the recipes containing added water, R3 and R4, the particles making up the gel backbone were slightly wider and less elongated. These spheres tended to be smaller and have much larger size distributions than Stöber particles formed on the ground. As shown by Bogush and Zukowski (15,16), the coexistence of large monodisperse spheres (50 - 250 nm) with smaller (~ 10 nm) aggregating primary particles implies that the growth of silica Stöber particles does not occur by the classical nucleation and growth model, where a fixed number of particles are produced in a single event. Rather Bogush and Zukowski deduced that nucleation of particles proceeds continuously throughout most of the reaction period. The smaller primary particles form by the classical monomer addition growth mechanism and then aggregate because of their small size, until they become colloidally stable. Bogush and Zukoski propose that the resulting stable aggregates are the building blocks for the formation of Stöber particles, collecting smaller aggregates and newly formed particles as they are transported through the solution. Therefore, in this view, reaction-limited conditions must persist to maintain smooth spherical particles. The final structure then coarsens through surface tension reorganization to form the resulting Stöber particle.

In contradiction with Bogush and Zukoski, Harris *et al.* (17,18) and also van Blaaderen and Vrij (19) have argued that if growth continued to occur through aggregation of subparticles, smooth spherical particles cannot result. In their view Stöber particles initially grow by aggregation of subparticles but monomer addition later fills in the nonuniformities, resulting in a smooth particle. The irregular shape of smaller Stöber particles is a remnant of the aggregation mechanism not yet enveloped by the subsequent monomer growth. The size difference between the subparticles and the resulting Stöber particles certainly supports this view, since this difference is likely too small even for reaction-limited conditions to yield a smooth surface. Furthermore, although only a few Stöber particles formed in microgravity, those that did form were smooth. Hence, the fact that smooth particles are obtained even in the absence of reaction-limited conditions further supports this view.

Thus, it is not valid to consider silica sol-gels as either particulate or polymeric, they are both. The small, ~10nm , subparticles are primarily polymeric representing the solubility limit of the molecule as a

result of its increasing size and degree of cross-linking [20]. As pointed out by Bailey and Mecartney [21], upon falling out of solution these polymeric precursors collapse, ultimately resulting in a compact particle due to continued hydrolysis and condensation. On the other hand, Stöber particles are at least to some extent particulate, initiated from stable "seeds" formed by aggregation of subparticles, and later smoothed out due to continued addition of monomers.

Colloid stability therefore plays an important role in silica particle formation and morphology to the extent that it determines the size of the aggregates that constitute and augment the particle early in the growth process. According to DLVO theory (22), colloid stability is greatly affected by ionic strength, and the presence of water stabilizes these constitutive aggregates at smaller radii. Hence particle nucleation and growth is more readily established in the presence of water, which in part explains the greater population of Stöber particles in the water-containing recipes R3 and R4. In addition, the kinetics of the formation of these aggregates depends on the degree to which the system is diffusion-limited or reaction-limited. Hence microgravity results in a decrease in the rate of formation of these constitutive aggregates due to a bias towards diffusion-limited conditions. Significant monomer depletion (into subparticles and smaller soluble species) then occurs faster than the time it takes for stable aggregates to form and initiate Stöber particle growth, leading to a preponderance of unstable subparticles and aggregates which eventually compose the loosely formed gel that we observe.

Since diffusion is present at any level of gravity, whereas buoyancy driven convection is not, the effect of microgravity on Stöber particle growth can be understood simply through its effect on diffusion. According to the Stokes-Einstein relation, the diffusion coefficient D for particles undergoing Brownian diffusion is

$$D \propto \frac{1}{r_{eff}} = \frac{1}{m^{1/d(g)}} \qquad (1)$$

where r_{eff} is the effective radius of the particle, m is the mass, and d(g) is the mass fractal dimension (which depends in some manner on gravitational acceleration g). Note that the diffusion coefficient only depends on gravity indirectly, through the dependence of the fractal dimension on gravitationally dependent transport mechanisms (convection and sedimentation). Various experiments and computer simulations have demonstrated that in general both diffusion-limited conditions and cluster-cluster aggregation produce more extended structures than reaction-limited monomer growth conditions, resulting in smaller fractal dimensions (23,24). Because in the Stöber route the dominant growth mechanism changes with substructure size, the bias towards diffusion-limited conditions obtained in microgravity leads to a larger decrease in d for larger substructures. Accordingly, from Equation 1 it can be seen that the diffusion coefficient is reduced to a greater degree for larger substructures (aggregates) in microgravity. Hence the activation barrier for Stöber particle formation is increased in microgravity. For Stöber particles that do manage to form, however, monomer addition again becomes important and the diffusion coefficient of incorporating species increases. The effect of microgravity is therefore to further increase the difference in the growth rates for different growth mechanisms. Equivalently, microgravity suppresses the coagulation of subparticles and aggregates more dramatically than it does their formation through addition of monomers and other small soluble species.

The importance of the aggregation of unstable clusters and subparticles to the formation and growth of silica Stöber particles makes the effect of microgravity on Stöber particle growth profound. Rather than simply retarding structure growth (in this case a silica sol) as would be expected for a singular growth mechanism, a pathway to an entirely different structure becomes available. Microgravity favors diffusion-limited conditions, which slows the formation of stable particle-forming aggregates. Monomers are

consumed more by unstable subparticles and aggregates than by Stöber particles. Eventually cluster-cluster aggregation is the only remaining growth mechanism which yields more extended structures leading ultimately to gel formation. These results suggest that microgravity favors the formation of more rarefied sol-gel structures, providing a bias towards diffusion-limited cluster-cluster aggregation.

REFERENCES

1. J.W. Vanderhoff, M.S. El-Aasser, F.J. Micale, E.D.Sudol, C.M. Tseng, and H.R. Sheu, *ACS Polymer Preprints* 28, 455 (1987); *Mater. Res. Soc. Symp. Proc.* 87, 213 (1987).
2. D.A. Noever, *Microgravity Science and Technology* 3, 14 (1994).
3. L. Sibille, R.J. Cronise, D.A. Noever, and A.J. Hunt, *Proc. Space Technology and Applications International Forum, 1st Conference on Commercial Development of Space*, Albuquerque, January 7-11, p. 451, 1996.
4. F.C. Wessling, S.P. McManus, J. Mathews, and D. Patel, *J. of Spacecraft and Rockets* 27 (8), 324 (1990).
5. V.B. Leontjev, Sh.D. Abdurakhmanov, M.G. Levkovich, "Study of polyacrylamide gels synthesized during microgravitation," *Proc. AIAA Microgravity Science Symposium*, Moscow, May 13 – 17, 274 (1991).
6. J.X. Zhu, M. Li, S.E. Phan, W.B. Russel, P.M. Chaikin, R. Rogers, M. Meyer, "Dynamics of disorder-order transitions in hard sphere colloidal dispersions in microgravity," *3rd Microgravity Fluid Physics Conference*, CP 3338, 397 (1996).
7. J.X. Zhu, M. Li, R. Rogers, W. Meyer, R.H. Ottewill, STS-73 Space Shuttle Crew, W.B. Russel, P.M. Chaikin, *Nature* 387, 883 (1997).
8. T. Okubo, A. Tsuchida, K. Kobayashi, A. Kuno, T. Morita, M. Fujishima, and Y. Kohno, *Colloid. Poym. Sci.* 277, 474 (1999).
9. C.J. Brinker, in *The Colloid Chemistry of Silica*, H.E. Bergna, Ed. (American Chemical Society, Washington, 1994), p. 361.
10. D.W. Schaefer, J.E. Martin, and K.D. Keefer, in *Physics of Finely Divided Matter*, N. Bocarra and M. Daoud, Eds. (Springer-Verlag, Berlin, 1985), p. 31.
11. M.Y. Lin, H.M. Linday, D.A. Witz, R.C. Ball, R. Klein, P. Meakin, *Nature* 339, 360 (1989).
12. W. Stöber, A. Fink, and E. Bohn, J. Colloid Interface Sci. 26, 62 (1968)
13. R. D. Averitt, D. Sarkar, and N.J. Halas, *Phys. Rev. Lett.* 78, 4217 (1997).
14. A. Yoshida in *The Colloid Chemistry of Silica*, H.E. Bergna, Ed. (American Chemical Society, Washington, 1994), p. 51.
15. G.H. Bogush and C.F. Zukoski, *Proc. of the 44th Annual Meeting of the Electron Microscopy Society of America*, G.W. Bailey, ed. (San Francisco Press, San Francisco, 1986), p. 846.
16. G.H. Bogush and C.F. Zukoski in *Ultrastructure Processing of Advanced Ceramics*, J.D. Mackenzie and D.R. Ulrich, eds. (Wiley, New York, 1988), p. 477.
17. M.T. Harris, O.A. Basaran, and C.H. Byers, in *Ultrastructure Processing of Advanced Ceramics*, J.D. Mackenzie and D.R. Ulrich, Eds. (Wiley, New York, 1998), p. 843.
18. M.T. Harris, R.R. Brunson, and C.H. Byers, *J. Non-Cryst. Solids* 121, 397, (1990).
19. A. van Blaaderen and A. Vrij in *The Colloid Chemistry of Silica*, H.E. Bergna, Ed. (American Chemical Society, Washington, 1994), p. 83.
20. P.J. Flory, *Principles of Polymer Chemistry* (Cornell University Press, Ithaca NY, 1953).
21. J.K. Bailey and M.L. Mecartney, *Colloids and Surfaces* 63, 151 (1992).
22. E.J.W. Verwey and J.Th.G. Overbeek, *Theory of the Stability of Lyophobic Colloids* (Elsevier, New York, 1948).
23. P. Meakin in *On Growth and Form*, H.E. Stanley and N. Ostrowsky, Eds. (Martinus-Nijhoff, Boston, 1986), p. 111.
24. P. Meakin, *Ann. Rev. Phys. Chem.* 39, 237 (1988).

POLYMERSOMES: TOUGH, GIANT VESICLES MADE FROM DIBLOCK COPOLYMERS

D.A. Hammer[1]*, D.E. Discher[1,2], F.S. Bates[3], B. Discher[1,2], Y.-Y. Won[3], C.-M. Lee[1,2], H. Bermudez[1], and A. Brannan[3]

[1] Departments of Chemical Engineering, Bioengineering and [2]Mechanical Engineering
University of Pennsylvania, Philadelphia, PA
[3]Department of Chemical Engineering and Materials Science,
University of Minnesota, Minneapolis, MN

Phospholipid vesicles have long been proposed as a method for encapsulating drugs or carrying oxygen and other solutes. However, phospholipid vesicles are mechanically weak and unstable, preventing their useful application or long-term storage. To improve the material properties of water-soluble spherical encapsulators, we hypothesized that amphiphilic block copolymers would, for some regime of molecular weights and block chemistries, serve as an effective substitute for phospholipids. We reasoned that block copolymers that form lamellar phases at dilute concentration at room temperature are likely candidates for making bilayer membranes. The ability to control the molecular weight and chemistry of block copolymers over a wide range, as well as the potential to crosslink polymers, suggests that we could modulate the material properties of the polymer membranes, and perhaps more closely approach the mechanical stability of biological cells.

Polymeric vesicles have been made from polyethylene oxide (PEO) diblock copolymers with either polyethylethylene (PEE) or polybutadiene (PB) tails. The vesicles were made by either electroformation of polymer from a platinum wire in aqueous solution using an oscillatory electric field, or by rehydration of polymers from a glass surface. They proved to be much tougher than typical phospholipid membranes, as measured by micropipette aspiration. We have also demonstrated that reagents such as oxygen binding molecules or fluorophores can be readily incorporated with the vesicle interior, leading toward potential applications such as artificial blood or imaging materials.

I. Materials and Methods

Polymers of PEO-PEE or PEO-PB were made by anionic polymerization (1). Most polymers used were in the range of molecular weights from 3700 to 10000, with hydrophilic block compositions from 0.27 to 0.39. Vesicles were made by drying polymer on 1 mm platinum wire electrodes at 5 mm separation in a 100 mM sucrose solution, and applying in a 10 Hz field with a 10 V amplitude for 15 to 60 minutes, followed by a period in which the frequency was decreased. Texas-Red or myoglobin were encapsulated by incorporating them in the solution during vesicle synthesis. Polymer vesicles can also be made by spontaneous formation in aqueous solution.

* Corresponding author

Materials properties of vesicles were measured by standard micropipette aspiration procedures (2). Micropipettes from 4 to 7 microns in inner diameter were connected to micromanipulators and pressure manometers and transducers. The deflection of the polymer vesicles within the pipette was generated with the manometer and monitored with optical videomicroscopy on the stage of a Nikon inverted microscope equipped with Hoffman and phase contrast optics.

II. Results and Discussion

Polymer vesicles were readily made using electroformation for PEO-PEE polymers of MW=3900 and ethylene-oxide block fraction of 0.39. These membranes proved to be fluid elastic shells. The tension in the membrane was calculated using the Law of Laplace, relating the pressure difference between the interior of the pipette and the external solution to the curvature of the membrane, assuming the portion of the vesicle outside the pipette was spherical, and the projection within the pipette was terminated by a hemispherical cap. The tension of a EO_{40}-EE_{37} vesicle was plotted as a function of areal strain, revealing two regimes: a low tension regime, from which the bending and area expansion moduli could be measured; and a high tension regime, in which the membrane was stretched and the area expansion modulus can be measured. Histograms of the bending and area expansion moduli show a single peak in these moduli, indicative of a unilamellar bilayer membrane. The values of the bending and area expansion moduli are 0.8×10^{-19} J and 180 mN/m, which are close to the values of these moduli for lipid vesicle membranes. However, the critical strain for membrane failure, and the membrane toughness are far greater than for stearoyl, oleoyl phosphatidylcholine membranes (SOPC). For example, the critical areal strain for SOPC is typically 0.04; for EO-EE vesicles, it is 0.19. Likewise, the toughness of SOPC membranes is 0.05 mJ/m^2, whereas for EO-EE vesicles it is 2.2 mJ/m^2, a factor of forty larger. Preliminary results indicate that vesicles made from larger molecular weight polymers exhibit far larger critical area strains and hence toughnesses. Further, we are systematically varying the molecular weight and block chemistry to assess which combinations can make giant vesicles and how the material properties of the resulting variables vary with these parameters.

Polymeric vesicles can be made from EO-PB block copolymers, and crosslinked using a donor-acceptor pair. Prior to crosslinking, the membrane behaves as a fluid, with the area expansion modulus and the critical areal strain increasing with molecular weight. However, crosslinking the vesicle leads to the generation of a solid like structure with a shear elasticity at least an order of magnitude greater than that of a red blood cell.

The vesicles also exhibit surprising shape transitions as a function of osmotic strength. Although passive structures, they can be induced to go through active shape transformations that suggest analogies with biological cells. These shape transitions will be influenced by gravity, so microgravity will modulate the dynamics and statics of these shape transitions.

REFERENCES

1. Hillmyer, M.A., and F.S. Bates. *Macromolecules* 29, 6994 (1996).
2. Evans, E., and D. Needham. *J. Phys. Chem.* 91, 4219 (1987).
3. Discher, B., Y.-Y. Won, D. Ege, J. C.M. Lee, F. S. Bates, D.E. Discher, and D.A. Hammer. *Science* 284, 1143 (1999).

RADIATION TRANSMISSION PROPERTIES OF *IN-SITU* MATERIALS

L. Heilbronn[1]*, L.W. Townsend[2], F. Cucinotta[3], M.Y. Kim[4], J. Miller[1], R. Singleterry[4], S. Thibeault[4], J. Wilson[4], and C.J. Zeitlin[1]

[1]Lawrence Berkeley National Laboratory
[2]Department of Nuclear Engineering, University of Tennessee
[3]NASA, Johnson Space Center
[4]NASA, Langley Research Center

INTRODUCTION

The development of a permanent human presence in space is a key element of NASA's strategic plan for the Human Exploration and Development of Space (HEDS). The habitation of the International Space Station (ISS) is one near-term HEDS objective; the exploration and settlement of the moon and Mars are long-term goals of that plan. Achieving these goals requires maintaining the health and safety of personnel involved in such space operations at a high level, while at the same time reducing the cost of those operations to a reasonable level.

Among the limiting factors to prolonged human space operations are the health risks from exposure to the space ionizing radiation environment. In order to keep the risk of radiation-induced cancer at acceptable levels, it is necessary to provide adequate shielding from the ionizing radiation environment. The cost of transporting shielding materials to the moon or Mars is prohibitive. One cost-effective method of providing adequate shielding in those environments is to utilize local, *in-situ* materials. Simple techniques may involve covering a transported habitat with local regolith, or using water found on Mars (and recently found on the moon) to augment shielding. Novel shielding techniques are being developed which combine local regolith with resin binders to construct structural materials for use in the building of habitats. The presence of water and a carbon dioxide atmosphere on Mars holds some promise as building blocks in the manufacturing of resin binders.

As the mass of shielding increases, radiation dose decreases. However, as the shielding mass increases, calculations predict (1-3) that the percentage of the dose from neutrons increases, due in part to the high penetrabilities of neutrons. For moderately thick (40 - 50 g/cm^2) shields on lunar and Martian bases, approximately 50% or more of the dose could come from neutrons. A recent workshop (4) conducted at the Johnson Space Center concluded that the dose from neutrons in the ISS could comprise 30 to 60 percent of the total dose. As evident from these predictions, the production of neutrons is an important consideration in the design and development of shielding to be used in various mission scenarios.

Because of the relatively short lifetimes of free neutrons, they are not present in space radiation. Essentially all neutrons in the radiation field are secondary neutrons produced by interactions of primary trapped, Galactic Cosmic Ray (GCR) and Solar Particle Event (SPE) particles in shielding materials and human tissue. The spectrum of primary particles covers a mass range from protons to

* Corresponding author

iron, and covers a range in energy from 50 MeV/nucleon to energies of a few TeV/nucleon. As such, the ability of any calculation to accurately predict the dose from neutrons depends on that calculation's ability to accurately model the production and transport of neutrons generated from an enormous range of interactions. Development and verification of model calculations depend upon a relevant experimental data base of neutron-production cross sections, neutron-interaction cross sections, and thick-target neutron yields.

Much of the experimental data base needed for the development of radiation transport models comes from experiments conducted at ground-based particle accelerators. Particle accelerators do not produce beams that simulate the entire GCR or SPE spectrum at any one time; however, they produce beams of GCR-like particles where the mass, charge, energy, direction, and number of particles interacting in the target is known to a high degree of precision and accuracy. Ground-based experiments that measure secondary neutron production provide highly detailed information in regards to neutron spectra over a large range in neutron energy and angle. Because of these features, the data resulting from such experiments are used to examine the details of physical processes of neutron production (such as nucleon evaporation from target and projectile remnants, breakup of the overlap region between projectile and target, and final-state interactions) which must be incorporated by transport models. These data, then, are of critical importance to the development of models that will ultimately be used to predict risk in complex radiation and shielding environments in space.

The ground-based experiments that are relevant to neutron transport can be divided into three categories: neutron-production cross-section measurements, thick-target neutron-yield measurements, and neutron-interaction cross-section measurements. Cross-section experiments measure neutron spectra created by a projectile at one specific energy, with no contributions from secondary interactions in the target. As stated above, cross-section measurements provide information on the details of the physical processes that produce neutrons in projectile-target interactions. Thick-target measurements refer to experiments where the target is thick enough such that secondary interactions produce a measurable effect on the neutron yield outside the target. Secondary interactions include both neutron production from secondaries interacting with target nuclei and neutron-flux attenuation due to neutron interactions with target nuclei. In addition to the effect of secondary interactions, thick-target measurements also sample primary projectile-target interactions over a large range of projectile energies, as opposed to interactions at one energy in cross section measurements.

The research presented here is a theoretical and ground-based experimental study of neutron production from interactions of GCR-like particles in various shielding components. An emphasis is placed here on research that will aid in the development of *in-situ* resource utilization. The primary goal of the program is to develop an accurate neutron-production model that is relevant to the NASA HEDS program of designing technologies that will be used in the development of effective shielding countermeasures. A secondary goal of the program is the development of an experimental data base of neutron production cross sections and thick-target yields which will aid model development.

I. Model Development

Comparisons of proton-induced neutron yields and cross sections with High Energy Transport Code (HETC) (5) and Bertini (6) intranuclear cascade model calculations have been made over a wide variety of systems (7-12) with incident proton energies similar to those found in space. Generally, the HETC and Bertini calculations do a good job of matching spectral shapes, and do an excellent job of reproducing the magnitudes of the cross sections for interactions with very heavy elements (W, Pb, U). However, the agreement deteriorates for lighter nuclei, where the calculations overestimate the production by a factor of two for low-energy (E = 20 MeV) neutrons (10). For all targets, HETC underestimates the yields at large angles for neutrons above 10 MeV, and underestimates the high-energy yield (above 100 MeV) at forward angles. Note that these observations were made on calculations using the version of HETC that was available between 1989 and 1993. No comparisons with that data have been made with later versions of HETC, and those comparisons may be worth investigating. Zucker, *et al.*, report (13) that LAHET calculations (which they report are similar to the 1996 version of HETC) of their 800-, 1000-, 1200-, and 1400-MeV data sets overestimate the data by 10 to 20 percent.

Boltzmann-Uehling-Uhlenbeck (BUU) calculations have been compared with thick-target neutron yields (14). The BUU calculations do a good job of fitting the data at large angles, both in magnitude and shape. However, at forward angles the BUU calculations either over-predict or under-predict the yield, depending on the angle. This may be due in part to the fact that forward-angle spectra from BUU calculations are sensitive to the cutoff density used to determine whether or not a particle has been emitted. Even though the BUU calculation misses the magnitude of the forward angle spectra, it does a fairly good job in reproducing the shape of those spectra. In comparing calculations with thick-target yields, any discrepancy between data and calculation does not necessarily indicate a problem with the calculated cross sections used as input because the problem may lay with the methodology used in applying those cross sections to produce thick-target yields.

BUU and intranuclear cascade model calculations have varying degrees of success in matching experimental data. The discrepancies between those models and data may suggest that uncertainties may still be large (on the order of 50%) when calculations are made of the neutron fluence behind shielding and tissue in space-related activities. Much of that uncertainty is due to the lack of relevant nuclear data to compare to, but it is also clear that improvements can be made in modeling neutron production. The neutron production model under development in this work is based on an abrasion-ablation fragmentation model (15,16). In the abrasion (knockout) step, the portions of the projectile and target nuclear volumes that overlap are sheared away by the collision. The remaining projectile piece, moving at velocities essentially the same as the pre-collision velocity, is highly excited and decays by gamma and particle emission. This step is called the ablation stage. Improvements to the existing model will include the decay of the overlap region and the decay of the target remnant.

II. Experimental Neutron Data (Ground-Based)

A variety of neutron cross-sections and thick-target yields have been measured from systems applicable to the general problem of radiation transport in space-related activities (see Ref. [4] and references contained therein). The data includes thick-target neutron yields measured from heavy-ion reactions in this project (14,17).

To get an idea of the neutron energies that may be important to consider in terms of crew risk assessment, the neutron yields reported (8) for 256-MeV protons stopping in Al (20-cm long, 54 g/cm^2) have been integrated over the angular range from 30 to 150 degrees. Table I lists the percentage of the total flux (above 0.5 MeV) contained within a specific range of neutron energy for several ranges of energy, along with the percentage of total dose-equivalent. Roughly half of the neutron flux (51%) is below 5 MeV, with 29% of the flux above 20 MeV. However, when considering the dose equivalent, the percentages shift towards higher neutron energies; roughly half (52%) of the dose equivalent is above 20 MeV. This evaluation most likely underestimates the relative importance of neutrons above 20 MeV in space environments because (1) data below 30 degrees, where much of the high-energy neutron flux is contained, is not considered, and (2) although 256 MeV is near the peak of the GCR proton energy distribution, the majority of the GCR proton flux is above 256 MeV. Proton interactions at higher energies will increase the yield of high-energy neutrons relative to the low-energy yield.

Table 1. Percentages of the total neutron flux and total neutron dose equivalent from 256-MeV protons stopping in Al, for the ranges of neutron energy.

Energy range (MeV)	% Neutron flux	% Dose-equivalent
0.5 - 1	13%	6%
1 - 5	38%	28%
5 - 10	13%	9%
10 - 20	7%	5%
20 - 50	9%	12%
50 - 100	13%	25%
100 - 200	6%	13%
>200	1%	2%

An analysis of the heavy-ion data suggests that the neutron multiplicity from interactions in one system can be deduced from the measured multiplicity in another system (at the same projectile energy per nucleon) using the following relationship:

$$\frac{M\,(system1, T>T_0)}{M\,(system2, T>T_0)} = \frac{\sigma(system2)}{\sigma(system1)} \times \left(\frac{(A_{tgt1})^{1/3} + (A_{proj1})^{1/3}}{(A_{tgt2})^{1/3} + (A_{proj2})^{1/3}} \right)^{a(T_0)}$$

where M(system1,$T>T_0$) and M(system2,$T>T_0$) are the neutron multiplicities of system 1 and system 2, T is kinetic energy, T_0 is the neutron energy threshold, σ(system1) and σ(system2) are the total reaction cross sections for systems 1 and 2, A_{tgt1} and A_{proj1} are the target and projectile mass numbers in system 1, A_{tgt2} and A_{proj2} are the target and projectile mass numbers in system 2, and $a(T_0)$ is a parameter from Reference (18). This formalism seems to work well with both neutron cross-section measurements and with thick-target yields in heavy-ion systems. Studies are currently being made to see whether this formalism can be used to reproduce the multiplicities from proton-induced interactions, using the data recently acquired from Meier 7-12.

In April 2000, neutron-production cross-section measurements were made from 290 MeV/nucleon C and 600 MeV/nucleon Ne interactions in prototype of an *in-situ* shielding block developed by NASA Langley Research Center. In addition, neutron cross sections from 400 MeV/nucleon Ne interacting in ISS crew quarter wall materials were also measured. Additional measurements of 290 MeV/nucleon Ne, 400 MeV/nucleon Ar, and 650 MeV/nucleon Ar interactions in *in-situ* materials are planned for late 2000 or early 2001.

REFERENCES

1. L.C. Simonsen, J.E. Nealy, L.W. Townsend and J.W. Wilson, "Radiation Exposure for Manned Mars Surface Missions," NASA Tech. Paper 2979 (1990).
2. L.C. Simonsen and J.E. Nealy, "Radiation Protection for Human Missions to the Moon and Mars," NASA Tech. Paper 3079 (1991).
3. F.A. Cucinotta, "Calculations of Cosmic-Ray Helium Transport in Shielding Materials," NASA Technical Paper 3354, (1993).
4. L. Heilbronn and L.W. Townsend, "Overview of ground-based neutorn measurements applicable to GCR and SPE transport through shielding materials in space," Proceedings of the Workshop "Predictions and Measurements of Secondary Neutrons in Space," Universities Space Reasearch Association, Center for Advanced Space Studies, 3600 Bay Area Boule vard, Houston, TX 77058.
5. T.W. Armstrong and K.C. Chandler, "HETC: A High Energy Transport Code," Nucl. Sci. Eng. 49, 110 (1972).
6. H.W. Bertini, "Intranuclear-Cascade Calculation of Secondary Nucleon Spectra from Nucleon-Nucleus Interactions in the Energy Range 340 to 2900 MeV and Comparison with Experiment," Phys. Rev. 188, 1711 (1969).
7. M.M Meier, W.B. Amian, C.A. Goulding, G.L. Morgan and C.E. Moss, "Differential Neutron Production Cross Sections and Neutron Yields from Stopping-Length Targets for 113-MeV Protons," Nucl. Sci. Eng. 102, 310 (1989).
8. M.M. Meier, C.A. Goulding, G.L. Morgan and J. Ullmann, "Neutron Yields from Stopping- and Near-Stopping-Length Targets for 256-MeV Protons," Nucl. Sci. Eng. 104, 339 (1990).
9. M.M Meier, W.B. Amian, C.A. Goulding, G.L. Morgan and C.E. Moss, "Differential Neutron Production Cross Sections and Neutron Yields from Stopping-Length Targets for 256-MeV Protons," Nucl. Sci. Eng. 110, 289 (1992).
10. W.B. Amian, R.C. Byrd, C.A. Goulding, M.M. Meier, G.L. Morgan, C.E. Moss and D.A. Clark, "Differential Neutron Production Cross Sections for 800-MeV Protons," Nucl. Sci. Eng. 112, 78 (1992).
11. W.B. Amian, R.C. Byrd, D.A. Clark, C.A. Goulding, M.M. Meier, G.L. Morgan, and C.E. Moss, "Differential Neutron Production Cross Sections for 800-MeV Protons," Nucl. Sci. Eng. 115, 1 (1993).
12. M.M. Meier, D.B. Holtkamp, G.L. Morgan, H. Robinson, G.J. Russell, E.R. Whitaker, W.B. Amian and N. Paul, "318 and 800 MeV (p,xn) Cross Sections," Radiat. Effects, 96, 73 (1986).
13. M.S. Zucker, N. Tsoupas, P.E. Vanier, U. von Wimmersperg, S. F. Mughabghab, and E. Schmidt, "Spallation Neutron Production Measurements," Nucl. Sci. Eng. 129, 180 (1998).
14. L. Heilbronn, R. Madey, M. Elaasar, H. Htun, K. Frankel, W.G. Gong, B.D. Anderson, A.R. Baldwin, J. Jiang, D. Keane, M.A. McMahan, W.H. Rathbun, A. Scott, Y. Shao, J.W. Watson, G.D. Westfall, S. Yennello, and W.-M. Zhang, "Neutron yields from 435 MeV/

nucleon Nb stopping in Nb and 272 MeV/nucleon Nb stopping in Nb and Al," Phys. Rev. C. 58, 3451 (1998).
15. F.A. Cucinotta, J.W. Wilson, and L.W. Townsend, NASA Tech. Mem. 4656, (1995).
16. F.A. Cucinotta, J.W. Wilson, and L.W. Townsend, "Abrasion-Ablation Model for Neutron Production in Heavy Ion Collisions," Nucl. Phys. A (1997).
17. L. Heilbronn, R.S. Cary, M. Cronqvist, F. Deak, K. Frankel, A. Galonsky, K. Holabird, A. Horvath, A. Kiss, J. Kruse, R.M. Ronningen, H. Schelin, Z. Seres, C.E. Stronach, J. Wang, P. Zecher, and C. Zeitlin, "Neutron Yields from 155 MeV/Nucleon Carbon and Helium Stopping in Aluminum," Nucl. Sci. and Eng. 132, 1-15 (1999).
18. R. Madey, B.D. Anderson, R.A. Cecil, P.C. Tandy, and W. Schimmerling, Phys. Rev. C 28, 706 (1983).

FORMATION OF $Y_xNd_{1-x}Ba_2Cu_3O_{7-\delta}$ ($0 \leq x \leq 0.7$) SUPERCONDUCTORS FROM AN UNDERCOOLED MELT VIA AERO-ACOUSTIC LEVITATION

D.E. Gustafson, W.H. Hofmeister, and R.J. Bayuzick

Materials Science and Engineering, Vanderbilt University

INTRODUCTION

Melt processing of RE123 superconductors has gained importance in recent years. While the first high temperature superconductors (HTSCs) were made using traditional ceramic press and sinter technology, recent fabrication efforts have employed alternate processing techniques including laser ablation and ion beam assisted deposition for thin film fabrication of tapes and wires and melt growth for bulk materials.[1-4] To optimize these techniques and identify other potential processing strategies, phase relation studies on HTSCs have been conducted on a wide variety of superconducting compounds using numerous processing strategies. This data has enhanced the understanding of these complex systems and allowed more accurate modeling of phase interactions. All of this research has proved useful in identifying processing capabilities for HTSCs but has failed to achieve a breakthrough for wide spread application of these materials. To overcome drawbacks of the sintered material, many researchers have developed new processing routes involving melt processing techniques. Melt processing has significantly advanced the state-of-the-art understanding of superconductivity in polycrystalline bulk materials and has produced materials with J_c of greater than 10^4 A/cm^2.[5] The melt processed materials produced, however, suffer from several shortcomings. Due to incongruent melting of RE123 at high temperatures, liquid phase flows out of the interior of the material resulting in voids, and Ba-Cu rich liquid inclusions may become trapped between grains reducing superconductive properties. Processing rates are very slow, *i.e.* on the order of 50 mm/h for a 25 mm^2 cross sectional area sample.[6] Slow processing rates can also expose the material to moisture and CO_2 which are highly reactive with copper oxide superconductors.[7] Also, distortions and macrocracks form due to severe shrinkage accompanying the melt processing. Large complex shapes are therefore difficult to fabricate by melt processing and the only shapes reported to date have been either disks or bars.[8]

Several researchers have examined the effect of mixed rare earth (RE) atoms in the 123 system referred to as RE123 alloys. Work to date has included oxygen-controlled-melt-growth of RE123 alloys, containerless drop tube processing of RE123 alloys, and directional solidification of RE123 alloys.[9-14] Interesting results include a higher crystallization rate for the alloy compared to the single RE system and a sharper critical temperature (T_c) as well as a higher critical current (J_c) in the alloy compared to the single RE system. Additionally, the liquidus for $Y_{1-x}Nd_xBa_2Cu_3O_{7-\delta}$ was measured by J. R. Olive by processing in a drop tube, and a minimum in the liquidus was found for composition $Y_{.1}Nd_{.9}Ba_2Cu_3O_{7-\delta}$ at 1500°C (±25°C).[15] Additional studies of mixed alloy systems may reveal thermodynamic and kinetic parameters favorable for the fabrication of HTSCs with superior properties.

This study examines the role of full to partial substitution of Nd in the Y123 structure under rapid solidification conditions. Aero-acoustic levitation (AAL) was used to levitate and undercool RE123 in pure oxygen binary alloys with RE = Nd and Y along a range of compositions corresponding to $Y_xNd_{1-x}Ba_2Cu_3O_{7-\delta}$ ($0 \leq x \leq 0.7$) which were melted by a CO_2 laser. Higher Y content spheres could not be melted in the AAL and were excluded from this report. Solidification structures were examined using scanning electron microscopy, electron dispersive spectroscopy, and powder x-ray diffraction to characterize microstructures and identify phases.

I. Experimental Method

Starting powders of orthorhombic RE123 were supplied by Superconductive Components, Inc., fabricated using standard ceramic press and sinter techniques. Levitation spheres were then fabricated in a copper hearth under flowing O_2. The aero-acoustic levitator (AAL) consisted of a O_2 gas jet coupled with a three-axis acoustic positioning system for levitation of samples.[16] The O_2 gas jet was pre-heated to approximately 400°C in the AAL. Melting of samples was accomplished using a CO_2 laser powered by a Rofin-Sinar 1700 SM power supply. The laser beam was split and focused onto opposing sides of each specimen, perpendicular to the gas jet flow. Samples were 2 mm diameter spheres having a mass of 30-50 mg. A typical experiment involved levitating the sample in the O_2 gas jet and heating it with the laser until liquid vortex currents were visible on the surface. After several seconds, the laser beam was shut off and the sample allowed to radiantly cool at 300-400°C/s. Temperature measurements were made using a two-color pyrometer with Si and InGaAs detectors, and recalescence events were recorded using a Kodak EKTAPRO HS Motion Analyzer Model 4540 operating at 4500 frames/s. The resulting samples were examined using scanning electron microscopy, energy dispersive spectroscopy, and powder x-ray diffraction to identify phases and characterize microstructures.

II. Results

Samples were melted by the laser while being levitated and were undercooled several hundred degrees relative to the liquidus before solidification. Solidification of the samples was accompanied by a distinct recalescence event which lasted between 0.2 and 0.3 seconds where the increased emissive intensity was visible to the naked eye. Solidification events varied considerably in duration and intensity depending upon the composition of the sample, but the general solidification mechanism appears to be similar. After the laser was blocked and the sample cooled a few seconds, swirling particles roughly 100 μm in size were seen on the surface of the melt as it spun while levitated. These particles increased in number as the undercooling increased. Solidification events recorded by the Kodak EKTAPRO camera confirmed these observations. Eddies in the swirling melt were observed drawing the particles to a preferred location near the top of the sphere. As the sample continued to cool, the particles continued to cluster until a solid front was seen growing from the top to the bottom of the sphere surface. This front wrapped around the surface of the sphere, enveloping the melt with a shell of solid material. The recalescence event occurred simultaneously and was marked by a distinct flash of light. In this study, the as-solidified morphology of samples fully melted in the AAL can be generalized into three zones, and the zones appear to be caused by thermal gradients across the samples during processing. The first zone encompasses the outer layer of the sphere which solidified first. Here, solidification of the melt proceeded quickly. This outer zone is composed of relatively void-free RE123 and the morphology can be described as faceted. The formation of this layer involved the release of latent heat and resulted in a recalescence event which was recorded by the pyrometer and EKTAPRO camera. The thickness of

this outer layer appears to be a function of composition and varied from a maximum of 500 μm for the Nd rich samples to 200 μm and less for the Y rich samples. In this region, the sample was undercooled, and RE123 formed directly from the undercooled melt. The second zone which lies between the outer zone and the center of the sphere is a relatively thin transitional region where RE211 dendrites are surrounded by RE123 dendrites. The temperature gradient in the sphere just prior to recalescence caused this region to be heated above the peritectic transformation temperature (T_p), and there was no undercooling relative to T_p. The local conditions for the second zone are also altered by formation of the outer zone which further slowed the cooling rate of the bulk of the sphere. The RE211 dendrites in this region solidified heterogeneously at the interface of the solid RE123 and the melt. The dendrites are fine but coarsen closer to the center of the sphere. The third zone is located near the center of the sphere generally adjacent to the shrinkage voids and is dominated by coarse RE211 dendrites with interdendritic Ba-Cu-O. This final zone was formed as the sphere continued to cool, and the microstructure indicates solidification of the zone without undercooling. The Ba-Cu-O liquid, cooled sufficiently and unable to react quickly with the RE211 to form RE123, solidified around the RE211 dendrites.

III. Discussion

Containerless processing with aero-acoustic levitation allows for cooling of molten ceramic samples several hundred degrees below the liquidus until spontaneous crystallization or recalescence occurs. Cooling curves for the processed samples reveal characteristic events which correspond to the release of the latent heat of fusion and the peritectic decomposition temperature (T_p) for RE123. In this work, the uncorrected recalescence temperatures for Nd123 was indicated to be 1043°C (±17°C), and the maximum recalescence temperature was assumed to correspond to T_p for each composition. This indicated temperature is below the previously reported value of T_p for Nd123 by 66°C. Prado *et al.* report the T_p to be 1109°C for Nd123 in pure oxygen.[17] Kambara *et al.* report the T_p for Nd123 in oxygen to be 1112°C.[18] The absolute differences between the reported values and the experiments detailed in this report are attributed to error in the pyrometer which was used to measure temperature in the experiments reported here. This disagreement could not be experimentally confirmed because the pyrometer failed prior to independent calibration. However, by using the difference between the experimental and reported values for Nd123 as an *in-situ* calibration factor, the experimental data was corrected to reflect the actual transformation temperatures for the compositions studied in this work.

Figure 1 is a compilation of the average recalescence events for the binary alloys composed of Nd-Y. For purposes of illustration the traces in Figure 1 are synchronized at the moment of recalescence. The curves were determined by ignoring the erratic events recorded and averaging the temperature as a function of time to represent the characteristic event for each composition. Also, the *in-situ* calibration factor has been applied to the curves to reflect the transformation temperatures. There appears to be some correlation between the size of the recalescence event, as given by the area under the time versus temperature plot, and the volume fraction of RE123 formed from the melt as shown by microstructural examination. The area fraction of RE123 in the micrographs or the volume fraction in the bulk and the size of the recalescence event decreases with increasing Y content of the alloy, or, equivalently, the fraction of RE211 increases with increasing Y content. Although the differences between alloys with less than 50% Y are less pronounced, increasing Y content above 50% dramatically increases the fraction of RE211 which forms during processing in the AAL. The binary alloy compositions rich in Nd revealed the most distinct recalescence events and were the most successful for obtaining relatively single phase RE123 during AAL processing.

Figure 2 is a plot of the experimental peritectic temperatures obtained in this report with error bars representing one standard deviation. These results are also plotted with the liquidus for the Nd-Y alloys for illustration in Figure 3.[19] This plot contains relevant data for researchers employing melt processing techniques. The minimum in the liquidus corresponds to a composition of $Nd_{.9}Y_{.1}123$ while the minimum in the peritectic corresponds to $Nd_{.7}Y_{.3}123$. The minimum in undercooling relative to the liquidus observed in these experiments, however, corresponds to 520°C (corrected) for samples with composition $Nd_{.8}Y_{.2}123$ and $Nd_{.9}Y_{.1}123$. Thus the range of compositions which undercooled less than 600°C to form RE123 directly from the melt extends from Nd123 to $Nd_{.7}Y_{.3}123$. The degree of undercooling for Nd123 to $Nd_{.7}Y_{.3}123$ samples corresponds to approximately 35% of the liquidus. Compositions more rich in Y undercooled more than 650°C below the liquidus to form RE123 directly from the melt, but a considerably larger volume fraction of RE211 appears in these specimens than in Nd rich specimens. The degree of undercooling for the Y-rich specimens was over 40% of the liquidus indicating that it is more difficult to form RE123 from the melt for Y-rich compositions.

Microstructural and pyrometry evidence seem to indicate that the volume fraction of RE123 formed directly from the melt increased as the Nd content in the Nd-Y composition increased. The compositional dependence of phase selection is also evident from a comparison of x-ray diffraction (XRD) spectra. Figure 4 is a comparative plot of XRD data for several Nd-Y alloys. Clearly evident in this plot is the large volume fraction of RE123 for all samples. Also prevalent is the appearance of RE211 peaks in the Y rich alloys. It is possible that the poor thermal conductivity and large degree of undercooling required combine to create large thermal gradients in the Y-rich samples. Thus, processing in the AAL resulted in only an outer shell of the sample which actually undercooled and formed RE123 directly from the melt. The phase stability of RE211 may also play a role in this outcome since RE211 is not a stable phase in the Nd123 system. Increasing the Y content may create favorable conditions for the formation of RE211 during rapid solidification processing in the AAL. The Nd rich binary alloys also have no appreciable second phases or byproducts indicating that the formation of RE123 is favored in the rapid solidification of a melt with a Nd-rich RE123 starting composition. Peaks corresponding to Pt which was present in the x-ray diffractometer are found in all XRD spectra in this report.

Previous processing studies of RE123 at near equilibrium conditions in high oxygen environments resulted in the partial substitution of RE^{3+} for Ba^{2+} and the formation of compounds with the formula $RE_{1+x}Ba_{2-x}Cu_3O_{7-\delta}$. This solid solubility behavior was determined to be undesirable since the RE123 solid solutions have inferior superconducting properties compared to the stoichiometric compounds.[20] Low oxygen partial pressure environments were used to avoid solid solution formation in near compensated by the addition of extra oxygen. Simply removing the oxygen removed the equilibrium melt processing because the substitution of RE^{3+} for Ba^{2+} must be opportunity for solid solution formation in those near-equilibrium processing techniques. In this study, no evidence of substitution of Nd^{3+} for Ba^{2+} was discovered even while processing the samples in pure oxygen. Thus it appears possible to solidify RE123 directly from the melt while effectively bypassing the formation of solid solutions using rapid solidification techniques in high oxygen partial pressure atmospheres.

IV. Conclusions

Aero-acoustic levitation is a very successful technique for melting, undercooling, and rapidly solidifying high temperature ceramic oxide superconductors. In this study, binary Nd/Y RE123 samples were melted, undercooled hundreds of degrees relative to the liquidus, and solidified to from RE123. Mixtures of Y123 and Nd123 result in a minimum for the peritectic temperature at

$Nd_{.7}Y_{.3}123$, 66°C below the peritectic of pure Nd123. Increasing Nd content in Nd/Y alloys results in the formation of a higher volume fraction of RE123. Nd-Ba solid solution behavior of the type $Nd_{1+x}Ba_{2-x}Cu_3O_{7-\delta}$ was not observed. The RE ratio in RE123 and RE211 structures formed during AAL processing mirrors the nominal starting composition of the bulk. Solidification structures are varied and complex but the processed sphere morphology can be summarized into three zones: relatively void-free RE123 at the surface, RE123 and RE211 transition, and RE211 with interdendritic Ba-Cu-O. Measurable changes occur in the RE211 lattice parameters because of Nd substitution for Y in the Y211 unit cell.

V. Acknowledgments

This work was supported by the National Aeronautics and Space Administration Office of Microgravity Science and Applications Division, Grant No. NAG8-1275. The authors acknowledge the contributions by K. Nagashio and K. Kuribayashi at The Institute of Space and Astronautical Science, Sagamihara, Kanagawa 229-8510, JAPAN.

REFERENCES

1. J.R. Hull, JOM 51, 7, 12 (1999).
2. Goyal, R. Feenstra, F.A. List, M. Paranthanman, D.F. Lee, D.M. Kroeger, D.B. Beach, J.S. Morrell, T.G. Chirayil, D.T. Verebelyi, X. Cui, E.D. Specht, D.K. Christen, and P.M. Martin, JOM 51, 7, 12 (1999).
3. S. Foltyn, P. Tiwari, R. Dye, M. Le, and X. Wu, Appl. Phys. Lett. 63 1848-50 (1993).
4. Y. Iijima, N. Tanabe, O. Kohno, and Y. Ikeno, Appl. Phys. Lett. 60 769-771 (1992).
5. S. Jin, T.H. Tiefel, R.C. Sherwood, M.E. Davis, R.B. van Dover, G.W. Kammlott, R.A. Fastnacht, and H.D. Keith, Appl. Phys. Lett. 52 2074 (1988).
6. K. Salama A.S. Parikh, and L. Woolf, Appl. Phys. Lett. 68 14, 1993-1995 (1996).
7. M. Murakami, Appl. Supercond. 6, 2-5, 51-59 (1998).
8. E.S. Reddy, T. Rajasckharan, G.R. Kumar, T.V. Chandrasekhar Rao, V.C. Sahni, Mater. Sci. Eng. B57, 179-185 (1999).
9. J.M.S. Skakle, Mat. Sci. Eng. R23, 1-40 (1998).
10. M. Murakami, S.I. Yoo, T. Higuchi, N. Sakai, J. Weltz, N. Koshizuka, and S. Tanaka, Jpn. J. Appl. Phys. 33, L715 (1994).
11. F. Prado, A. Caneiro, and A. Sequis, Physica C 295, 235-246 (1998).
12. M. Boffa, A Di Trolio, S. Pace, A. Saggese and A. Vecchione, IEEE Trans. Appl. Supercond. 7, 2 (1997).
13. M. Muralidhar and M. Murakami, Appl. Supercond. 5, 1-6, 127-131 (1997).
14. J.R. Olive, Ph.D. Dissertation, Vanderbilt University (1998).
15. J.R. Olive, W.H. Hofmeister, R.J. Bayuzick, and M. Vlasse, J. Mater. Res. 14, 10, 3851-58 (1999).
16. J.K.R. Weber, D.S. Hampton, D.R. Merkley, C.A. Rey, M.M. Zatarski, and P.C. Nordine, Ceram. Bull. 70, 1, 71 (1991).
17. F. Prado, A. Caneiro, and A. Sequis, Physica C 295, 235-246 (1998).
18. M. Kambara, M. Nakamura, Y. Shiohara, and T. Umeda, Physica C 275, 127-134 (1997).
19. J.R. Olive, W.H. Hofmeister, R.J. Bayuzick, and M. Vlasse, J. Mater. Res. 14, 10, 3851-58 (1999).
20. M. Kambara, T. Umeda, M. Tagami, X. Yao, E.A. Goodilin, and Y. Shiohara, J. Am. Ceram. Soc. 81 [8] 2116 (1998).

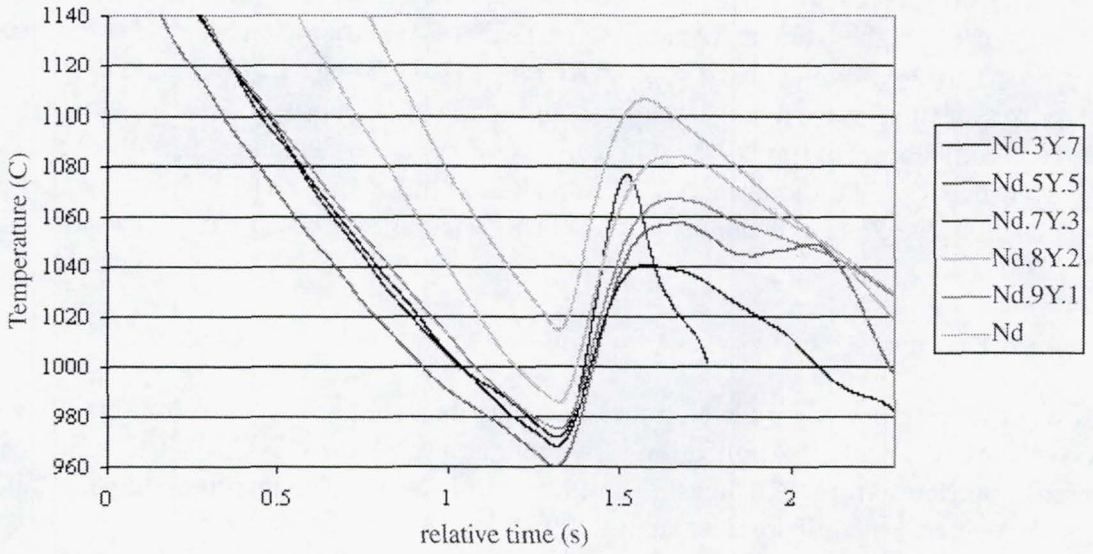

Figure 1. A compilation of pyrometry data for Y/Nd123 alloy samples. The curves were obtained by determining the average trace of several recalescence events for each composition, synchronizing the time-temperature plots at the moment of recalescence, and adjusting the temperature by the *in-situ* calibration factor.

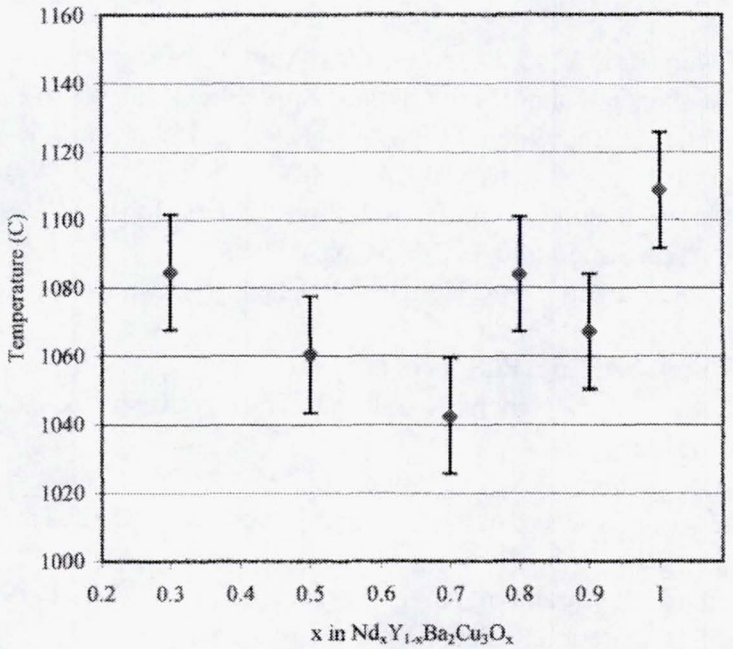

Figure 2. Experimentally determined average peritectic temperatures for Nd/Y123 binary alloy samples processed in the AAL. The temperature has been corrected using Nd123 as an *in-situ* calibration. The standard deviation in the data was used to calculate the magnitude of the error bars.

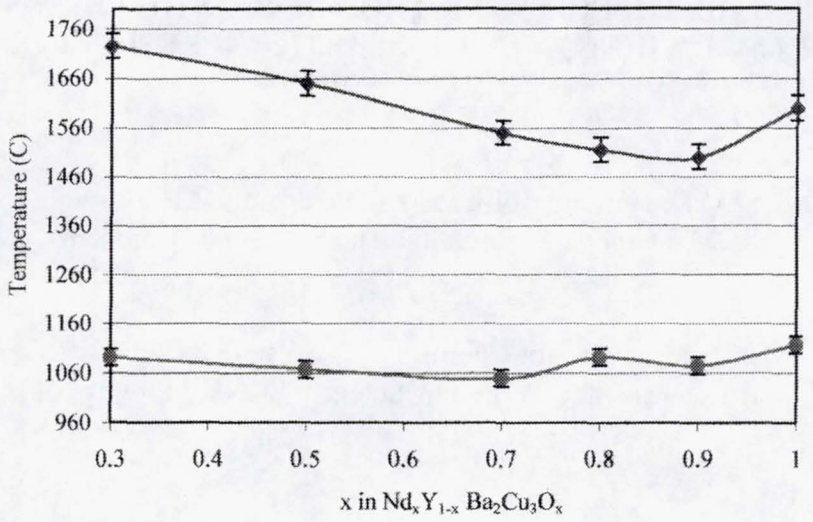

Figure 3. Trace of the Nd/Y123 liquidus and peritectic in pure O_2. Liquidus temperatures were obtained from drop tube work performed by Olive and peritectic temperatures represent corrected experimental data from this work.

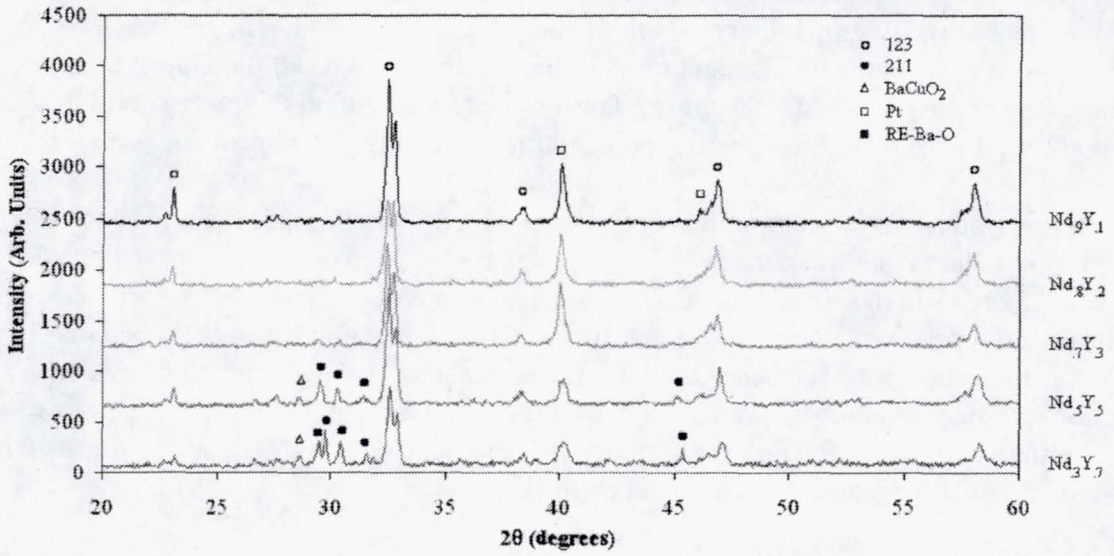

Figure 4. A compilation of XRD spectra for Y/Nd123 alloys processed in the AAL. RE123 is the dominant phase for all compositions. The appearance of RE211 in the scans becomes more prevalent in Y-rich compounds.

TAILOR-MADE IMPURITY CONTROL OF ELASTIC VERSUS PLASTIC DOMAIN SWITCHING IN FERROELASTIC INCLUSION COMPOUNDS

M.D. Hollingsworth[1] *, M.L. Peterson[1], M.E. Brown[1],
M. Dudley[2], B. Raghothamachar[2], and G. Dhanaraj[2]

[1]Department of Chemistry, Kansas State University
[2]Department of Materials Science, SUNY, Stony Brook

In this work we seek an understanding of the cooperative, elastic phenomenon of domain switching through comparison of physical properties and defect structures of a series of closely related inclusion compounds that undergo domain switching under applied anisotropic stress (ferroelasticity). These inclusion compounds are based upon the same urea channel framework, but they differ according to the orientation, dimensionality and cooperativity of specific hydrogen bonding networks. By growing crystals in the presence of tailor-made impurities, one can disrupt specific hydrogen bond networks and observe measurable changes in the kinetics and reversibility of the ferroelastic response. This comparative method therefore serves as a unique method for understanding the specific molecular mechanisms that control domain switching.

The ferroelastic inclusion compounds in question exhibit twinning, dislocations and other types of defect structures that can perturb the ferroelastic response. With ground-based crystallizations, increasing the concentration of tailor-made impurities increases the numbers and kinds of defect structures, which makes it more difficult to isolate the intrinsic or "molecular" roles that the impurities play in the ferroelastic response. Because we have videographic evidence that solution turbulence causes twinning, we expect that crystallization in the microgravity of space will dramatically reduce the defect structures in these crystals and therefore provide us with crystals whose ferroelastic properties can be reliably compared.

Synchrotron white beam X-ray topography (SWBXT) is one of the most powerful physical methods for studying the defect structures and symmetry of twinned and disordered crystals. Because each twinned region is able to select different diffraction wavelengths, the SWBXT images are split at twin boundaries and thus reveal both microstructural and structural information about large twinned crystals. Further information about lattice strain at twin boundaries is also available. This technique is useful for evaluating not only the quality of crystals that we grow on the ground and in space, but also the actual process of domain switching itself with *in situ* stress experiments.

Following our earlier work on defect structures in 2,10-undecanedione/urea, we have conducted *in situ* SWBXT studies of ferroelastic domain switching on several ferroelastic inclusion compounds. Using a device constructed for use at beamline X-19C at the National Synchrotron Light Source, we applied stress to crystals of 2,10-undecanedione/urea containing various levels of 2-undecanone and used X-ray topographs and videomicroscopy to monitor changes in the state of

* Corresponding author

strain and domain switching in these inclusion crystals. For these solid solutions of 2-undecanone and 2,10-undecanedione in urea, the responses shown in the topographs varied dramatically with the applied force and the composition of the crystal. In particular, a striking transition between plastic and elastic domain switching was observed as the impurity concentration was increased from 0 to 20 percent. This suggests a mechanism in which the impurity disrupts the cooperative hydrogen bonded system that controls the barrier to domain switching.

SOLID STATE ELECTROCHEMICAL OXYGEN CONVERSION FOR MARTIAN AND LUNAR ENVIRONMENTS

Ali Reza Alemozafar, Turgut M. Gür and George M. Homsy

Stanford University, Stanford, CA 94305

ABSTRACT

This work involves an innovative solid state electrochemical approach to address the need for on-site generation and recovery of oxygen for resource utilization and life-support systems for Martian and Lunar landing missions, and is concerned with the investigation of heterogeneous kinetics, materials and fluid dynamic issues presented by this electrochemical system in achieving this goal.

I. Introduction

Human exploration and development of space and space resources has been a long sought goal. Major challenges include the scientific and technological difficulties associated with the critical issues of how to sustain life during travel and at the destination site, and how to produce the energy required to propel the space vehicle back to Earth. Energy conversion is key to meeting both these challenges. Practical and obvious solution to this problem lies in the safe, cost effective and imaginative utilization of resources that are available locally. This is especially true for missions to Mars and Moon, where *in-situ* resource utilization (ISRU) is particularly compelling.

Since the proposed research is just starting, there are no experimental results to report at this time. The program presents a novel scheme utilizing a solid state electrochemical reactor concept intended for on-site generation of oxygen and other useful chemicals (such as hydrogen and methane) necessary for sustained missions to Mars and the Moon as well as their colonization. It will involve investigation and development of specialized materials and chemical processes specifically designed to attain this goal.

Ideas regarding extraterrestrial resource utilization have been the subject matter of numerous studies [1-7] . In the context of a mission to Mars, there have been several chemical schemes that were investigated for *in-situ* recovery of oxygen from Martian atmosphere. However, many require two process steps to generate oxygen [8-11] and also suffer from coke deposition problems [10-12].

One such scheme, proposed initially by Ash *et al.* [8] is the Sabatier reaction

$$CO_2 + 4\,H_2 = CH_4 + 2\,H_2O \qquad (1)$$

which envisions to utilize CO_2 from the Martian atmosphere and H_2 carried from Earth to make methane and water vapor over Ni or Ru catalysts. A primary disadvantage of this scheme is its dependence

on the availability of H_2 which needs to be transported from Earth. It also needs an additional process step to convert H_2O to O_2 by electrolysis.

Another chemical scheme [9] that was investigated for oxygen recovery from Martian atmosphere is based on the water gas shift reaction

$$CO_2 + H_2 = CO + H_2 \qquad (2)$$

It also utilized the water vapor electrolysis strategy as a second step to generate oxygen.

Others [10,11] have used a different scheme where CO_2 was first subjected to thermal dissociation at temperatures in excess of 1000 °C according to the reaction

$$2\ CO_2 = 2\ CO + O_2 \qquad (3)$$

In a second step, the resulting O_2 was transported electrochemically through a solid oxide electrolyte and subsequently recovered in pure form in a separate compartment. Similarly, direct electrolysis of CO_2 into O_2 was also investigated using a zirconia solid electrolyte cell [12]. The major disadvantage of these schemes is coke formation in the presence of transition metal catalytic electrodes.

II. Strategy for Oxygen Conversion

This program is significantly different from these earlier approaches. It is known that CO_2 constitutes about 95% of the Martian atmosphere and both the Martian and Lunar soil is believed to contain significant amounts of water. We will utilize these locally available chemical resources for on-site generation of oxygen via the endothermic reaction

$$CO_2 + 2\ H_2O = CH_4 + 2\ O_2 \qquad (4)$$

Reaction (4) constitutes the central theme of this proposal for the conversion and recovery of O_2. Thermodynamically, this reaction is not favorable at all due to its large, positive free energy change of 95.8 kcal/mole of O_2 (i.e., 401 kJ/mole of O_2) at 1000 K. Hence, this uphill reaction cannot be achieved via ordinary chemical routes.

The solid state electrochemical concept, however, makes it possible to drive this otherwise unfavorable reaction far removed from equilibrium to completion by electrochemically removing the oxygen from the reaction environment, thus shifting the reaction equilibrium to the right in accordance with Le Chatelier's principle. In fact, in Gür *et al.* [13], we have shown earlier that a similar reaction

$$CO_2 + 2\ H_2 = CH_4 + O_2 \qquad (5)$$

which is also thermodynamically unfavorable with a similarly large and positive free energy change of 99.2 kcal/mole of O_2 (*i.e.*, 415 kJ/mole of O_2) at 1000 K was successfully driven to completion on Pt electrodes in a solid state electrochemical reactor where O_2 was recovered in pure form. We also reported a high methane turnover frequency of 20 sec^{-1} at 973 K, and a strong dependence of the rate constants on the applied electrical potential.

This strategy has numerous and significant advantages over ordinary chemical routes, namely, it

- drives the uphill reaction (4) to completion
- generates O_2 in pure form eliminating costly post-separation and purification processes
- produces CH_4, a useful by-product as fuel, power generation, or further chemical processing
- provides a single step process route for the conversion of CO_2 to O_2 and CH_4
- eliminates carbon deposition and the need for regeneration of catalytic activity
- operates at lower temperatures than it is customary for CO_2 electrolysis

III. Solid State Electrochemical Concept For Catalysis

Catalysis is traditionally considered to be appropriate or necessarily applicable only for chemical reactions that are thermodynamically downhill. The solid state electrochemical approach to catalysis presented in this work deviates significantly from this conventional wisdom. It relies critically on the unusual properties and creative use of solid electrolytes which makes it possible to monitor the activity of surface species during a heterogeneous reaction as originally suggested by Wagner [14]. In earlier work, Gür [13,15-18] and others [19,20] took this concept one step further and demonstrated the "active," as distinct from "passive," role of a solid state electrochemical reactor for *in situ* control and modification of the surface activity of electroactive species on one side of the solid electrolyte with respect to a fixed reference activity of the same species on the other side via an externally applied electrical potential across the electrolyte. In other words, this technique provides the opportunity both to study the local reaction environment by direct measurement of surface activities, and also to affect the reaction sequence involving these surface intermediates. This important concept is central to the experimental procedures adopted in this work to study and exploit the active role of solid state electrochemical tools in the catalysis of oxygen conversion reactions from CO_2 and H_2O.

IV. Experimental Aspects

The schematic design of the solid state electrochemical reactor is illustrated in Figure 1. It consists of a tubular solid oxide electrolyte with appropriate catalytic electrodes coated on the inner and outer walls. An external DC power source is connected to the inner and outer electrodes through appropriate electrode leads. The electrolyte tube resides inside an external tubular jacket of larger diameter. A reaction mixture of CO_2 and H_2O flows inside the electrolyte tube. The reactants dissociatively adsorb on the surface of the catalytic electrode and give up their oxygen. This is facilitated by the high concentration of oxygen vacancies in the catalytic electrode induced by the electrical potential across the solid electrolyte which drives the electrode/electrolyte interface starved of oxygen. This low oxygen activity at the interface provides the chemical driving force for the oxygen from the surface region of the electrode to diffuse downhill through the chemical potential gradient to the electrode/electrolyte interface where it is incorporated inside the solid electrolyte via a charge transfer reaction and transported across the tube to the other compartment in the presence of the externally applied bias. The surface site on the catalytic electrode thus depleted of oxygen is then set up to start the next catalytic cycle by abstracting oxygen from the adsorbed reactants.

The electrochemical reactor can be represented by

$$(-)\ H_CO + CO_C\ ,\ CH_C,\ MC\ /\ Electrolyte\ /\ MC,\ O_2\ (+) \qquad (6)$$

where MC represents a mixed-conducting catalytic electrode. The strategy is that one can electro-

chemically drive the oxygen activity at the gas/catalyst interface to sufficiently low values such that the C-O bonds in CO_2 and correspondingly the H-O bonds in H_2O become thermodynamically unstable and readily dissociate on the catalyst surface, eliminating the rate-limiting step. The formation of this surface carbon by the scission of the C-O bond has been identified previously as the rate determining step in methane production from synthesis gas [21,22]. Known thermochemical data indicates that at 700 °C, for example, electrical potentials in excess of 1 V suffice to decompose CO as well as CO_2 and H_2O. The active surface carbon resulting from the electrochemical abstraction of oxygen from adsorbed CO_2 is then readily hydrogenated by a mechanism previously proposed by Wagner [14].

Electrochemical Reactor

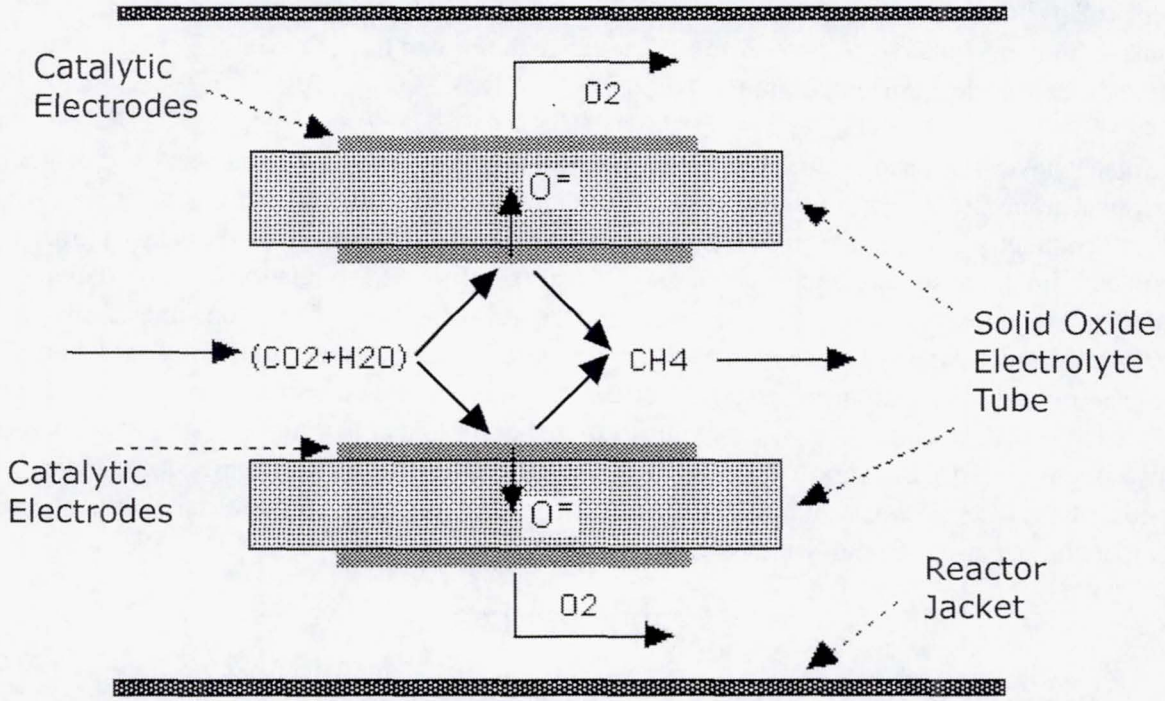

Figure 1. Schematic design of the solid state electrochemical reactor.

V. Materials Development

Oxide Ion Conducting Solid Electrolytes

Stabilized zirconia maintains predominantly ionic conduction over a wide range of oxygen activities from about 5 atm of oxygen down to unusually low values of 10^{-28} atm at elevated temperatures [23]. Thus, it is a suitable electrolyte for the electrochemical reactor of Figure 1. Zirconia partially stabilized with 3 mole % yttria (PSZ) is also a viable candidate and exhibits superior mechanical properties and slightly higher conductivity than its fully stabilized counterpart [24]. This imparts better thermal cycling behavior as well as the ability to operate at moderate temperatures without much reduction in the ionic conductivity.

Recently, Ishihara *et al* [25,26] reported a new family of ionically conducting oxide electrolytes based on the $LaGaO_3$-family of perovskites. They exhibit oxide-ion conductivity values higher than those for

stabilized zirconia solid electrolytes. The activation energy for ionic conduction is also significantly lower in these perovskites which provides an important advantage to operate the $LaGaO_3$-based electrolytes at significantly lower temperatures than zirconia-based electrolytes [26].

VI. Mixed Conductors

The development of electrode materials that possess high catalytic activity for reaction (4) and concurrently exhibit sufficient electronic and ionic conductivity is one of the primary challenges of this work. For this purpose, we will explore mixed (electronic-ionic) conducting oxides where electrical charge is carried both by ionic and electronic species, and the net ionic transport rate is usually governed by chemical diffusion [27-29] of the ionic species under a chemical potential gradient.

Interestingly, the chemical diffusion coefficient of oxygen in many of these oxides is rather high, reaching values of 10^{-6} - 10^{-7} cm^2/sec [27,28] at elevated temperatures. They also have relatively large oxygen nonstoichiometry, where values for δ are about 0.25 in the case of $La_{1-x}Sr_xMnO_{3-\delta}$ and may vary up to 1.0 in the case of the high temperature superconductor $YBa_2Cu_3O_{7-\delta}$ [29].

We plan to investigate and evaluate doped members of the perovskite family that possess the right mix of critical properties for effective and viable oxidation/deoxidation catalysis. This includes wide oxygen nonstoichiometry important to provide high solubility for oxygen necessary for the catalyst to act as source or sink for adsorbed oxygen on the catalytic surface during the oxidation (or deoxidation) reaction. This allows lattice oxygen to actively participate in the catalytic reaction. Indeed, in Gür *et al* [30], we provided experimental evidence about the role of lattice oxygen in the partial oxidation of methane on mixed-conducting catalytic electrodes. We will also seek perovskites with high mobility for lattice oxygen. It is critical that the catalytic electrode has the ability to remove or supply much needed surface active oxygen from and to the catalytic sites, respectively, through bulk diffusion in the mixed conducting catalyst. Moreover, ready availability of electronic species for the surface active species at the reaction site also promotes catalysis.

REFERENCES

1. K. Ramohalli, W. Dowler, J. French, and R. Ash, J. Spacecraft 24, 236 (1992)
2. W. W. Mendell, Acta Astronautica 26, 3 (1992)
3. E. M. Jones, Acta Astronautica 26, 15, (1992)
4. K. Ramohalli, T. Kirsch, and B. Preiss, J. Propulsion 8, 240 (1992)
5. B. Cordell and O. Steinbronn, Acta Astronautica 26, 19 (1992)
6. K. Ramohalli, W. Dowler, J. French, and R. Ash, Acta Astronautica 15, 259 (1987)
7. L. B. Weaver and E. Laursen, Acta Astronautica 26, 61 (1992)
8. R. L. Ash, W. L. Dowler, and G. Varsi, Acta Astronautica 5, 705 (1978)
9. R. Zubrin, M. B. Clapp, and T. Meyer, AIAA-97-0895, 35th Aerospace Sciences Meeting and Exhibit, Reno, Nevada, January 6-10 (1997)
10. K. Ramohalli, E. Lawton, and R. Ash, J. Propulsion 5, 181 (1989)
11. J. Colvin, P. Schallhorn, K. Ramohalli, J. Propulsion and Power 8, 1103 (1992)
12. K. R. Sridhar, B. Vaniman, Solid State Ionics 93, 321 (1997)
13. T. M. Gür, H. Wise, and R. A. Huggins, J. Catal. 129, 216 (1991)
14. C. Wagner, Adv. in Catal. 21, 323 (1970)
15. T. M. Gür and R. A. Huggins, J. Electrochem. Soc. 126, 1067 (1979)

16. T. M. Gür and R. A. Huggins, Solid State Ionics 5, 563 (1981)
17. T. M. Gür and R. A. Huggins, Science 219, 967 (1983)
18. T. M. Gür and R. A. Huggins, J. Catal. 102, 443 (1986)
19. M. Stoukides and C. G. Vayenas, J. Catal. 64, 18 (1980)
20. M. Stoukides and C. G. Vayenas, J. Catal. 64, 18 (1981)
21. P. R. Wentreck, B. J. Wood, and H. Wise, J. Catal. 43, 363 (1976)
22. M. Araki and V. Ponec, J. Catal. 44, 439 (1976)
23. J. W. Patterson, E. C. Bogren, and R. A. Rapp, J. Electrochem. Soc. 114, 752 (1967)
24. W. Weppner and H. Schubert, Advances in Ceramics, v. 2, "Science and Technology of Zirconia III." S. Somiya (ed.), p. 212, The American Ceramic Society Inc., Columbus, OH (1988)
25. T. Ishihara, H. Matsuda, and Y. Takita, J. Am. Ceram. Soc. 79, 3801 (1994)
26. T. Ishihara, M. Higuchi, H. Furutani, T. Fukushima, H. Nishiguchi, and Y. Takita, J. Electrochem. Soc. 144, L122 (1997)
27. A. Belzner, T. M. Gür, and R. A. Huggins, Solid State Ionics 57, 327 (1992)
28. S. Sunde, K. Nisancioglu, and T. M. Gür, J. Electrochem. Soc. 143, 3497 (1996)
29. R. Beyers, B. T. Ahn, G. Gorman, V. Y. Lee, S. S. P. Parkin, M. L. Ramirez, K. P. Roche, J. E. Vazquez, T. M. Gür, and R. A. Huggins, Nature 340, 619 (1989)
30. T. M. Gür, H. Wise, and R. A. Huggins, Catal. Lett. 23, 387 (1994)

POROSITY AND VARIATIONS IN MICROGRAVITY AEROGEL NANO-STRUCTURES
II. New Laser Speckle Characterization Methods

A.J. Hunt*[1], M.R. Ayers[2], L. Sibille[3], and D.D. Smith[4]

[1,2]E. O. Lawrence Berkeley National Laboratory, Berkeley, CA
[3,4]NASA, Marshall Space Flight Center

INTRODUCTION

The transition from sol to gel is a process that is critical to the properties of engineered nano-materials, but one with few available techniques for observing the dynamic processes occurring during the evolution of the gel network. Specifically, the observation of various cluster aggregation models[1], such as diffusion-limited and reaction-limited cluster growth can be quite difficult. This can be rather important as the actual aggregation model can dramatically influence the mechanical properties of gels, and is significantly affected by the presence of convective flows, or their absence in microgravity.

We have developed two new non-intrusive optical methods for observing the aggregation processes within gels in real time. These make use of the dynamic behavior of laser speckle patterns produced when an intense laser source is passed trough a gelling sol. The first method is a simplified time-correlation measurement, where the speckle pattern is observed using a CCD camera and information on the movement of the scattering objects is readily apparent. This approach is extremely sensitive to minute variations in the flow field as the observed speckle pattern is a diffraction-based image, and is therefore sensitive to motions within the sol on the order of the wavelength of the probing light. Additionally, this method has proven useful in determining a precise time for the gel-point, an event often difficult to measure.

Monitoring the evolution of contrast within the speckle field is another method that has proven useful for studying gelation. In this case, speckle contrast is dependent upon the size (correlation length) and number of scattering centers, increasing with increasing size, and decreasing with increasing numbers. The dynamic behavior of cluster growth in gels causes both of these to change simultaneously with time, the exact rate of which is determined by the specific aggregation model involved. Actual growth processes can now be observed, and the effects of varying gravity fields on the growth processes qualitatively described. Results on preliminary ground-based measurements have been obtained.

I. Experimental

Samples studied by these methods consisted of standard base-catalyzed (NH_3) tetraethyl-orthosilicate (teos) sols[2,3]. Fifteen mL of each sol was prepared and filtered through 0.45 μm PTFE filters immediately after mixing into glass scintillation vials. Laser radiation was provided by either

a 50 mW diode laser (532 nm) or the 488 nm line of a 100 mW argon ion laser. Speckle patters were recorded using a Pulnix TM-1040 CCD camera (1024 x 1024 pixels, 10-bit ccd, 30 fps), and analyzed in real time with a standard PC running XCAP v 1.1 (Epix, Inc.) image analysis software. The sample vial and camera were placed in an acoustically quiet chamber to minimize interferences from ambient vibrations. Figure 1 gives a schematic of the experimental arrangement used to obtain specklegrams, an example of which appears in Figure 2.

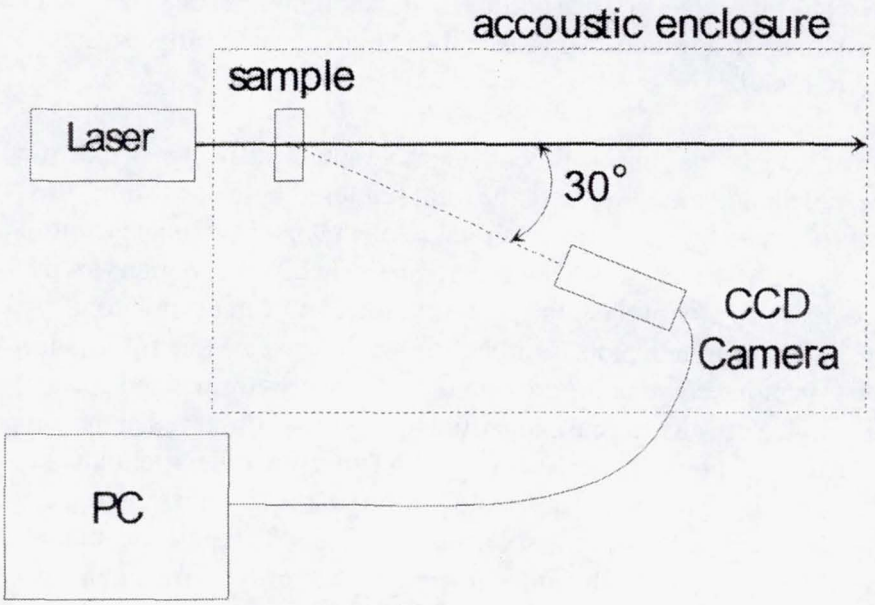

Figure 1. Schematic diagram of the dynamic laser speckle system.

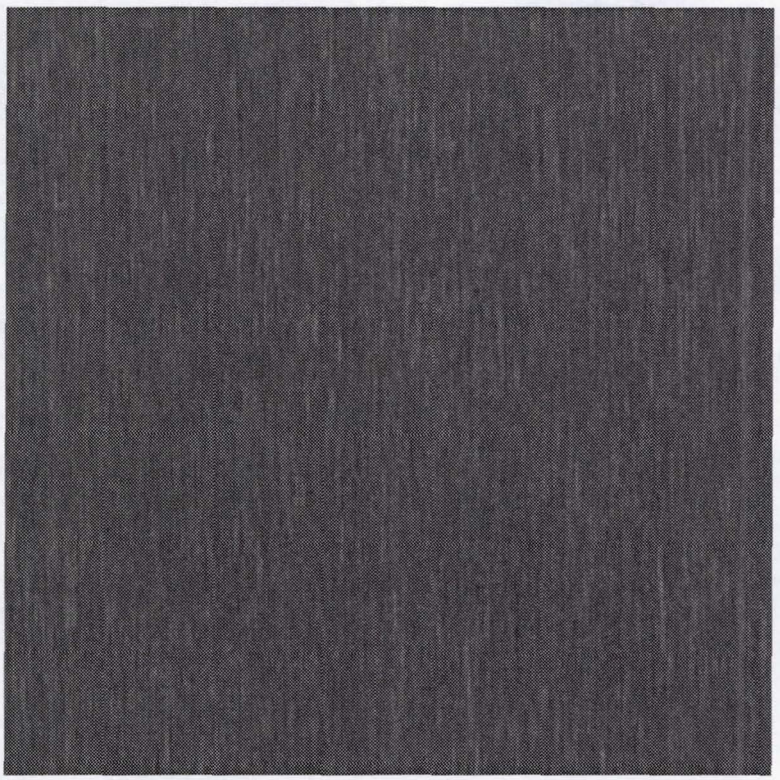

Figure 2. A typical specklegram for a silica sol.

II. Results and Discussion

Speckle methods have been used extensively to study the micro-scale properties of both static and dynamic systems[4]. However, in the case of dynamic systems, the use of speckle methods has most often been employed for systems in which the nature of the scattering centers remain fixed, such as the observation of small particles in a flowing fluid. In the case of the sol-to-gel transition, both the mobility of the scattering centers (silica particles) and their number and size, are changing simultaneously. We wish to learn as much as possible about both of these properties as sols evolve in normal and microgravity.

The mobility of silica particles in sols is conveniently monitored using speckle methods. The system we have developed measures both the total scattered light and a simplified 0.033 sec. correlation map (obtained by measuring the total intensity of a new image resulting from the absolute value of the difference of two adjacent frames) at 60 second intervals during the gelation process. Figure 3 gives a plot of the total scattering intensity versus time for a typical sol. The information available from such plots is rather limited, however. More information can be obtained from the correlation plot, shown in Figure 4, and the intensity-normalized correlation plot given in Figure 5. In Figure 4, a drastic decrease in particle mobility is observed at the gel point (marked by an arrow). The actual gel point is often difficult to detect using other methods. In the normalized plot, a decrease in particle mobility is observed prior to the gel point as aggregates of silica particles grow in size. The convective flow in the sol itself will also affect these correlation plots as the particle motion will be expected to be much lower under microgravity. The use of this system during parabolic flights may provide important information on the role of convective flows in gelation behavior.

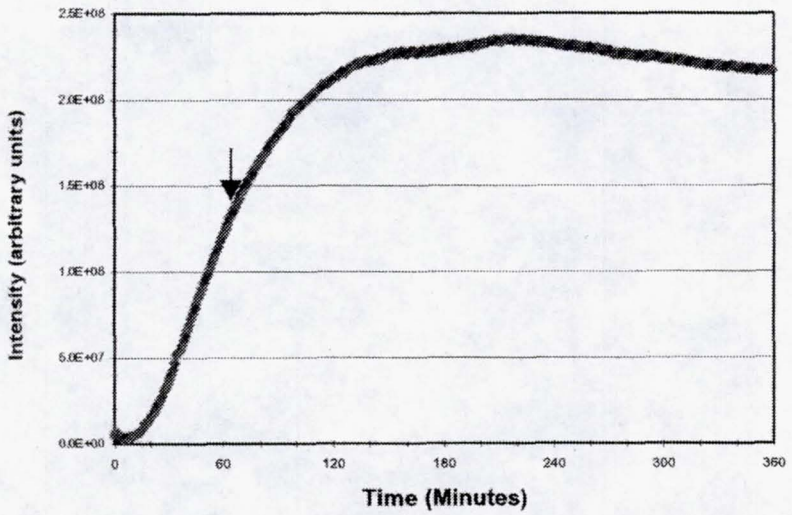

Figure 3. Plot of total scattering intensity versus time for a typical silica sol. The gel point is marked by an arrow.

The evolution of contrast in the specklegrams also provides important information on the aggregation process occurring in the sol. Speckle contrast has been widely used to measure surface roughness in a variety of systems [5-8]. In qualitative terms the contrast of a speckle image is :

$$\text{contrast} = \frac{\sigma_I}{\langle I \rangle} \propto \frac{(\text{size of scatterers})}{(\text{number of scatterers})}$$

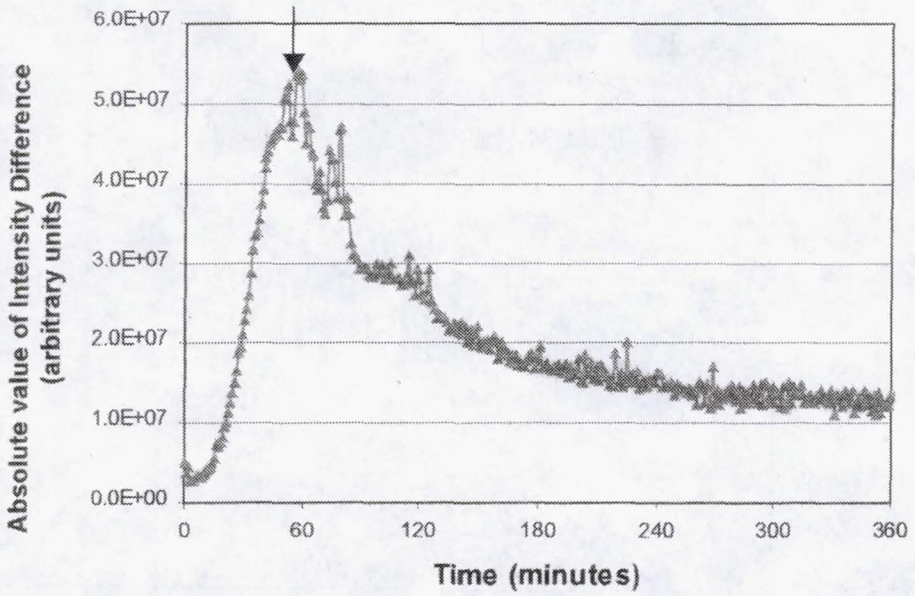

Figure 4. Plot of the 0.033 second correlation intensity versus time for the same sol as Figure 3. The gel point is marked by an arrow.

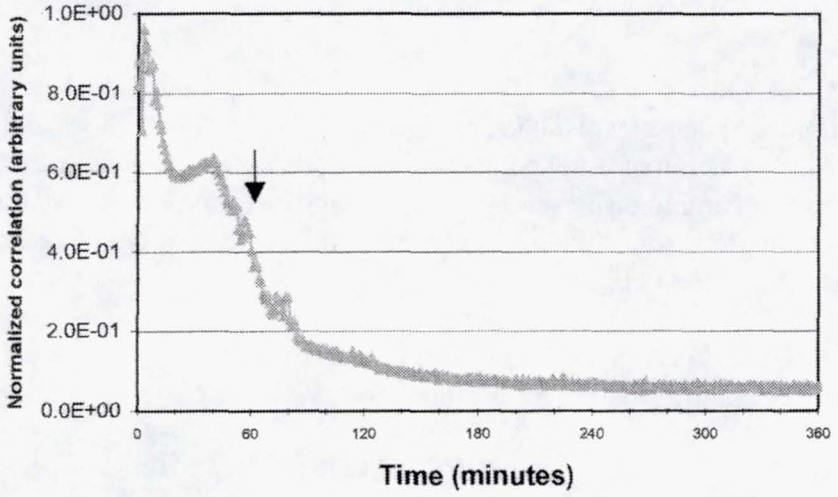

Figure 5. Intensity (total) normalized 0.033 second correlation plot for the same sol as Figure 3. The gel point is marked by an arrow.

Where σ_I is the standard deviation of the image intensity, and I is the intensity. In general, small numbers of large scatterers will produce the maximum image contrast, while large numbers of small scatterers, the minimum. As sols evolve towards the gel point, the size of scatterers increase and their numbers decrease. The rate and magnitude of these changes depend intimately on the specific aggregation mode employed by the sol. The evolution of contrast versus time for various silica sols appears in Figures 6 and 7.

A clear pattern of particle growth is apparent. The contrast of the speckle image decreases as the sol evolves, to a minimum ranging between 0.4-0.7 times the gel time. From there the speckle contrast increases, reaching its maximum shortly after the gel point. This shows a change in the particle growth behavior, from an increasing number of small particles at the beginning of the process, to the onset of aggregation and the growth of fewer, but larger particles. Variation of teos

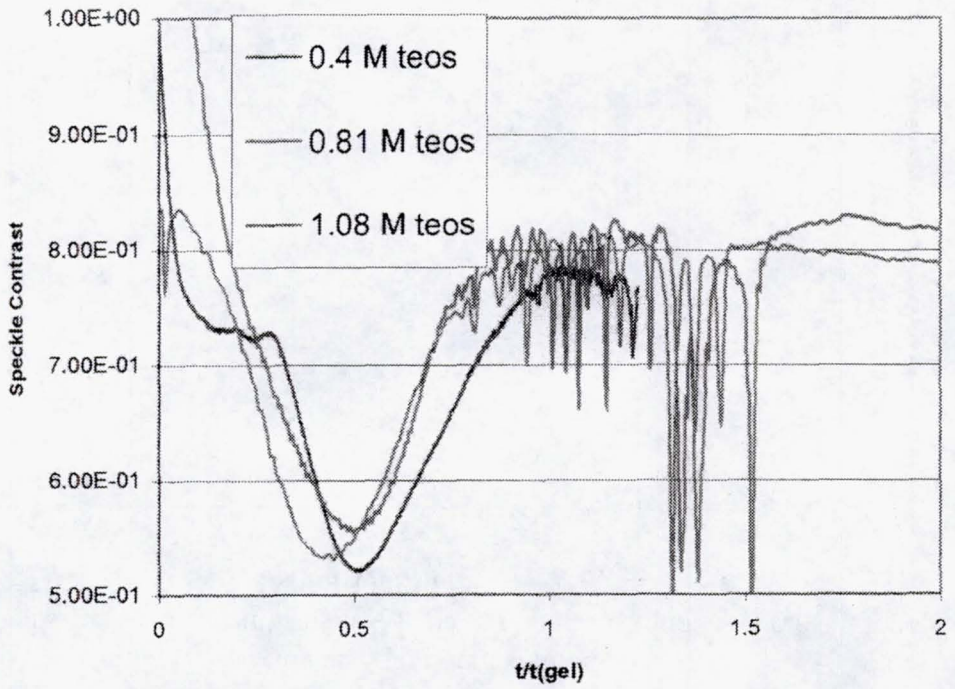

Figure 6. Speckle contrast versus time (normalized to gel time) for various teos concentrations.

concentration (Figure 6) does not result in any significant change in the onset of the aggregation phase. Similarly the variation of water content in the sol also does not alter this behavior. However, adjusting the amount of ammonia present (the determining factor in colloidal stability) significantly affects the onset of aggregation. Higher levels of ammonia delay the start of aggregation to late in the gelation process, as seen in Figure 7.

Earlier flight experiments on silica sols have shown a definite effect of gravity on their aggregation behavior. This new technique may prove useful in observing these changes during future flight experiments.

REFERENCES

1. P. Meakin, "Models for Colloidal Aggregation" *Ann. Rev. Phys. Chem.* 39, (1988) 237-267.
2. A. J. Hunt, *et al.* "Effects of Microgravity on the Formation of Aerogels" Proceedings of the NASA Microgravity Materials Science Conference (1999) 325.
3. W. Cao, and A.J. Hunt, "Improving the Visible Transparency of Silica Aerogels," *J. Non-Crystalline Solids*, 176, (1994) 18-25.
4. N. A. Fomin, "Speckle photography for fluid mechanics measurements" (1998) Springer, Berlin; New York
5. H. M. Pedersen, "Theory of Speckle Dependence on Surface Roughness" *J. Opt. Soc. Am.* 66, (1976) 1204-1210.
6. H. Fujii, *et al.*, "Measurement of Surface Roughness Properties by Using Image Speckle Contrast" *J. Opt. Soc. Am.* 66, (1976) 1217-1222.
7. H. Fujii and T. Asakura, "Roughness Measurement of Metal Surfaces Using Laser Speckle" *J. Opt. Soc. Am.* 67, (1977) 1171-1176.
8. J. W. Goodman "Statistical Properties of Laser Speckle" in "Laser Speckle and Related Phenomena", *Topics in Applied Physics*, 9, (1975) 9-77. Springer, Berlin, New York.

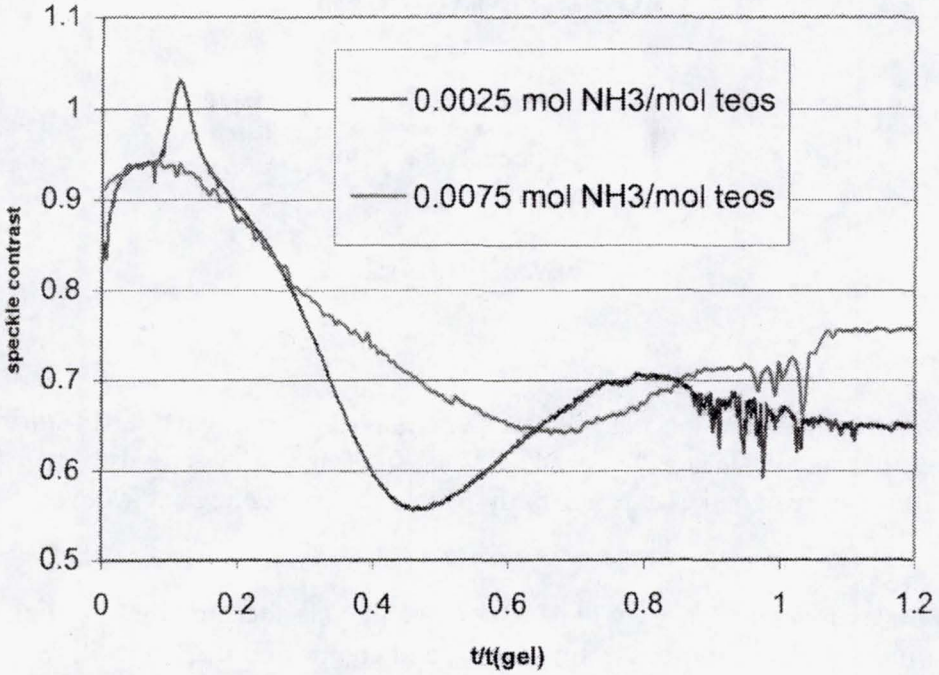

Figure 7. Speckle contrast versus time (normalized to gel time) for two NH_3 to teos ratios.

GROWTH OF ROD EUTECTICS

Kenneth A. Jackson

University of Arizona

This study, which has just been funded, will have two components: one will be an *in-situ* microscopic study of rod eutectic growth in facet/facet and facet/non-facet eutectic systems using transparent organic materials. The second part of the study will be the Monte Carlo modeling of the growth of facet/facet and facet/non-facet eutectic systems.

The goal of the experimental study will be to observe the interface and the resulting microstructures for various growth conditions, growth rates, and compositions. This will permit direct comparison of the microstructures with those found in semiconductor-metal systems, and will provide insights into how these microstructures develop. The phenomenology of these alloys is rich, and the *in-situ* studies will help to define the conditions for the growth of uniform coupled rod eutectic microstructures.

The simulations will be at the atomic level, and will incorporate both crystallization kinetics and diffusion processes. Appropriate use of scaling of the growth rates and of the roughening transitions of the phases of the alloy system will be employed to achieve the control and the faceting of the interface. The power of Monte Carlo modeling has not previously been exploited to study these eutectic alloys, which can be treated analytically only if simplifying assumptions are made. The results of these simulations will be directly comparable with the microstructures of corresponding metallic alloys, and with the microscopic observations on transparent eutectic alloys.

These studies are intended to provide insight into differences between the behavior of facet/facet and facet/non-facet metallic eutectic systems which have been observed in ground-based and reduced gravity environments.

NON-EQUILIBRIUM PHASE TRANSFORMATIONS

Kenneth A. Jackson

University of Arizona

The objective of this program is to develop an understanding of segragation during phase transformations which take place far from equilibrium. Thermodynamics provides the basic framework for analyzing phase equilibria, and it is well known that during rapid phase transformations, non-equilibrium phenomena such as solute trapping, extended solid solubilities, or even the suppression of the formation of a phase indicated on the phase diagram can occur. When a transformation occurs far from equilibrium, the progress of the phase change is dominated by kinetics, and it can proceed rapidly to a non-equilibrium state which has a lower free energy than the initial state but a higher free energy than the lowest free energy equilibrium state. Our objective is to develop an understanding of these processes based on experimental studies and the insights provided by computer simulations, so that the occurrence and progress of these phenomena can be predicted and controlled.

Projects supported by NASA using levitation and the microgravity environment are making major contributions to our understanding of nucleation and crystallization in the regime where these non-equilibrium effects are very important. Indeed, the structure and properties of materials produced by transformations that occur under conditions that are far from equilibrium is one of the central topics of materials science, and in many instances rapid phase transformations provide a means of developing materials with novel structures and properties. A variety of commercial processes operate in this regime, including processes such as rapid solidification, laser melting, plasma spraying, splat quenching, spray powder formation, condensation processes, glass formation, as well as some conventional solidification and crystal growth processes. The non-equilibrium phenomena and segregation effects which are observed during rapid crystallization are not predicted by the standard quasi-equilibrium thermodynamic model for phase transformations. Our Monte Carlo computer simulations capture the essence of these effects. On the simulations, these non-equilibrium phenomena depend on the undercooling, on the growth rate, and on the diffusion coefficient in the fluid phase. These simulation results provide a new framework for the interpretation of these phenomena, and for predicting when they will occur.

Monte Carlo computer modeling which exhibits these non-equilibrium effects has been pursued to provide insights into them. The simulations have been used to explore in detail the transition between two limiting regimes: 1) the diffusionless regime, where the interface must incorporate all the atoms as it moves, and 2) the rapid diffusion regime, where the atoms move rapidly compared to the rate of motion of the interface, and atoms rejected by the growing phase can diffuse away ahead of an advancing interface, producing classical segregation effects. In the transition region between these two extremes both the non-equilibrium distribution coefficient (k-value) and the "kinetic phase diagram" depend on the growth rate and the diffusion coefficient

in the liquid. Our computer simulations predict the magnitude and orientation dependence of these effects, in agreement with experimental results on dopant incorporation into silicon. Simulations of other semiconductors as well as other materials systems, such as the crystallization of glasses, are being pursued. Our experiments involve an analysis of microsegregation that will ultimately require experimentation in a microgravity environment where the effects of convection are minimized. The program combines simulations with experimental studies, and both aspects are viewed as essential in that the simulations provide new insights for the experimental work, and the experiments verify important aspects of the simulations and keep them relevant to the real world.

EXPERIMENTAL AND NUMERICAL INVESTIGATIONS OF GROWTH MORPHOLOGIES OF PERITECTIC REACTIONS

David R. Johnson and Matthew John M. Krane

School of Materials Engineering, Purdue University
West Lafayette, IN 47907

INTRODUCTION

Coupled growth in a number of peritectic alloys has recently been reported. At compositions less than (but near) the peritectic composition, peritectic alloys generally form a coarse two-phase microstructure when processed under low G/V conditions (G = thermal gradient, V = interface velocity) and banded microstructures for high G/V values. However, at intermediate values, both lamellar and rod-like coupled microstructures have been observed with a much finer interphase spacing then would be expected from cellular or dendritic growth. The goal of this research is to explain the morphological development of two-phase peritectic alloys by coupled experimental and numerical procedures.

I. Peritectic Solidification

A schematic phase diagram of a system containing a peritectic reaction of the form $L+\alpha \rightarrow \gamma$ is shown in Figure 1. A wide variety of interesting microstructures can result from directional solidification of peritectic alloys and the means by which they form are not well understood. Perhaps the most interesting are the two phase alloys produced between C_a and C_p (as denoted in Figure 1) for growth conditions near the limit of constitutional supercooling.

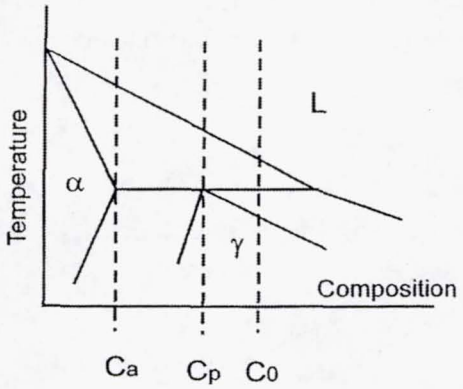

Figure 1. Schematic peritectic phase diagram.

Chalmers [1] first suggested that coupled growth may be possible for peritectic systems if dendritic growth could be suppressed by the application of a high thermal gradient. Boettinger examined such a possibility in his classic paper concerning directional solidification of Sn-Cd peritectic alloys [2]. For a range of compositions grown under high G/V conditions, coupled growth was not found, but rather a microstructure consisting of alternating layers of the primary and peritectic phases. Boettinger modified

the Jackson-Hunt analysis [3] for coupled growth in eutectic systems to explain the lack of such growth in peritectic systems. Directional solidification of other peritectic systems has also revealed banded microstructures without evidence of coupled growth [4-7]. Recently, Trivedi and coworkers [8,9] have developed a theory to describe the formation of banded layers found in directionally solidified peritectic alloys.

The formation of a layered microstructure is a natural consequence of suppressing dendritic growth in two-phase peritectic alloys. Because the two phases cannot grow together, they alternate as a way of maintaining a planar solid-liquid interface. However, there is recent evidence that it may be possible to maintain coupled growth, in which the two phases grow together with an interface perpendicular to the isothermal, planar solid-liquid interface. Lee and Verhoeven [10] noted that a finely spaced cellular-like microstructure formed during directional solidification of a peritectic Ni-Ni_3Al alloy. For large G/V growth conditions, the familiar banded microstructure formed. However, at moderate G/V conditions (but still in the range for planar growth as originally defined by Boettinger [2]), a type of coupled growth occurred. This structure consisted of cells of Ni_3Al surrounded by a Ni solid solution, with the growth front terminating at a sharp isothermal interface. Lee and Verhoeven termed this microstructure "cellular coupled growth." If the required undercooling to drive the solidification is dominated by diffusional terms alone, then a negative undercooling results, requiring the solid-liquid interface temperature to be above the peritectic temperature. However, Lee and Verhoeven found that the interface temperature for the cellular coupled growth was below the peritectic temperature [10].

Another example of coupled growth was reported by Busse and Meissen [11] for alloys grown in the Ti-Al system near the TiAl peritectic. For compositions grown near the peritectic composition and at high G/V conditions, they found a coarse lamellar microstructure consisting of α-Ti and TiAl. The lamellar microstructure was aligned parallel to the growth direction and occurred over distances of several millimeters. Because γ-TiAl is an intermetallic phase, if the α-Ti liquidus can be depressed, then the metastable extension of the TiAl liquidus will allow the formation of a eutectic, as proposed by Hillert [12] and Laraia and Heuer [13]. However, as noted by Busse and Meissen, the formation of this microstructure is unclear since the coarseness of the microstructures precludes a significant depression of the liquidus by curvature effects alone. Similar microstructures have recently been reported by Ma *et al.* [14] for Zn-Cu alloys containing up to 7.37wt% Cu in which plate-like cellular growth was observed.

II. Preliminary Results from the Ti-Al system

Directional growth experiments with Ti-Al alloys of a composition near Ti-54at.%Al were performed by the floating zone method [15]. A schematic of the center portion of the Ti-Al phase diagram is shown in

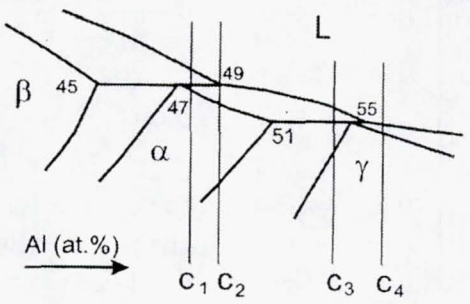

Figure 2. Schematic of the Ti-Al phase diagram showing two peritectic reactions near the equal-atomic composition.

Figure 2; the compositions under consideration are near C_3. Directional solidification produced a banded microstructure as shown in Figure 3. However, a continuous layer of single phase α was never formed as can clearly be seen by the γ grain boundary passing undisturbed through the banded regions as marked in Figure 3(a). A cross-sectional view through one of the layers is shown in Figure 3(b), where the microstructure consists of an array of cells surrounded by a γ matrix. At higher magnification, the cells are found to consist of the γ/α_2 microstructure which formed from the cellular α-phase by a solid state reaction during cooling.

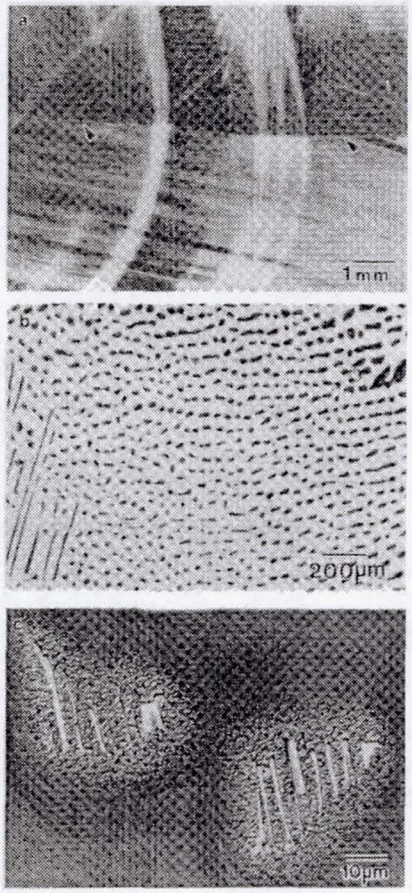

Figure 3. Directional solidified Ti-54 Al at.% alloy showing (a) longitudinal and (b)&(c) transverse views of banded regions.

The cellular growth of the α-phase indicates that the G/V growth conditions were insufficient to produce a planar solid-liquid interface. However, the banded microstructure indicates that the steady-state growth temperature of the α-cell tips is below the peritectic temperature. Using the same argument as Trivedi [8], once below the peritectic temperature, the steady state γ/liquid interface temperature would be higher than that for the α-phase. Thus, the growth velocity of the γ/liquid interface would supercede that of the γ/liquid interface, leaving behind 'α-stringers' as a planar γ/liquid interface forms.

It is also seen in Figure 3 that the layered microstructure is formed without the renucleation of either phase. The γ-phase is clearly continuous throughout the ingot as shown in Figure 3(a). Furthermore, the α-phase was found to branch from surface grains on the ingot (less than 1 mm thick) towards the center when the growth conditions were favorable to produce the banded cellular layers. During cooling, the α-phase transforms to the γ/α_2 lamellar microstructure following a specific crystallographic orientation relationship [16]. Thus, the crystallographic orientation of the prior α-phase can be deduced

from the orientation of the γ/α_2 lamellar microstructure. Large groups of the cells are found to have the same orientation thus indicating that they branch out from the same surface grain.

III. Research Plan

The research plan incorporates an iterative cycle between experiments and simulations which will provide insight into the microstructural development of peritectic alloys. Experimentation will provide the initial basis for developing the simulation model. However, once developed, simulation of the peritectic solidification will provide predictive results over a wide range of variables which can then be checked by experiment when possible. Details are outlined below for both lines of research.

In three instances of coupled growth of peritectics reported in the literature, all involve an intermetallic phase that can exist over a wide compositional range. Initially, one of these systems (Zn-Cu), for which a lamellar morphology was reported for the coupled microstructure, will be explored in this research program. The Zn-Cu alloys have relatively low melting points, which greatly improves the ease of processing and allows quantification of the processing conditions without overly sophisticated instrumentation.

A. Modeling of Coupled Growth of Peritectic Alloys

The main thrust of the modeling effort in this research is the prediction of the microstructural development in solidifying alloys, beginning with nucleation and growth of the solid from the melt and following the solid through all of the phase changes associated with the peritectic reaction. Kerr and Kurz [17] identify the different types of phase changes which are important during the $L + \alpha \rightarrow \gamma$ transformation. The first is the reaction itself, in which the three phases react with each other directly by diffusion of solute (mostly through the liquid phase). The second type is the solid-solid ($\alpha \rightarrow \gamma$) phase change, conducted by mass diffusion across the solid γ layer, and the final stage is the more prosaic solidification of γ on that same γ layer directly from the liquid. As Kerr and Kurz point out, it is the interaction between these transformation phenomena which determine the microstructural morphology.

The rationale for such detailed modeling is also provided by Kerr and Kurz [17], as they point out that the different types of phase transformation found during the peritectic reaction are difficult to separate experimentally. The simulations, after confidence in them is gained by favorable comparisons with experimental results derived from solidified ingots, will be able to show clearly the relative importance of each of these transient effects under different processing conditions. It is this insight into the kinetics of the peritectic reaction which will also allow us to quantify phenomena such as transient solute distributions in all of the phases, as well as capillarity phenomena, and to understand their role in the production of the final, room temperature microstructure.

But how to predict the transient behavior of the developing microstructure? One method which shows promise for these simulations is cellular automata (CA) modeling. With these models, a grid is laid out and rule-based growth algorithms are applied to determine the developing morphology of the dendrites. These rules are derived from the relevant physics of solid phase growth and transformation, including undercooling, composition, and interface curvature. Published studies have shown that the basic technique appears to be sound for predictions of grain structures and single phase solid growth [18-26], but work must be done to make the resulting dendritic structures realistic and to verify them experimentally.

The first phase of the proposed numerical research is to improve the current state of transient morphology modeling using CA techniques by increasing their realism so that they may provide better predictions of local microstructure. One significant improvement which needs to be made to CA modeling of dendrite growth is the precipitation of secondary phases in metal alloys. Current CA models only predict primary solidification. Predicting the morphology of all of the developing solid phases is important for the prediction of microsegregation and phase development in cast alloys. Most current microsegregation models (*e.g.*, [27-29]) tend to treat solute profiles in the solid as one dimensional, with a separate distribution in each control volume of the macroscopic domain. The more complicated morphologies of peritectic systems would be predicted better by a CA technique, which will also be able to predict phase distributions in a solidifying three dimensional structure.

Among other effects to be included is simultaneous calculation of local composition fields. Previous work has included microscopic diffusion models mapped on to the CA models [25, 26], which have simulated composition fields in the liquid and one solid phase. The composition calculations should be enhanced to include diffusion between the different solid phases and the coupled phase changes. The temperature calculations will be treated in a similar manner as previous work, except that a procedure will be developed to account for local distribution of latent heat release. It is the interaction between microscopic temperature and composition fields which affects local remelting of solid as well as solid-solid phase change (with composition playing the larger role). These phase changes are not modeled in current CA models for grains or dendrites.

B. Experimental Study of Coupled Growth of Peritectic Alloys

The directional solidification experiments will be designed to examine the effects of convection. Buoyancy driven convective flow is likely to play a major role in the microstructural development as has recently been described by Trivedi and coworkers [9]. To estimate the convection effects for a given geometry and processing condition, computational procedures as previously developed [30-33] will be used to predict fluid flow and solute redistribution. Thus by varying the size of the system, directional solidification experiments will be carried out for conditions with and without convection. The resulting microstructure as a function of processing conditions will be documented. Compositions for directional solidification experiments will be chosen to lie between C_a and C_p as defined in Fig.1. However, compositions near C_p will be considered initially. Initial growth conditions will employ a high G/V as predicted by the constitutional supercooling criteria to produce a planar solid-liquid interface and possibly a banded microstructure. The G/V values will gradually be lowered to produce cellular and dendritic microstructures which will be characterized by quantitative metallography. Convective effects will be varied by changing the diameter of the containment crucible and the length of the melt zone ahead of the solid-liquid interfaces.

C. Predictive numerical simulation procedures combined with experimentation will provide insight into the nature of coupled microstructure in peritectic systems

From the literature, regions of coupled growth are often found after a peritectic banding cycle. Thus the banding cycle can be used as a vehicle for exploring the possibility of coupled growth. For example, the layered microstructure shown in Figure 3 consists of bands containing a two-phase phase cellular microstructure and regions containing only the pertitectic phase. During the process of alternating from one morphology to the other, the morphological development of the solid-liquid interface must pass through a state where the solid-liquid interface for both phases lie along the same isotherm. Numerical

simulations will provide information as to what experimental parameters can be varied to promote metastable couple growth. Experiments will then be carried out to check the predictions. The phase distributions from the samples will be found with image analysis of micrographs and an electron microprobe will be used to measure phase distributions and microsegregation profiles. The phase morphologies and compositional fields will provide the check for the numerical simulations studies performed in parallel with the experimental investigation. In addition, the temperature of the solid-liquid interface will be measured from crucibles instrumented with thermocouples and from quenching experiments. By an iterative approach between simulation and experimentation, the key parameters controlling the morphological development of the microstructure can be identified.

Once the enhanced CA models have be developed and evaluated, the linkage to the macroscopic solidification model will be examined. The CA models will be used to simulate larger ingots with more likelihood of convection. Because the convection can have an effect on the morphology, through disruptions in the temperature and (especially) the composition fields, the microscopic CA models will be linked to the existing macroscopic solidification codes in order to quantify that effect. If we can show that gravity has a significant influence on the ability to produce coupled growth in these alloys, these simulations results will help determine the processing parameters for solidification experiments on reduced gravity flights.

REFERENCES

1. Chalmers, B., *Physical metallurgy*, John Wiley, New York, p. 271, 1959.
2. Boettinger, W. J., *Met. Trans.*, v. 24, pp. 2023-2031, 1974.
3. Jackson, K. A., and J. D. Hunt, *Trans. AIME*, v. 236, pp. 1129-1142, 1966.
4. Ostrowski, A., and E. W. Langer, *Int. Conf. Solidification and Casting*, Institute of Metals, London, vol. 1, pp.139-143, 1977.
5. Brody, H. D., and S. A. David, *Int. Conf. Solidification and Casting*, Institute of Metals, London, vol. 1, pp.144-151, 1977.
6. Oliver, B. F., and B. Kad, *J. Less-Common Metals*, v. 168, pp. 81-90, 1991.
7. Bi, Y. J., and J. S. Abell, *Scripta Met et Mater.*, v. 31, pp. 751-756, 1994.
8. Trivedi, R., *Metall. Mater. Trans. A*, v. 26A, pp. 1583-1590, 1995.
9. Karma, A., W.-J. Rappel, B.C. Fuh, and R. Trivedi, *Metall. Mater. Trans. A*, v. 29A, pp. 1457-1470, 1998.
10. Lee, J. H., and J.D. Verhoeven, *J. Crystal Growth*, v. 144, pp. 353-366, 1994.
11. Busse, P., and F. Meissen, *Scripta Mater.*, v.36, pp.653-658, 1997.
12. Hillert, M., *Int. Conf. Solidification and Casting*, Institute of Metals, London, vol. 1, pp.81-87, 1977.
13. Laraia, V. J., and A.H. Heuer, *Scripta Mat. et. Mater.*, v. 25, pp. 2803-2808, 1991.
14. Ma, D., Li, Y., Ng, S.C., and Jones, H., Acta mater. , v. 48, pp. 419-431, 2000
15. Johnson, D. R., H. Inui, and M. Yamaguchi, *Intermetallics*, v. 6, pp. 647-652, 1998.
16. M. J. Blackburn, *The Science, Technology, and Application of Titanium*, ed. R. I. Jaffee and N. E. Promisel. Pegamon Press, Oxford, 1970, p 663.
17. Kerr, H. W., and W. Kurz, *Int. Mat. Rev.*, v. 41, pp. 129-164, 1996.
18. Rappaz, M., and Ch.-A. Gandin, *Acta metall. mater.*, v. 41, pp. 345-360, 1993.
19. Gandin, Ch.-A., M. Rappaz, and R. Tintillier, *Met. Trans. A.*, v. 24A, pp. 467-479, 1993.
20. Gandin, Ch.-A., and M. Rappaz, *Acta metall. mater.*, v. 42, pp. 2233-2246, 1994.
21. Gandin, Ch.-A., M. Rappaz, D. West, and B. L. Adams, *Met. Trans. A.*, v. 26A, pp. 1543-1551, 1995.

22. Gandin, Ch.-A., and M. Rappaz, *Acta metall. mater.*, v. 45, pp. 2187-2195, 1997.
23. Desbiolles, J.-L., Ch.-A. Gandin, J.-F. Joyeux, M. Rappaz, and Ph. ThJvoz, in *Modeling of Casting, Welding and Advanced Solidification Processes - VIII*, B. G. Thomas and C. Beckermann (eds.), TMS, pp. 433-440, 1998.
24. Brown, S. G. R., T. Williams, and J. A. Spittle, *Acta metall. mater.*, v. 42, pp. 2893-2898, 1994.
25. Dilthey, U., and V. Pavlik, in *Modeling of Casting, Welding and Advanced Solidification Processes - VIII*, B. G. Thomas and C. Beckermann (eds.), TMS, pp. 589-596, 1998.
26. Napolitano, R. E., Jr., and T. H. Sanders, Jr., in *Processing of Metals and Advanced Materials*, B. Q. Li (ed.), TMS, pp. 63-74, 1998.
27. Greven, K., M. Fackeldey, A. Ludwig, T. Kraft, M. Rettenmayr, and P. R. Sahm, in *Modeling of Casting, Welding and Advanced Solidification Processes - VIII*, B. G. Thomas and C. Beckermann (eds.), TMS, pp. 187-194, 1998.
28. Voller, V. R., and C. Beckermann, *Metall. Mater. Trans. A*, v. 30, pp.2183-2189, 1999.
29. Voller, V. R., and C. Beckermann, *Metall. Mater. Trans. A*, v. 30, pp.3016-3019, 1999.
30. Krane, M. J. M., Ph.D. Dissertation, School of Mechanical Engineering, Purdue University, West Lafayette, Indiana, 1996.
31. Krane, M. J. M., and F. P. Incropera, *ASME J. Heat Trans.*, v.119, pp. 783-791, 1997.
32. Krane, M. J. M., F. P. Incropera and D. R. Gaskell, *Metall. Mat. Trans. A*, v. 29A, pp. 843-853 1998.
33. Krane, M. J. M., in *Fluid-Flow Phenomena in Metals Processing*, N. El-Kaddah, et al., (eds.), TMS, pp. 431-440, 1999.

PHYSICAL PROPERTIES AND PROCESSING OF UNDERCOOLED METALLIC GLASS FORMING MELTS

W.L. Johnson, U. Geyer, J. Schroers, and C. Hays

138-78 Keck Laboratory of
Engineering, California Institute of Technology, Pasadena, CA 91125

Well known examples of diffusion-controlled reactions in solids and liquids are nucleation of new phases, precipitation and dissolution of phases, decomposition, diffusive phase transformations, recrystallization, diffusive creep, and thermal oxidation. Diffusion in liquids and non-crystalline media is of particular interest because it is strongly connected with atomic rearrangement phenomena like structural relaxation, decomposition, and crystallization, which are specific for these disordered systems. Precise and reliable diffusion experiments in the equilibrium melt and undercooled liquid state of metal alloys have, to our best knowledge, still to be performed. More particularly, the temperature dependence of atomic diffusion, along with viscosity in bulk metallic glass forming liquids, is a direct signature of the glass transition. Over the undercooled range, both atomic diffusion constants and viscosities change by roughly 14 orders of magnitude. The temperature dependence has been discussed in terms of the concept of "fragility" [Angell 1997]. The functional form of the temperature dependence and the scaling relations between atomic diffusion coefficients and fluidity are of particular interest. In other organic and non-metallic glass formers, the atomic diffusion coefficients have been observed to "decouple" from fluidity [see for example Angell *et al.* 1999]. On going from pure metals to binary alloys to bulk metallic glass formers, it has been shown that the undercooled liquid progressively changes from a "fragile" (pure metals) to a "strong" (silicates and bulk metallic glass forming alloys) behavior. As such, one can traverse the full range of liquid behavior. Viscosity measurements have already successfully been conducted in ground-based experiments using a variety of methods such as beam bending, parallel plate rheometry, capillary flow viscometry, and rotating cup viscometry [Masuhr *et al.* 1999, Bakke *et al.* 1995, Busch *et al.*1998a, Busch *et al.* 1998b]. High temperature viscosity of glass forming liquids was obtained by using drop oscillation techniques under microgravity conditions using the TEMPUS facility during the IML-2 and MSL-1 missions of the space shuttle. [Egry 1999].

To date little experimental data exists for atomic diffusion. The problems arising from contamination by convective flows in earth based experiments are the primary reason for the absence of reliable data. Knowledge of diffusion coefficients and their temperature and mass dependence would be a most important contribution for the understanding of the relaxation dynamics, the relationship between atomic viscosity and atomic transport (*e.g.* Stokes-Einstein relationship etc.) glass transition, liquid/liquid phase separation, and crystallization mechanisms in undercooled metallic liquids. Although some atomic diffusion measurements on alloys of this type have already been done, they have been limited to temperatures near or slightly above the glass transition [see for example, Geyer *et. al.*, 1995, Faupel, 1990, Knorr *et. al.*, 1998, and others].

The goal of the present experiments is the determination of atomic diffusion coefficients from high temperatures in the equilibrium melt, to lower temperatures in the undercooled liquid regime, ultimtately down to the glass transition of a bulk metallic glass forming multicomponent alloy (for example, Vit 106a, a Zr-Nb-Ni-Cu-Al alloy). This alloy can be directly vitrified by free radiative cooling of a spherical drop in an electrostatic levitator and processed for laboratory time scales at any temperature in the undercooled regime. As such, diffusion measurements can potentially be done over the entire range from the glass transition to the equilibrium melt. Such alloys as Vit106a have been shown to be rheologically "strong" liquids. For comparison, we will also carry out atomic diffusion measurements on a simpler binary ($Zr_{64}Ni_{36}$) and ternary (a Zr-Ni-Al alloy) metallic glass forming alloys which exhibit relative "fragile" glass behavior. The diffusion coefficients will be derived from diffusion profiles produced by isothermal processing of the molten alloy in an electrostatic levitator facility and in-situ deployment of the diffusing species during annealing. Prior to isothermal annealing and tracer deployment, the time-temperature-transformation (TTT) and continuous-cooling-transformation (CCT) diagrams of the sample will be determined. These diagrams provide the maximum isothermal processing time possible at the target temperature if one wants to avoid crystallization during annealing and radiative cooling of the samples. Analysis of the profiles will be *ex-situ* and ground-based.

The motivation for use of microgravity our experiments is the minimization of convection in the liquid samples during isothermal diffusion experiments. Convection contaminates the diffusion profiles and makes interpretation of diffusion profiles ambiguous. Only microgravity environment can minimize the impact of natural gravity-driven convection. By contrast, Marangoni surface tension driven convection effects diffusion experiments in both high and low gravity. Minimization of the effects of Maragoni convection will require precise management and control of temperature gradients and concentration gradients during our diffusion experiments. A more detailed explanation of the experimental issues, problems, requirements, mitigation of these problems, and the need for a microgravity will be outlined in the talk.

REFERENCES

1. Angell C.A., B.E. Richards, and V. Velikov, J. of Physics – Cond. Matter, 11, A75, (1999)
2. Angell, C.A., ACS Symp. Series, 676, 14 (1997)
3. Bakke E., R. Busch, and W.L. Johnson, Appl. Phys. Lett., 67, 3260 (1995);
4. Busch R. and W.L. Johnson, Mater. Sci. Forum, 269, 577 (1998a)
5. Busch R., A. Masuhr, E. Bakke, and W.L. Johnson, Mater. Sci. Forum, 269, 547 (1998b)
6. Egry I., J. Non Cryst. Sol., 250, 63-69, (1999)
7. Faupel F., P. W. Hüppe, and K. Rätzke, Phys. Rev. Lett. 65, 1219 (1990)
8. Knorr K., M.-P. Macht, K. Freitag, and H. Mehrer, Proceedings of the 10th International Conference on Liquid and Amorphous Metals, Dortmund 1998; to appear in J. Non-Cryst. Solids (1998)
9. Geyer U., S. Schneider, W. L. Johnson, Y. Qiu, T. A. Tombrello, and M. P. Macht, Phys. Rev. Lett. 75, 2364 (1995)

HIERARCHICAL ASSEMBLY OF COLLAGEN

Regina Valluzzi, Raquel Martin, Donna Wilson, David L. Kaplan

Tufts University, Department of Chemical Engineering & Biotechnology Center
Medford, Massachusetts 02155

INTRODUCTION AND OVERVIEW

An understanding of macromolecular assembly is a cornerstone in polymer science, since the ability to design polymers that can 'assemble themselves,' starting from the molecular scale, offers exciting opportunities in future materials design and fabrication on the ground as well as in space. Collagen is a critical component in almost all tissues in the human body. These protein polymers function as the main structural components or scaffolds in tissues. Collagens provide surfaces upon which cell growth and development occurs and are involved in many disease states that can severely impact physiological function. Despite these essential roles for collagens in our body, very little is known about how complex collagen structures in tissue are formed. While there is a good understanding of how collagen proteins become organized into triple helices or rope like structures, the formation of more complex organized structures that form the basis of bone, ligaments, skin and many other tissues is not understood. This process can be called self-assembly or long-range order generation, since all of the information required for this process has to be contained within the sequences of the collagen proteins themselves, or influenced by some environmental factor during the assembly. Liquid crystallinity, the formation of an organized and orientated liquid prior to solidification, provides a pathway for self-assembly of long-range ordered structures. An analogy to this problem on a larger scale would be the structure of wood composites, such as plywood. The layers in plywood are organized in different orientations. This structural organization forms a material with mechanical properties that exceed those of the individual layers. This type of structural organization also ensures that there is no weak direction or orientation for the material, since each layer resists cracking or breaking most strongly in a different and complimentary direction. The scale at which this level of structural control is achieved in biological systems such as collagens is significantly smaller than that in this plywood analogy, and this leads to important functional properties. In contrast to the plywood analogy, self-assembled proteins can be designed with different functional regions along their length, resulting in a pattern of functional group availability and orientation at the surface of the material when it solidifies from a liquid crystalline phase.

The goal of this research program is to gain insight into the factors that control the formation and structure of organized liquid phases, as material precursors. To achieve this goal chemically synthesized model collagen sequences as well as genetically engineered longer versions of these sequences will be used to gain a full picture of the role of polymer chain length in the process. This approach will enable the precise tailoring of primary sequence, block size and molecular weight in order to understand how these factors influence the assembly process. Aqueous and solvent environments will be used to understand how environmental changes influence the assembly from the molecular to macromolecular scales. Changes in the structures of the collagen assemblies that form under the different conditions will

influence their mechanical properties, patterning of functional features within and on the material, and control of optical properties, among others. Since the interactions that control the assembly process are anticipated to be very subtle, microgravity environments will provide a unique opportunity to reduce gravitational and convection influences to gain additional insight into the process.

Materials that can be designed and programmed for assembly and disassembly have many potentially important applications in space, such as in the preservation of limited resources on long-duration space missions. In addition, insight into the formation of well-defined material structures, composites and laminates, all based on molecular recognition and self-assembly, will be an outcome of the study. These types of materials would be useful in many NASA-specific applications, such as reactive surfaces to 'clean' or purify water, air or surfaces. The research will provide important new insights into the role of collagen structures as biomaterials and in tissue engineering. Insight into collagen long-range self-assembly and the parameters used to control this process will allow a variety of engineered protein scaffolds to be synthesized for biomedical research applications. Since little is known about the influence of extracellular protein organization and chemical patterning on cells (in vitro or in vivo), these materials would provide useful tools to study a range of biological phenomena. Impacts in tissue engineering, collagen-related diseases and cell biology are all possible.

I. Hypothesis

Our hypothesis is that novel and important insight can be gained into the process of self-assembly and hierarchical assembly of materials through the study of collagen-like sequences in well-defined environments. Furthermore, an understanding of these processes has tremendous implications for future materials fabrication and function in space environments as well as on earth. Much of the research on protein structure has focused on globular proteins, which fold into a compact natured state. Another class of proteins is the fibrous proteins, which are typically helices and serve as structural materials in biological systems. The fibrous proteins, in addition to forming fibers, are often found in ordered domains with orientations strongly resembling liquid crystalline phases, but which are solid helicoids rather than liquids. However one of the differences between the protein textures observed and a true liquid crystalline phase is that the protein forms a solid helicoidal material. In some cases small oriented crystallites reinforce the helicoid, making these protein-based materials interesting as potential self-composite materials. Liquid crystallinity immediately suggests itself as a likely mechanism for the portion of the self-assembly process that occurs prior to specific recognition and binding. An in depth understanding of the forces controlling collagen hierarchical assembly will provide new avenues for the formation of collagen-based peptide and polypeptide "glasses" and retaining the orientation of the liquid crystalline mesophase of the solution from which the material was solidified. The role of specific interactions and fabrication methodology to control fibril formation and degree of crystallinity will also be explored, with the aim of creating tunable composites for a variety of NASA-related needs. Because the molecules being used to generate these structures are collagen-like proteins and polypeptides, it should also be possible to create materials with periodically varying surface chemistry. For example, if a cholesteric liquid crystalline peptide "glass" were made from a helical mesogen with hydrophilic endblocks, the hydrophilic residues on the ends of the helix would be available and buried at the surface in a pattern resulting from the cholesteric orientation. A hydrophilic/hydrophobic pattern could be built into the surface chemistry with a periodicity similar to those observed for cholesteric textures in collagens: on the order of 1 – 10 microns. Because of the synthetic techniques used to produce monodisperse populations of collagens, varying environmental parameters allows a second long-range self-assembled phase to be accessed – the chiral smectic phase. Chiral smectic phases typically have

twisted periodicities bringing the material patterning into the nanoscale. Furthermore, the smectic phase organizes rod-like molecules into layers, resulting in chemical patterns on the scale of the length of a single triple helical molecule. Unlike some of the chemical printing techniques involving thiol terminated alkanes adsorbed onto gold, there is no separate printing step with a material based on polypeptide liquid crystalline self-assembly. The chemical pattern is propagated throughout the material in 3-D, opening up the possibility of a variety of surface texture/ chemical patterning/ composite structure combinations. A microgravity environment will provide important advantages to the study of fibrous protein liquid crystalline self-assembly in a manner analogous to the influence of microgravity on globular protein crystal growth. In analogy to the large single crystals of globular protein grown in microgravity, we expect to obtain large well - organized domains of cholesteric collagen, which even in the glassy form is very delicate. Ideal liquid crystalline grains formed in this manner would be invaluable in understanding the factors driving and controlling self-assembly at different length scales. Synthetic peptides and biosynthetic polypeptides incorporating systematic variations in the collagen tripeptide consensus sequence (from triple helix forming portions of the chain) will enable us to study the effects of sequence, amino acid blocks, and secondary structure on pattern generation in model collagen-based materials. The initial ground based studies will focus on establishing the fundamental driving forces and influences of primary sequence on assembly. These data will provide the foundation for inquiry using microgravity experiments. The pursuant microgravity experiments will provide a unique window through which to understand the assembly without confounding factors such as convection gravitational effects, and boundary conditions imposed by a container.

II. Preliminary Results

The conformation, crystal structure and self-assembly behavior of three peptides with collagen-like repetitive sequences, $(Glu)_5(Gly\text{-}Ala\text{-}Pro\text{-}Gly\text{-}Pro\text{-}Pro)_6(Glu)_5$, peptide <**1**>, $(Glu)_5(Gly\text{-}Val\text{-}Pro\text{-}Gly\text{-}Pro\text{-}Pro)_6(Glu)_5$, peptide <**2**>, and $(Glu)_5(Gly\text{-}Ala\text{-}Pro\text{-}Gly\text{-}Pro\text{-}Ala)_6(Glu)_5$, peptide <**3**> were compared. The peptides were characterized using Transmission Electron Microscopy (TEM), Electron Diffraction (ED) and Fourier Transform Infrared Spectroscopy (FTIR) in order to determine how the conformation dictated by each sequence affects the spontaneous generation of long-range ordered structures, such as liquid crystalline mesophases, under a variety of conditions. Samples of each peptide, at ambient temperature and at 5° C, were examined as films dried from aqueous solution, air-water interfacial films, and chloroform-water interfacial films. The sample of peptide <**1**> prepared at 5°C and dried from bulk solution was found to have a collagen-like triple helical structure, as evidenced by electron diffraction. A sinusoidally textured gel, suggestive of cholesteric behavior was observed for peptides <**1**> and <**2**> at the aqueous peptide-chloroform interface at 5°C. Peptide <**3**> also formed a gel, but less reproducibly and the sinusoidal texture was less clear. The periodicity of the texture was reproducibly 10 μm for peptide <**1**> and 7 μm for peptide <**2**>; a texture with a periodicity of 6 μm was observed for peptide <**3**>. The differences in the periodicity of the banded structure and in the crystallization behavior the peptides <**1**> and <**2**> is attributed to differences in the symmetry of the preferred packing arrangement for each peptide, as evidenced by electron diffraction from crystallites that coexist with the sinusoidal gel. These differences are believed to be a measure of the effective symmetry and shape of the molecular cross section.

III. Experimental Plans

A. Synthesis and Characterization of Model Collagens

To gain insight into assembly and patterning of collagens, we will synthesize a series of collagen analogs in which the primary sequence is systematically modified to incorporate bulkier hydrophobic amino acids and charge residues. Peptides (~30 residues) will be prepared by peptide synthesis and larger proteins (15 kDa and 30 kDa) will be synthesized as recombinant proteins generated in *E. coli.* We plan to utilize molecular mechanics calculations to evaluate the effect of residue sequence on the helical period of the collagen triple helix for the variants synthesized. Additional insights into systematic bends or twists with these sequences, other geometric factors that may contribute to molecular asymmetry, and their influence on secondary structure and subsequent liquid crystalline behavior, will also be gained from energy minimization studies.

B. Formation and Characterization of Collagen Assemblies

These collagen-based materials will be assembled and fabricated in two systems: (1) pure water and (2) aqueous buffer to observe the effect of electrostatic screening on self-assembly of the liquid crystal. Bulk studies will help us to understand initial stages of crystallization and mesophase formation. In addition, a series of interfacial experiments will be used to probe specific aspects of triple helix formation and conformation on liquid crystalline behavior. The solution state structures will be characterized by Circular Dichroism and Fourier Transform Infrared Spectrometry. Electron Microscopy, Atomic Force Microscopy, X-ray diffraction, and solid state FTIR microscopy will be used in the bulk and interfacial studies to characterize morphology.

C. Exploration of Utility of the New Collagen Materials

In collaboration with other laboratories and ongoing studies in our own laboratory, we will begin to explore the benefits of these new patterned collagen materials. These studies will include collaborations on tissue engineered cartilage in NASA-funded bioreactor studies (G. Vunjak – MIT), tissue engineered anterior crucial ligaments (our own laboratory), and patterned collagen as substrates for cell response and biomineralization (U. Connecticut Health Sciences Center and our own laboratory). The collagenous assemblies will be utilized in studies involving cell and tissue growth and differentiation wherein surface morphology and patterning play a major role in directing cell differentiation and matrix formation.

D. Microgravity

In the later stages of the program microgravity-based experiments will be pursued based on the insights gained in the ground-based studies. The ground-based studies will provide the refined window of conditions and collagen sequences with which to probe in NASA equipment available for microgravity.

IV. Relevance to the Research to NASA

Most biological structural materials contain fibers or crystallites which reinforce the matrix material. The crystalline or fibrous phase often possesses an orientation that varies as one proceeds through the material. For example there are "helicoid" materials, where the orientation changes in a continuous fashion, and materials resembling laminates, where the orientation varies discontinuously. The variation

in orientation of these "reinforcements," whether fibers, microcrystallites or the rod-shaped molecules, leads to materials that have similar elastic moduli in many directions. Designed composites, for example plywood, use a similar scheme to ensure that there is no weak direction–each layer resists cracking or breakage most strongly in a different and complimentary direction. However, the scale at which this level of structural control in biological systems is significantly smaller than that achieved today in plywood or similar synthetic materials. Biological molecules, specifically fibrous proteins, can create complex or very finely engineered structures that would be difficult to duplicate with conventional processing. An understanding of the liquid crystalline self-assembly of biological structural materials and the factors influencing the orientation and liquid crystalline length-scales that are obtained could be generalized and applied to the design of engineered polymers. Thus, a major outcome of the proposed research will be fundamental insight into the design requirements to control materials assembly at different length scales, so that through the process of self-assembly and macromolecular assembly well-defined material architectures can be formed. These insights will be facilitated with microgravity studies due to the subtle nature of the interactions that will be probed. These insights can provide important options for future materials assembly and fabrication in space wherein finer control of the interactions can be achieved without the confounding influences of gravitational or convection flow. These insights will have broader implications related to fundamental insights into polymer physics related to the formation of molecular architecture, conformation and interactions. For example, soft materials wherein intermolecular forces control morphological details are weak, thus, other weak forces such as gravity have a greater influence. This is quite different than crystallization, nucleation and growth processes where the effects of gravitational disturbances in the surrounding fluid are indirect. Liquid crystal drying to a 'soft' solid will be directly impacted by the effects of gravity because the fluid phase is not separated from the organized phase.

The study of collagen sequence variations and the effects of interfacial chemistry on the morphology of fabricated fibrous collagen membranes and three-dimensional structures will yield techniques for fabricating these membranes or other structures to desired specifications. Collagen peptide sequences needed to form specific membrane porosities, surface features for laminates or recognition, or to promote cell adhesion or enzymatic activity, will yield a range of membranes and fibers containing bulk chemical patterns to which other molecules could then be attached or reacted. Thus, a second major theme for the proposed studies will be the formation of well-defined material structures, composites and laminates, all based on molecular recognition and self-assembly. These types of materials would be useful in many NASA-specific scenarios, such as reactive surfaces to 'clean' or purify waters, air or surfaces. For example, interfacial chemistry can be used to create membranes that are not symmetric, having different chemical functionalities preferentially partitioned to opposite sides of the interface, and to opposite sides of the resulting collagen membrane films.

The patterning of the collagenous matrix, along with the chemical functionalities present in this pattern, is directly involved in cellular growth processes. Therefore, the insights that will be gained with the proposed studies will provide a window into a number of biochemical and biomedical applications with these materials. Patterned functionalized collagen membranes may have applications in tissue engineering, as novel drug delivery systems, and in other biomedical applications. In their mineralized form, collagens form the basis of strong yet lightweight tissues such as bone. In addition, they are routinely used in reprocessed forms to generate biomaterials and scaffolds for cell and tissue growth. Despite this widespread use, there has been little effort to understand the details of the self-assembly process *in vitro*. This insight will be critical to the full understanding of biological responses to collagen-based

materials. Thus, a third key area of significance to the proposed studies will be insight into collagen assembly that may have implications in biomaterials and tissue engineering, as well as insights into collagen-related diseases possibly influenced by gravitational induced control of assembly that is absent in the space environment. Collagenous materials are produced commercially for a variety of biomedical uses. These products, including collagen sponges and fibers, are used for autologous tissue regeneration, suture materials, cell growth matrices and related needs. Currently, the structural features of these materials are controlled at the macroscopic level. For example, the pore sizes in collagenous membranes and sponges are usually determined by removal of water in the form of ice from frozen samples. There is little attention paid to lower levels of structural organization in these materials, including the molecular and mesoscale levels. These levels of organization are critical to the mechanical properties and biological functions of these materials.

PHASE-FIELD SIMULATIONS OF EQUIAXED DENDRITIC GROWTH AT LOW UNDERCOOLING: CONFRONTING THEORY AND EXPERIMENT

Alain Karma

Department of Physics, Northeastern University, Boston, MA 02115

INTRODUCTION

Dendrites are complex growth morphologies that are the building blocks of the microstructure of many important commercial alloys processed by solidification. Although dendritic growth has been the main focus of fundamental research in pattern formation and crystal growth for decades, it is only quite recently that numerical simulation techniques have reached the point of making realistic predictions that can be meaningfully compared with experiments, or used to critically test analytical theories. Among various techniques that have been developed, the phase-field approach has clearly emerged as the leading computational technique for simulating dendritic growth and other interfacial pattern formation phenomena both efficiently and accurately in three dimensions (3-D).

The goal of this new project is to carry out fully quantitative phase-field simulations of 3-D equiaxed dendritic growth in a pure undercooled melt at low undercooling, which can be compared quantitatively with NASA's space Isothermal Dendritic Growth Experiments (IDGE) on succinonitrile (SCN) and pivalic acid (PVA).

I. Experimental Background

Detailed experiments have been carried out on the transparent substances succinonitrile (SCN) [1, 2], pivalic acid (PVA) [3, 4], and Xenon (Xe) [5, 6, 7], which all have a cubic crystal structure. The morphology of the dendrite can be directly observed through a microscope, and the dendrite shapes can be analyzed *ex situ* from video tape recordings of the growth. Terrestrial data have been supplemented by the results from the Isothermal Dendritic Growth Experiment (IDGE) performed in a microgravity environment for SCN [8] and PVA [9].

Tip velocities and tip radii have been measured as a function of the undercooling. For SCN, detailed terrestrial and microgravity data are available; for PVA, tip velocities and tip radii are available from earth-based experiments; only preliminary data on the tip velocity have been released from the IDGE PVA experiment. Both data sets show an important difference between terrestrial and microgravity data. Typically, growth rates are larger on earth because the transport is enhanced by convection.

Usually, the tip radius is obtained by fitting the contour of the dendrite to a parabola. For SCN, LaCombe *et al.* have shown that this procedure becomes inaccurate already quite close to the tip [10]

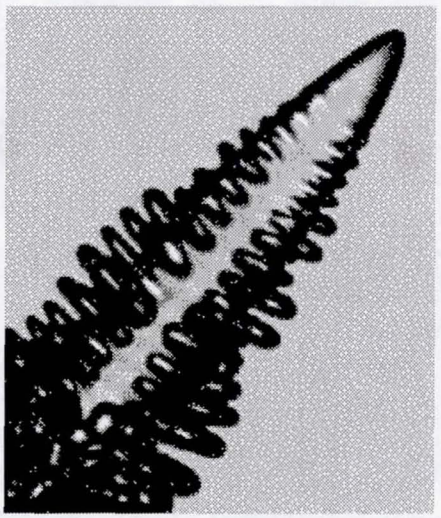

Figure 1. Tip of a PVA dendrite grown during the IDGE space experiment (Glicksman *et al.*).

and proposed a fit with a fourth order polynomial. The same study also revealed that the detailed non-axisymmetric structure of SCN dendrite tips can be described as a paraboloid with a small four-fold perturbation, which develops further behind the tips into pronounced fins, as can be clearly seen for PVA in Figure 1. No comparable study has been published for PVA. In Xe dendrites, it was found that the shape of the dendrite close to the tip can be well described by a power law [6, 7].

To characterize the large scale structure of the dendrite far from the tip, where the well-developed sidebranches form a complicated structure, Bilgram and coworkers have measured the properties of a dendrite contour obtained by projection normal to the growth direction and to a (100)-plane for Xenon dendrites [5]. In particular, they calculated the contour length U(z) measured from the tip and the projected area F(z) between the contour and the growth axis as a function of the distance z from the tip measured along the growth axis. They found remarkably simple scaling laws. A similar analysis has recently been performed for the SCN data of the IDGE experiments [11].

II. Theoretical Background

The operating state of a dendrite is characterized by the tip velocity v and the tip radius of curvature ρ. Both quantities are selected by the interplay between long-range diffusive transport of heat and the effects of surface tension and/or interface kinetics at the tip. Ivantsov solved the diffusive transport problem for an isothermal solid-liquid interface, *i.e.* neglecting surface tension and attachment kinetics [12]. He found a family of paraboloids (or parabolas in two dimensions) growing at constant velocity. The consistent incorporation of surface tension and attachment kinetics led to the advent of microscopic solvability theory [13]. The inclusion of surface tension constitutes a singular perturbation of the Ivantsov problem, leading to a nontrivial solvability condition. The central result is that steady-state solutions only exist when the surface tension is anisotropic, and that the selected velocity and tip radius strongly depend on the anisotropy of the surface tension, as well as on the kinetic anisotropy if the effect of attachment kinetics is important. The stable growth directions are the directions of maximal surface tension, usually the low-index planes of the crystal structure.

In three dimensions, the shape of the dendrite rapidly becomes non-axisymmetric away from the tip. Ben Amar and Brener [14] have predicted that capillary effects lead to a universal four-fold deviation

from a paraboloid of the form

$$z = -\frac{r^2}{2} + A_4 r^4 \cos 4\phi \qquad (1)$$

where $A_4 = 1/88$ is independent of anisotropy strength and (r, ϕ) are the polar coordinates in the plane normal to the growth axis z with all lengths scaled by ρ_{Iv} . The improved prediction $A_4 = 1/96$ has been obtained in a subsequent analysis. We have recently carried out a detailed phase-field simulation study of the 3-d dendrite tip morphology at low undercooling in the absence of interface kinetics [15]. Simulations have yielded a value of $A_4 \approx 0{:}004$ that is about twice smaller than predicted by solvability theory, and in remarkably good agreement with experiments in SCN [10] when the difference between the actual shape and the (measured) projected shape is taken into account [15].

It has been proposed that sidebranches result from the selective amplification of thermal fluctuations [16, 17]. An interesting prediction of theories based on this hypothesis is that the sidebranch amplitude is extremely dependent on the shape of the steady-state tip. Langer's original calculation, which used a paraboloidal tip shape [16], seemed to show that the magnitude of thermal fluctuations was too small to account for the observed sidebranching. Later, Brener and Temkin repeated the calculation, but using Brener's non-axisymmetric dendrite shape and found that the sidebranching is drastically enhanced [17]. Their prediction appears to agree with experimental results on Xenon dendrites [6, 7], although these experiments may be strongly influenced by convection. We have recently carried out a phase-field modeling study of dendritic sidebranching with thermal noise in 2-D [18] and found a good agreement with the predictions noise amplification theories. The extension of this study to 3-D, however, remains needed to determine if thermal noise is sufficient to produce the experimentally observed sidebranching activity.

III. Phase-Field Modeling

Over the last decade, the phase-field method has emerged as a method of choice for simulating microstructural pattern formation [19, 20, 21, 22, 23]. Simulations in this project will be based on a computationally efficient phase-field approach developed by the Principal Investigator and coworkers that combines two key ingredients. The first is an improved asymptotic analysis of the phase-field model [24, 25]. This analysis makes it possible to choose the width of the spatially diffuse interface region much larger than the microscopic capillary length, thereby dramatically reducing the simulation time and lowering the limit of accessible undercooling. In addition, it permits to freely choose the strength of interfacial attachment kinetics, including the case of local equilibrium at the interface (*i.e.* negligible interface kinetics). The second key ingredient is an adaptive-step diffusion Monte Carlo method that provides an efficient solution of the diffusion equation at low undercooling [28]. This algorithm offers the same advantage as adaptive mesh refinement [26, 27], in that the computational cost scales as the area of the growing structure rather than the volume containing the diffusion field, but is simpler to implement numerically in three dimensions without significant compromise in accuracy. To our knowledge, our method is the first one to date capable of quantitatively modeling three-dimensional dendritic growth in a range of dimensionless undercooling (0.01-0.1) that is directly relevant for microgravity experiments.

Simulations will focus on investigating three main aspects of equiaxed dendritic growth that can all be compared directly with experiments: (i) the selection of the tip operating state characterized by the tip velocity, tip radius, and non-axisymmetric tip morphology, (ii) the sidebranching activity characterized by the amplitude and spacing of sidebranches as a function of distance behind the tip, and (iii) the identifica-

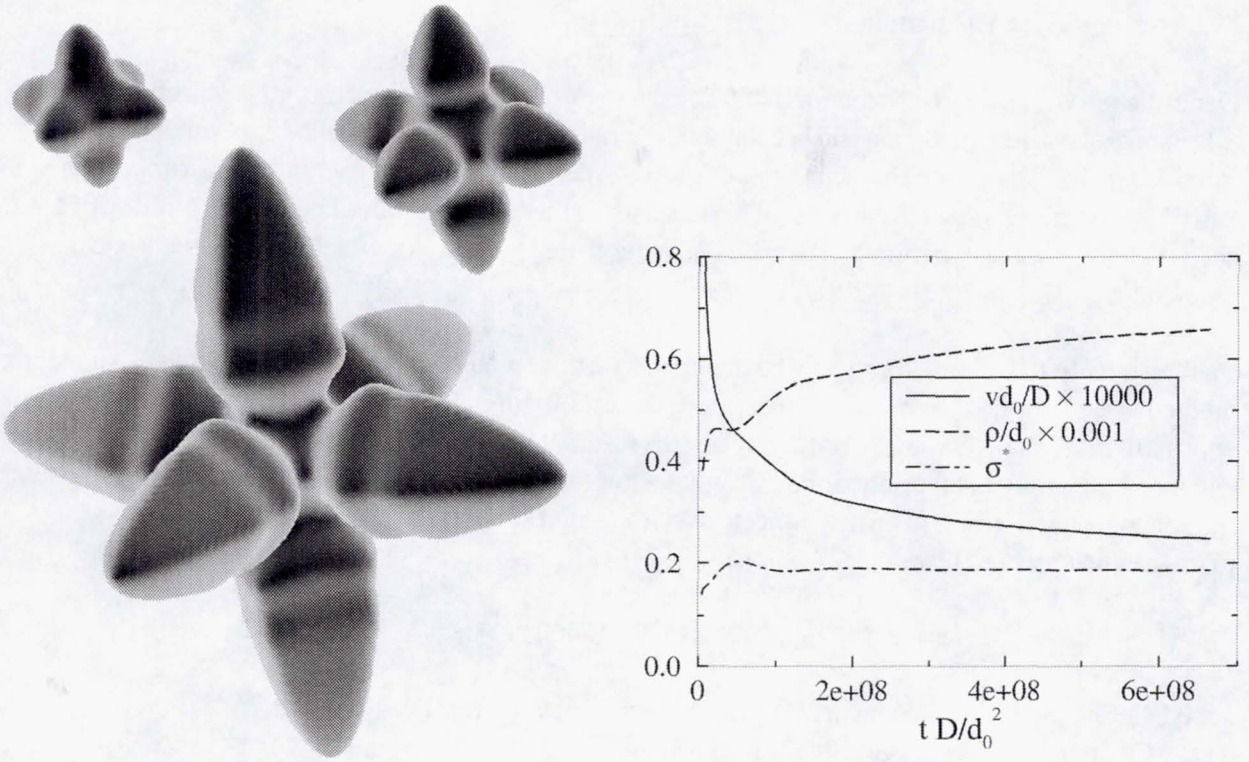

Figure 2. Left: snapshot pictures of a three-dimensional dendrite simulated using an adaptive stepping diffusion Monte Carlo algorithm [28] for a dimensionless undercooling $\Delta = 0.05$ and a surface tension ansiotropy $e_4 = 0.025$. Right: plot of the instantaneous tip velocity, tip radius and selection constant versus time. Whereas the velocity decreases and the tip radius increases, σ^* remains constant. The asymptotic velocity is much higher than the one measured for PVA at the same undercooling. For capilary length 3.8 nm and thermal diffusivity 0.7×10^{-3} cm^2 / s measured for pivalic acid [4]. The pictures correspond to solidification times of 0.23 s, 0.46 s, and 1.38 s, respectively, and the diameter of the largest dendrite is 160 μm dendritic growth in a range of dimensionless undercooling (0.01-0.1) that is directly relevant for microgravity experiments.

tion of scaling laws to characterize how the length and width of primary branches vary with time during the transient development of the equiaxed structure starting from a small structureless seed. Scaling laws have been predicted analytically in 2-D but have not yet been investigated in detail in 3-D. Their elucidation represents a new frontier in our fundamental understanding of dendritic microstructural evolution in undercooled melts.

Whereas the measured velocity and tip radius of the selected tip operating state agrees very well with microscopic solvability theory for SCN, preliminary microgravity data from IDGE show that for PVA the observed growth velocities are much lower than predicted on the basis of the measured surface tension anisotropy value. Possible explanations for this effect are the presence of strong interfacial kinetics, or an influence of the sidebranching activity on the selection of the operating state. Both hypotheses can be quantitatively investigated using the phase-field method. In addition, our simulations will enable us to directly test current theories of sidebranching and to probe scaling laws which have recently been proposed to describe the initial growth transient and the global large scale characteristics of equiaxed 3-D dendrites.

IV. Microgravity Relevance

Dendritic growth theory has been for many years a major focus of research because of its fundamental role in microstructure modeling and because of the availability of well-controlled experiments which provide precise data on the characteristics of growing dendrites. The microgravity experiments on SCN and PVA play a key role in the process of understanding the fundamentals of dendritic solidification because they provide experimental data on convection-free growth, for which detailed theoretical predictions exist.

The full benefit of these data can only be obtained by a quantitative comparison with accurate modeling predictions. Phase-field simulations will allow us to establish this comparison without uncontrolled approximations, and therefore to critically test the foundations of dendritic growth theory. Moreover, the enhanced capability of precisely simulating microstructural pattern formation in a purely diffusive growth regime, which will result from this project, is an important support for past and future NASA microgravity materials research.

REFERENCES

1. M. E. Glicksman, R. J. Schaefers, and J. D. Ayers, Metall. Trans. A 7 1747 (1976).
2. S.-C. Huang and M. E. Glicksman, Acta Metall. 29 , 701 (1981).
3. M. E. Glicksman and N. B. Singh, J. Cryst. Growth 98 , 277 (1989). [4] E. R. Rubinstein and M. E. Glicksman, J. Cryst. Growth 112 , 84 (1991).
5. E. H. Urlimann, R. Trittibach, U. Bisang, and J. H. Bilgram, Phys. Rev. A 46 , 6579 (1992).
6. U. Bisang and J. Bilgram, Phys. Rev. Lett. 75 , 3898 (1995).
7. U. Bisang and J. Bilgram, Phys. Rev. E 54 , 5309 (1996).
8. M. E. Glicksman, M. B. Koss, and E. A. Winsa, Phys. Rev. Lett. 73 , 573 (1994).
9. M. E. Glicksman, Microgravity News, NASA 4 , 4 (1997).
10. J. C. LaCombe, M. B. Koss, V. E. Fradkov, and M. E. Glicksman, Phys. Rev. E 52 , 2778 (1995).
11. Q. Li and C. Beckermann, Phys. Rev. E 57 , 3176 (1998).
12. G. P. Ivantsov, Dokl. Akad. Nauk SSSR 58 , 567 (1947).
13. D. A. Kessler, J. Koplik, and H. Levine, Adv. Phys. 37 , 255 (1988).
14. M. Ben Amar and E. Brener, Phys. Rev. Lett. 71 , 589 (1993).
15. A. Karma, Y.H. Lee, and M. Plapp, Phys. Rev. E 61 3996 (1999).
16. J. S. Langer, Phys. Rev. A 36 , 3350 (1987).
17. E. Brener and D. Temkin, Phys. Rev. E 51 , 351 (1995).
18. A. Karma and W.-J. Rappel, Phys. Rev. E 60 , 3614 (1999).
19. J. S. Langer, in Directions in Condensed Matter , ed. by G. Grinstein and G. Mazenko (World Scientific, Singapore, 1986), p. 164.
20. J. B. Collins and H. Levine, Phys. Rev. B 31 , 6119 (1985).
21. R. Kobayashi, Physica D 63 , 410 (1993).
22. G. B. McFadden, A. A. Wheeler, R. J. Braun, S. R. Coriell, and R. F. Sekerka, Phys. Rev. E 48 , 2016 (1993).
23. A. A. Wheeler, W. J. Boettinger, and G. B. McFadden, Phys. Rev. A 45 , 7424 (1992).
24. A. Karma and W.-J. Rappel, Phys. Rev. Lett. 77 , 4050 (1996).
25. A. Karma and W.-J. Rappel, Phys. Rev. E 53 , R3017 (1996); ibid. 57 , 4323 (1998).
26. R. J. Braun and M. T. Murray, J. Cryst. Growth 174 , 41 (1997)
27. N. Provatas, N. Goldenfeld, and J. Dantzig, Phys. Rev. Lett. 80 , 3308 (1998).
28. M. Plapp and A. Karma, Phys. Rev. Lett. 84 , 1740 (2000).

ROLE OF DYNAMIC NUCLEATION AT MOVING BOUNDARIES IN PHASE AND MICROSTRUCTURE SELECTION

Alain Karma[1]
Rohit Trivedi[2], Co-Investigator

[1]Department of Physics and Center for Interdisciplinary Research on Complex Systems, Northeastern University, Boston, MA 02115
Ames Laboratory of the Department of Energy and
[2]Department of Materials Science and Engineering, Iowa State University, Ames, Iowa 50011

We report the results of a combined experimental and theoretical investigation of microstructure formation in directionally solidified (Pb-Bi and Sn-Ca) peritectic alloys. This study focuses on a growth regime of large thermal gradient to pulling speed (G/V) ratio where both the primary and secondary solid phases are morphologically stable. In this regime, the richness of possible microstructures results from the competition between the growth and nucleation of the two solid phases, which turns out to be strongly influenced by convection. Experiments were based on a Bridgman set up where thin diameter tubes of different diameters could be simultaneously solidified. This set up was key to examine the critical influence of varying levels of radial convection on the microstructure. In one set of experiments, convection was enhanced by mechanical stirring. Theoretical studies were based on numerical simulations of sharp interface models that assume a planar solidification front, but incorporate both diffusive and convective transport, and a phase-field model that relaxes this assumption but only incorporates diffusive transport. The critical parameters that were varied in both experiments and simulations include the tube diameter, the composition, and the G/V ratio. In very thin diameter tubes, we were able to obtain banded structures formed by alternate nucleation and growth of the primary and secondary phases. Compositional analysis of the solidified samples revealed that nucleation of the parent and secondary phases do indeed occur above and below the peritectic temperature, respectively, thereby directly validating the basic concept and predictions of the diffusive growth model. Quantitave comparison of experimental data and the model predictions allowed us to extract the values of the nucleation undercoolings for the two phases. For larger tube diameter, careful serial sectioning revealed the existence of a single tree-like structure that is formed by the continuous growth of the two phases with only initial nucleation. The existence of this structure is predicted by numerical simulations with diffusive and convective transport. Phase-field model simulations predict the formation of a particulate banded structure in large samples with multiple nucleation events and purely diffusive growth conditions.

EFFECT OF MARANGONI CONVECTION GENERATED BY VOIDS ON SEGREGATION DURING LOW-G AND 1-G SOLIDIFICATION

M. Kassemi[1], A. Fripp[2], N. Rashidnia[1], and H. de Groh[3]

[1]NCMR, NASA GRC, Cleveland OH,
[2]NASA LaRC, Hampton, VA, [3] NASA GRC, Cleveland OH

INTRODUCTION

Solidification experiments, especially microgravity solidification experiments, are often compromised by the evolution of unwanted voids or bubbles in the melt. Although these voids and/or bubbles are highly undesirable, there is currently no effective means of preventing their formation or of eliminating their adverse effects, particularly during microgravity experiments. Marangoni convection caused by these voids can drastically change the transport processes in the melt. Recent microgravity experiments by Matthiesen (1) , Andrews (2) and Fripp (3) are perfect examples of how voids and bubbles can affect the outcome of costly space experiments and significantly increase the level of difficulty in interpreting their results.

Formation of bubbles have caused problems in microgravity experiments for a long time. Even in the early Skylab mission an unexpectedly large number of bubbles were detected in the four materials processing experiments reported by Papazian and Wilcox (4). They demonstrated that while during ground-based tests bubbles were seen to detach from the interface easily and float to the top of the melt, in low-gravity tests no detachment from the interface occurred and large voids were grown in the crystal. More recently, the lead-tin-telluride crystal growth experiment of Fripp *et al.*(3) flown aboard the USMP-3 mission has provided very interesting results. The purpose of the study was to investigate the effect of natural convection on the solidification process by growing the samples at different orientations with respect to the gravitational field. Large pores and voids were found in the three solid crystal samples processed in space. Post-growth characterization of the compositional profiles of the cells indicated considerable levels of mixing even in the sample grown in the hot-on-top *stable* configuration. The mixing was attributed to thermocapillary convection caused by the voids and bubbles which evolved during growth. Since the thermocapillary convection is orientation-independent, diffusion-controlled growth was not possible in *any* of the samples, even the top-heated one. These results are consistent with recent studies of thermocapillary convection generated by a bubble on a heated surface undertaken by Kassemi and Rashidnia (5-7) where it is numerically and experimentally shown that the thermocapillary flow generated by a bubble in a *model* fluid (silicone oil) can drastically modify the temperature field through vigorous mixing of the fluid around it, especially under microgravity conditions.

In the present research effort we investigate both numerically and experimentally the effect of thermocapillary convection generated by a void/bubble on the growth of a typical single crystal alloy. In this paper, we only present some of the microgravity numerical simulations to demonstrate in detail the manner in which the void-generated convection can modify the temperature stratifica-

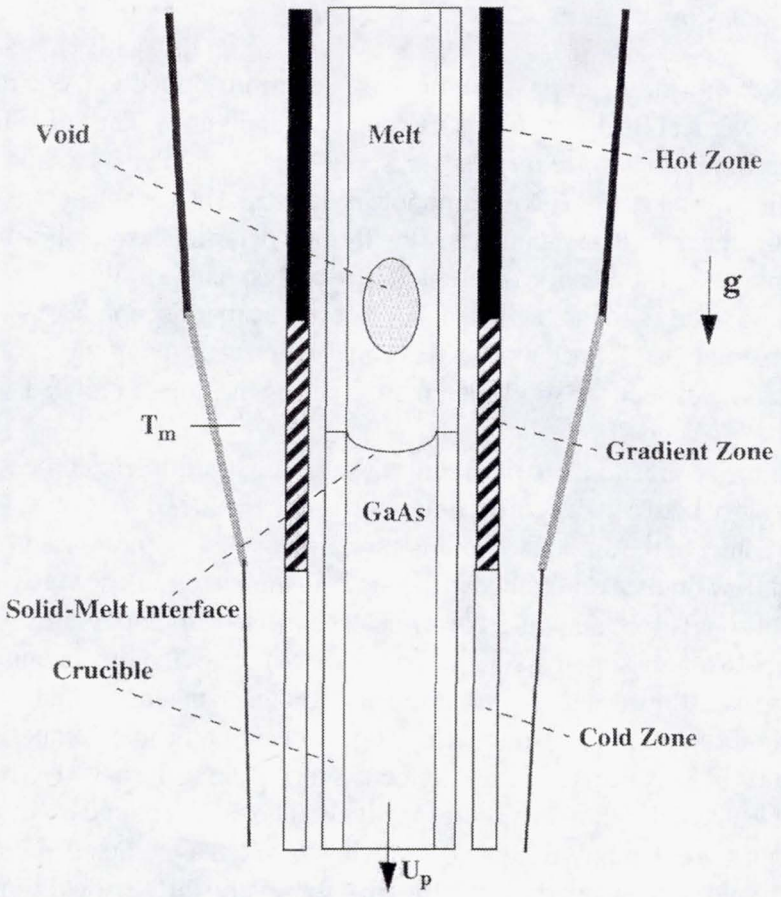

Figure 1. Schematic of the Bridgman Growth Configuration.

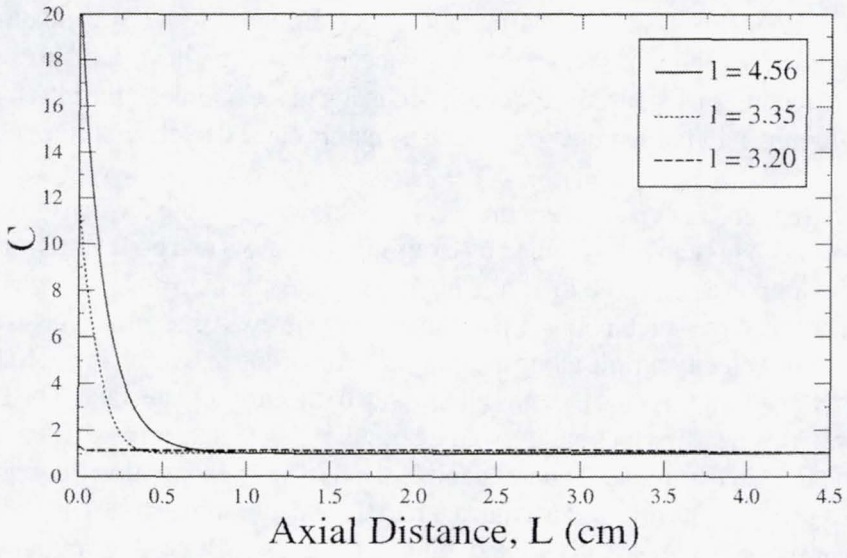

Figure 2. Concentration along the central axis of symmetry for different void-interface distance, *l*(cm).

tion and the segregation patterns in the dilute binary melt during various stages of a microgravity solidification experiment. These results characterize and quantify for the first time the serious impact of voids and/or bubbles on the growth of single crystal in space. The ground-based SCN experiments and the associated numerical simulations will be covered in future papers and reports.

I. Results and Discussion

Consider the growth of a single crystal (in this case selenium-doped GaAs) from a dilute two-component melt in a vertical Bridgman furnace as depicted in Figure 1. The ampoule is placed in a three- zone furnace which consists of fixed hot and cold zones separated by a sharp gradient region. Directional solidification takes place as the ampoule is translated at a constant rate. The transport of heat among the solid, the melt, the ampoule, and the furnace determines the solid-melt interface shape and position. The numerical simulations presented here correspond to a situation where a void is present in the melt. The quasi-steady simulations show the effect of the thermocapillary convection generated by the void on the temperature and concentration fields in the melt at different stages of the solidification process as the distance between the solid-melt inter-face and the void is reduced.

The first case examined corresponds to the initial stages of the solidification process where there is a relatively large distance between the growth interface and the void ($l = 4.56$ cm). The axial concentration profile (at the center of the ampoule) for this case is presented in Figure 2 and the temperature, concentration, and flow fields are presented in Figure 3. In this situation, the void is in the shallow gradient region (hot zone) of the ampoule. Nevertheless a thermocapillary vortex is generated in the vicinity of the bubble as shown in Figure 3a. The vortex recirculates the fluid along the void interface in a clockwise direction. The flow is not too strong and is restricted to the mostly uniform temperature and concentration regions of the ampoule, therefore, it does not affect the melt temperature and concentration fields appreciably. The concentration and velocity profiles along the axis of symmetry (ampoule centerline) are presented in Figures 2 and 4, respectively. The solutal boundary layer at the growth interface is very thin and extends only about 0.75cm into the melt as depicted in Figure 2. The velocity boundary layers around the void are shown in Figure 4 for several different void-interface locations. Note that for the $l = 4.56$ *cm* case, the flow dies long before it can penetrate the solutal boundary layer. As a result at $l = 4.56$ cm, the solidification process is unaffected by the void-generated convection. The radial concentration profile along the growth interface for this case and several other void-interface distances are included in Figure 5. The $l = 4.56$ *cm* concentration profile is parabolic at the melt-solid interface with the maximum dopant concentration occurring in the middle of the interface. This indicates an appreciable amount of radial segregation, which is mainly caused by the interface curvature.

The interfacial segregation pattern changes drastically as shown in Figure 5 when the void-interface distance, l, is reduced. This can be explained by examining the flow and concentration fields of the $l = 3.2$ *cm* case, for example, as included in Figure 6a. In this case, the thermocapillary vortex shown in Figure 6a has penetrated the solutal build-up region near the growth interface. This is corroborated by an examination of the velocity profile along the ampoule centerline in Figure 4 which shows that the velocity boundary layer for this case extends all the way to the growth interface. The strong thermocapillary vortex nearly wipes out the solute boundary layer at the growth interface as indicated by the concentration field in Figure 6a and homogenizes the dopant concentration throughout the ampoule through vigorous mixing. The $l = 3.2$ *cm* axial and radial concentration profiles included in Figures 2 and 5a are both indicative of an almost fully-mixed regime. But a closer look at the radial segregation pattern on an expanded scale as shown in Figure 5b still indicates a noticeable nonuniformity in the interfacial concentration profile. The thermocapillary mixing effect becomes more pronounced as the void and the interface get closer to each other. At $l = 1.95$ *cm* the void is in the high temperature gradient region. Consequently, the thermocapillary flow intensifies with an almost five-fold increase in the maximum velocity as shown in Figure 4. This creates a substantial amount of mixing near the interface as indicated by the concentration and flow fields in Figure 6b which produces an even more uniform concentration profile at the growth interface.

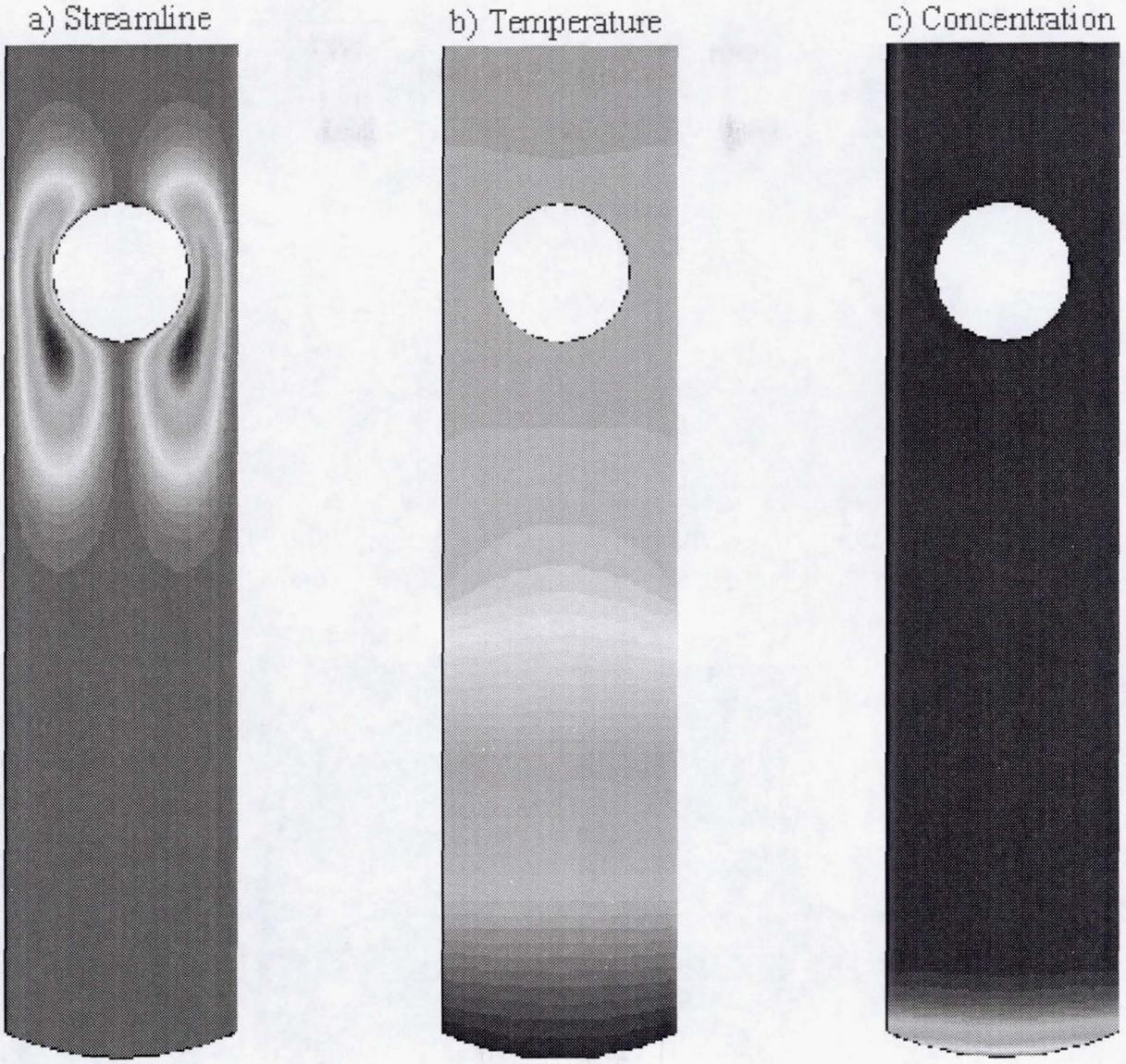

Figure 3. Streamline (a), Temperature (b), and Scaled Concentration (c) fields for l=4.56cm case.

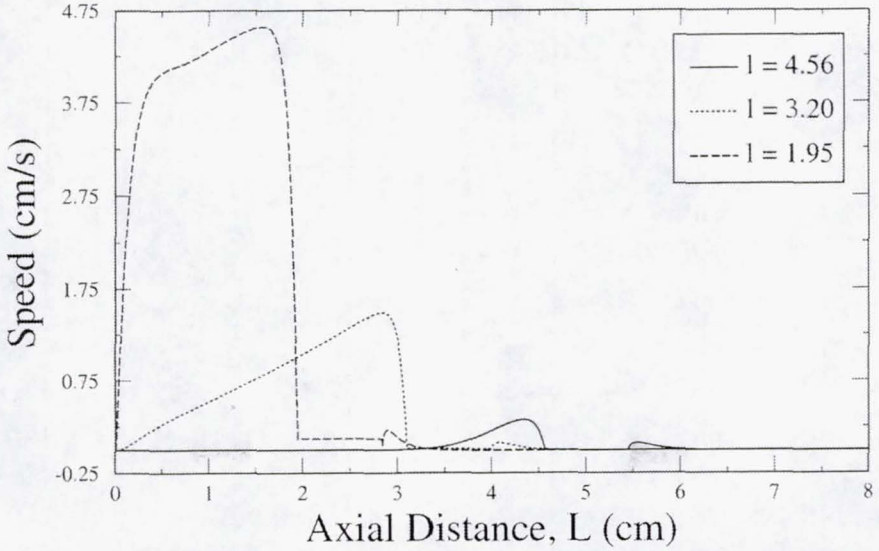

Figure 4. Speed along the central axis of symmetry for different void-interface distances, l(cm).

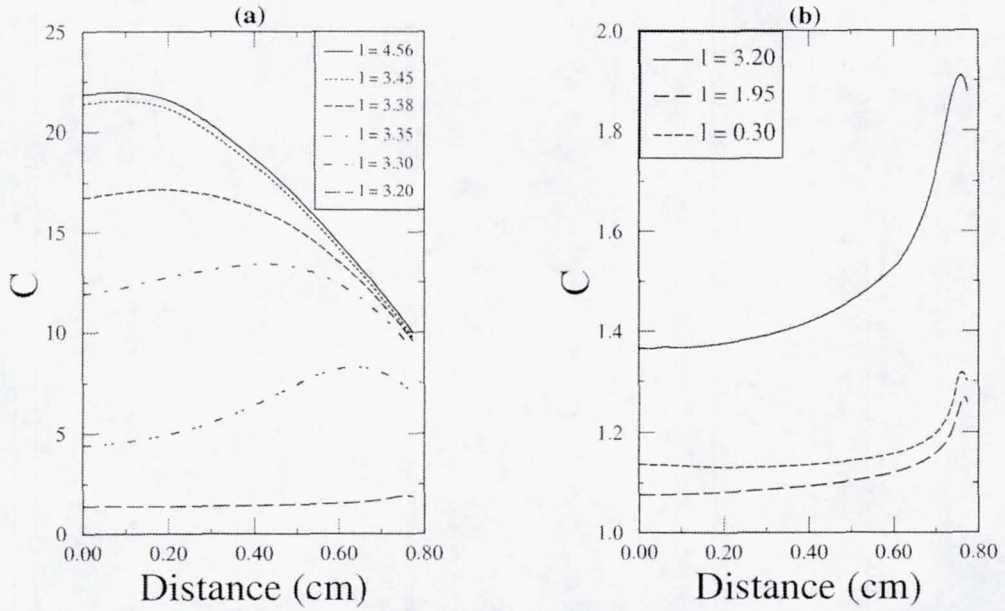

Figure 5. Concentration along the solid-melt interface for different void-interface distances l (cm).

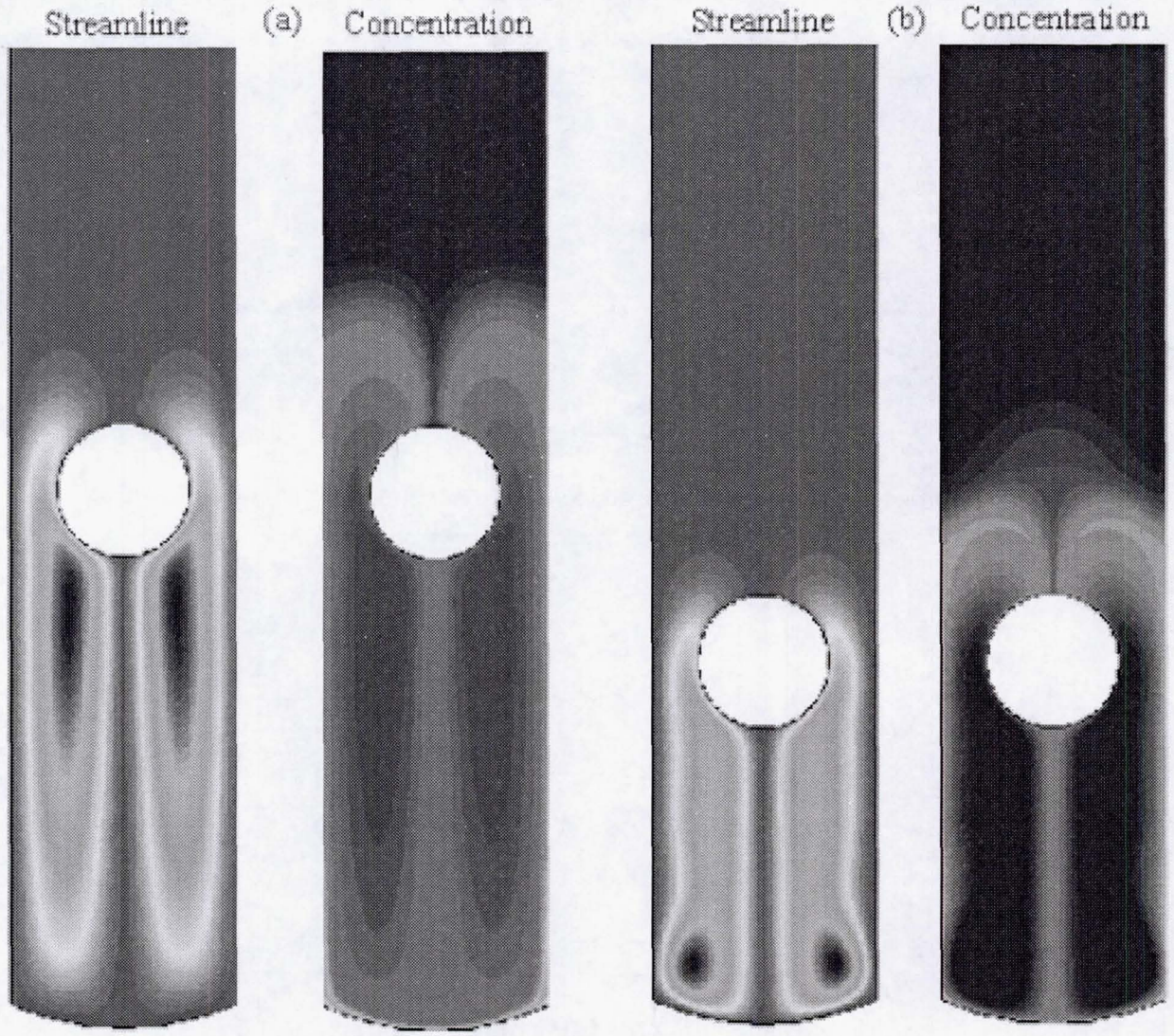

Figure 6. Streamline and scaled concentration fields for l=3.20 cm (a) and l =1.95 cm (b) cases.

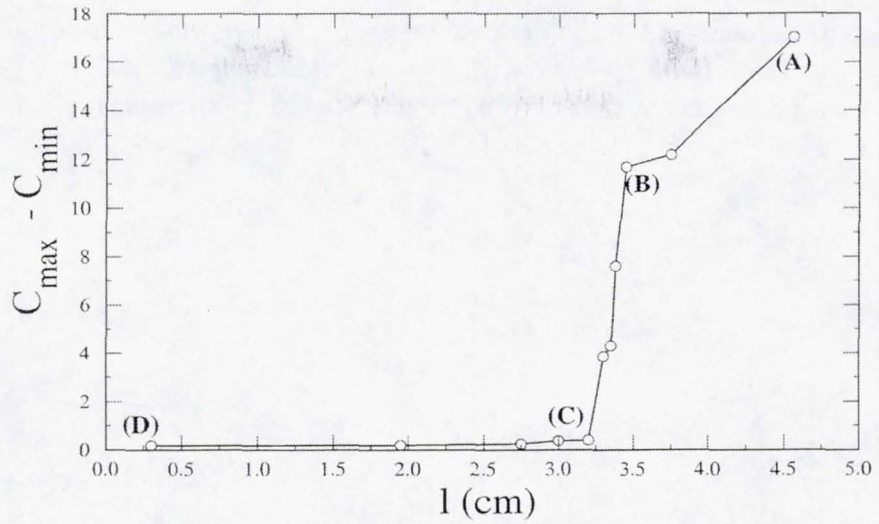

Figure 7. Plot of radial segregation versus void-interface distance.

II. Conclusion

The results of this analysis can be succinctly summarized by plotting the magnitude of the radial segregation against the void-interface distance as shown in Figure 7. From a transport point of view, there are three distinct regions on this plot. Points (A) to (B) correspond to the region where the solutal boundary layer is minimally affected by the void-generated thermocapillary convection. The segregation behavior in this region is dominated by diffusion and is caused almost entirely by the interface curvature. Points (B) to (C) designate a region where the thermocapillary flow begins to influence the segregation pattern considerably (see Figure 5a) but has not yet penetrated the solutal boundary layer at the growth interface. In this region the extent of the radial segregation and the distribution of the interfacial composition change drastically with small variations in the void-interface distance. Finally, the segment bounded by points (C) to (D) correspond to the region where the vigorous thermocapillary flow wipes out the solutal boundary layer and a fully-mixed regime is approached.

REFERENCES

1. Matthiesen D.H., and Majewski, J.A., *The Study of Dopant Segregation Behavior During the Growth of GaAs in Microgravity*, In Joint Launch + One Year Review of USML-1 and USMP-1, NASA CP 3272, Vol1, p223, May 1994.
2. Andrews, J. B., Hayes, L.J., Arikawa, Y., and, Coriell, S.R., *Microgravity Solidification of Al-In Alloys*, AIAA 97-1012, 1997.
3. Fripp, A.L., and et al., *The Effect of Microgravity Direction on the Growth of PbSnTe,* AIAA 97-0676, 1997.
4. Papazian, J. M. and Wilcox, W. R., *Interaction of Bubbles with Solidification Interfaces*, AIAA J., Vol. 16, 447- 451, 1978.
5. Kassemi, M., and Rashidnia, N., *Steady and Oscillatory Thermocapillary Flows Generated by a Bubble in 1-G and Low-G Environments*, AIAA 97-0924, presented in the 35th AIAA Aerospace Conference, 1997.
6. Kassemi. M., Rashidnia, N. and Mercer, C., *Numerical and Experimental Visualization of Oscillatory Temperature and Velocity Fields Generated by a Bubble*, Proceedings of The 8th International Symposium in Flow Visualization, Eds. G.M. Carlomagno and I. Grant, pp. 284.1-284.11, 1998

7. Kassemi. M. and Rashidnia, N., *Oscillatory and Steady Thermocapillary and Natural Convective Flows Generated by a Bubble: Numerical-Experimental Comparisons*, Proceedings of the Joint Xth European and Russian Symposium on Physical Sciences in Microgravity, Eds V.S. Avdyevsky and V.I Polezhaev, Vol I, pp. 110-117, 1997.

STUDIES OF NUCLEATION, GROWTH, SPECIFIC HEAT, AND VISCOSITY OF UNDERCOOLED MELTS OF QUASICRYSTALS AND POLYTETRAHEDRAL-PHASE-FORMING ALLOYS

K.F. Kelton[1] *, T.K. Croat[1], A. Gangopadhyay[1], D. Holland-Moritz[2], Robert W. Hyers[3], Thomas J. Rathz[4], Michael B. Robinson[3], Jan R. Rogers [3]

[1]Department of Physics, Washington University, St. Louis, MO 63130
[2]Institut fur Raumsimulation, DLR, D-51170, Köln, Germany
[3]NASA/George C. Marshall Space Flight Center, Huntsville, AL 35812
[4]University of Alabama, Huntsville, AL

ABSTRACT

Undercooling experiments and thermal physical property measurements of metallic alloys on the International Space Station (ISS) are planned. This recently-funded research focuses on fundamental issues of the formation and structure of highly-ordered non-crystallographic phases (quasicrystals) and related crystal phases (crystal approximants), and the connections between the atomic structures of these phases and those of liquids and glasses. It extends studies made previously by us of the composition dependence of crystal nucleation processes in silicate and metallic glasses, to the case of nucleation from the liquid phase. Motivating results from rf-levitation and drop-tube measurements of the undercooling of Ti/Zr-based liquids that form quasicrystals and crystal approximants are discussed. Preliminary measurements by electrostatic levitation (ESL) are presented.

I. Introduction

Many metallic liquids can be significantly undercooled below their equilibrium melting temperature without crystallization. This is often taken as evidence for a large amount of polytetrahedral order (generally assumed to be icosahedral) that is incompatible with the translation periodicity of crystal phases. This constitutes a nucleation barrier, which is manifest as a large interfacial energy. Nucleation of a phase of the same composition as the parent phase has been studied extensively, both experimentally and theoretically (e.g. [1,2]). Interestingly, only limited studies exist for phase transformations involving a composition difference between the initial and final phase. This common case for most practical phase transformations warrants systematic study.

Quasicrystals are a new type of condensed matter; they contain extended polyhedral order that is believed to be similar to the short-range order in the undercooled liquid [3]. This is supported by diffraction experiments and by studies of the nucleation of quasicrystals from undercooled liquids and glasses [4]. The amount of undercooling appears to be less than for simpler crystal phases of similar composition, indicating a smaller interfacial energy, presumably reflecting a similar order in the quasicrystal and the interfacial liquid [5]. Similar results are found for complex crystal

* K. F. Kelton, Department of Physics, Washington University, St. Louis, MO 63130 U.S.A.

phases (crystal approximants), which are believed to have a local order that is similar to that of the quasicrystal. It appears reasonable, then, to expect a strong composition dependence of the undercooling for liquid alloys that crystallize directly to quasicrystals or crystal approximants.

Ti/Zr-based quasicrystals are particular interesting [3]. The Ti-TM-Si-O quasicrystals require prodigious amounts of oxygen, between 10 and 20 at.%, to form the quasicrystals and crystal approximants. This is true of no other quasicrystal. Experimental and theoretical studies suggest that the oxygen bonds with the Ti atoms, forming a network of stable clusters that may exist even in the undercooled liquid. The mechanism of phase transformation from the liquid to the quasicrystal or the approximant is unclear. In these alloys, the crystal approximant is stable, but the quasicrystal is metastable. The quasicrystal is the stable phase in Ti-Zr-Ni alloys. Further, those quasicrystals may have technological applications as hydrogen storage materials. Several fundamental questions for quasicrystals remain unanswered. Key among these are: (i) what are the local atomic structures of quasicrystal and related complex crystal phases and what is their relation to undercooled liquids; (ii) what are the nucleation and growth mechanisms for such complex periodic and non-periodic phases?

Extensive measurements of the undercooling and growth velocity as a function of composition in these alloys will lead to improved understanding on these points. Containerless conditions are critical for the success of the proposed experiments. The samples of interest are highly reactive and have high liquidus temperatures; the transformations are often dominated by heterogeneous nucleation on container walls or gas impurities. As will be discussed, limited ground-based studies have been made by drop-tube and electromagnetic (rf) and electrostatic levitation techniques. These can be extended and necessary thermophysical properties can be measured by levitation studies in microgravity. Such studies are planned using the rf-levitation facility, Advanced TEMPUS, on the International Space Station (ISS).

II. Ti-(Cr,Mn,Fe)-Si-O Alloys

The α-1/1 phase is a bcc phase, a_0 = 13.1 Å, constructed from two double-shell Mackay icosahedra, one located at the cube corner and the other at the cube center. Because the local structure of α-1/1 phase is presumed to be similar to that of the quasicrystal [6], the nucleation properties of these two phases should be comparable. Undercooling studies were therefore made on rf-levitated droplets of Ti-(Cr,Mn,Fe)-Si-O alloys with compositions near that of α-1/1[7,8]. The samples were inductively heated above their liquidus temperatures, and subsequently cooled at tens of degrees per second using a helium gas jet. Heating and cooling cycles were applied multiple times to ensure repeatability. The maximum undercooling on solidification (ΔT) was measured using a one-color pyrometer. Microstructure and phase information of the solidified droplets were obtained by powder x-ray diffraction (XRD) using CuK_α radiation, scanning electron microscopy (SEM), using an Hitachi S-4500 SEM equipped with a backscattered electron detector, and transmission electron microscopy (TEM) using a JEOL 2000-FX TEM. Phase composition was determined in SEM and TEM by energy dispersive x-ray spectroscopy (EDS).

The α-1/1 phase is the dominant phase in as-cast Ti-Cr-Si-O and Ti-Mn-Si-O alloys of the compositions studied. SEM microstructural investigations of containerlessly solidified drops, however, showed that the primary crystallizing phases are the hexagonal α-Ti and the bcc β-Ti solid solution phases. The 1/1 approximant, α(TiFeSiO), is the primary crystallizing phase in undercooled Ti-Fe-Si-O alloys of the appropriate composition, making that a more suitable system for the nucleation studies

discussed. Based on x-ray diffraction and SEM studies of annealed samples of as-cast alloys, the α-1/1 has a narrow stoichiometry near $Ti_{72}Fe_{24}(SiO_2)_4$. From preliminary solidification data and consideration of the binary phase diagrams, a simplified sketch of the vertical section of the phase diagram near the 1/1 composition can be made as a function of Ti/Fe, for constant Si and O (Figure 1a). The primary crystallizing phase is a strong function of the oxygen concentration of the alloy; increasing it only slightly moves from the β(TiFe) primary field to the α(TiFe) primary field and leads to the formation of Ti_2Fe at lower temperatures.

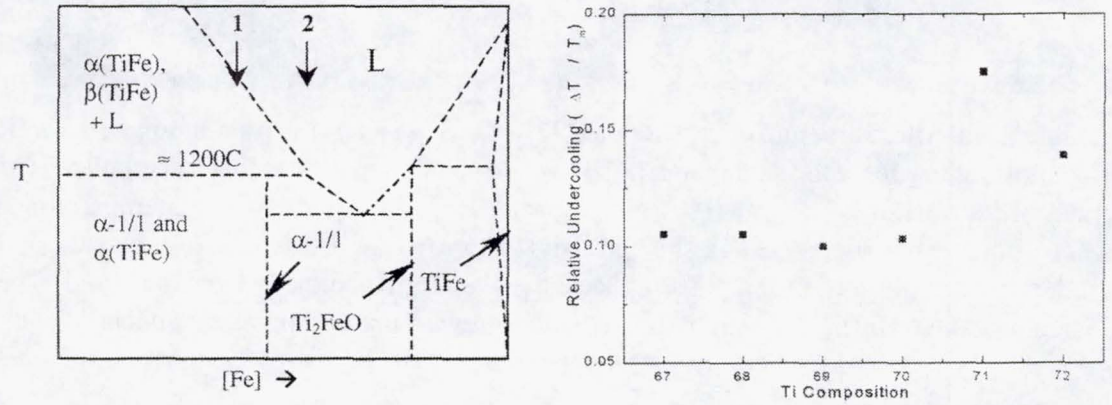

(a) (b)

Figure 1(a). Simplified preliminary schematic of the vertical section of the phase diagram for TiFeSiO alloys (constant Si and O) near the α-1/1 crystal approximant composition as a function of increasing Fe/Ti. Strictly, the Ti_2Fe phase appears at slightly higher oxygen concentrations than for this cut. (b) Relative undercooling as a function of [Ti] for constant Si and O. Figure 1b. shows the maximum reduced undercooling ($\Delta T_r = \Delta T/T_l$) for alloys as a function of Ti and Fe in $Ti_{94-x}Fe_xSi_4(SiO_2)_2$ alloys, $22 \le x \le 27$ (near the α-1/1 stoichiometry). ΔT_r falls sharply as the Ti composition is decreased below 71 at.% and remains constant over a significant range, corresponding to the region of primary solidification of α(TiFeSiO).

Figure 2a shows a backscattered SEM image of solidified $Ti_{71}Fe_{23}Si_4(SiO_2)_2$, close to the ideal 1/1 composition (Fgure 1a). The dendrites of the β solid solution phase (bcc, $a_o = 3.0$ Å) are the primary crystallizing phase; α(TiFeSiO) forms at lower temperatures. The microstructure for $Ti_{68}Fe_{26}Si_4(SiO_2)_2$, near the peritectic liquid composition (Figure 1a), is shown in Figure 2b. Here, the α-1/1 nucleates from the liquid, followed by the later formation of TiFe (CsCl-type, $a_o = 3.0$ Å). The lower relative undercooling of alloys that solidify first to the α-1/1 presumably reflects a higher nucleation rate due to the strong similarity in local atomic structures between the crystal approximant and the liquid.

III. TiZrNi

As cast-samples of TiZrNi prepared near $Ti_{41.5}Zr_{41.5}Ni_{17}$ contain primarily the C14 Laves phase (an hexagonal, polytetrahedral, Frank-Kasper phase that forms over a wide composition range) and the α(Ti/Zr) solid solution phase. When annealed at 570°C these samples form the stable icosahedral quasicrystal phase (i-phase)[6]. Higher temperatures lead to a 1/1-crystal approximant that is different from the one in the Ti-TM-Si-O alloys, the W-phase. Higher-order crystal approximants that are very similar to the quasicrystal have also been reported in these alloys [3]. Because this alloy system is replete with polytetrahedral phases, the nucleation behavior of these from the liquid is of great interest.

The phase diagram near the i-phase forming region is under investigation; it has been best studied at 600°C, near the formation temperature for the i-phase and W-phase. Anneals of as-cast samples for

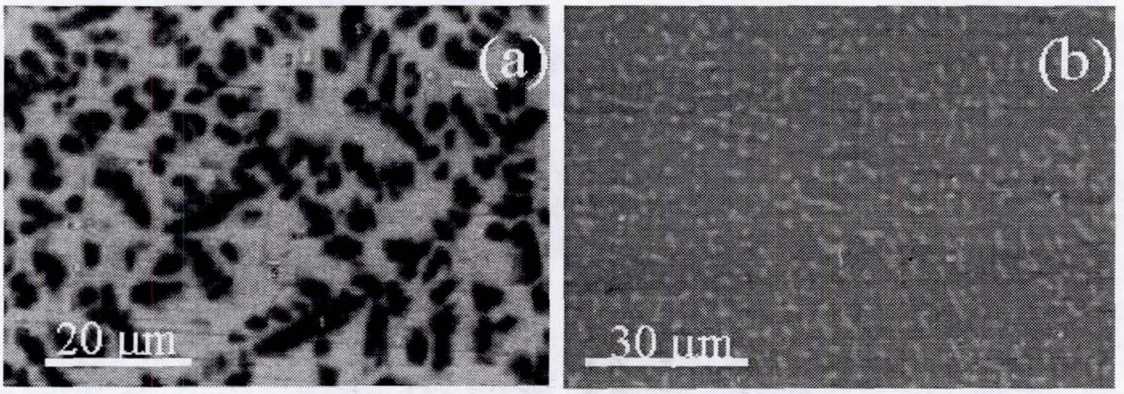

Figure 2. (a) Microstructure of undercooled $Ti_{71}Fe_{23}Si_4(SiO_2)_2$ (arrow 1 in Figure 1.a). The dendritic character of the dark phase, β(TiFe) solid solution, indicates that it crystallized first (possibly as α(TiFe)). The gray α-1/1 phase formed from the liquid at a lower temperature. (b) Microstructure of undercooled $Ti_{68}Fe_{26}Si_4(SiO_2)_2$ (arrow 2 in Figure 1.a). The convex shapes of the grains of the gray, α-1/1, phase indicate that they formed directly from the liquid. These are surrounded by the TiFe (light) phase, which grew from the remaining liquid at a lower temperature.

7-10 days produced the W-phase in a phase field between 0.32 and 0.4[Zr], 0.44-0.52 [Ti], and 0.13-0.17 [Ni]. While this bcc phase was originally reported to form at an optimum composition of $Ti_{44}Zr_{40}Ni_{16}$, more recent studies gave a better-ordered version at $Ti_{50}Zr_{35}Ni_{15}$[9]. The composition range for i-phase formation is smaller, centered near 17 at.% Ni, 40 at.% Ti, and 43 at.% Zr, in reasonable agreement with the i-phase composition reported in previous studies. Initial studies suggest that the i-phase forms by a peritectoid reaction from the C14 phase and α(Ti/Zr).

Unfortunately, the high density and low liquidus temperatures of the TiZrNi prohibit terrestrial rf-levitation studies near the quasicrystal or crystal approximant forming compositions in these alloys. For electrostatic levitation (ESL), charged droplets are held between two charged plates and melted by laser heating, decoupling the power required for levitation and allowing the study of TiZrNi alloys. X-ray diffraction patterns of as-cast alloys made near the 1/1-phase composition contain peaks corresponding to the C14 phase and α(Ti/Zr). SEM backscattered images of the microstructures of these alloys show dendrites of a low [Ni] phase (presumably α(Ti/Zr)) imbedded in the higher [Ni] C14 phase (Figure 3.b). That the polytetrahedral C14 phase is not the primary phase (although the nucleation barrier should be less than for the solid solution phase) indicates that the phase field of the C14 must lie at a lower temperature. These conclusions are supported by initial undercooling studies in the ESL (Figure 3). The microstructure of undercooled alloys that were superheated to 1150°C showed equiaxed grains of the solid solution phase, with the C14 phase forming between the grains. The size and morphology of the solid solution phase indicated incomplete melting; the temperature was only above the solidus temperature for the C14 phase. By contrast, samples that had been superheated to 1350°C showed a finer grain structure, which is consistent with the primary crystallization of the solid solution phase from the liquid.

IV. Conclusions

Ground-based investigations have identified two alloy systems, Ti-Fe-Si-O and Ti-Zr-Ni, of interest for studies of the formation of ordered condensed phases with strong tetrahedral order. The 1/1 icosahedral crystal approximant, α(TiFeSiO), $Ti_{72}Fe_{24}(SiO_2)_4$, forms by a peritectic transformation at approxi-

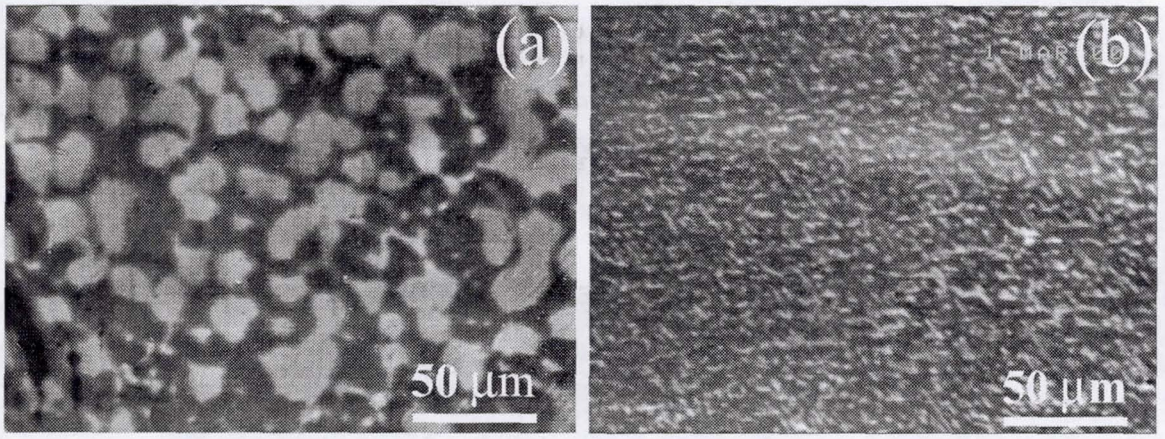

Figure 3. (a) Undercooled $Ti_{41.5}Zr_{41.5}Ni_{41.5}$ sample that had been superheated to 1150°C, showing large grains of the α(Ti/Zr) solid solution phase (light), indicating incomplete melting of sample; (b) undercooled sample after superheating to 1350°C, showing finer grain structures, indicating solidification of complete sample.

mately 1200°C. The TiZrNi crystal approximant, W-phase, forms by a peritectoid transformation from the C14 Laves phase and the α(Ti/Zr) solid solution phase. Undercooling studies of the C14 phase, also a polytetrahedral phase, are of interest in that alloy system. Undercooling studies in Ti-Fe-Si-O alloys show a broad minimum in the relative undercooling for alloy compositions near $Ti_{67\text{-}70}Fe_{27\text{-}24}Si_4(SiO_2)_2$, close to the peritectic liquid composition. This presumably reflects the ease of nucleation of the crystal approximant, due to a similar local atomic structure of that phase and the undercooled liquid.

To ensure that these results reflect homogeneous nucleation, to minimize convective effects so that diffusion effects on nucleation [10] and growth might be observed, and to obtain measurements of the thermophysical properties of the undercooled liquid, studies on the ISS using Advanced TEMPUS are planned. These future results will be coupled with continuing ground-based results of the undercooling. The local structures of the polytetrahedral phases will be contrasted with those of the liquids using x-ray scattering measurements of the undercooled liquids, made in collaboration with S. Krishnan.

V. Acknowledgements

We thank D. Herlach and S. Krishnan for useful conversations. The work at Washington University was partially supported by NASA under contracts NCC 8-85 and NGT 5-50030. The work at DLR was supported by Deutsche Forschungsgemeinschaft (DFG) under contract No. HO 1942/2 and by DLR-BO.

REFERENCES

1. Kelton, K.F., "Nucleation," in *Solid State Physics*, H. Ehrenreich and D. Turnbull, Editors. 1991, Academic Press: Boston. p. 75-177.
2. Wu, D.T., "Nucleation Theory," in *Solid State Physics*, H. Ehrenreich and F. Spaepen, Editors. 1997, Academic Press: Boston. p. 37-187.
3. Kelton, K.F., "Icosahedral and Quasi-periodic Structures," in *Intermetallic Compounds: Principles and Practice*, J.H. Westbrook and R.L. Fleishcher, Editors. 1995, John Wiley: New York. p. 453-491.

4. Holzer, J.C. and Kelton, K. F. "The Structural Relations Between Amorphous, Icosahedral, and Crystalline Phases," in *Crystal-Quasicrystal Transitions*, M. J. Yacaman and M. Torres, Editors. 1993, North Holland. p. 103-142.
5. Holland-Moritz, D., Int. J. of Non-Eq. Processing, 11, 169-199 (1998)
6. Kelton, K.F., Mater. Res. Soc. Symp. Proc., vol. 553 , 471-482 (1999).
7. Croat, T.K, Kelton, K. F., Holland-Moritz, D., Rathz, T. J., Robinson, M. B., Mater. Res. Soc. Symp. Proc., vol. 553 , 43-8 (1999).
8. Croat, T.K., Holland-Moritz, D., Robinson, M. B., Rathz, T. J., Kelton, K. F., J. Mat. Res, 14, 4208-13 (1999).
9. Davis, J.P., Majzoub, E. H., Simmons, J. M., Kelton, K. F., Mat. Sci. and Eng. A (in press).
10. Kelton, K. F., Acta Materialia (in press).

NANOCRYSTAL SUPERLATTICES: SYNTHESIS AND PROPERTIES

X.M. Lin[2], S. Stoeva[1], C.M. Sorensen[2], K.J. Klabunde[1]

[1]Department of Chemistry and [2]Department of Physics,
Kansas State University,
Manhattan, KS 66506

We are developing methods to synthesize large nanocrystal superlattices (NCSL), which are arrays of nanocrystal particles arranged in order analogous to common crystals for which atoms or molecules are building blocks. These superlattices, in general, should exhibit novel properties due to coherent collective interactions of the particles. A key factor in creating these superlattices is control of nanocrystal size distribution, which must be very narrow. In recent work we have developed a digestive ripening process which has proven to narrow the size distribution of gold nanocrystals, which then quickly form NCSL. The size of the NCSL are about 500 nm which are formed from 6 nm gold nanocrystals. The unusual optical, solubility, and specific heat properties have been elucidated, and will be discussed. Work toward growing larger NCSL of gold, and extending to other materials, such as silver and cadmium sulfide will also be discussed.

As this project is in its very beginning stages, the effects of microgravity have not yet been investigated. However, the key to growing larger, defect free NCSL will be to carefully control the crystallization of the nanocrystals. This will require, in addition to a large amount of nanocrystals ligated with protective surface organic ligands, careful control of temperature, concentration, and probably gravitational forces. This is because gravity induced flows can cause gradients in temperature and composition in the solution, which in turn could cause nonuniformities, defects, and solvent inclusions in the growing NCSL.

THE TRANSIENT DENDRITIC SOLIDIFICATION EXPERIMENT (TDSE)

M.B. Koss[1] *, M.E. Glicksman[1], J.C. LaCombe[1], A. Chait[2], and V. Pines[2]

[1]Materials Science and Engineering Department, Rensselaer Polytechnic Institute [2]Computational Microgravity Laboratory, NASA Glenn Research Center

Dendritic solidification is a common mode of solidification. It is also an important model problem in non-equilibrium physics and pattern formation physics. Current theories couple the transfer of latent heat with selection mechanisms at the interface. Measurements of succinonitrile (SCN) dendrites in microgravity show reasonable agreement between heat transfer predictions and experiment. However, data and analysis for assessing interfacial physics theories are less definitive. We are studying, and will present data on, transient effects in dendritic growth of SCN. We employ the Clapeyron pressure/melting temperature effect to make a rapid change in a sample's hydrostatic pressure, and thereby rapidly change the specimen's melting temperature, forcing the dendrite to select a new steady-state. These initial measurements show some surprising and non-intuitive effects.

I. Introduction

Dendritic solidification is a well-studied model problem in the fields of pattern formation, non-equilibrium physics, and computational condensed matter and material physics. There is also considerable engineering interest in dendrites because of the role they play in the determination of microstructures in cast materials, which in turn influence a material's physical properties [1].

Most theories of dendrite crystal formation consist of two components [2, 3], the first concerns the transport of heat and solute from the solid-liquid interface into the melt. The second involves the interfacial physics that selects the unique growth velocity and tip radius of curvature from a spectrum of such possibilities that are consistent with transport and conservation of energy at the crystal-melt interface. Until recently, neither of these two aspects of the theory could be tested critically because of the effects of gravity-induced convection, which modifies the transport processes, and alters the growth kinetics [4].

II. Background

Benchmark data consisting of dendritic tip growth speed and radii of curvature were obtained for succinonitrile (SCN) dendrites grown in a convection-free microgravity environment. Analysis shows that although the theory yields predictions that are in reasonable agreement with the experiment, there were significant discrepancies observed, particularly in assessing interfacial pattern selection [4].

As a follow-up to the microgravity experiments, we are investigating transient and time-dependent dendritic growth by employing the relatively large Clapeyron pressure effect in SCN [5]. A change in a solidifying system's hydrostatic pressure changes the liquidus temperature, and induces a change in the

* Corresponding author

temperature gradients at the interface. With this approach, the kinetics of isolated dendrites were measured as they evolved from one well-defined steady-state velocity, at the initial supercooling, through a transient stage, to a final well-defined steady-state velocity at the altered pressure-supercooling state. By using fast pressure changes, the time-scale for pressure-related changes in growth behavior becomes well separated from the much slower thermal time-scale for long-range heat transfer.

The equilibrium melting temperature T_m is the temperature at which the liquid and solid phases co-exist in equilibrium for some specified pressure. For most materials that contract on melting (the well-known exceptions being water and silicon), increased pressure favors the crystalline phase, as atoms or molecules are squeezed (on average), slightly closer together. This effect is classical, and can be derived from general thermodynamic principles and is known as the Clapeyron equation [6].

As such, the Clapeyron effect is well known in solidification science and for example has been hypothesized as the explanation for cavitation-induced nucleation. However, it is usually assumed that the Clapeyron effect is too small to be of interest in the solidification of metals and alloys. This may be a reasonable assumption for many materials, but in the unusual case of SCN, that has a Clapeyron effect of 24.5±0.5 mK/atm [5], it is not. The Clapeyron effect in SCN is many times larger than in most metals, moreover the characteristic supercooling of ~23 K is many times smaller. Thus, the ratio of the Clapeyron effect to the unit supercooling is 25 to 200 times larger for SCN than for typical metals. The large Clapeyron effect and the small characteristic supercooling may be exploited in a straightforward manner to effect fast changes in SCN's crystal-melt equilibrium temperature. Changing the interfacial temperature relative to the surrounding melt temperature changes the supercooling. This allows acquisition of non-steady-state dendritic growth kinetics, and permits observations during the transient evolution of the morphology between steady states.

When the pressure-mediated melting temperature change is carried out for an isolated dendrite growing at steady state under the initial supercooling, the dendrite responds by eventually adopting a new steady-state that is appropriate to the new supercooling. To calculate the final supercooling properly, one must also account for the influence of any pressure-volume work done throughout the adiabatic crystal/melt system. From the combined first and second laws of thermodynamics, the effect can be calculated. For SCN, the adiabatic temperature change has been measured to be 12.81±0.03 mK/atm, which is in reasonable agreement with calculation [7].

III. Experiment Description

The experiments reported here used the ground-based hardware built and used originally in the above-mentioned, convection-free microgravity study of dendritic growth [4]. The experimental apparatus surrounded the sample material, contained by a glass and stainless steel growth chamber, located within a precision (± 2mK) temperature-controlled bath. The growth chamber interior volume communicated with the bath via a stainless steel bellows, permitting the pressure field in the bath to be transmitted into the chamber interior. Nucleation of dendritic crystals was achieved through the use of a hollow stinger tube that penetrated the wall of the growth chamber. The exterior end of the stinger tube was capped and surrounded by a well-isolated thermoelectric cooler. The interior end was open, allowing the sample material in the chamber to also fill the stinger.

During the operation of the experiment, each dendritic growth cycle began by completely melting the SCN, followed by lowering the melt's temperature to the desired supercooling, measured to within

0.001 K spatially and temporally. After the supercooled melt's temperature reached steady state, the thermoelectric cooler was activated. This nucleated a small crystal in the end of the stinger, which then propagated down the stinger tube to emerge into the chamber as a freely growing dendrite which was recorded using video equipment. Upon achieving steady state growth, the hydrostatic pressure of the surrounding thermal bath was changed suddenly via a pneumatically operated piston. The typical monotonic, exponential, smooth pressure took *ca.* 0.2s, whereas a comparable decrease took *ca.* 0.4s. The pressure was immediately transmitted to the sample via the bellows, causing a change in the final operating state of the dendrite.

Once a crystal emerged from the stinger, images of the dendrites were obtained from two perpendicular views using electronic cameras with an imaging chip array of 640 x 480 pixels, 256 gray-scale levels, at a magnification of 0.46 and a storage rate of approximately 30 frames per second. Each pixel images a region of the growth chamber that is 22.15 μm high and 21.52 μm wide, however image processing and analysis techniques allowed us to locate the position of the dendrite tip to a resolution of approximately 2 microns (~1/10 pixel). This approach does not attempt locating the crystal-melt interface at the tip. Instead, it uses additional image data to obtain a consistent reference with respect to the dendrite that serves to track the dendrite's advance over time.

IV. Experiment Results

The experiments described above were conducted for two pressure change magnitudes, with both increases and decreases, for a variety of initial supercooling levels between 0.9 and 0.3 K. An increase in hydrostatic pressure is expected to result in an increase in the interface's equilibrium temperature, an increase in the far field temperature, and a net increase in supercooling — resulting in an increase in the temperature gradient which enhances the solidification process. Using a pressure increase of 6.6 atm (applied within the initial steady state), the growth rate does indeed increase as expected from 15.3 μm/s to 26.0 μm/s. However, if the period of time immediately after the pressure change is examined more closely, it becomes apparent that prior to the overall increase in growth rate, the dendrite actually first slows down, and in this case, momentarily melts back.

Although the melt-back of the interface was observed in several growths with pressure increases, it was not universal. In a growth with $\Delta T_{init} = 0.58$ K and a larger initial velocity of 67.7 μm/s, there was a change to $\Delta T_{fin}=0.63$ K, and a final velocity of 84.0 μm/s after a pressure increase of 4.2 atm. But, in the transient period immediately after the pressure increase, the dendrite only slows down, never quite melting back prior to accelerating to its eventual higher final speed. The initial decrease in velocity before the final increase is however, consistent for all cycles with pressure increases regardless of the initial velocity.

The comparison and examination of the transition region is best accomplished by an examination of the instantaneous and moving average velocity. For an increase in pressure of 6.6 atm, the velocity drops momentarily, prior to approaching the final, higher value (Figure 1). For a pressure drop of 6.8 atm, (Figure 2), we see precisely the reverse situation. In this case, the intermediate transient is evident through a brief, unexpected rise in velocity.

For the investigated range of supercoolings and pressure changes, the characteristic time necessary to re-acquire the new steady-state velocity was quantified by the time needed for the residuals from a linear fit of the displacement data to decrease to 37% of their initial magnitude (at the onset of the

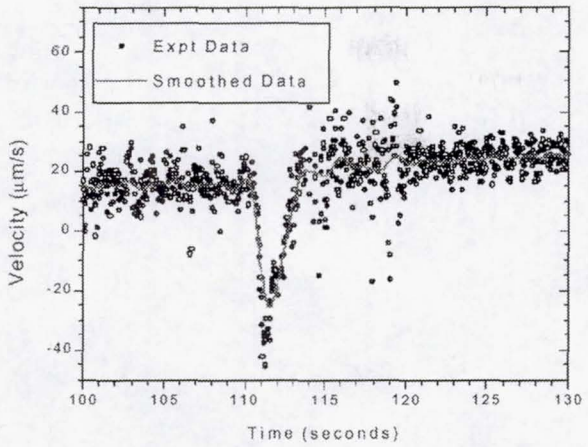

Figure 1. Velocity vs. time plot for pressure increase that causes a supercooling increase from $\Delta T_{init} = 0.25$ K to $\Delta T_{init} = 0.33$ K.

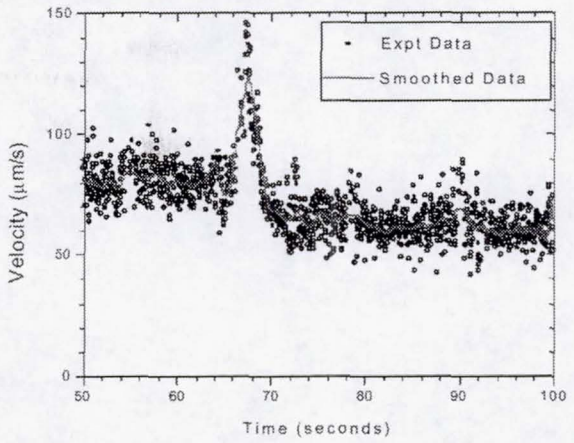

Figure 2. Velocity vs. time plot for pressure decrease that caused a supercooling decrease from $\Delta T_{init} = 0.60$ K to $\Delta T_{init} = 0.52$ K.

transient). In these experiments, this time was observed to be on the order of two seconds and was independent of both the mean supercooling and the change in supercooling linked to the change in pressure.

V. Simulation Results

We have explored several key features of the solution obtained from the numerical simulations of the experiment. The time-dependent calculations were performed using finite difference techniques and using the Triad Field Formalism (Pines *et. al* [8]). We begin by imposing a pressurization/de-pressurization cycle of ca. 265 psi, with a time constant for the exponential pressure changes of 2 seconds. The supercooling was set to approximately 0.1 K. For this simulation, the tip position verses time (Figure 3) behaves similarly to the experimental data discussed previously. It is evident that pressurization produces a faster tip velocity (the slope of the line). An interesting feature is that the tip velocity changes to a higher value quickly at first, then decreases slightly, after which it slowly evolves to a final steady state. Additionally, there is a decrease in tip velocity upon de-pressurization. The down-pressurization does exhibit the slight over-response as did the up-pressurization, but then rapidly achieves its final steady state.

VI. Discussion

While the simulations are in agreement with some of the experimental data, it is in disagreement with the key experimental observation of the meltback. The initial reversal effect we report above after fast pressure changes has to our knowledge not been observed previously, not observed in our initial simulations, nor was this effect noted by Börzsönyi *et al.* [9], who performed phase-field calculations of dendritic solidification of liquid crystals subject to step-wise pressure oscillations.

In the experiments, for the case of down pressurization, the general form of the local temperature gradients appears to change so that the net heat flux is into the interface. The pressurization change was monotonic and therefore, is not the cause of the net flux into the interface. Additionally, the characteristic time of the velocity transient is seen to be largely insensitive to the supercooling regime.

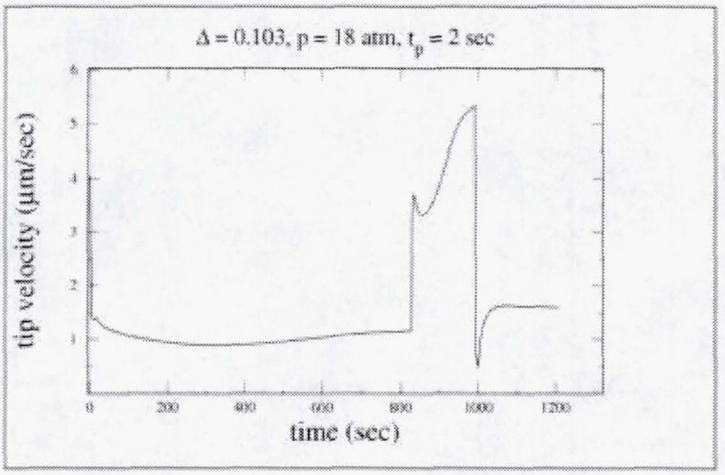

Figure 3. Velocity vs. time plot for a pressure increase of 264 psi from an initial supercooling of $\Delta T_{init} = 0.103$ K over 2 seconds, followed by a pressure drop of 264 psi.

In trying to explain this newly observed phenomena, we note that in principle, dendritic solidification is always a non-equilibrium process. In practice, dendritic growth and many other solidification processes are successfully treated as "quasi-equilibrium" processes, where the "local equilibrium" melting temperature has proven to be a useful physical construct. We suggest that the local equilibrium of the interface may in fact be violated. Thus the Clapeyron and adiabatic effects take place essentially instantly, while the interface temperature follows that of the adjacent solid and liquid. Here, the interface is not at the equilibrium temperature, but is being driven to it during the subsequent growth process, and this yields the melt back or slowing down. Thus, our observations suggest that this conventional approach does not suit the careful experiments described herein during the early transition from an initial steady-state.

This proposed scenario is phenomenological. We offer here a specific mechanism to understand how this occurs based on a non-equilibrium Clapeyron effect where the ability of a phase to accommodate molecules from the other phase can be very different. To illustrate this non-equilibrium process, we used the previously discussed transient solidification simulation code, with the added physical description of a non-equilibrium Clapeyron coefficient. In these simulations, the relaxation time constant, τ, was fixed at 1.6 seconds for two different pressurization-depressurization cycles using characteristic times for the pressure application of t_p,= 0.2 and 2 seconds. For these simulations, the tip displacement with time varies with different pressurization rates. The important observation is that, in this model, the short-term behavior (slowing down or growth reversal) is clearly present. This reversal, depending on the simulation pressurization rate, occurs even though the final steady state velocity is independent of the pressurization rate (Figure 4). This behavior is consistent with experimental observations to date in that it both eliminated the rapid increase and over response with the proper reverse in velocity, and the total time for the achievement of the new steady-state is decreased to reasonable agreement with the experiment.

VII. Conclusions

The observed transient phenomena described above were not part of the TDSE's original scientific objectives. Instead, they constitute important early findings of both the experimental and modeling components of this effort. Additionally, preliminary investigation indicates that although this intermediate-transient behavior reveals a new, fundamental kinetic effect in dendritic growth processes. Further-

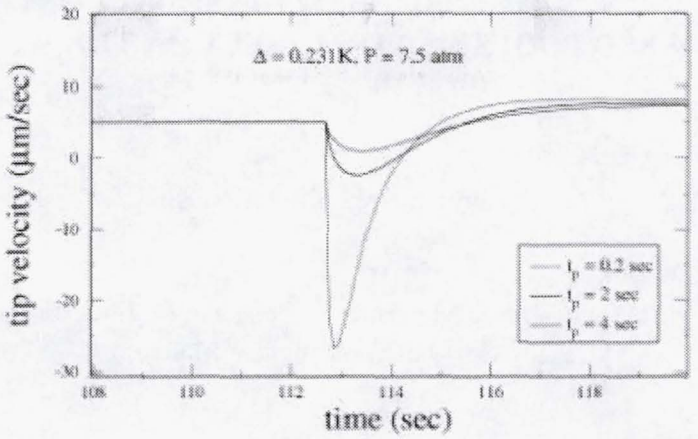

Figure 4. Velocity verses time plot for a pressure increase of 110 psi from an initial supercooling of $\Delta T_{init} = 0.231$ K over 4.0, 2.0, and 0.2 seconds, respectively.

more, this interfacial effect has much broader concerns to solidification in that it may also apply to non dendritic solidification phenomena.

VIII. Acknowledgements

This work is supported by NASA's Microgravity Science and Application Division under contract number NAG8-1488, with liaison through A. Jackman, Z. Hester and D. Smith at NASA's Marshall Space Flight Center. We also thank for their assistance, D. Schrage, J. Ogrin and J. McDade, who are associated with NASA's Glenn Research Center.

REFERENCES

1. Condensed Matter and Materials Physics: Basic Research for Tomorrow's Technology. 1999, National Academy Press: Washington, DC.
2. J.S. Langer, Reviews of Modern Physics, 52 (1) (1980), 1.
3. P. Pelcé, ed. Dynamics of Curved Fronts. 1988, Academic Press, Inc.: New York. 514.
4. M.B. Koss, et al., Metallurgical and Materials Transactions A, (2000),
5. J.C. LaCombe, et al Journal of Crystal Growth, 194 (1998), 143-148.
6. A.B. Pippard, Elements of Classical Thermodynamics, (New York): Cambridge University Press. 1957.
7. M.B. Koss, et al., *Unpublished Research,* (1998).
8. V. Pines, M. Zlastkowski, and A. Chait, Physical Review A, 42, (1990), pgs 6137 and 6129.
9. T. Börzsönyi, et al., Physical Review Letters, 83 (14) (1999), 2853-2856

EXPERIMENTS TO OBSERVE MARANGONI CONVECTION IN SIMULATED WELD POOLS AND ITS EFFECT ON THE WELD POOL SHAPE

C. Limmaneevichitr and S. Kou *

Department of Materials Science and Engineering
University of Wisconsin at Madison

ABSTRACT

A transparent pool of sodium nitrate ($NaNO_3$) was heated with a defocused CO_2 laser beam to simulate Marangoni convection in arc weld pools *without* a surface-active agent. The flow patterns were revealed by flow visualization with a laser light-cut technique. The observed Marangoni convection was expected to resemble that in welding because the Marangoni number was close to those in welding. The maximum velocity was at the pool surface, the outward surface flow was much faster than the inward return flow, and the centers of the cells were near the pool edge. These characteristics suggest Marangoni convection dominate in the pool over buoyancy convection. The results of flow visualization provided interesting insights for understanding the significant effect of Marangoni convection on the weld pool shape, as demonstrated in stationary welds of $NaNO_3$ (a high Prandtl number material) and Ga (a low Prandtl number material). Both the flat and convex pool bottoms are a clear indication that Marangoni convection dominated over buoyancy convection. It is proposed that, unless a surface-active agent or a significant electromagnetic force is present, pool bottom convexity increases with increasing Peclet number.

I. Introduction

Marangoni convection, also called surface-tension driven convection, in the weld pool is of practical interest in welding. Unfortunately, Marangoni convection cannot be visualized in arc welding because of the opaque molten metal, the electromagnetic force and the arc shear force. To avoid this problem, Marangoni convection in weld pools is simulated using a transparent pool of $NaNO_3$, which is heated by a laser beam defocused to the size of the arc. The objectives of the study are: (1) to observe Marangoni convection in a simulated weld pool, (2) to study the effect of Marangoni convection on the weld pool shape in light of the flow visualization experiments, and (3) to relate the weld pool shape to the Peclet number (Pe) and the Prandtl number (Pr).

II. Experimental Procedure

A. Materials and Sample Preparations

$NaNO_3$ was used for flow visualization because of its transparent melt and well-documented physical properties. The Marangoni number (Ma) for the simulated weld pool of $NaNO_3$ to be studied here is close to those for steel and aluminum weld pools [1]. According to the similarity law of hydrodynamics, similarity in Marangoni convection between two fluid systems can be

* Corresponding author

expected if the Marangoni numbers are close to each other [2]. $NaNO_3$ and Ga were selected for welding because of their high and low Prandtl numbers, respectively. The physical properties of $NaNO_3$ and Ga are listed in Table 1. The purity of $NaNO_3$ and Ga are 99+ % and 99.9999 %, respectively. Samples of $NaNO_3$ and Ga were cast, ground flat, and cleaned before welding. The dimensions of the samples were 10 cm x 10 cm x 2 cm for $NaNO_3$, and 2.5 cm diameter by 1 cm height for Ga.

Table 1. Physical Properties of $NaNO_3$ and Ga Melts [3-7].

Properties	$NaNO_3$	Ga
Melting point, T_m, °C	306.8	29.9
Temperature coefficient of surface tension, $\partial\gamma/\partial T$, dyne/(cm °C)	- 0.056	- 0.10
Surface tension, γ, dyne/cm	119.96 at T_m	718 at T_m
Dynamic viscosity, μ, g/(cm s)	0.0302 at T_m	0.0194 at T_m
Density, ρ, g/cm^3	1.904 at T_m	6.1 at T_m
Specific heat, C_p, J/(g °C)	1.71 at T_m	0.398 at T_m
Thermal conductivity, k, W/(cm °C)	5.65×10^{-3} at T_m	0.33 at T_m
Thermal expansion coefficient, β, °C^{-1}	6.6×10^{-4}	9.2×10^{-5}
Thermal diffusivity, $\alpha = k/(\rho C_p)$, cm^2/s	1.74×10^{-3} at T_m	0.136 at T_m
Prandtl number, $Pr = C_p\mu/k$	9.12 at T_m	2.34×10^{-2} at T_m

B. Apparatus

The apparatus for flow visualization (Figure 1) consisted of: (1) A hemispherical pool of $NaNO_3$ held in a glass tube of 10 mm ID, (2) $NaNO_3$ melt held in a square glass beaker, (3) A CO_2 laser beam shone at the center of the pool to induce Marangoni convection, and (4) A He-Ne laser light sheet passed through the meridian plane of the pool to reveal the flow pattern. The apparatus was transparent and free from optical distortions. A laser light sheet was produced with the help of a 20-mW He-Ne laser and cylindrical lenses. 20-μm aluminum powder was used as the tracer. Photographs of the flow patterns were taken at the exposure time of 0.625 second.

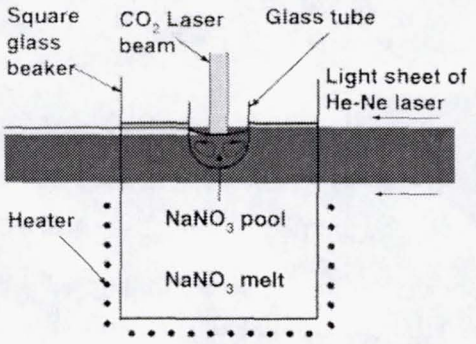

Figure 1. Apparatus for visualization of Marangoni convection in a simulated weld pool of $NaNO_3$.

Welding and Pool Shape Measurement: Stationary welds were made with a CO_2 laser beam, with Ar shielding to protect the pool surface from oxidation in the case of Ga. The welding times, 3 minutes for $NaNO_3$ and 4 minutes for Ga, were sufficient for the pools to stabilize in size. The melt was then decanted from the pool immediately. The shape of the emptied pool was determined by using a digital x-y stage with a resolution of 0.01 mm and a fine-tip dial indicator with a resolu-

tion of 0.025 mm. The depth of the pool was measured every 0.25 mm along the diameter *in two directions perpendicular to each other.*

III. Results and Discussion

Effect of Heat Source Diameter: At the beam diameter of 5.9 mm and the beam power of 2.5 W, the flow was outward along the free surface and the centers of cells are close to the edge of the pool surface (Figure 2a). With the beam diameter reduced to 1.5 mm, the flow becomes significantly faster, the surface flow accelerates sharply and centers of the cells move closer to the pool edge. The return flow gains extra momentum to penetrate deeper into the pool (Figure 2b). The effect of the beam diameter is summarized in Figure 3.

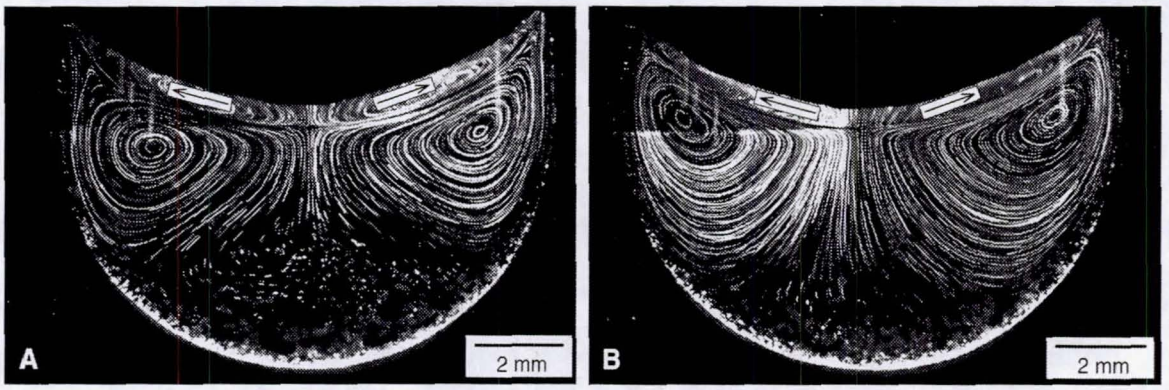

Figure 2. Flow patterns induced by a 2.5 W CO_2 laser beam at the diameters of: (a) 5.9 mm; (b) 1.5 mm.

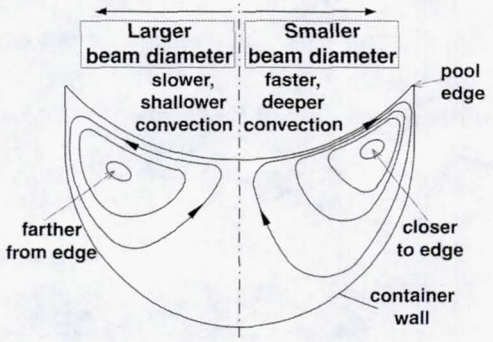

Figure 3. Effect of the diameter of the laser beam on the flow pattern.

$NaNO_3$ Pool Shapes: At the beam diameter of 5.9 mm and 12.4 W, the pool bottom is surprisingly flat (Figure 4a). With the beam diameter reduced to 1.5 mm, the pool bottom becomes convex toward the melt (Figure 4b).

Ga Pool Shape: At the power of 7.5 W and the beam diameter of 5.9 mm, the pool is concave (Figure 5a). As the beam diameter is reduced to 1.5 mm, the pool becomes narrower and deeper to be nearly hemispherical (Figure 5b).

Peclet Number and Marangoni Number: The Peclet number (Pe) is defined as follows [8]:

$$Pe = \frac{LV}{\alpha} = \frac{LV\rho C_p}{k} = \frac{V\rho C_p \Delta T}{k\Delta T/L} = \frac{\text{heat transport by convection}}{\text{heat transport by conduction}} \quad (1)$$

where L is the characteristic length (the radius of the pool surface), V the characteristic velocity

(the maximum outward surface velocity at the pool surface), α the thermal diffusivity, ρ the density, C_p the specific heat, k the thermal conductivity, and ΔT the temperature drop from the center of the pool surface to the edge.

The Marangoni number (Ma) is defined as:

$$Ma = \frac{-\frac{\partial \gamma}{\partial T}(\Delta T)L}{\mu\alpha} \qquad (2)$$

where ΔT is temperature difference between center and edge of the pool surface and L is the radius of the pool surface. When the beam diameter is reduced, ΔT increases very significantly (especially when the thermal conductivity is low [1]) and Ma increases significantly. In any case, the Marangoni convection is stronger and V is higher with higher Ma.

$NaNO_3$ Pools: At the beam diameter of 5.9 mm diameter and 12.4 W (Figure 4a), V was estimated from video recording to be 2 cm/s: Pe is, therefore, 670. Since heat is transported to the pool edge by convection parallel to the pool surface, the resultant pool bottom is wide and flat. As the beam diameter is reduced to 1.5 mm, Marangoni convection becomes much faster. V was estimated to be at least 6 cm/s and Pe is, therefore, about 1900. The high V forces the return flow to turn and carry heat downward near the pool edges, resulting in a convex pool bottom (Figure 4b).

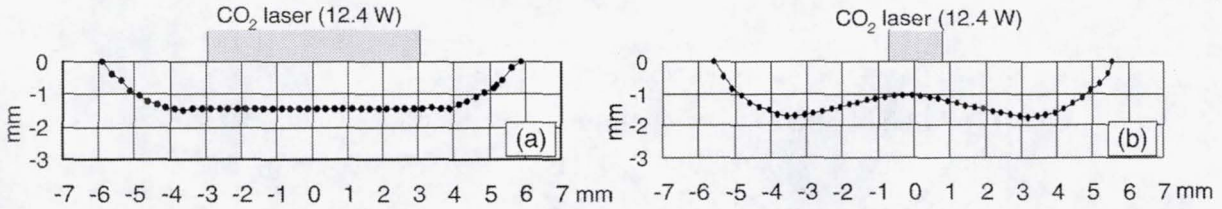

Figure 4. Shapes of stationary weld pools in $NaNO_3$ produced by CO_2 laser beams of: (a) 12.4 W and 5.9 mm diameter; (b) 12.4 W and 1.5 mm diameter.

Ga Pools: For Ga, the Pe is very low because k is very high and V is expected to be rather small in view of the very small Ma. Hence, heat transport in a Ga pool is dominated by conduction. The downward as well as outward heat conduction results in a concave weld pool (Figure 5a). As the beam size is reduced under the same power, the pool becomes nearly hemispherical (Figure 5b).
Peclet Number and Pool Shape: With Pe << 1, heat transport in the weld pool is dominated by conduction and the pool is concave. The actual pool shape depends on the size of the heat source; with a small size heat source the pool is hemispherical (Figure 6a). With Pe >>1, heat transport in the weld pool is dominated by convection and the shape of the pool bottom can change from concave to flat or even convex (Figures 6b through d). With strong outward surface flow carrying heat to the pool edge, the pool bottom becomes flat (Figure 6c). With even stronger flow to carry heat downward near the pool edge, the pool bottom becomes convex (Figure 6d).

Welds in Materials of Various Prandtl Numbers: Figure 7 is a grid showing examples of welds with a hemispherical, concave, flat or convex bottom. Heat transport in the weld pool ranges from "conduction highly dominating" (low Pe) in the bottom left corner to "convection highly dominating" (high Pe) at the top and the right. These welds were made by laser beam welding (LBW), electron-beam welding (EBW) or gas-tungsten arc welding (GTAW). The LBW and EBW here refer to conduction-mode welding. The grid is described in greater detail elsewhere [9].

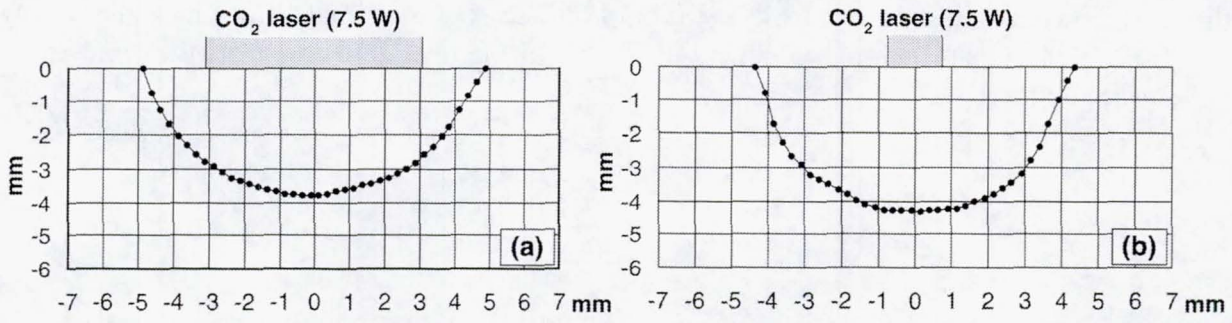

Figure 5. Shapes of stationary weld pools in Ga produced by a 7.5 W CO_2 laser beam at the diameters of: (a) 5.9 mm; (b) 1.5 mm.

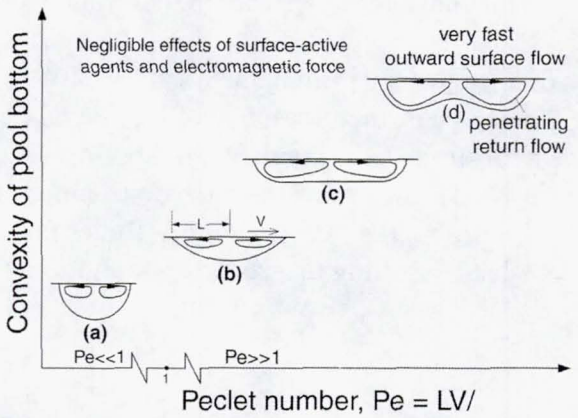

Figure 6. Proposed of effect of Peclet number on weld pool shape: (a) conduction dominating (Pe<<1); (b) through (d) convection dominating (Pe>>1).

IV. Conclusions

Marangoni convection similar to that in arc welding can be observed clearly in simulated weld pool of $NaNO_3$. Reducing the beam diameter makes Marangoni convection stronger and the centers of the cells move closer to the pool edge. For a high Pr material such as $NaNO_3$, Marangoni convection dominates heat transport in the weld pool, and the outward surface flow makes the pool bottom flat. With strong outward surface flow, the return flow deepens the pool bottom near the pool edge and makes the pool bottom convex. For a low Pr and low melting-point material such as Ga, Marangoni convection is weak and conduction dominates heat transport in the weld pool, resulting in a concave pool bottom. It is proposed that a concave pool bottom can become flat or even convex as Pe increases to reflect increasing dominance of heat transport by the outward surface flow.

REFERENCES

1. Limmaneevichitr, C. and S. Kou, *Flow visualization of Marangoni convection in simulated weld pools.* Welding Journal, 2000. 79(5): p. 126s - 135s.
2. Schwabe, D., *et al.*, *Experiments on surface tension driven flow in floating zone melting.* Journal of Crystal Growth, 1978. 43: p. 305-312.
3. Atomergic Chemetals Corporation, *Data sheet*, : Farmingdale, NY.
4. White, L.R. and H.T. Davis, *Thermal conductivity of molten alkali nitrates.* Journal of Chemical Physics, 1967. 47(12): p. 5433-5439.

5. Janz, G.J., Journal of physical chemistry, 1972. 1(3): p. 583 - 704.
6. Preisser, F., D. Schwabe, and A. Scharmann, *Steady and oscillatory thermocapillary convection in liquid columns with free cylindrical surface.* Journal of Fluid Mechanics, 1983. 126: p. 545-567.
7. Iida, T. and R.I.L. Guthrie, *The physical properties of liquid metals.* 1988, Oxford: Oxford University Press.
8. Bird, R.B., W.E. Stewart, and E.N. Lightfoot, *Transport phenomena.* 1960, New York: Wiley.
9. Limmaneevichitr, C. and S. Kou, *Experiments to simulate effect of Marangoni convection on weld pool shape.* Welding Journal (to be published).

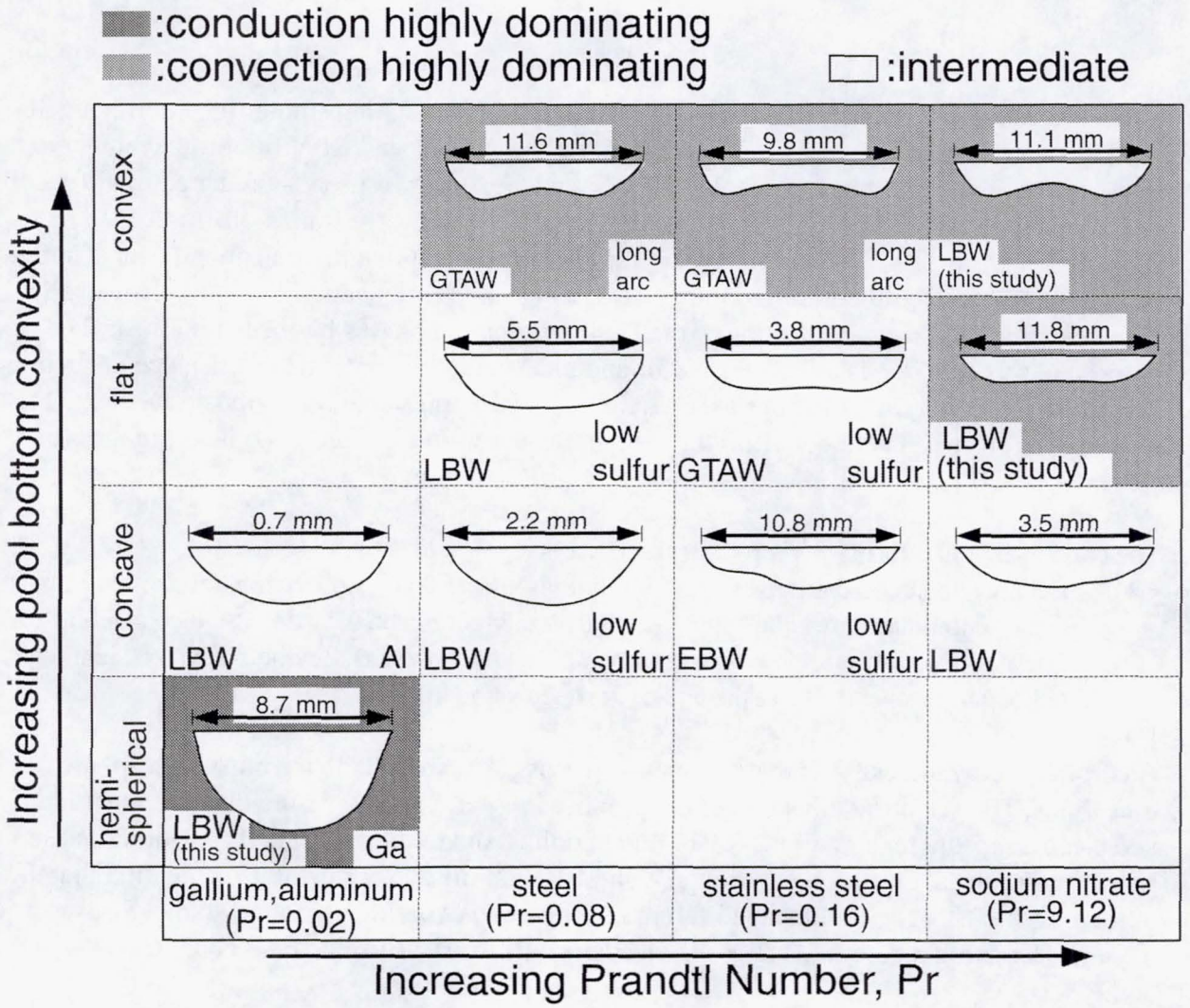

Figure 7. Welds of various materials with various shapes.

STRUCTURE-PROPERTY CORRELATION AND PHASE TRANSITIONS IN GROUP IV AND III-V LIQUIDS

Shankar Krishnan[1], David L. Price[2] and Marie-Louise Saboungi[2]

[1]Containerless Research, Inc., Evanston, IL
[2]Argonne National Laboratory, Argonne, IL

Molecular dynamics (MD) simulations [1-3] and laser pulse-heating studies on amorphous Si [4,5] have recently been performed which indicate that Si, Ge, and III-V liquids may undergo a first-order liquid-liquid phase transition. For Si and Ge, this transition is predicted in the deeply undercooled liquid. Group III-V liquids are expected to exhibit the transition closer to their respective melting temperatures. The MD simulations predict that the transition occurs from the metallic liquid to a tetrahedrally-coordinated, viscous and semiconducting liquid. However, no direct experimental characterization of the low-coordination phases has been obtained. The purpose of this research is to: (1) search for and independently confirm the existence of such first-order transitions, (2) determine the liquid phase structures across the transition, and (3) measure the electrical conductivities throughout the accessible undercooled liquid ranges for these materials.

The two key hypotheses of the proposed research are:

1. Deeply undercooled group IV and III-V liquids undergo a first-order phase transition from a higher-coordinated metallic liquid to a tetrahedrally-coordinated, viscous, semiconducting liquid.
2. The atomic structure and electronic properties of Group IV and III-V liquid exhibit significant temperature dependence as the liquids are deeply undercooled.

A corollary of hypothesis 1 is that a decrease in mass diffusivity will accompany the phase transitions. The scientific objective of the proposed research is to measure changes in structural and electrical properties as a function of undercooling and to demonstrate if first-order phase transitions occur in undercooled Group IV and III-V liquids. Experimental verification that the phase transitions occur could lead to future microgravity experimentation to study key aspects of the transformation including changes in viscosity, diffusivity, and electrical conductivity.

The following experimental techniques will be employed in this research program:

(1) X-ray diffraction measurements of the structure factors (partial and total), pair distribution functions, and changes in coordination of deeply undercooled liquids including Si, Ge, Si-Ge alloys, and III-V materials including GaSb, InSb, and ternary (GaIn)Sb systems. Synchrotron X-ray diffraction will be performed at the Advanced Photon Source at Argonne National Laboratory. The apparatus has been extensively used in previous studies of other liquid systems including liquid Si [6].

(2) Non-invasive measurements of the electrical conductivity of deeply undercooled melts using a recently developed resonant coil inductance system [7]. The method permits accurate and

rapid measurements of the electrical conductivity of levitated liquids during rapid cooling experiments at rates of up to 10 measurements per second. A large change in the electrical conductivity is expected across the predicted first-order transition.

(3) Establish if there are correlations between atomic structure, electronic properties and the occurrence of first-order phase transformations.

Prior work has already shown significant structure and property changes with temperature can occur in liquid Si [6], both in the normal and undercooled regimes. In some cases, data on the resistivity, viscosity, and density of Group IV and the III-V liquids show anomalous temperature dependencies. These anomalies are related to structural, bonding and electronic changes which occur as the temperature changes and will be measured in the proposed research.

This ground-based research could lead to future microgravity experiments to investigate first-order liquid-liquid phase transitions in deeply undercooled Group IV and III-V liquids. A host of properties such as density, viscosity, self diffusion coefficients, electrical and thermal conductivities etc. will undergo dramatic changes across this transition. Measurement of these changes will require microgravity experimentation to eliminate convective transport and sedimentation effects.

REFERENCES

1. M. H. Grabow and G. H. Gilmer, *Mater. Res. Soc. Symp. Proc.,* 141, 341 (1989).
2. C. A. Angell, J. Shao, and M. Grabow, in *Non Equilibrium Phenomena in Supercooled Fluids, Glasses and Amorphous Materials,* M. Giordano, D. Leporini, and M. P. Tosi, Eds., World Scientific, Singapore, 1996, pp. 50-57.
3. G. T. Barkema and N. Mousseau, *Phys. Rev. Lett.,* 77, 4358 (1996).
4. M. O. Thompson, G. J. Galvin, J. W. Mayer, P. S. Peercy, M. J. Poate, D. C. Jacobson, A. G. Cullis, and N. G. Chew, *Phys. Rev. Lett.,* 52, 2360 (1984).
5. E. P. Donovan, F. Spaepan, D. Turnbull, J. M. Poate and D. C. Jacobson, *J. Appl. Phys.,* 57, 1795 (1985).
6. S. Ansell, S. Krishnan, J. J. Felten and D. L. Price, *J. Phys. Cond. Matt.,* 10, L73 (1998).
7. J. E. Enderby, S. Ansell, S. Krishnan, D. L. Price, and M-L. Saboungi, *Appl. Phys. Lett.,* 71, 116 (1997).

DEFECTS NUMERICALLY DECREASED

Dr. David J. Larson, Jr. and Dr. Hui Zhang

State University of New York at Stony Brook
Stony Brook, New York 11794-2275

Many of the most useful detector crystals solidify with a zincblende crystal structure. These zincblende structures are subject to pervasive twinning terrestrially because of low stacking fault energies and low critical resolved shear stress at temperatures near the solidification temperature. These important materials would be enormously benefited by an advance in the understanding of twin generation, which catastrophically diminishes yield. Further, they would benefit from improved defect minimization strategies during crystal growth and post-solidification processing.

The primary objective of this program is to investigate the influences of gravitationally-dependent phenomena (buoyant and hydrostatic) on the growth and quality of zincblende semiconductor crystals . Specifically, we will develop experiments that will use the unique microgravity environment to test the origins of twinning and dislocation generation, multiplication, annihilation, and propagation in Zn-alloyed CdTe (Zn:CdTe). Further, we will test the concept of a soft ampoule wall that will contain the molten liquid and growing crystal but will not plastically deform the solidified crystal, thus eliminating any dislocations resulting from hoop stresses.

Our terrestrial experiments will first generate a one-g baseline for a low specific gravity fluid that expands on solidification, water. These measurements will develop our surface energy measurement and process control capabilities and test our fluid geometry/heat transfer/wetting concepts with and without soft ampoules. The latter half of the program will apply this understanding to the more challenging case of Zn:CdTe. Novel experiment geometries with respect to twin and dislocation generation will be used to test theory, and a unique flight experiment series will be developed.

This talk will elaborate on our program plans.

GROWTH OF SOLID SOLUTION SINGLE CRYSTALS

Sandor L. Lehoczky, F.R. Szofran and Donald C. Gillies

Space Sciences Laboratory
NASA Marshall Space Flight Center
Huntsville, AL 35812

The solidification of a solid solution semiconductor, having a wide separation between liquidus and solidus has been extensively studied in ground based, high magnetic field and Spacelab experiments. Two alloys of mercury cadmium telluride have been studied; with 80.0 mole percent of HgTe and 84.8 mole percent of HgTe respectively, the remainder being cadmium telluride. Such alloys are extremely difficult to grow by directional solidification on earth due to high solutal and thermal density differences that give rise to fluid flow and consequent loss of interface shape and composition. Diffusion controlled growth is therefore impossible to achieve in conventional directional solidification. The ground based experiments consisted of growing crystals in several different configurations of heat pipe furnaces, NASA's Advanced Automated Directional Solidification Furnace (AADSF), and a similar furnace incorporated in a superconducting magnet capable of operating at up to 5T. The first microgravity experiment took place during the flight of STS-62 in March 1994, with the AADSF installed on the second United States Microgravity Payload (USMP-2). The alloy was solidified at 3/4 inch per day over a 9 day period, and for the first time a detailed evaluation was performed correlating composition variations to measured residual acceleration. The second flight experiment took place in the fourth United States Microgravity Payload Mission (USMP-4) in November 1997. Due to contamination of the furnace system, analysis shows that the conditions prevailing during the experiment were quite different from the requirements requested prior to the mission. The results indicate that the sample did accomplish the desired objectives.

As with the USMP-2 mission, the results of the ground based experiments were compared with the crystal grown in orbit under microgravity conditions. On the earth, it has been demonstrated that the application of the magnetic field leads to a significant reduction in fluid flow, with improved homogeneity of composition. Theoretically the field strength required to suppress flow increases with the diameter of the material. The 8 mm diameter sample used here was less than the upper diameter limit for a 5T magnet. As the configuration for USMP-4 was changed so that the material was seeded and other processing techniques were also modified, it was decided to examine the effects of a strong magnetic field under the modified configuration and parameters. A further change from USMP-2 was that a different composition of material was grown, namely with 0.152 mole fraction of cadmium telluride rather than the 0.200 of the USMP-2 experiment. The objective was to grow highly homogeneous, low defect density material of a composition at which the conduction band and the valence band of the material impinge against each other.

As indicated, the furnace was contaminated during the mission. As a result of solid debris remaining in the furnace bore, the cartridge in this experiment was significantly bent during the insertion phase. During translation the cartridge scraped against the plate which isolates the hot and cold zones of the furnace. Thermocouples indicated that a thermal asymmetry resulted. The scraping in the slow translation or crystal growth part of the processing was not smooth and it is probable that the jitter was sufficient to give rise to convection in the melt. Early measurements of composition from the surface of the sample showed that the composition varies in an oscillatory manner. Following sectioning, microprobe analysis confirmed that there was considerable compositional variation in both radial and transverse directions.

PHASE BEHAVIOR OF ASYMMETRIC BINARY COLLOID MIXTURES: INFLUENCE ON COLLOIDAL PROCESSING OF CERAMICS

J.A. Lewis *

Materials Science and Engineering Department
University of Illinois

OBJECTIVES

This ground-based research program aims to develop a fundamental understanding of the phase behavior of binary colloidal suspensions. Such systems are utilized in numerous applications including advanced ceramics, photonic band gap materials, and porous assemblies for sensors and membranes. Specifically, we have studied transitions between the fluid, gel, and crystalline states exhibited by asymmetric binary colloid mixtures of attractive, large colloidal spheres and highly repulsive nanoparticles. In addition, we have investigated the impact of such transitions on the stability, rheological properties, and structural evolution during assembly of these complex systems.

I. Microgravity Relevance

This ground-based research effort would benefit greatly from a microgravity environment because complications arising from particle-size and density-driven segregation in suspension would be minimized allowing a broader range of experimental conditions to be probed.

II. Background

Colloidal processing is well known to be an optimal approach for tailoring the structure and, hence, properties of ceramic films and bulk forms. Through careful control of interparticle interactions, suspensions can be prepared as stable fluids or flocculated gels. In the stable state, discrete particles exist which repel one another upon close approach when the repulsive barrier $>> kT$. In the flocculated state, particles undergo rapid aggregation to yield a 3-D space filling, colloidal gel.

Binary mixtures of hard-sphere colloids, which interact only through infinite repulsion on contact, exhibit a rich phase behavior that depends on three dimensionless parameters: the volume fractions of large (ϕ_L) and small (ϕ_S) spheres, respectively, and their radii ratio (a_L/a_S). [1-3] The addition of small species to otherwise stable suspensions of large colloidal spheres is known to induce a depletion attraction (refer to Figure 1). [4] This subtle force, whose magnitude scales with ϕ_S and a_L/a_S, has been shown to broaden the fluid + crystal coexistence region in systems where $\phi_L > \phi_S$. [1-3] In contrast, little is known about the phase behavior and structural evolution of asymmetric binary systems that begin in a nonequilibrium (or gel) state.

* Corresponding author (jalewis@staff.uiuc.edu)

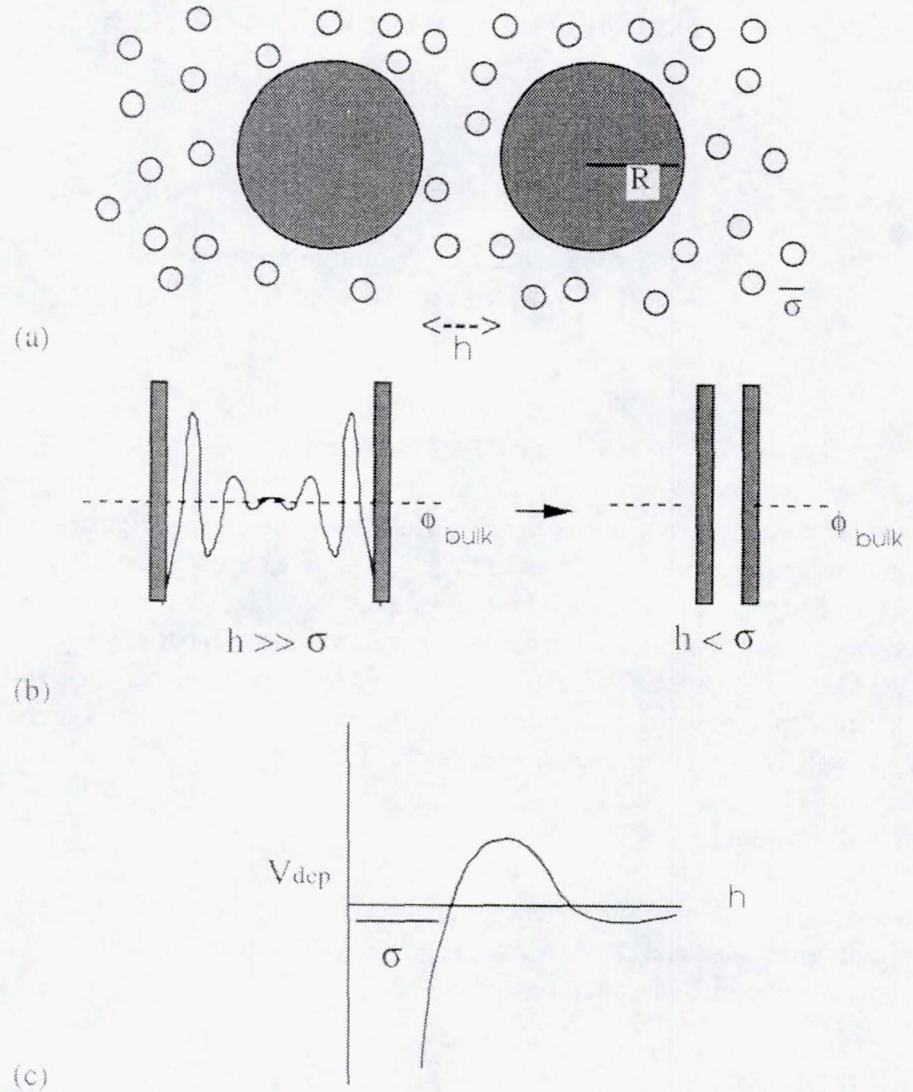

Figure 1. Schematic representation of (a) large, primary colloidal spheres interacting in a solution of smaller colloidal depletants, (b) depletant concentration profile as a function of interparticle separation distance, h, and (c) attractive, depletion potential energy resulting from such interactions ($h < \sigma$), where ϕ_{bulk} is the depletant volume fraction bulk solution.[5-6]

III. Significant Results

The large, attractive colloids consisted of uniform silica spheres (radius, a_L, of 285+ 10 nm) and the highly repulsive nanoparticles consisted of hydrous zirconia (average radius, a_L, of 5 nm). Bare silica spheres were suspended in an aqueous solution at pH = 1.5, near their isoelectric point. Upon the addition of an appropriate nanoparticle concentration, the samples were mixed (shear melted) and further characterized. Their rheological behavior was studied as a function of varying colloid and nanoparticle volume fraction using a controlled stress rheometer (Bohlin CVO and CS-10). In the absence of nanoparticle species, SiO_2 suspensions exhibited strong shear thinning behavior indicative of a flocculated system (refer to Figure 2). Upon the addition of a critical nanoparticle volume fraction, the suspension rheology changed dramatically. Both the low shear apparent viscosity and degree of shear thinning behavior decreased indicative of complete stabilization. At even higher nanoparticle concentrations, the system stability was again reversed.

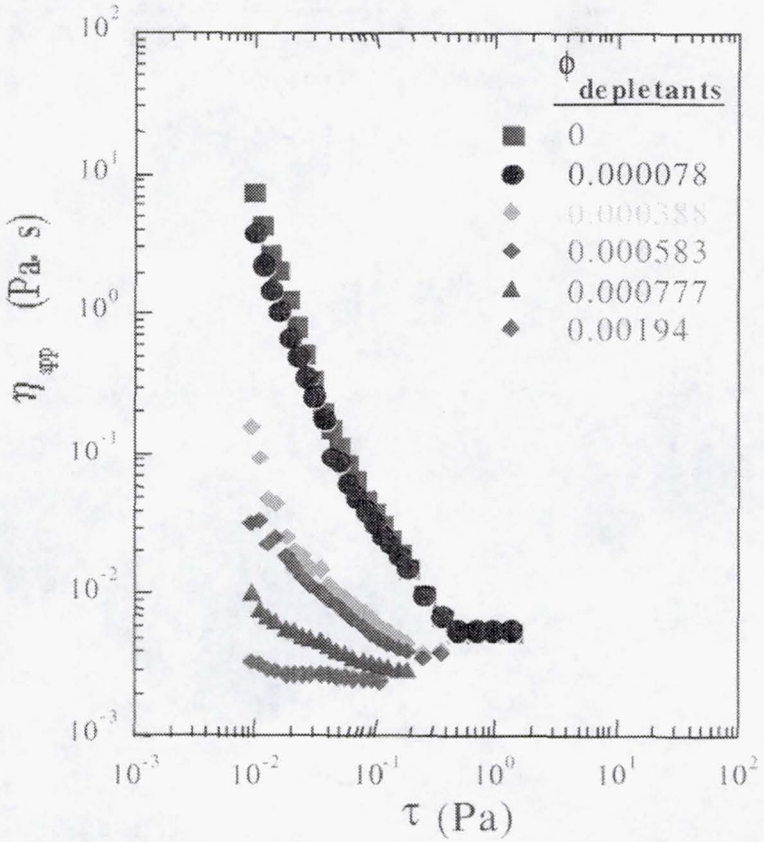

Figure 2. Log-log plot of apparent suspension viscosity versus shear stress for SiO_2 suspensions ($\phi_{colloid} = 0.10$) of varying depletant volume fraction.

To further probe their phase behavior, samples were prepared over a broad concentration range, *i.e.*, ϕ_L - ϕ_S space. Following the same procedure, samples were shear melted and then visually observed for several weeks. The general trends are shown in Figure 3. In the absence of nanoparticle species ($\phi_S = 0$), the system begins in a nonequilibrium state. Bare silica spheres undergo rapid flocculation to yield either a transient or stable gel (G_L). Transient gels settled quickly to form a loose sediment, whereas stable gels could support their own mass and therefore did not undergo further consolidation in response to gravitational forces. Above the lower critical volume fraction ($\phi^{L,C}$) of nanoparticle species, a dramatic change in stability was noted. All samples were initially opaque white because large silica spheres strongly scatter visible light. Some samples remained that way for several days, until the individual silica spheres settled under gravity to yield a close-packed, colloidal array. This assembled array exhibited strong opalescence due to Bragg scattering from its periodic structure. Such samples were considered stable in the homogeneous, binary fluid (F) phase. Above the upper critical volume fraction ($\phi^{U,C}$) of nanoparticle species, this dramatic change in stability was reversed. Outside the concentration range of $\phi^{L,C} = \phi_S < \phi^{U,C}$, large silica spheres flocculated yielding either a transient or stable gel (G_L) in coexistence with a nanoparticle fluid phase (F_S). The origin of this unusual transition from unstable → stable → unstable behavior will be addressed on the basis of energetic and entropic considerations.

Ongoing experimental work is aimed at probing the structure of both the fluid state using ultra-small angle x-ray scattering (USAXS) (in collaboration with G. Long) and the assembled periodic colloidal arrays using confocal microscopy (in collaboration with P. Braun and P. Wiltzius). Such observations will be critical to understanding the nature of the colloidal interactions in these assemblies and will be compared to theoretical predictions outlined below.

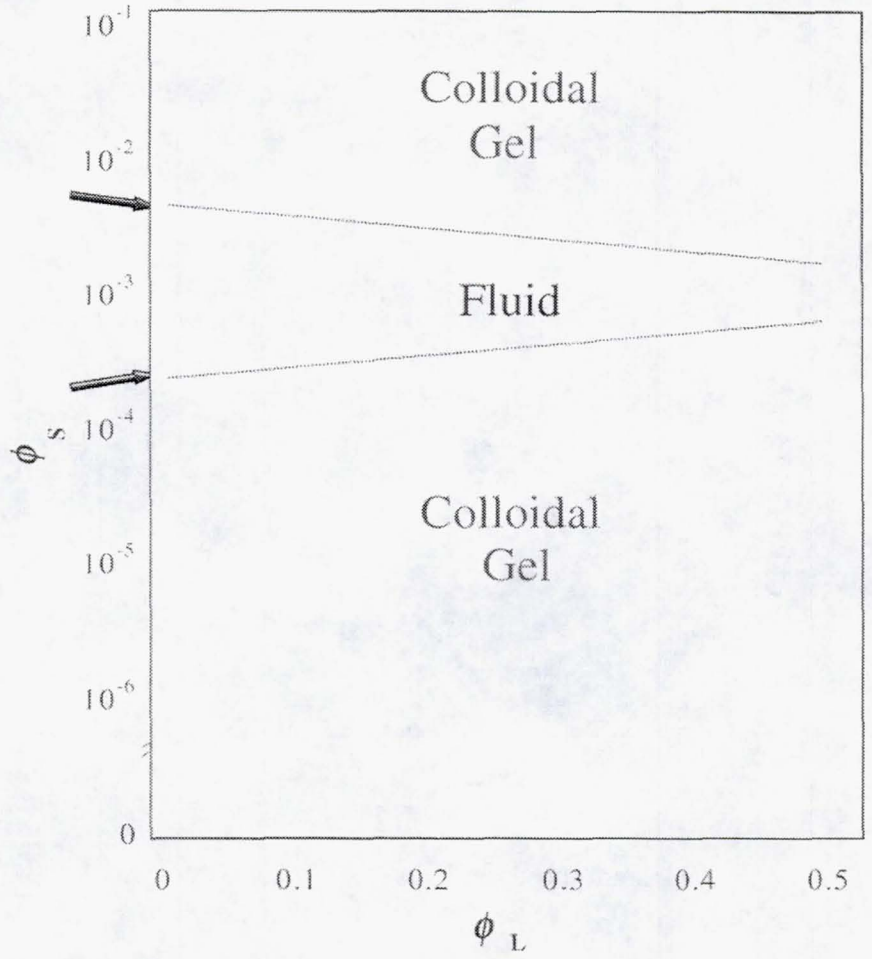

Figure 3. Phase behavior of binary mixture of large (silica) and small (zirconia) colloids. [Note: Arrows denote lower and upper critical volume fractions.]

IV. Modeling of Colloidal Interactions

The stability of a given colloidal system is determined by the total interaction potential energy, To model the experimental systems described above, we account for long range van der Waals, electrostatic, short-range hydration, and depletion interactions.[5-8] The attractive van der Waals interaction potential energy, V_{vdw}, exhibits a power law distance dependence whose strength depends on the dielectric properties of the interacting colloidal particles and intervening medium. The repulsive electrostatic interaction potential energy, V_{elect}, exhibits an exponential distance dependence whose strength depends on the surface potential induced on the interacting colloidal particles and the dielectric properties of the intervening medium. Exact analytical expressions for the electrostatic potential energy cannot be given, thus analytical approximations or numerical solutions will be used. The short-range hydration interaction potential energy, V_{struct}, exhibits an exponential distance dependence with a characteristic decay length of roughly 1 nm. The depletion interaction potential energy, V_{dep}, can be calculated using the approach developed by Walz and Sharma[5], which predicts the depletion force between two charged spheres in a solution of smaller, charged spheres and accounts for second-order effects arising from two-body depletant interactions through a virial expansion of the single particle distribution function correct to $O(p_8^2)$, where p_8 is the bulk depletant concentration. These ongoing calculations are expected to provide important insight regarding the origin of the observed phase behavior.

V. Collaborators

V. Tohver, P. Braun (UIUC), P. Wiltzius (Lucent), J. Walz (Yale), G. Long (NIST)

REFERENCES

1. Biben, T.; Hansen, J., *Phys. Rev. Lett.* 66, 2215-18 (1991).
2. Imhof, A.; Dhont, J.K.G., *Phys. Rev. Lett.* 75, 1662-65 (1995).
3. Dinsmore, A.D.; Yodh, A.G., Pine, D.J., *Phys. Rev. E.* 52, 4045-57 (1995).
4. Asakura, S.; Oosawa, F., *J. Poly. Sci.* 33, 183-92 (1958).
5. Walz, J. Y.; Sharma, A. *J. Colloid Interface Sci.* 1994, *168*, 485.
6. Mao, Y.; Cates, M.E.; 1Lekkerkerker, H.N.W. *Physica A* 1995, 222, 10-24.
7. Ogden, A.; Lewis, J.A.; *Langmuir.* 1996, *12*, 3413.
8. Hunter, R.J. *Foundations of Colloid Science, Vol.1*, Oxford Science, 1989.

A COMPARATIVE MODELING STUDY OF MAGNETIC AND ELECTROSTATIC LEVITATION IN MICROGRAVITY

Ben Q. Li

School of Mechanical and Materials Engineering
Washington State University
Pullman, WA 99164 - 2920

ABSTRACT

Mathematical models are developed to represent the complex electrodynamic and hydrodynamic phenomena in magnetically and electrostatically levitated droplets in microgravity environment. The numerical model development is based on the solution of the Maxwell equations using either the boundary element technique or the coupled boundary/finite element technique and the solution of the Navier-Stokes equations and energy/mass balance equations by the finite element method. The models are applied to address the following key issues concerning the behavior of magnetically and electrostatically positioned droplets in space: (1) electromagnetically or electrosatically induced surface deformation, (2) internal flows driven by electromagnetic forces or surface tension, (3) viscous surface oscillation and heat transfer of droplets levitated magnetically, and (4) turbulent flow behavior in magnetically-levitated droplets.

I. Introduction

Magnetic levitation and electrostatic levitation are two important containerless processing technologies in materials science research for studying fundamental phenomena such as nucleation and solidification microstructure formation and for measuring thermophysical properties of molten materials under microgravity conditions, such as heat capacity, surface tension, thermal conductivity, electrical conductivity and viscosity [1-3]. In fact, there has been an operational magnetic levitation system, the TEMPUS system, specifically designed for these microgravity applications. An electrostatic levitation device is being tested on the ground and is to be installed in the International Space Station for microgravity applications.

Mathematical models have been developed based on the finite element solution of the Maxwell and transport equations and extensive numerical simulations have been carried out to develop a fundamental understanding of, and to be able to predict, the electrodynamic and transport phenomena associated with drops in electrostatic and magnetic levitators. These models were applied to obtain information on the internal flow and thermal field, electromagnetic field, surface deformation and oscillation, viscous decay and sample stability will be obtained for the levitated drops as a function of various processing parameters such as the drop size, applied voltage, applied current and voltage. This information should be indispensable in providing rational guidelines for selecting the levitation process best suited for particular applications.

II. Numerical Models for Magnetically Levitated Droplets

Numerical models have been developed to represent the electromagnetic, transport and free surface phenomena associated with levitated drops in magnetic and/or electrostatic levitation systems. The model assumes an axial symmetry. The model development is based on the finite element and boundary element computational methodologies that have been developed by our research group in recent years [4,5]. In essence, a coupled boundary/finite element method is applied to solve the Maxwell equations. By this method, finite elements are used to discretize the droplet region where information on electromagnetic field and temperature field distributions is needed, while boundary elements are applied in the free space outside the droplet region. The finite element and boundary element regions are then coupled through the interface boundary conditions. The model for fluid flow and temperature distribution in the levitated droplets is developed based on the finite element solution of the transient Navier-Stokes equations and energy balance equations with the Lorentz forces as momentum sources and Joule heating as energy sources. The details of the model development and numerical simulations are documented in a recent dissertation [6].

Some of the calculated results are given in Figures 1 and 2. The internal fluid flow and temperature distribution in a liquid silver sphere of 10 mm diameter magnetically positioned by TEMPUS in microgravity are shown in Figure 1, which are calculated using different turbulent models. The calculations considered heating coils only as they are the dominant force in driving strong recirculating flows in the droplet. It can be seen that heating coils generate strong magnetically driven flows, characterized by two anti-rotating flow loops. The effect of the fluid flow also has an effect on the temperature distribution as seen in the left half of the sphere. It is important to note that all of the turbulence models predict roughly the same level of velocity in the droplet and that this velocity is about 20% lower than that predicted by only increasing the molecular viscosity of the droplet by a factor of 10.

One of the techniques used for measuring viscosity and surface tension is to oscillate the surface of the droplet after it is being deformed. A deforming finite element model is also developed to represent the oscillation behavior of a droplet in the TEMPUS device when heating coils are turned off. A set of computed results is given in Figure 2, along with the internal velocity. Figure 3 shows the viscous damping of the surface oscillation of the droplet.

III. Numerical Models for Electrically Levitated Droplets

Numerical models have also been developed to represent the electric field distribution, electrically induced droplet deformation, temperature field and fluid flow in electrostatically levitated samples. The model development is based on the modification of the models used for magnetic levitation as described above. Details of the model development and numerical simulations are documented elsewhere [7,8].

Some of the results obtained from the numerical models for electrostatically levitated droplets in microgravity are given in Figures 4 to 6. The surface deformation (see Figure 4) is caused by electrostatic forces which are induced by the surrounding electrodes. This set of calculations assumes that the electrodes are placed far away from the droplet sample. Calculations using the electrode arrangements being used at NASA Marshall Center are being made. It is noteworthy that electrostatically induced surface deformation is different in principle from that caused by induced elecromagnetic forces. In the former, deformation is caused by pulling the two poles of the droplet by electrostatic forces, while in the latter it is caused by the strong dipole forces generated at the equator.

The internal flow in electrostatically levitated droplets, as shown in Figures 5 and 6, is primarily attributed to surface tension effects, which in turn result from non-uniform heating. Calculations presented here are based on the laser heating used for similar studies. Numerical simulations [8] showed that a more uniform heating results in a smaller flow level and that higher melting point materials require high heating power and thus a higher velocity occurs in these droplets for a same distribution of heating source.

IV. Future Work

Study of turbulent magnetically-driven flow is currently underway using direct numerical simulations (DNS). While the current Low Reynolds number turbulence models are consistent in predicting the velocities driven by electromagnetic forces, a critical assumption has been made in placing the boundary conditions for those calculations. A somewhat ad hoc or empirical approach is to assume that both kinetic energy and dissipation quantities are prescribed as zero on a free droplet surface. This assumption needs to be verified. One of the viable methods to do so is to carry out the direction numerical simulations of the turbulent flows in the free droplet. Also, the flow relaminarization occurs during the free surface oscillation after heating coils are switched off and requires a more accurate description of turbulence. The DNS will allow an accurate representation of turbulence in the droplets and assess the error associated with the k-ε based turbulence models for transitional flows and relaminarization. With DNS, information on the Reynolds stresses, turbulent intensities, instantaneous flow structure, and turbulent transport will be obtained and will be crucial for us to understand the turbulence structure in the droplets and hence flow relaminarization. We have initiated the work in this direction.

Numerical models will be further extended to include temperature effects associated with magnetically induced droplet oscillation and to further extended to study force oscillation of free droplet of electrostatically positioned droplets.

REFERENCES

1. Femings, M. C., Trapaga, G. and Hyers, R. (1996) The measurement of the viscosity and surface tension of undercooled melts under microgravity conditions and supporting MHD calculations. Microgravity Materials Science Conference, Huntsville, AL pp. 76-77.
2. Rim, W. K., Chung, S. K., Barber, D. Man, K. F., Gutt, G. and Rulison, A. (1993) An electrostatic levitator for hihg-temperature containerless materials processing in 1-g. *Rev. Sci. Instrum*, Vol. 64 (10), pp. 2961-2970.
3. Hyes, R., Johnson, W. L., Savage, L. and Rogers, J. R. (2000) Reduction of sample rotation in electrostatic levitation. In 12th International Symposium on Experimental Methods for Microgravity, TMS, Nashville, TN.
4. Song, S. P. and Li, B. Q. (1998). A boundary/finite element analysis of magnetic levitation systems: surface deformation and thermal phenomena. *ASME J. Heat Transf.*, Vol. 120, pp.492-504.
5. Song, S. P., Li, B. Q. And J. A. Khadadadi (1998). Coupled boundary/finite element solution of magnetothermal problems. *Int. J. Num. Meth. Heat Fluid Flow*, Vol. 8, pp. 1369-1383.
6. Song, S. P. (1999) Finite element analysis of surface oscillation, fluid flow and heat transfer in magnetically and electrostatically levitated droplets. Ph.D. Dissertation, Washington State University.
7. S. P. Song and B. Q. Li (1999). Coupled boundary/finite element computation of magnetically and electrostatically levitated droplets. *Int. J. Num. Meth. Eng.*, Vol 44. No. 8, 1999, pp. 1055-1077.
8. S. P. Song, P. Dailey and B. Q. Li,Effects of heating source arrangements on internal convection in electrostatically levitated droplets. *AIAA J. Thermophy. Heat Trans.*, in print.

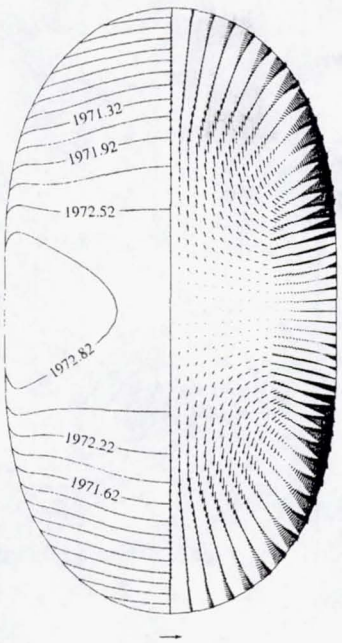

(a) V_{max}=13.1 cm/s

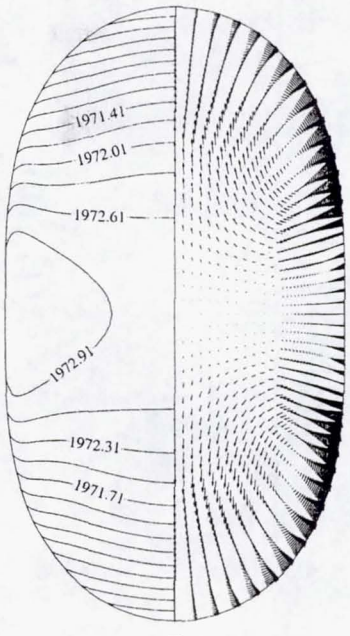

(b) V_{max}=12.7 cm/s

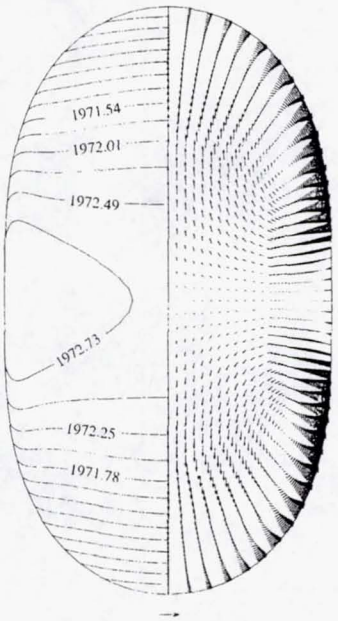

(c) V_{max}=13.7 cm/s

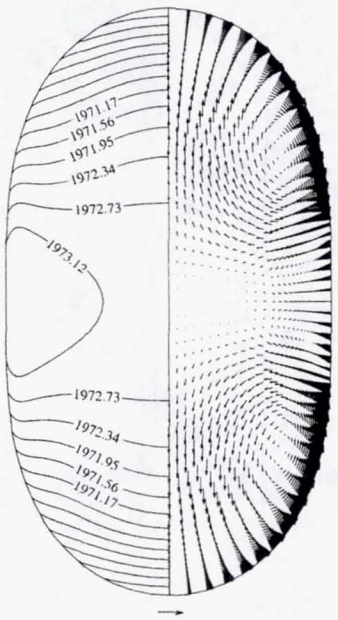

(d) V_{max}=13.5 cm/s

Figure 1. Surface deformation, internal velocity and temperature (left, in K) distribution in a magnetically positioned silver droplet (10-mm initial dia) in the TEMPUS device - heating coils only. Turbulence models used: (a) LS, (b) JL, (c) RNG and (d) k-ω.

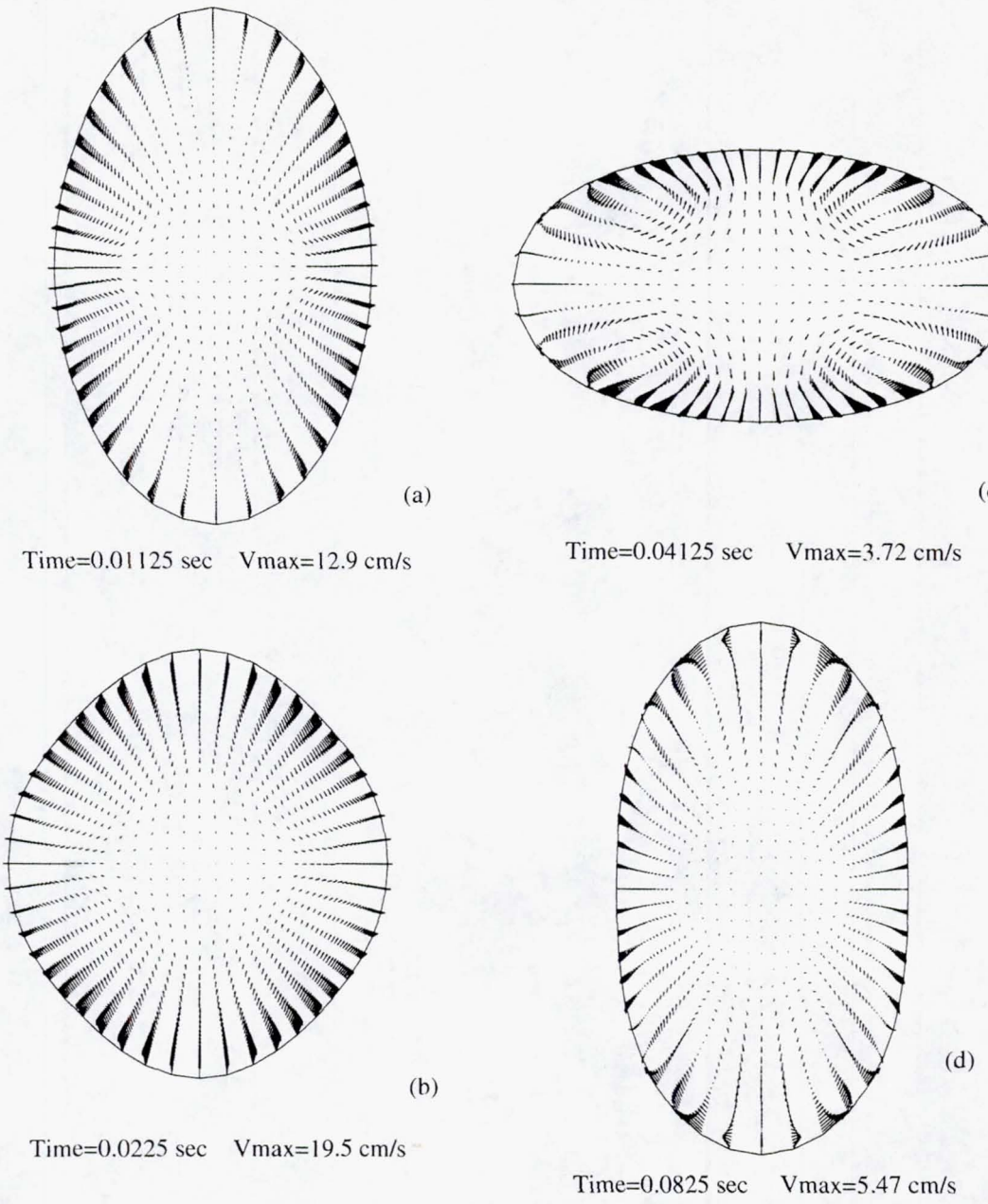

Figure 2. Oscillation of a silver droplet in TEMPUS device under microgravity condition. The initial diameter of the droplet is 10 mm. The conditions for the calculations: current = 200 A (Peak) and frequency = 4.27×10^5 Hz for heating coils, and current = 140 A (Peak) and frequency = 1.44×10^5 Hz for positioning coils.

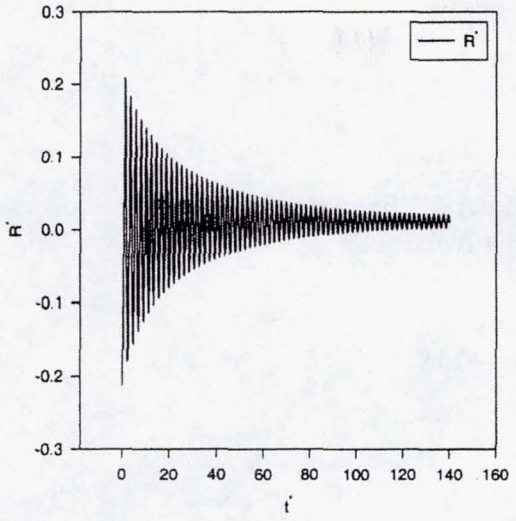

Figure 3. Viscous decay of oscillation amplitude of a magnetically-positioned droplet in TEMPUS device: $R^*=(R(t)-R_0)/R_0$ and $t^* = t/\sqrt{\rho R_0/\gamma}$, where R_o is the initial radius of the liquid sphere and $R(t)$ the radius at the equator.

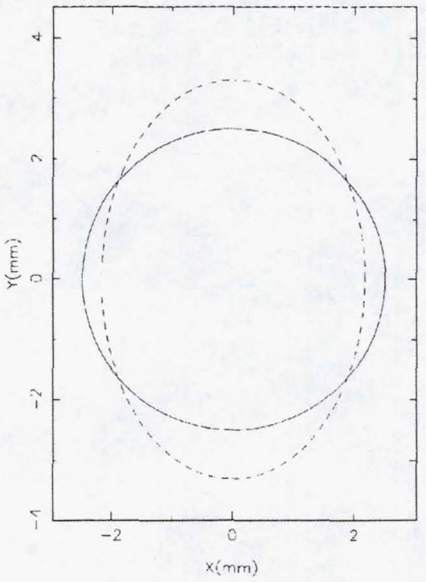

Figure 4. Electrostatically deformed free surface shape of a molten silicon drop (dashed line) in microgravity: the sample initial diameter is 5 mm, as indicated by the solid line, and the applied electric field is 2.5×10^6 V/m.

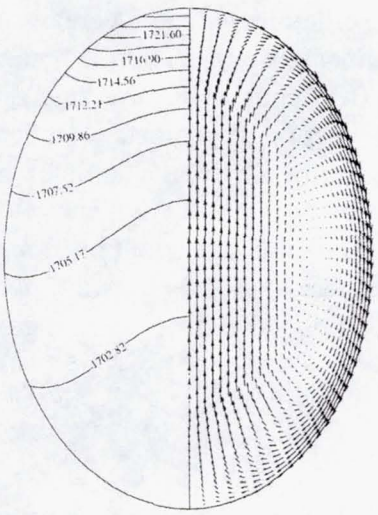

V_{max}=21.8 cm/s

Figure 5. Temperature (in K) distribution and internal velocity field in a Si droplet with heating at the north pole only (a_l = 1.25mm, Q_0=3.0 x 10^6 W/m^2) in microgravity.

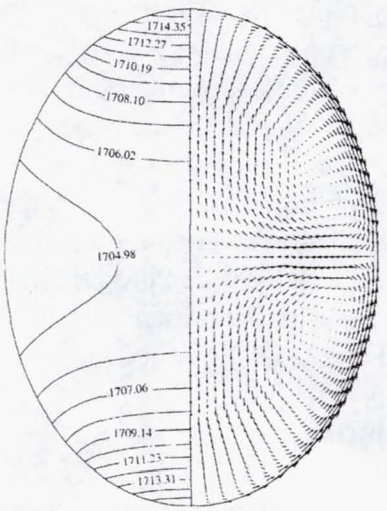

V_{max}=13.1 cm/s

Figure 6. Temperature (in K) distribution and Marangoni velocity field in a Si droplet with heating at the two poles (a_l = 1.25mm, Q_0=1.5 x 10^6 W/m^2) in microgravity.

STUDY OF MAGNETIC DAMPING EFFECT ON CONVECTION AND SOLIDIFICATION UNDER G-JITTER CONDITIONS

Ben Q. Li[1] and H. C. de Groh III[2]

[1]School of Mechanical and Materials Engineering
Washington State University
Pullman, WA 99164
[2]NASA Lewis Research Center
Cleveland, OH 44135

ABSTRACT

As shown in space flight experiments, g-jitter is a critical issue affecting solidification processing of materials in microgravity. This study aims to provide, through extensive numerical simulations and ground based experiments, an assessment of the use of magnetic fields in combination with microgravity to reduce the g-jitter induced convective flows in space processing systems. Analytical solutions and 2-D and 3-D numerical models for g-jitter driven flows in simple solidification systems with and without the presence of an applied magnetic field have been developed and extensive analyses were carried out. A physical model was also constructed and PIV measurements compared reasonably well with predictions from numerical models. Some key points may be summarized as follows: (1) the amplitude of the oscillating velocity decreases at a rate inversely proportional to the g-jitter frequency and with an increase in the applied magnetic field; (2) the induced flow oscillates at approximately the same frequency as the affecting g-jitter, but out of a phase angle; (3) the phase angle is a complicated function of geometry, applied magnetic field, temperature gradient and frequency; (4) g-jitter driven flows exhibit a complex fluid flow pattern evolving in time; (5) the damping effect is more effective for low frequency flows; and (6) the applied magnetic field helps to reduce the variation of solutal distribution along the solid-liquid interface. Work in progress includes developing numerical models for solidification phenomena with the presence of both g-jitter and magnetic fields and developing a ground-based physical model to verify numerical predictions.

I. Introduction

Microgravity and magnetic damping are two mechanisms applied during the melt growth of semiconductor or metal crystals to suppress buoyancy driven flow so as to improve macro and micro homogeneity of the crystals. As natural convection arises from gravity effects, microgravity offers a plausible solution to reduce the convective flow. However, recent flight experiments indicate that residual accelerations during space processing, or g-jitter, can cause considerable convection in the liquid pool, making it difficult to realize a diffusion controlled growth, as originally intended, when experiments were conducted in microgravity [1]. Further studies showed that g-jitter is a random phenomenon associated with microgravity environment and has both steady state and transient effects on convective flow. Since molten metals and

semiconductor melts are electrically conducting, magnetic damping may be explored to suppress the unwanted g-jitter induced convection during solidification [2].

The objectives of this project are to: (1) determine the behavior of g-jitter induced convection in a magnetic field, (2) assess the abilities of magnetic fields to suppress the detrimental effects of g-jitter during solidification and (3) develop an experimentally verified numerical model capable of simulating transport processes and solidification phenomena under g-jitter conditions with and without a magnetic field. These goals are to be achieved through both theoretical analyses and ground based laboratory experiments. We have carried out asymptotic analyses and developed 2-D and 3-D numerical models for g-jitter driven flows in simple solidification systems with and without the presence of an applied magnetic field. Research findings obtained from analyses and numerical simulations are reported in refs. [2-7]. A physical model for ground-based measurements has been completed and some measurements of the oscillating convection are currently being taken on the physical model. Comparison of the measurements with numerical simulations is in progress. Numerical and physical models are now being modified to study the solidification phenomena with the presence of both g-jitter and magnetic fields.

II. Analytical Solution for A One-D Simple System

This simple one dimensional analysis is intended to provide some perspective on the asymptotic behavior of magnetic damping effects on g-jitter induced flow in a parallel plate configuration, in which a temperature gradient exists across the channel. A g-jitter field, assumed to follow time harmonic oscillation but spatially independent, acts in the direction parallel to the plates. A DC magnetic field is applied perpendicularly to the plates. Analyses show that the applied field is more effective in suppressing the flows associated with g-jitter with lower frequencies but only has a moderate effect on the high frequency g-jitter flows [3].

III. Development of 2-D and 3-D Finite Element Models

We have developed both 2-D and 3-D numerical models for the transient fluid flow, heat transfer and solutal transport under the influence of g-jitter with and without the presence of an external magnetic field. The model development was based on the finite element solution of the transport equations with the Lorentz forces as a momentum source and entails the modification of our in-house finite element fluid flow and heat transfer code. The numerical models were further tested against the analytical solution for the application of magnetic damping to suppress the g-jitter induced convective flows, and excellent agreement exists between the two approaches [4,5].

The 2-D model was applied to study a simplified Bridgman-Stockbarger system for the melt growth of Ga-doped germanium single crystals. The simplification, among others, treats the solidification front being flat. Numerical simulations illustrate that the application of an external magnetic field reduces the convective velocities in the system studied. Some of the results obtained from 2-D numerical model are given in Figure 1. It is apparent from these figures that the application of the magnetic field reduces the g-jitter induced convective flow effect and thus decreases the solutal striation.

As g-jitter in microgravity is time dependent and changes its direction because of the maneuver of space vehicles, a fully 3-D model is more appropriate. Simulations from 3-D numerical models developed in our group show that the fluid flow driven by g-jitter is very complex and also

evolves in time. This can be especially true when all three g-jitter components with composite frequencies and amplitudes are considered. Results illustrate that with the absence of the magnetic field, g-jitter induces strong recirculation in the vertical plane within which it is acting. With a magnetic field applied in the vertical direction, the convective flows and the recirculation loops are suppressed by the opposing Lorentz forces. Fluid flow results in other planes further indicate that with an applied magnetic field, the perturbance from g-jitter may be reduced to a level far smaller than the plug flow resulting from the inlet inertia of the fluid [6]. Table 1 and Figure 2 summarize the results obtained from the 3-D numerical simulations of the magnetic damping effects on the g-jitter induced flows.

IV. Physical Model

A physical model has been developed to partially simulate oscillating behavior of g-jitter force and its effects on natural convection. The detailed physical model construction and entire experimental setup are detailed in a recent thesis [7]. The flow is induced in the system by an oscillating wall temperature gradient combined with the gravitational force. At the present, water is used as a working fluid and a laser-based PIV is used to visualize the thermally induced fluid flow. The measured velocity field was then compared with the finite element computations. Figure 3 compares the calculated and measured oscillating velocity fields. Apparently, the computations agree reasonably well with the measurements and in particular the oscillating flow behavior is revealed in both numerically computed and experimentally measured results.

V. Work in Progress

The work in progress involves extensive experimental measurements and numerical simulations to obtain more information that will help to enhance our fundamental understanding of magnetic damping effects on g-jitter induced flow and solidification phenomena in space processing systems and to help design damping facilities for microgravity applications. Numerical simulations will be continued to study magnetic damping of g-jitter flows and solutal striation and to quantify the effects of the field strength and direction, and the g-jitter frequency, orientation and amplitude, on the convective flows and solutal distribution and evolution in solidification systems. Solidification phenomena will be included in the 2-D model so as to better understand the effects of g-jitter and magnetic fields. Ground-based measurements of oscillating flows and their effects on solidification will be conducted in the physical. The physical measurements will be compared with the numerical model predictions.

REFERENCES

1. Lehoczky, S., Szofran, F. R. and Gillies, D. C. (1994). Growth of solid solution single crystals. Second United States Microgravity Payload, Six Month Sciences Report, NASA MSC.
2. Li, B. Q. (1996) G-jitter induced flows in a transverse magnetic field. *Int. J. Heat & Mass Trans.*, Vol. 39, No. 14, pp. 2853-2860.
3. Li, B. Q. (1996) The effect of magnetic fields on low frequency oscillating natural convection. *Int. J. Eng. Sci.*, Vol. 34, No. 12, pp. 1369-1383.
4. Pan, B. and Li, B. Q. (1998) Effect of magnetic fields on oscillating mixed convection. *Int. J. Heat & Mass Transfer*, Vol. 41, No. 17, pp. 2705-2710.
5. Pan, B., Li, B. Q. Li and de Groh, H. C. (1997) Magnetic damping of g-jitter induced flow in microgravity. *Spacebound-97*, Montreal, (published in CD-ROM, ed: R. A. Schiffman), Canadian Space Agency, Canada.

6. Shang, D-Y, Li, B. Q. and de Groh, H. C. (1999) Magnetic damping of g-jitter driven flows: 3-D calculations. *Pan-Pacific Basin Workshop*, pp. 108-113.
7. Higgins, M. L. (2000) PIV study of oscillating natural convection flow within a horizontal rectangular enclosure. WSU MS Thesis.

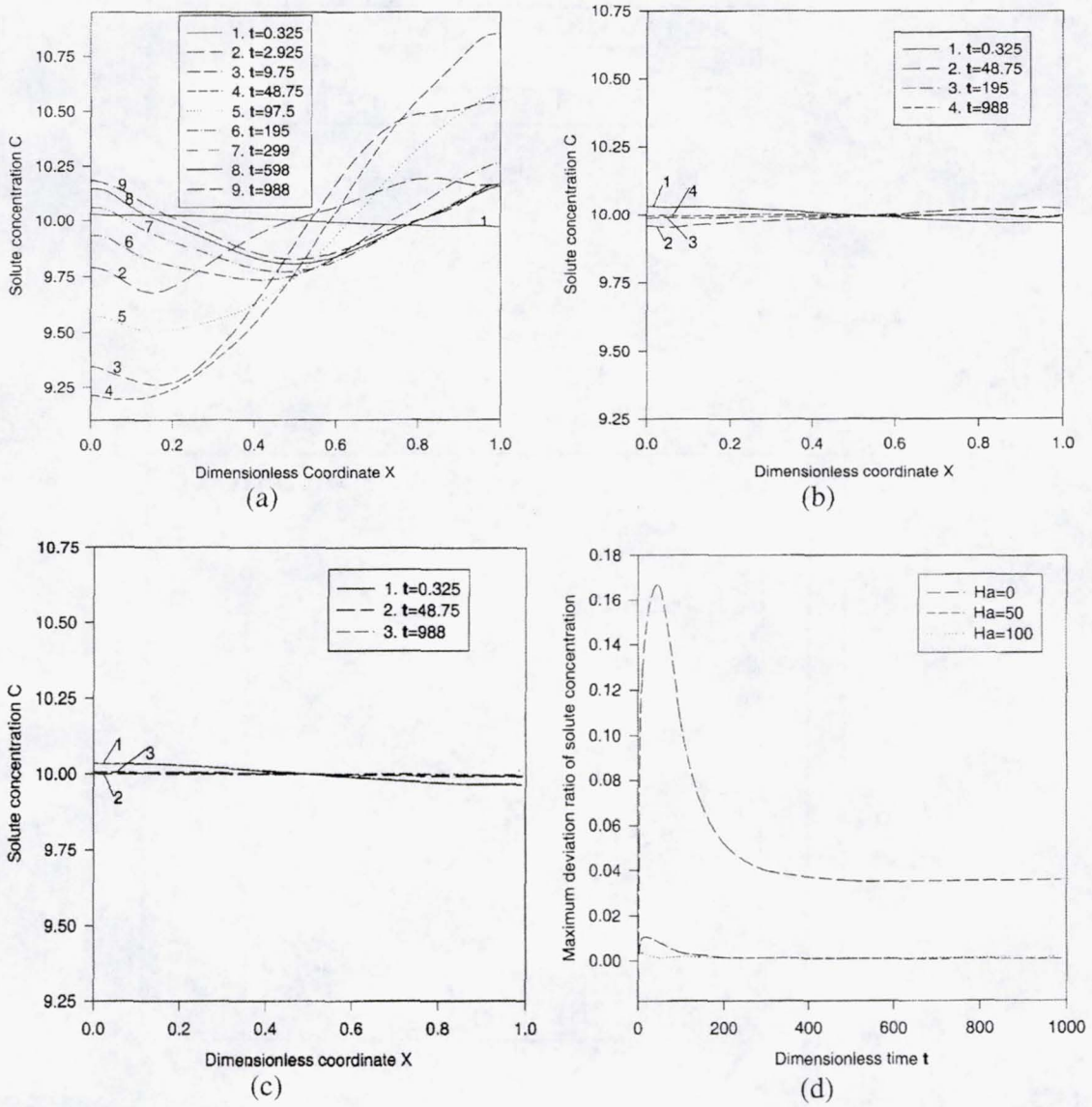

Figure 1. The effect of magnetic fields on the time variation of solutal distribution along the solid-liquid interface (y=0) with a starting steady state in microgravity: (a) Ha=0, (b) Ha=50, (c) Ha=100 and (d) maximum deviation of concentration [5]. The applied magnetic field reduces the convec tive flow induced by g-jitter and thus the concentration striation. Futhermore, a higher magnetic field results in a more effective damping effect.

Table 1. Summary of the computed results from 3-D numerical model.

g-jitter	U_{max}
$g=g_0 10^{-3}$	0.463
$g=g_0 10^{-4}$	5.56E-02
$g=g_0 10^{-5}$	9.83E-03
$g=g_0 10^{-6}$	5.48E-03
$g=g_0 10^{-3}$ with Ha=100	2.06E-02
$g=g_0 10^{-4}$ with Ha=100	6.56E-03
$g=g_0 10^{-5}$ with Ha=100	5.16E-03
$g=g_0 10^{-6}$ with Ha=100	5.02E-03

* $U_{growth} = 0.005$ (normalized)

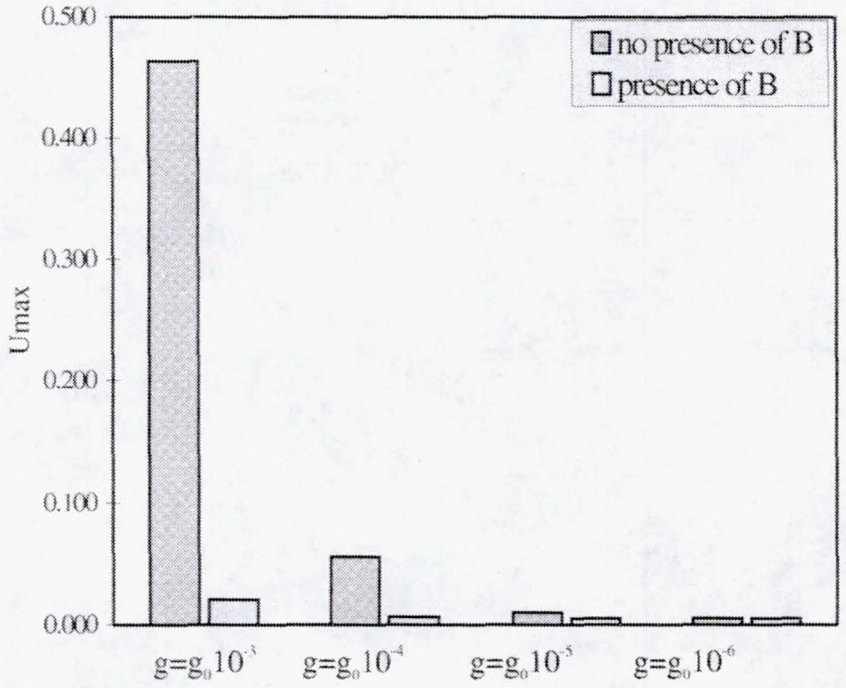

Figure 2. Maximum velocity (in logarithmic scale) calculated using the 3-D numerical model in the presence and absence of an applied magnetic field (Ha=100).

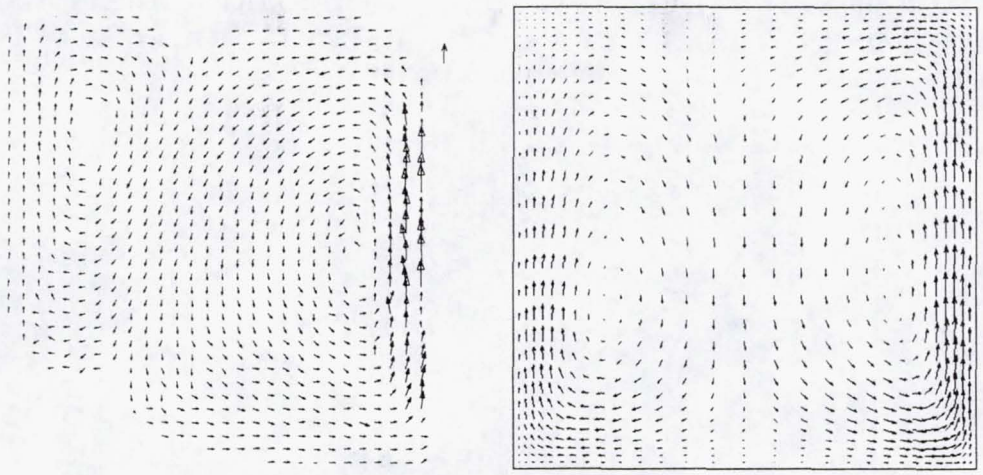

(a)

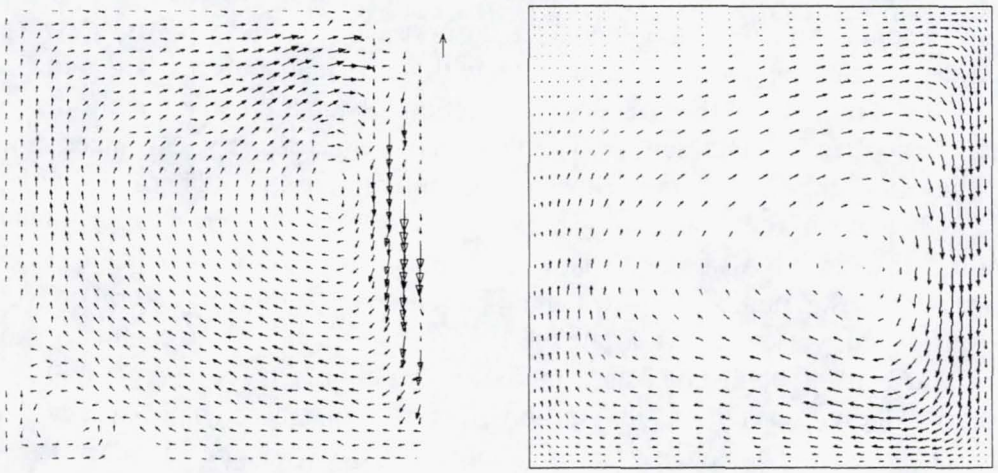

(b)

Figure 3. Comparison of measured (left) and computed (right) velocity field at diferent times. The flow field is induced by an oscillating wall temperature gradient. (a) maximum velocity: 0.62 mm/s measured vs. 0.57 mm/s computed att=8 sec from the start of an oscillating cycle, (b) maximum velocity: 0.88 mm/s measured vs. 0.93 mm/s computed at t=46 sec from the start of an oscillating cycle. Temperature gradient oscillates at 0.02 Hz [7].

INFLUENCE OF NATURAL CONVECTION AND THERMAL RADIATION ON MULTI-COMPONENT TRANSPORT AND CHEMISTRY IN MOCVD REACTORS

S. Lowry[1], S. Mazumder[1], D. Sengupta[1]

[1]CFD Research Corporation

INTRODUCTION

The influence of natural convection and thermal radiation number on multi-component transport and chemistry in Metal Organic Chemical Vapor (MOCVD) reactors is systematically investigated under NASA Research Project NAS8-40846, entitled, "Influence of Natural Convection and Thermal Radiation on Multi-Component Transport and Chemistry in MOCVD Reactors." This research uses empirical data in conjunction with numerical analysis. The numerical code includes advanced models for the effects of convection, conduction, and radiation as well as multi-component diffusion and multi-step surface/gas phase chemistry. Advanced radiation models include non-gray effects, thin films, and specular reflections. Thermal simulations are performed and validated for a range of operating condition for a tube reactor in collaboration with empirical studies at NASA LaRC. This same reactor is used to evaluate the relationship between the Richardson number (Gr/Re^2) and the relative magnitude of natural convection. The reactor is subsequently used to investigate the significance of multi-step chemistry mechanisms for InP and GaAs, using published data from the University of Virginia. In parallel, the need and benefits of microgravity conditions for a proposed North Carolina high pressure pulsed reactor study are demonstrated. The numerical model, improved in part under this study, is being successfully applied by commercial equipment manufactures to analyze their systems. Selected examples are provided for the analysis of some these commercial reactors for normal and off-design operating conditions.

I. Significance of the MOCVD Process

Metal Organic Chemical Vapor Deposition (MOCVD) has evolved into the industry standard for the production of compound semiconductors. MOCVD is the primary technique used to produce compound semiconductors comprised of elements from group III and V in the periodic table. These compounds include commercially important materials such as AlGaAs, AlGaInP, and (In)GaN used to fabricated ultra-high brightness LED's. Group III nitrides have been identified as a key material for optical electronics with a large market potential [Punle and Bour, 1997]. MOCVD produced III-V materials have advanced the science of signal and lighting technology. They have found application in displays, lasers, High Performance Transistors (HBT) for cellular phones, light signal transmitters/receivers for fiber optics, and in satellite dishes [Navigator, Edition 1, 1999].

II. Convection in Commercial Reactors

In the final phase of the NASA Research Project NAS8-40846, entitled, "Influence of Natural Convection and Thermal Radiation on Multi-Component Transport and Chemistry in MOCVD Reactors," the effort has focused on commercial ground-based systems. Often this information is proprietary and therefore difficult to obtain. In many cases, companies prefer to perform in house validation, in order to protect their intellectual property. To a large extent, that has been the case for the current research effort. Major MOCVD and CVD equipment manufactures such AIXTRON and Applied Materials are currently using the code to evaluate the performance of their reactors. In parallel, when available, analysis of the transport mechanisms and resulting deposition performance of selected ground-based commercial reactors have been performed under this NASA NRA. The results for two commercial reactors are presented below.

A. AMAT Reactor

The effects of pressure, and chamber height on the natural convection were investigated for a typical AMAT Reactor for deposition of III-V materials. At a typical operating condition, the wafer is maintained between 950 and 1073K, and the chamber pressure is held at 275 torr. For our simple flow study, we have used N_2 with a flow rate of 7000 sccm. The flow rate of purge gas (N_2) is kept at 3000 sccm. The parametric studies were performed both inside and outside the normal design conditions to determine the sensitivity of the reactor to these parameters, with respect to the onset of buoyancy driven convection. The reactor was modeled as axi-symmetric. Figure 1 shows the geometry and boundary conditions used in the model.

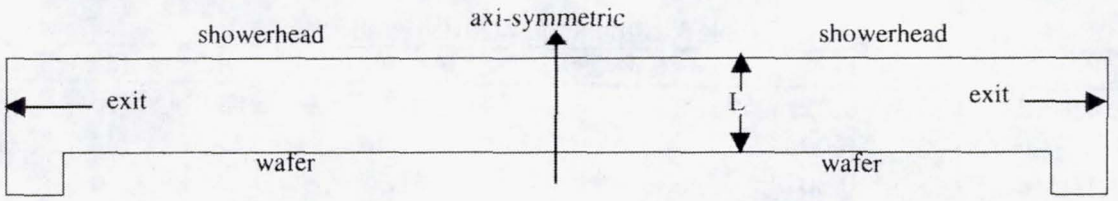

Figure 1. Geometry of the Model Reactor (2D Model)

The first set of studies investigated the effects of pressureTable 1 provides the range of parameters investigated. The Reynolds Number ($Re = UL\rho/\mu$) for this simulation ranges from 0.06 to 54. This is based on a fixed length scale of 0.01143 meters, corresponding to the interior height, L, of the reaction chamber. The viscosity and density (taken at the inlet) are computed using Sutherland's law and the ideal gas law, respectively. The reference velocity, U, is the average inlet velocity of 0.0163 m/s corresponding to normal operating condition.

The Grashof Number ($Gr = g\,\beta\,[T_{hot} - T_{cold}]\,L^3/\nu^2$) for the pressure study ranges from 1.03 to 9.82e5. The T_{hot} is the substrate temperature of 950K and the T_{cold} is the showerhead temperature of 473 K. For an ideal gas, the thermal coefficient of expansion (β) is equal to 1/T. For this case, β is approximated as a constant, $\beta = 1/T_{ref}$, where T_{ref} is set to the susceptor temperature (950 K). The length scale, L, and the kinematic viscosity $n = \mu/\rho$ m^2/s are the same as used for the Reynolds number (Figure 1) and g is one earth's gravity. The resulting Richardson (Gr/Re^2) number ranges over a narrow band from 286 to 338. A second study was performed by varying the viscosity, μ. For this set of parametrics, the Grashof number ranged from 2.1 to 6.72e8, and the Reynolds number from 0.16 to 1617. Again, this corresponded to a narrow band of Richardson numbers, ranging from 328 to 333.

Table 1. Simulations with pressure variation.

μ	ρ	Pressure	Gr	Re	Gr/Re**2	Recirculation
2.38E-05	6.93	1013000	9.82E+05	54	337	Yes
2.29E-05	3.56	506500	2.79E+05	29	332	Yes
2.30E-05	0.709	101300	1.10E+04	5.7	338	No
2.31E-05	0.305	50650	2.00E+03	2.5	320	No
2.33E-05	0.07	10130	1.04E+02	0.6	289	No
2.34E-05	0.007	1013	1.03	0.06	286	No

Table 2. Simulations with viscosity variation

μ	ρ	Pressure	Gr	Re	Gr/Re**2	Recirculation
8.18E-08	0.71	101300	8.72E+08	1617	333	Yes
1.70E-07	0.71	101300	2.00E+08	778	330	Yes
1.68E-06	0.696	101300	2.00E+06	77	334	Yes
8.17E-06	0.71	101300	8.70E+04	16	323	Yes
1.70E-05	0.704	101300	2.00E+04	7.79	329	borderline
8.27E-05	0.704	101300	839	1.58	336	No
1.66E-04	0.704	101300	208	0.8	325	No
8.32E-04	0.702	101300	8.2	0.16	320	No
1.66E-03	702	101300	2.1	0.08	328	No
U = 0.0163	L=0.01143	T(hot) = 950	T(cold) = 473	β= 0.0015		

Table 3. Simulations with L variation

μ	ρ	L	Pressure	Gr	Re	Gr/Re**2	Recirculation
2.32E-05	0.2579	0.01143	36663	1.42E+03	2.07	334	No
2.28E-05	0.2579	0.00943	36663	832	1.74	275	No
2.28E-05	0.2579	0.00743	36663	407	1.37	217	No
2.41E-05	0.2579	0.00643	36663	236	1.12	188	No
2.42E-05	0.2579	0.00543	36663	141	0.94	159	No
2.42E-05	0.2579	0.00443	36663	77	0.77	130	No
U = 0.0163			T(hot)=950	T(cold)=473	β= 0.0015		

Figure 2 shows a comparison of the vorticity in the reactor at low and high Grashof numbers. At the high Grashof number, which corresponds to off design operating conditions, there is significant recirculation. Unlike for the Crystal Specialties tube reactor, for which the Richardson number is the best indicator of the onset of recirculation, for all simulations, the Grashof number is the best indicator of the onset of recirculation. The transition to recirculation occurs at approximate Gr = 2e4. The reason that the Grashof number is a better indicator than the Ri number is that the axi-symmetric geometry of the reactor may reduce the relative effectiveness of the throughflow (the strength of which is indicated by the Reynolds number) in suppressing the natural convection. Mathematically, a Richardson number (Gr/Re^2) with a lower exponent for the Reynolds number may be a more accurate indicator of the relative effects of natural versus forced convection for such axi-symmetric geometries.

An important conclusion is that the recirculation due to natural convection is suppressed under normal operating conditions. For example, the highest Grashof number corresponding to the design conditions is 2.6E3, which is well below the threshold value of 2e4. This controlled flow results in a uniform deposition of the substrate material.

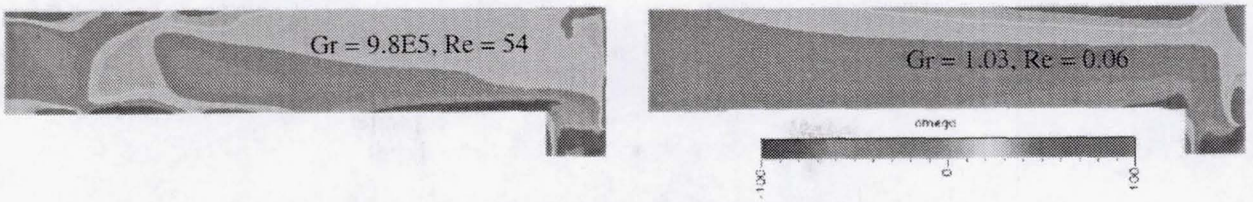

Figure 2. Vorticity in a generic AMAT reactor.

B. AIXTRON Reactors

The capability to model the effects of natural convection and thermal radiation in MOCVD reactors was applied and validated under this study using commercial MOCVD reactors. Much of this validation has been done in collaboration with AIXTRON AG, Aachen Germany. AIXTRON is the leading MOCVD equipment manufacturer in the world. They produce over fifty percent of the MOCVD equipment in the compound semiconductor industry [Bachmann, 1998]. They produce a variety of reactors including the AIX 200 series for small scale production and the Planetary Reactor® series AIX 2000 up to AIX 3000 for large scale production (Figure 3). In these reactors, precise control of the temperature has been identified as critical for ensuring high quality deposition. Accurate modeling of the thermal environment requires advanced radiative and conductive heat transport models. AIXTRON is currently using the Monte Carlo Radiation and Thermal Gap models described earlier, for inhouse predictions and validations. Under this NASA funding, studies have been conducted at CFDRC on the sensitivity of the reactors to natural convective effects, the results of which are presented below.

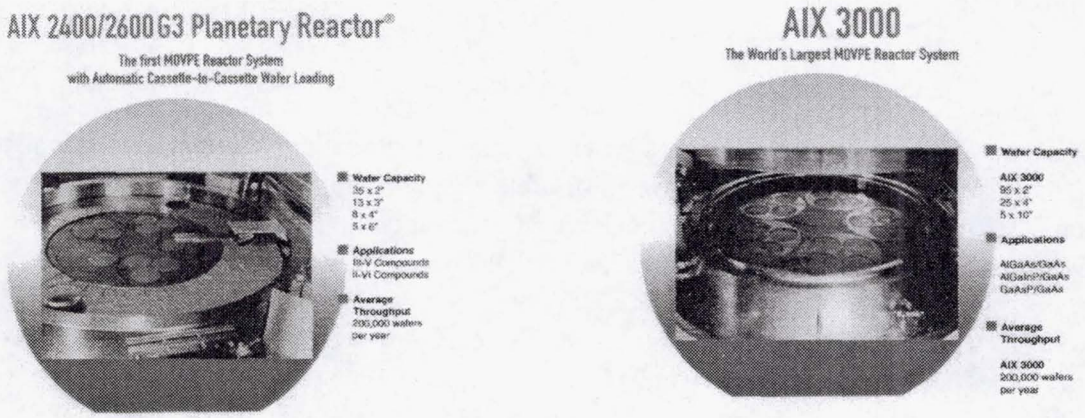

Figure 3. AIX 2000/3000 Series MOCVD Reactors

C. AIX2000: Planetary Reactor

The AIXTRON 2000 Planetary Reactor® was selected as the focus of the convective studies. This reactor is called Planetary because it is comprised of a system of rotating wafers (planets) orbiting the precursor inlet. The wafers are heated inductively, and the lid above the wafers is actively controlled to maintain the optimum temperature. Figure 4 shows a top view of a three-dimensional model of the system.

For the convective studies, the above reactor was modeled as 2-D axi-symmetric. Figure 5 shows a schematic of the numerical model. The wafer temperature and top wall temperature were fixed. The simulations were performed by varying the gap between the wafer and inner roof (L) of the reactor. The matrix of operating conditions is provided in Tables 4 and 5. Since the normal operating conditions for

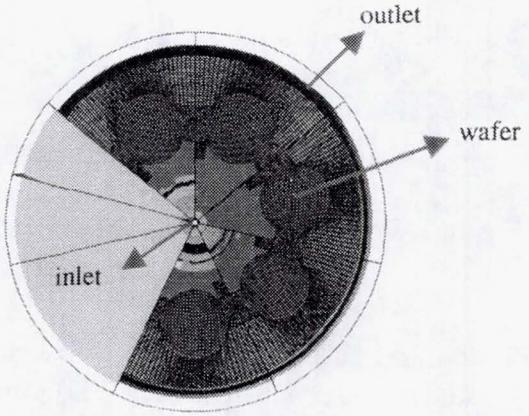

Figure 4. CFD-ACE 3D Model of AIXTRON 2000 Reactor

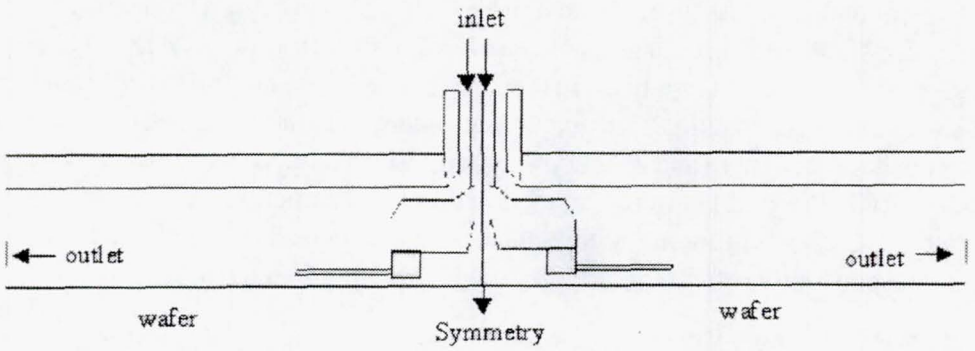

Figure 5. Schematic of the 2-D numerical model of the AIX 2000 reactor

this reactor are proprietary, the values are provided relative to the standard conditions. For all these calculations, radiation was included using the discrete ordinate method. Figure 6 shows plots of the vorticity. At lower values of L, recirculation is absent (corresponding to lower values of Grashof number), while at higher values of L, substantial recirculation occurs at the center of the reactor.

Tables 4 and 5 show that the recirculation occurs above a Grashof number of 500. The Richardson number varies between 0.27 and 0.33, and is relatively insensitive to the variation of the pressure and L. As with the SiNgen reactor, the Grashof number is the best indicator of the recirculation (as opposed to the Richardson number). Under normal operating conditions, the reactor is well below the critical Grashof number and buoyancy driven flows are suppressed. Only under off-design conditions does the Grashof number exceed the critical value and recirculation occurs.

III. Conclusions

The general conclusions of this project are:

1) The majority of commercial reactors has evolved into designs that eliminate the effects of natural convection on the ground by using narrow gaps, low pressure, and/or reduced temperature gradients.
2) Temperature control is the single most important parameter in MOCVD reactors and radiation is the dominant heat transfer mechanism that dictates temperature.
3) Optical properties in the reactors are important in determining radiative transport and can be expected to vary during operation due to growth of thin films.

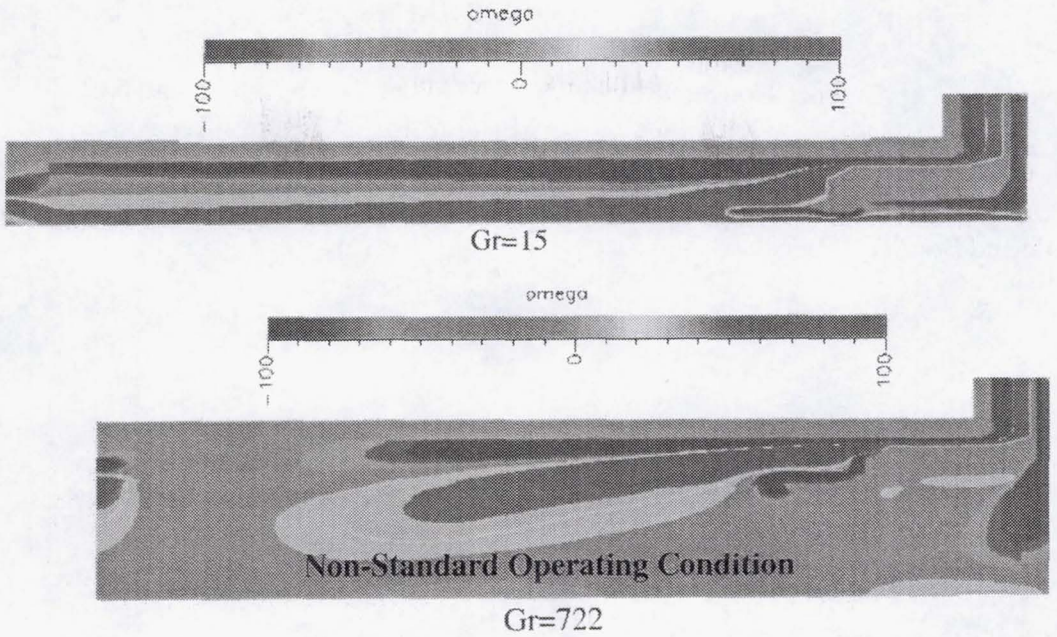

Figure 6. Vorticity plots at two different gaps between the wafer and inner roof. Larger gap shows recirculation.

Table 4. Simulations with L Variation

μ	ρ	Pressure	L	Gr	Re	Gr/Re**2	Recirculation
1.46E-5	0.0490	Standard	Standard+0.045	722	49	0.30	Yes
1.35E-5	0.0094	Standard	Standard+0.005	40	7.1	0.27	No
1.38E-5	0.0089	Standard	Standard	15	6.7	0.33	No

Table 5. Pressure Variation

μ	ρ	Pressure	L	Gr	Re	Gr/Re**2	Recirculation
1.09E-5	0.6430	50*Standard	Standard	1.22E5	582	0.36	Yes
1.16E-5	0.2930	25*Standard	Standard	2.24E4	261	0.33	Yes
1.27E-5	0.0512	5*Standard	Standard	571	42	0.32	Yes
1.38E-5	0.0089	Standard	Standard	15	6.7	0.33	No

4) Rate limited deposition on cooler surfaces away from the substrate can significantly reduce the reactor efficiency and influence optical property.
5) If reactor pressure is increased beyond today's norms, as proposed for some materials, natural convection may become significant. In some cases, reduced gravity is the only means of achieving non-turbulent non-recirculating flows for these systems.
6) Grashof and Richardson numbers are reasonable indicators of a reactor's propensity for natural convection but, in general, MOCVD systems are sufficient complex that they cannot be categorized on the basis of these dimensionless parameters alone.
7) Multi-disciplinary models are required to properly simulate the complex coupled physics in MOCVD reactors. These must include advanced heat transport models and complex chemistry.
8) There remains a strong need for well controlled empirical measurements of reactor temperatures, growth rates, and morphologies as a function of potential operating conditions in order to develop reduced reaction mechanisms, which could be used in efficient computations during the design stages.

REFERENCES

1. Bachmann *et al.*, Science Concept Review, NASA Collaborative Agreement, NCC8-95, MSFC Oct. 1998.
2. Navigator, Edition 1, May 1999, AIXTRON AG, Kackerstrasse 15-17, D-52072 Aachen, Germany
3. Punle and Bour (1997), Nature 368

MODELS OF MASS TRANSPORT DURING MICROGRAVITY CRYSTAL GROWTH OF ALLOYED SEMICONDUCTORS IN A MAGNETIC FIELD

Nancy Ma

University of Missouri at Rolla

INTRODUCTION

Alloyed semiconductor crystals, such as germanium-silicon (GeSi) and various II-VI alloyed crystals, are extremely important for optoelectronic devices. Recent rapid advances in optoelectronics have led to a great demand for more and larger crystals with fewer dislocations and other microdefects and with more uniform and controllable compositions. Currently, alloyed crystals grown by bulk methods have unacceptable levels of segregation in the composition of the crystal. The present research is focused on developing asymptotic models which investigate the effects of the transport phenomena during the Bridgman growth of these alloyed semiconductors in a magnetic field on the segregation in the entire crystal. This research supports experiments being conducted at the Marshall Space Flight Center (MSFC) and future experiments on the International Space Station (ISS).

Several studies have been conducted which contribute to the understanding of the melt motion and of the dopant segregation during crystal growth by the Bridgman process with a magnetic field both (1) on earth and (2) in microgravity. (1) The effects of various process parameters on the dopant segregation in the entire crystal during the vertical Bridgman process[1,2] and during an idealized horizontal Bridgman process[3] in the presence of a magnetic field has been investigated. (2) The effect of a steady transverse residual acceleration on the buoyant convection[4] has been investigated, while the effect of a steady axial residual acceleration on the buoyant convection and on the dopant segregation[5] has been investigated. These models of melt motion and dopant transport provide very important basic understanding of mass transport during crystal growth, and a mechanism to develop ways to treat the transient mass transport during alloyed crystal growth. They also provide a benchmark for the treatment of more complicated problems involving alloyed crystal growth and residual accelerations.

I. Segregation during Growth of Doped Semiconductors

For a range of practical magnetic field strengths, the characteristic velocity U_c for electromagnetically damped melt motion is never small enough to completely suppress the flow and achieve diffusion-controlled mass transport.[6] The characteristic ratio of convection to diffusion of dopant is the mass transport Péclet number $Pe_m=U_cR/D$ where R is the characteristic length for the melt and D is the diffusion coefficient for the dopant in the molten semiconductor. The convection of dopant can be due to many different melt motions including buoyant convection, thermocapillary convection, and thermoelectric effects. For a typical crystal growth process, resolution of thin

mass-diffusion boundary layers having $O(Pe_m^{-1})$ thicknesses is often very challenging because the mass transport Péclet number can have values as large as Pe_m=20,000.[7] Several grid points must be concentrated inside each layer in order to give accurate results, because these boundary layers play critical roles in the transport. As the magnetic flux density B of the externally applied magnetic field is increased, the value of Pe_m decreases and the mass-diffusion boundary layers become thicker, but the value of the Hartmann number $Ha=BR(\sigma/\mu)^{1/2}$ increases, where σ and μ are the electrical conductivity and viscosity of the melt. Since there are viscous boundary layers with $O(Ha^{-1})$ thicknesses, there are thin mass-diffusion or viscous boundary layers for every value of B. In addition, for a molten semiconductor, the thermal diffusivity α is 100 times larger than the kinematic viscosity ν and 1000 times larger than the mass diffusion coefficient D, so that the characteristic time for diffusion of mass is 1000 times the characteristic time for diffusion of heat and 10 times the characteristic time for diffusion of momentum. Therefore the simultaneous numerical time integration of the full Navier-Stokes, internal energy and species transport equations must always have a very fine spatial grid and a very small time step. Kaiser and Benz[8] stated that the hardware requirements and needed supercomputing time for accurate resolution of concentration and velocity gradients are impractical. Motakef[9] stated that asymptotic methods give solutions which retain the physics of the problem and have the following characteristics: (i) their solutions have patterns and parametric dependencies which can be easily detected, and (ii) their solutions can be simulated rapidly with minimal computational resources. Using asymptotic models, we have provided the first predictions of the dopant distribution in an entire crystal for any combination of process variables.[1,2,3,6,7] Thus, our models can be used to systematically determine optimal electromagnetic control systems. Solutions of the full equations will also be needed for more accurate predictions for these optimal systems.

In a pair of studies,[1,2] we treated the mass transport of a dopant silicon in a germanium melt in a terrestrial vertical Bridgman ampoule with a uniform, steady, axial magnetic field. The balance of the convective to the diffusive dopant transport in the melt depends on the process parameters, namely the magnetic flux density, the growth rate U_g and the aspect ratio a. Here, a is the ratio of the ampoule's length to the ampoule's inner radius. The unsteady convective mass transport depends on the melt motion. For a melt motion caused by thermally-driven buoyant convection, the thermal gradients are concentrated in a region of the melt near the crystal-melt interface because this region of the ampoule is adjacent to the furnace's thermal-gradient zone. The hot fluid adjacent to the ampoule wall rises and flows vertically upward, turns at the top of the ampoule, sinks along the centerline of the ampoule, and flows radially outward adjacent to the crystal-melt interface. A rigorous asymptotic analysis reveals that the vertically upward flow in a parallel layer adjacent to the ampoule is $O(Ha^{1/2})$ compared with the O(1) flow in the rest of the melt. When the electrically-conducting melt flows radially across the vertical magnetic field, it generates an induced electric field which drives an azimuthal electric current. This electric current flows across the magnetic field, creating an electromagnetic body force which opposes the radial velocity. There is no electromagnetic body force opposing flow along magnetic field lines. Therefore, the electromagnetic body force damps the flow that crosses magnetic field lines and elongates the flow along magnetic field lines, so that there is buoyant convection in the entire melt as shown in Figure 1 for B=0.4 T and a=2.

Before solidification begins, the dopant concentration is uniform, and this initial value is used to normalize the concentration C, so that this initial melt concentration is C(r,z,t)=1 at t=0 everywhere. Here, r and z are the radial and axial coordinates normalized by R, and t is time normal-

ized by R/U_c. Once crystal growth begins, the crystal absorbs much of the silicon during solidification, leaving a dopant-depleted region near the crystal-melt interface. The melt motion convects the low dopant concentration into the rest of the melt. We assumed that the dopant concentrations were small, so that the dilute approximation was appropriate, *i.e.* we assumed that the density had no effect on the buoyant convection. At each time, the dopant distribution in the crystal C_s, normalized by the initial uniform dopant concentration in the melt, was given by a product of the segregation coefficient k_s and the concentration of the melt at the crystal-melt interface, where k_s=4.2 for germanium doped with silicon. We assumed that there was no diffusion of dopant in the solid crystal.

The constant-concentration contours for the crystal with B=0.4 T, U_g=23 μm/s and a=2 are presented in Figure 2. Here, U_c=1204 μm/s for magnetically damped buoyant convection, Ha=132.7 and Pe_m=451.5. For the first-grown part of the crystal near z=-2, as r increases from 0 to 1, C_s is first relatively uniform, then increases to a maximum at some $r=r_o$, and finally decreases to a value

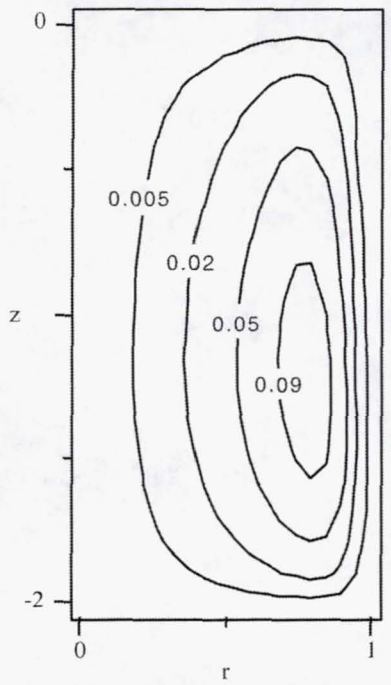

Figure 1. Streamlines for a typical Bridgman ampoule with B=0.4 T and a=2.

below the C_s at r=0. As r increases from 0 to 1, (a) the value of v_z near the crystal-melt interface is negative and increases in magnitude until roughly $r=r_o$, (b) then v_z increases rapidly from this minimum to a large positive value, corresponding to the upward flow inside the $O(Ha^{-1/2})$ thickness parallel layer at r=1, and (c) finally v_z decreases to zero at r=1. Here, $\mathbf{v}=v_r\hat{\mathbf{r}}+v_z\hat{\mathbf{z}}$ is the melt velocity normalized by U_c. For $0<r<r_o$, the downward buoyant convection augments the upward motion of the crystal-melt interface, so that there is strong convection of melt with C=1 toward the interface. Since v_z has its largest negative value near $r=r_o$, the convection of dopant toward the interface is strongest here, explaining the humps in the C_s=1.98 and C_s=1.85 contours in Figure 2. For $r>r_o$, v_z has a large positive value, so that the buoyant convection and crystal-melt interface motion partially cancel, producing much smaller local melt motion relative to the interface. Thus the local melt does not receive more dopant by convection, and the local value of C decreases quickly as the crystal absorbs most of the local dopant.

For the later-grown parts of the crystal, C_s is much more radially uniform for $r<r_o$, with much lower values for $r>r_o$. The strong downward buoyant convection near $r=r_o$, which previously convected C=1 toward the interface, now convects dopant-depleted melt which has circulated from the crystal-melt interface to the top and back to the interface. The slower moving fluid near r=0 has a much higher concentration because it left the mass-diffusion boundary layer adjacent to the crystal-melt interface at a much earlier time before the dopant was so depleted. For the C_s=0.4 contour in Figure 2, C_s actually decreases as r increases from 0 to r_o, because the stronger downward flow near $r=r_o$ is carrying very little dopant while the slower moving melt near r=0 retains a higher concentration. This dependence of the crystal concentration on the lengths of time for different parts of the melt to circulate from the interface layer to the ampoule top and back to the interface layer illustrates that the mass transport problem is intrinsically unsteady and the melt concentration is far from well mixed.

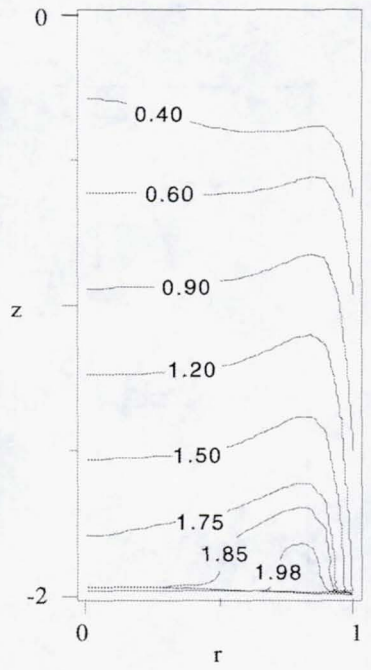

Figure 2. Contours of the crystal's concentration $C_s(r,z)$ for B=0.4 T, U_g=23 μm/s and a=2.

Dopant distributions for several different combinations of process parameters, namely different values of B_o, U_g and a, have been investigated.[1,2] Convective mass transport dominates over diffusive mass transport for moderate magnetic field strengths. Since the convection of dopant-rich melt toward the growth interface is non-uniform and there is convection of dopant-depleted melt away from the interface near the periphery, there is radial macrosegregation. For strong magnetic fields, the electromagnetic damping suppresses the convection, so that diffusive mass transport dominates, and the crystal composition is relatively radially uniform, except near r=1 where the large axial velocity inside the parallel layer still convects the dopant-depleted melt away from the interface. As the growth rate is decreased with constant field strength, the melt motion makes more complete circuits during the longer time to grow a crystal, so that the dopant distribution approaches the well-mixed limit. For fixed values of B and U_g and for two different values of a, the composition of the dopant in the two crystals were simply scaled accordingly in the axial dimension.

The dopant concentration in the melt is non-uniform at each stage during growth, and the dopant transport is intrinsically unsteady for magnetic fields which are strong enough to eliminate oscilla-

tory melt motions, but which are not strong enough to achieve diffusion-controlled mass transport. During crystal growth without a magnetic field, the mixing may produce a dopant composition in the crystal that is close to the well-mixed limit. When a magnetic field is applied to the electrically-conducting melt, the magnetic field provides electromagnetic damping of the melt motion. As the magnetic field strength is increased, the magnetic field provides stronger electromagnetic damping and the ratio of the diffusive to convective mass transport increases. Therefore, as the magnetic field strength is increased from a relatively weak magnetic field to a strong magnetic field, the axial variation of the radially-averaged crystal composition should transition from the well-mixed limit to the diffusion-controlled limit.

This phenomena is demonstrated in Figure 3 for a=2, where the distribution of the radially-averaged crystal composition transitions from the well-mixed limit for a weak magnetic field B=0.4 T to the diffusion-controlled limit for a strong magnetic field B=4 T. The axial variation for the diffusion-controlled limit depends on growth rate, and the results for case d with B=4 T are essentially identical to those for diffusion-controlled growth with U_g=23 μm/s. The parameter which predicts the relative position of the axial variation between the well-mixed and diffusion-controlled limits is the number of complete circuits made by the melt motion during the length of time to grow the crystal. If the melt motion makes many complete circuits during crystal growth, the dopant distribution approaches the well-mixed limit, but if the melt motion does not even complete one circuit, the dopant distribution approaches the diffusion-controlled limit. The number of complete circuits during the growth of the crystal is proportional to $U_c/U_g=\omega^{-1}$. For curve a in Figure 3, the magnetic field is weak, so that the melt motion is strong. The growth rate is slow, so that the strong melt motion makes many complete circuits during the long time needed to grow a crystal. For curve a, ω^{-1}=401.28, and the results approach the well-mixed limit. For curve b, the strength of the melt motion is the same, but U_g is larger so that the buoyant convection makes fewer complete circuits in the much shorter time to grow the entire crystal. For curves c and d, the growth rate is the same as that for curve b, but the melt motion is more damped by the strong magnetic fields, so that there are fewer complete circuits of the convection and less mixing. For curve d, ω^{-1}=0.52, and the distribution is close to the diffusion-controlled limit.

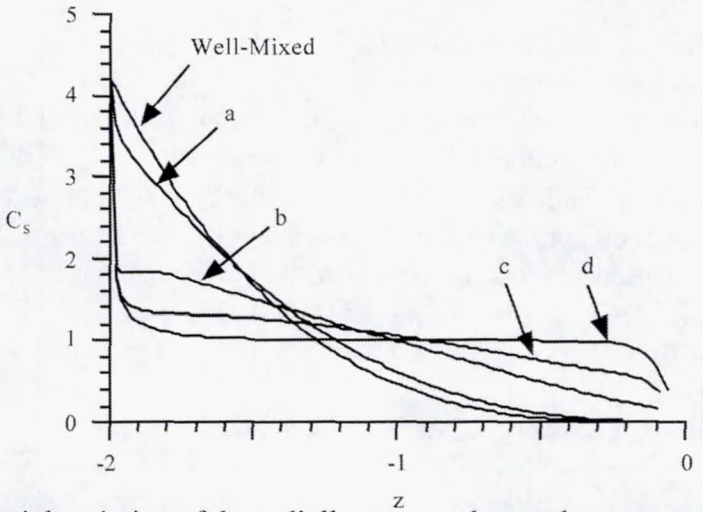

Figure 3. Axial variation of the radially-averaged crystal concentration for four cases with a=2 and the variation for the well-mixed limit. Cases: (a) U_g=3 μm/s, B=0.4 T and ω=0.002492, (b) U_g=23 μm/s, B=0.4 T and ω=0.0191, (c) U_g=23 μm/s, B=1.0 T and ω=0.1193, (d) U_g=23 μm/s, B=4.0 T and ω=1.910.

II. Segregation During Growth of Alloyed Semiconductors on Earth and in Microgravity

Experiments being conducted in the High Magnetic Field Solidification Facility at MSFC will validate our models. Experiments have shown that the radial variation between the maximum and minimum concentrations can be decreased by more than a factor of three with the application of a 5 T magnetic field.[10] In these experiments, one compositional profile indicated only a 0.04 mole fraction difference of CdTe in the radial macrosegregation of a HgCdTe crystal,[10] arising because the magnetic field retards the sinking of the heavier melt to the center of the ampoule resulting in less radial macrosegregation. Ramachandran and Watring[11] reported a reduction in the radial segregation in all of their samples which were grown in a magnetic field. Watring[12] found that radial uniformity sometimes occurred with weaker magnetic fields, so that there is an important need to accurate models in order to guide process optimization.

An initial benchmark model will treat the convection driven by compositional variations in the terrestrial vertical Bridgman process in an axial magnetic field. Once validated by comparison to terrestrial experimental results, our transient mass transport model for alloyed crystal growth can be confidently applied to crystal growth in microgravity. The effects of steady acceleration vectors at various angles to the axis of the Bridgman ampoule on the segregation in the crystal will be investigated.

REFERENCES

1. N. Ma and J. S. Walker, "A model of dopant transport during Bridgman crystal growth with magnetically damped buoyant convection," ASME *Journal of Heat Transfer*, 122 (2000) 159-164.
2. N. Ma and J. S. Walker, "A parametric study of segregation effects during vertical Bridgman crystal growth with an axial magnetic field," *Journal of Crystal Growth*, 208 (2000) 757-771.
3. J. M. Hirtz and N. Ma, "Dopant transport during semiconductor crystal growth. Axial versus transverse magnetic fields," *Journal of Crystal Growth*, 210 (2000) 554-572.
4. N. Ma, K. O. Homan and J. S. Walker, "Magnetic damping of buoyant convection during semiconductor crystal growth in microgravity. Steady transverse residual acceleration," *Physics of Fluids*, 9 (1997) 2789-2797.
5. N. Ma and J. S. Walker, "Segregation during Bridgman crystal growth in space with an axial magnetic field," *Magnetohydrodynamics*, 35 (1999) 155-159.
6. N. Ma and J. S. Walker, "Dopant transport during semiconductor crystal growth with magneti cally damped buoyant convection," *Journal of Crystal Growth*, 172 (1997) 124-135.
7. N. Ma and J. S. Walker, "Validation of strong magnetic field asymptotic models for dopant transport in semiconductor crystal growth," *Journal of Crystal Growth*, 180 (1997) 401-409.
8. Th. Kaiser and K. W. Benz, "Floating-zone growth of silicon in magnetic fields. III. Numerical simulations," *Journal of Crystal Growth*, 183 (1998) 564-572.
9. S. Motakef, "Modelling of crystal growth processes: Techniques, capabilities and limitations," AACG *Newsletter*, 27 (1998) 8-15.
10. D. A. Watring and S. L. Lehoczky, "Magneto-hydrodynamic damping of convection during vertical Bridgman-Stockbarger growth of HgCdTe," *Journal of Crystal Growth*, 167 (1996) 478-487.
11. N. Ramachandran and D. A. Watring, "Convection damping by an axial magnetic field during the growth of HgCdTe by vertical Bridgman method – Thermal effects," AIAA paper #97-0450, 35th AIAA Aerospace Sciences Meeting and Exhibit, Reno, NV (1997).
12. D. A. Watring, "Effects of static axial magnetic fields on directional solidification of HgCdTe," Ph.D. Dissertation, Massachusetts Institute of Technology (1997).

CARBON NANOTUBES GROWTH AND CONTAINER-LESS DIRECTIONAL CRYSTALLIZATION (CDC) IN MICROGRAVITY FOR ELECTROMECHANICAL ACTUATION APPLICATIONS

A.A. Zakhidov[1 *], I.I. Khayrullin[1,2], R. Morris[3], A. MacKnight[1], R.H. Baughman[2]
V. Rakov[4], A. Kartavykh[4], V. Ufimtsev[4], O. Jouravlev[4,5]

[1]Honeywell Technology Center, Honeywell International, Morristown, NJ 07960
[2]New Jersey Institute of Technology, University Heights, Newark, USA
[3]Morris Research, Flanders, NJ, USA
[4]Institute of Chemical Problems of Microelectronics, Moscow, Russia
[5]RF Research, Lindenhurst, New York, USA

We have demonstrated a new type of electromechanical actuator, which is based on both a new type of actuator material (single-wall carbon nanotubes) and a new type of actuation mechanism (double-layer charge injection). Like natural muscles, the macroscopic actuators are assemblies of billions of individual nanoscale actuators [1]. Higher stress generation capabilities than natural muscles and higher strains than high modulus ceramics were obtained in investigations of both all-solid-state and liquid-electrolyte-based devices. Analysis of experimental results suggest that these actuators have the potential of providing order of magnitude advantages over prior-art technologies in work per cycle and stress generation. Also, they operate at very low voltages and high temperatures. However, realization of these expected advantages of carbon nanotube actuators has been frustrated by materials limitations that restrict the mechanical properties of carbon nanotube sheets.

Key issues are the development of methods for the synthesis of extra long and impurity-free nanotubes that have low defect concentrations, the separation of these nanotubes into metallic and semiconducting tubes, and the assembly of these nanotubes into strong, high-surface-area structures in which the nanotubes are largely unbundled. First, two tasks can be solved in a microgravity synthesis, when CNT are levitating in a reaction zone and have a chance to grow longer than the conventional synthetic conditions. The program being initiated will focus on improving nanotube synthesis in arc-discharge chamber and processing by mimicking some of the advantages of microgravity processing. The talk will describe the present status of nanotube actuator development, and the strategies being pursued to improve the quality of carbon nanotubes and carbon nanotube sheets.

In the first part, we describe the measurements of actuation in conventional bundled CNTs which are mixtures of metallic and semiconducting tubes, and particularly demonstrate the viscoelastic properties of bundled CNTs, which are due to inter-bundle and intra-bundle displacements of single tubes. In the second part, we describe a design of the arc-discharge chamber which simulates the microgravity conditions, by a rotating-wheel carbon electrode. The electrical and mag-

* Corresponding author

netic fields are imposed over the collector of the chamber with the aim to selectively separate metallic tubes from semiconducting ones.

A new method - Containerless Directional Crystallization (CDC) - is also proposed for crystal growth under reduced gravity conditions. This method combines the advantages of both the Bridgman and the floating zone techniques. Such combination results in configuration of the melt which is confined in a cylindrical container, thereby avoiding any contacts between the melt and lateral container walls. This permits control over the melt zone geometry. The free melt surface is attached to the growing crystal and is pinned to the edge formed by the end of the cylinder and lateral walls. To successfully implement the technique for two-component advanced semiconductors such as GaSb, it is necessary to predetermine the size and shape of the stable volume of the melt that can be achieved in practice. This has forced us to implement a mathematical simulation approach.

We worked in the following directions for the limiting case of negligible gravity: (i) analyzing the shape and stability of the free surface of an isothermal melt volume in the above configuration, (ii) defining the range of system parameters for which stable melt configurations can be obtained and the method that can be realized in practice; (iii) evaluating literature data on the wetting angle values of semiconductor melts to the solid seed and to various substances that can be used in experimental ampoule design and as the edge endplate material opposite to the seed. The results of computer modeling and simulations will be presented for the simplest case of single component crystals Ge, and the strategies for two-component systems, like GaSb will be analyzed.

The advantages of the CDC method over the standard floating zone method [2] are discussed in terms of better control over the melt volume and shape and improved heat transfer properties due to the proximity of the melt crystal to the ampoule wall. CDC will allow creation of a new type of advanced composites of CNT with semiconductors at the synthetic stage, which should be specially favorable for some applications, including actuators and thermoelectrics.

REFERENCES

1. Ray Baughman, *et. al.*, *Science,* 284 (1999) 1380.
2. A.V. Kartavykh*, E. S. Kopeliovich, M. G. Mil'vidskii and V.V. Rakov, *Microgravity Sci, Technol.* XII/1 (1999) 16.

NOVEL MICROSTRUCTURES FOR POLYMER-LIQUID CRYSTAL COMPOSITE MATERIALS

Jules J. Magda[1], Grant D. Smith[1], Matthew A. Glaser[2], Noel A. Clark[2], Christopher Bowman[2], Leo Radzihovsky[2]

[1]University of Utah
[2]University of Colorado-Boulder

ABSTRACT

Key to understanding and optimizing the structure of polymer/liquid crystal composites and to developing novel electro-optic applications of these materials is control over the liquid crystal interface. Two molecular-based computer simulation models are being used in tandem to improve scientific understanding of the liquid crystal interface, and to predict the effects of changes in the chemical structure of the liquid crystal molecule.

I. Methods

Molecular dynamics is a computer-based method by which the macroscopic properties of a material can be rigorously obtained, provided that the correct intermolecular and intramolecular potentials are known [1]. Intermolecular and intramolecular potential functions can either be chosen empirically, or by using the methods of quantum mechanics [2]. Potential functions are now sufficiently well-developed that molecular dynamics can be used to accurately predict the bulk and interfacial properties of materials that are isotropic at rest [1,3], and perhaps even the bulk properties of simple liquid crystals. However, little is known about the molecular behavior of liquid crystals at interfaces. For example, one would like to know the orientation of a given liquid crystal molecule at a free surface and the associated surface tension, information which is readily obtained using molecular dynamics, provided that the appropriate potential function (*i.e.*, molecular model) is known. Toward this end we are developing idealized liquid crystal models which capture the general features of liquid crystals at minimal computational expense, and atomistic molecular models for simulating liquid crystals of specific chemical structure. Probably the most important general feature of liquid crystals is molecular shape – liquid crystals are composed of disc or lath-shaped molecules, often with "floppy" tails [4]. This is captured at minimal computational expense using bead-spring models [5-6]. By varying the number of beads and freezing out certain degrees of freedom, idealized liquid crystals of any shape or aspect ratio can be obtained. At the same time, atomistic models of specific, novel liquid crystals are being developed and tested in molecular dynamic simulations of bulk material, far from any interface [7]. Simulations of interfaces using atomistic models are computationally intensive. Hence, once the correct atomistic model is known, an idealized bead-spring model will be developed to mimic it. This idealized model can then be used to predict interfacial properties of specific liquid crystal chemical structures at a fraction of the computational expense.

Award Dates: May 2000 – May 2004

REFERENCES

1. M.P. Allen and D.J. Tildesley, Computer Simulation of Liquids (Oxford University Press, New York, 1989).
2. G.D. Smith, O. Borodin, M. Pekny, B. Annis, D. Londono, and R.L. Jaffe, *Spectrochimica Acta A* 53,1273 (1997).
3. D.Y. Yoon, M. Vacatello, and G.D. Smith in Monte Carlo and Molecular Dynamics Simulations in Polymer Science, K. Binder, ed. (Oxford University Press, New York, 1995).
4. P.J. Collings, Liquid Crystals: Nature's Delicate Phase (Oxford University Press, New York, 1990).
5. P.E. Rouse, Jr. *J. Chemical Physics* 21, 1272 (1953).
6. W. Tschop, K. Kremer, J. Batoulis, T. Burger, and O. Hahn, *Acta Polym.* 49, 61 (1998).
7. M.A. Glaser in Advances in the Computer Simulation of Liquid Crystals, C. Zannoni and P. Pasini, eds (Kluwer, Dordrecht, 1999).

CO_2 ACQUISITION MEMBRANE (CAM) PROJECT

L.W. Mason[1] *, J.D. Way[2], and M. Vlasse[3]

[1]Lockheed Martin Space Systems Company
[2]Colorado School of Mines
[3]NASA Marshall Space Flight Center

OBJECTIVE

The CO_2 Acquisition Membrane (CAM) project will develop, test, and analyze membrane materials for separation and purification of carbon dioxide (CO_2) from mixtures of gases, such as those found in the Martian atmosphere. The CAM technology will enable passive separation of these gases, allow energy efficient acquisition and purification of these important resources, and lay the foundation for future unmanned sample return and human space missions. The CAM membranes are targeted toward *In Situ Resource Utilization* (ISRU) applications, such as *In Situ Propellant Production* (ISPP) and *In Situ Consumables Production* (ISCP).

I. Planned Activities

CAM is a ground-based project that is cooperative among three institutions: Lockheed Martin (LM), the Colorado School of Mines (CSM), and Marshall Space Flight Center (MSFC). Each of these institutions plays an important role in the development of these new materials. CSM will design, model, and fabricate a series of membranes; LM will test the membranes to measure the gas separation performance under simulated Mars and other conditions, and MSFC will perform materials characterization analyses to determine lattice parameters and dimensional structures.

In microporous materials, such as zeolite and carbon molecular sieves, the pore size approaches the size of the molecules being separated. Due to the close proximity of the pore wall, non-bond interactions between the penetrant molecule and the pore wall become important. Under these conditions, very selective separations can be attained from interactions among several different transport mechanisms, including surface diffusion and size discrimination. Both of these mechanisms may be utilized in the separation of CO_2 from N_2 for ISRU applications on Mars. Since CO_2 is both smaller (kinetic diameter of 0.33 nm) and more strongly adsorbing than the larger N_2 molecule (0.364 nm), a microporous inorganic membrane is ideal for the separation of CO_2. Additionally, zeolite membranes may be used to separate molecules by molecular size using a molecular sieve-like mechanism. Zeolites are aluminosilicates with a well-defined, crystalline structure. The pore openings in the crystal are on the order of molecular dimensions (typically 3 to 7 Å), a size through which small molecules may pass, but bulky or high molecular weight molecules will not. For over thirty years researchers have been attempting to develop crack free zeolite membranes, and the scientific literature lists very few successful fabrication and test activities.

* Corresponding author

Recently, however, several researchers have independently formed defect-free zeolite membranes. For example, ongoing projects at CSM have formed selective silicalite films on porous stainless steel supports. Using this technology and other methods, a variety of candidate membranes will be identified, designed, modeled, and fabricated for the CAM project.

Once the candidate membrane types have been identified and fabricated, experiments will be conducted to characterize the separation performance under simulated Martian conditions using the Membrane Test Facility (MTF) at LM. The MTF is designed to produce a wide range of temperature and pressure conditions, and control the gas composition to simulate the Mars atmosphere. A membrane characterization experiment will consist of sealing the membrane sample in place within the MTF, and subjecting the sample to a wide range of conditions while measuring the trans-membrane pressure, gas flow rate, and composition of gas that passes through the membrane. In addition to performance tests, the thin-film membrane samples will also be analyzed using a variety of materials characterization techniques that are available through the Microgravity Science and Applications Department (MSAD) of NASA/MSFC. The analyses will include: (1) x-ray microscopy to view sequential steps in the fabrication process at various temperatures, allowing the crystalline pore size distribution to be determined as a function of temperature, (2) microprobe analyzer for quantitative analysis of the elemental composition, (3) x-ray diffraction analysis to determine lattice dimensions and measure surface variability, and (4) scanning electron microscopy to image the grains present in the thin film, and measure the size, orientation, distribution, and morphology of the crystals.

The data from these experiments and characterization activities will be analyzed to determine how well the membranes separate CO_2 from other atmospheric gases, define the conditions for optimal separation, and elucidate the relative merits of heating the membrane or compressing Mars atmosphere prior to separation. Additionally, the materials characterization results will be correlated with measured separation performance to reconcile the data, establish the relative contribution of different transport mechanisms, and optimize fabrication variables.

II. Requirement for Microgravity

There is no requirement for microgravity. The CO_2 Acquisition Membrane project is a ground-based program geared toward development of materials for use with ISRU systems.

III. Significant Results

The development of thin-film membrane materials for passive separation of CO_2 from other gases will have significant impact on the design and implementation of ISRU systems that utilize CO_2 on Mars. In addition, the results from the CAM activities will allow factors to be determined to scale ISRU processes for use in various Mars missions and scenarios. The gas separation is essentially passive, requiring only that atmosphere gases pass through the membrane to either purify CO_2 for ISRU processes, or nitrogen and argon buffer gases for ISCP applications. Alternative techniques to separate buffer gases primarily use bulk adsorption to selectively bind CO_2. While these processes have shown successful operation, the large mass of the sorbent bed, many times the mass of the separated gas, restricts the applicability. These systems require large swings in thermal energy to cycle the temperature, significant power, and the use of large, massive radiators. The simplicity of a passive thin film to perform the same function with no power is quite attractive.

DIFFUSION PROCESSES IN MOLTEN SEMICONDUCTORS

D.H. Matthiesen*, M.L. Kaforey, and L.A. Keefer

402 White Building, Case Western Reserve University
10900 Euclid Avenue, Cleveland, OH 44106
(216) 368-1366 voice, (216) 368-3209 FAX
DHM5@po.cwru.edu E-mail

SCIENCE OBJECTIVES

The DPIMS project has concentrated on Phase I, which flew on the MSL-1R (STS-94) spacelab mission in June, 1997. The Phase I objectives are to provide purely diffusive experimental measurements of the isothermal diffusion coefficients of Ga, Sb and Ga/Si dopants in molten germanium with sufficient accuracy and precision to:

a) Differentiate between model predictions of the temperature dependence.
b) Determine the effect of dopant size and type.
c) Determine if a "wall effect" is present.
d) Provide input to continuum and atomistic model development.
e) Provide a preliminary evaluation of dopant-dopant interactions.

Another objective is to develop a 2-dimensional, fully time dependent continuum numerical model of the germanium diffusion column, shear cell, cartridge and furnace for both earth-based and space-based experiments which accurately predicts the measured concentration profile as a function of distance in the diffusion column.

A final objective is to develop atomistic models which accurately predict:

a) The purely diffusive isothermal diffusion coefficient of a dopant in a molten semiconductor
b) The temperature dependence of the dopants in molten semiconductors, and which
c) Attempts to explain the "wall effect"
d) Develops new empirical potentials useful for predicting other diffusion and transport properties for other molten semiconductor systems.

I. Justification of the Need for Space Environment

Convection in the melt and convection during the solidification process, both of which typically confound data interpretation, hamper terrestrial experiments designed to measure diffusion coefficients in the liquid state. This has resulted in wide variations in the few reported data in the literature. Arnold and Matthiesen [1] have predicted, based on numerical simulations, that for the Ga-doped Ge system, convection effects increase the measured diffusion coefficient for capillaries even as small as 2 mm in diameter. The experimental data, combined with the numerical simulations of convective effects, predict a nonexistent range of capillary diameters that allow the mea-

surement of the actual diffusion coefficient on Earth. As a result, the microgravity environment, in which convective effects are minimized, is required.

II. Program Description

This program of study is directed at the fundamental and applied issues pertaining to diffusion of species in the liquid state as driven by convection gradients (Fickian diffusion) and thermal gradients (Soret diffusion). The fundamental materials systems of interest for the near term study are the dilute binary systems of gallium (Ga), antimony (Sb), and a dilute ternary system of gallium and silicon (Si) in germanium (Ge). Systems of commercial interest for future study include the binary systems of germanium and silicon. This research program consists of three major components: an experimental measurement portion, a continuum numerical simulation portion and an atomistic numerical simulation portion.

The experimental measurement portion is designed to provide definitive measurements of the purely diffusive component of mass transfer in molten semiconductor systems. A shear cell technique will be used to directly measure the diffusion coefficients in semiconductor melts. For the Fickian diffusion case, isothermal measurements will be used to determine the diffusion coefficients on temperature, dopant type and column diameter. For the Soret diffusion case, measurements will be made in a thermal gradient.

III. Program Significance

The fundamental mechanisms of mass diffusion in the liquid state are still unclear to the degree necessary for the prediction of diffusion of one species into another or even within itself. This observation is especially true with respect to the dependency of diffusion mechanisms on temperature and on concentration levels, as well as, on the dopant type. Present estimates of the diffusivity in molten semiconductors can typically provide an order of magnitude estimate only, without any information on their dependency on concentration levels and types, and on temperature and temperature gradients.

The availability of these data is of paramount importance for practical reasons as well. The relevancy of numerical modeling for the analysis and design of ground-based and space-based experiments is directly dependent upon the accuracy of the fundamental material properties used in simulations. These data are also important for the correct characterization and interpretation of experimental results from ground-based and space-based experiments.

The need for precise measurements of the diffusion coefficients in molten semiconductors has been repeatedly pointed out. These data are required both to interpret the experimental results from previous space-based (and Earth-based) experiments and also to optimize newly envisioned experiments. Difficulties in experimental techniques and theoretical interpretations are cited for the lack of these data. This is a comprehensive program which addresses both of these issues.

IV. Program Results for Reporting Period

A. Characterization of Samples

In anticipation of analyzing the MSL-1R flight results, an extensive effort has been underway to extend the number of independent characterization techniques to insure the reliability of the measured data. Previously the Inductively Coupled Plasma-Atomic Emission Spectroscopy (ICP-AES) technique was used exclusively and a complimentary technique was sought to verify the ICP-AES measurements.

A statistically designed round robin set of experiments has been underway to compare the following characterization techniques:

1) Inductively Coupled Plasma-Atomic Emission Spectroscopy (ICP-AES)
2) Inductively Coupled Plasma-Mass Spectrometry (ICP-MS)
3) Graphite Furnace-Atomic Absorption Spectroscopy (GF-AA)
4) Neutron Activation Analysis (NAA)

Initially, these techniques will be compared to singly-doped single crystalline samples of germanium, which have previously had Hall effect measurements conducted to determine their doping type and level. In this report, the results from the NAA study will be reported.

B. Neutron Activation Analyis (NAA) Characterization

In the Neutron Activation Analysis technique, [2, 3, 4] an unknown sample is place in a known neutron flux for a known amount of time. After a sufficiently long waiting period, the gamma ray emission of the sample is then measured as the activity of the sample. The S.I. unit of activity is 1 disintegration/second, or 1 Becquerel (Bq). There is an older unit of activity in common use that measures 3.7×10^{10} disintegration/second, or 1 Curie (Ci), which is about the activity of 1 gram of radium. Both units are usually normalized by the mass of the samples. The units of activity reported here are in nano-Curie per gram (nCi/g).

In theory, if the neutron flux is precisely known, the identity and amount of an unknown sample can be determined. However, in practice this is usually not the case and external standards are used. The consequence of this statement is that for every 'run,' or set of samples irradiated, chemical standards at several levels must also be irradiated. Thus, a methodology had to be developed that allowed for the fabrication of large numbers of chemical standards at multiple levels.

One very large advantage of the NAA technique, is that it is a nuclear technique. Thus, the chemical bonding of the standards did not have to be the same as the intended unknowns. This allowed oxide powders to be used for the chemical standards. Also, in theory, since the amount of activity is directly proportional to the amount of material, there should exist a linear relationship across the entire composition range. Thus, only one composition is needed if this relationship holds true.

NAA will not work for all of the dopants that were used in this study. Germanium can decay to form gallium and silicon has no gamma ray emitters when activated. Thus, the reported results are for antimony (Sb)-doped germanium only.

C. Development of Chemical Standards

Powders of GeO_2 and Sb_2O_3 were obtained [5] and their particle sizes were characterized using a sieve stack. The average particle size of 100-120 microns was determined to be too large for the anticipated mixtures to be made. Thus, a sample of each of the original powders was ball milled in a polyethylene container using polyethylene-coated balls. A 10 gram sample of each powder, which was measured to be < 325 mesh (< 20 micron) particle size, was divided up into one hundred 0.1 gram samples. These samples represented the pure GeO_2 and pure Sb_2O_3 materials.

The appropriate amount of powders were weighed out and balled milled to achieve a uniform mixture of one hundred 0.1 gram samples for each level of concentration. This was done for concentration levels at 10, 1.0, 0.1, 0.01, 0.001, and 0.0001 mol % Sb. To convert mol % Sb to the units of at/cm^3, multiply the mol % Sb by $4.4x10^{20}$ thus, these concentrations range from $4.4x10^{21}$ to $4.4x10^{16}$at/cm^3.

Test samples were also fabricated from Czochralski grown Sb-doped Ge single crystals. Segregation analysis was conducted on these crystals, assuming complete mixing behavior. These predictions were verified using Hall effect measurements on adjacent wafers to those used for NAA measurements.

The chemical standards and the test samples were sent to the Nuclear Reactor Laboratory at the Ohio State University, which operates a 500 kW open pool research reactor. They were typically irradiated for 2 hours at a power of 350 kW. This generated an average thermal neutron flux of $1.05x10^{13}$ ncm^{-2}s^{-1}. The samples were allowed to decay for 1 to 3 weeks and then their activity was counted, using a Ge (Li) detector, for 8 to 24 hours depending on their activity level.

The results from all the chemical standards are shown in Figure 1, where the activity of the sample is plotted against the concentration level of the mixed powder samples. This data appears to have a sigmoid behavior instead of the expected linear behavior. A statistical analysis of the data, revealed that a natural log transformation yielded a uniform error structure, as shown in Figure 2.

It appears in Figure 2, that at the extremes of the data, both at the high end and especially at the low end, that the data 'tail' off from the expected linear behavior. At the high end, this maybe due to self-shielding of the large number of activated nuclei and the detector. At the low end, it is currently believed that the Puratronic grade GeO_2 material is contaminated with antimony. This grade material is only certified to a 1-ppm level, which is approximately $1x10^{16}$ at./cm^3 as seen in Figure 2. Testing with the ICP-MS technique will be used to further investigate this hypothesis.

Using the range of data from 1 to 0.0001 mol % Sb, a calibration curve was developed and is shown in Figure 3. Statistically pooling the data from all the concentration levels yields 95% certainty confidence bounds on the regression fit of the means. These are shown as dashed lines in Figure 3.

Figure 4 shows the results of the test samples as compared to their previously measured Hall effect results. As can be seen, the agreement is excellent and indicates that NAA can be used for this type of analysis.

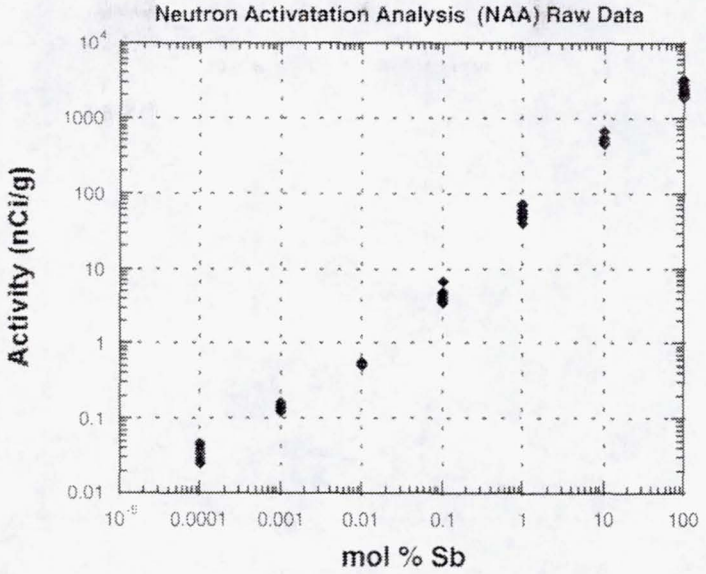

Figure 1. Plot of the raw activity, in nCi/g, for the Neutron Activation Analysis (NAA) of Sb_2O_3+GeO_2 mixtures containing a predetermined mol % of Sb. Each level contains six samples. The samples were irradiated for 2 hours with a thermal neutron flux of $1.05x10^{13}$ $ncm^{-2}s^{-1}$.

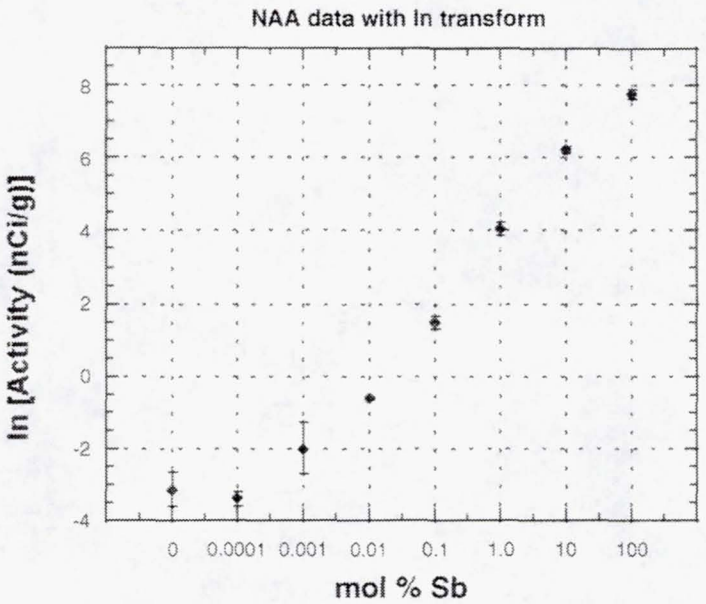

Figure 2. Plot of the transformed activity measurements verses the predetermined mol % Sb for the Sb_2O_3+GeO_2 mixtures. The natural log transformed was used to create a uniform error structure, as indicated by the error bars, for statistical analysis of this data.

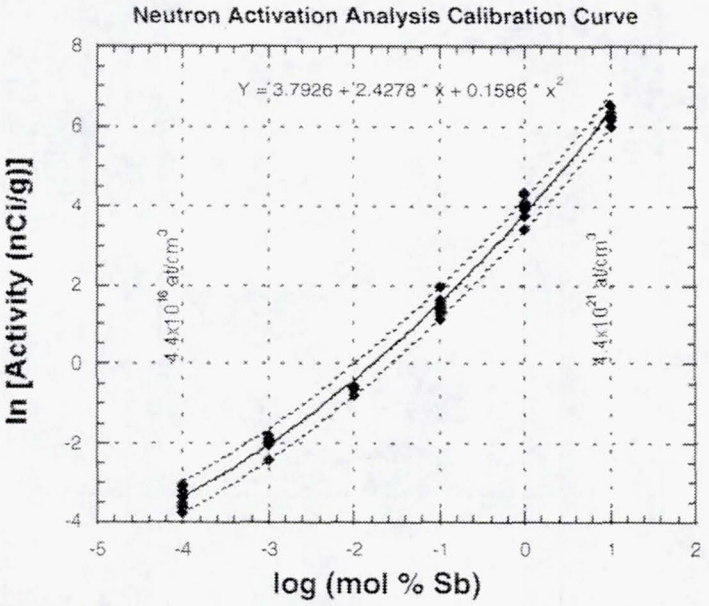

Figure 3. Calibration curve for the Neutron Activation Analysis (NAA) of predetermined mixtures of Sb_2O_3+GeO_2 samples. A 2nd order polynomial fit has been placed through the means of the data sets. The dashed lines represent 95% confidence intervals around these means. A conversion of log(mol % Sb) to at/cm^3 is indicated for comparison of units.

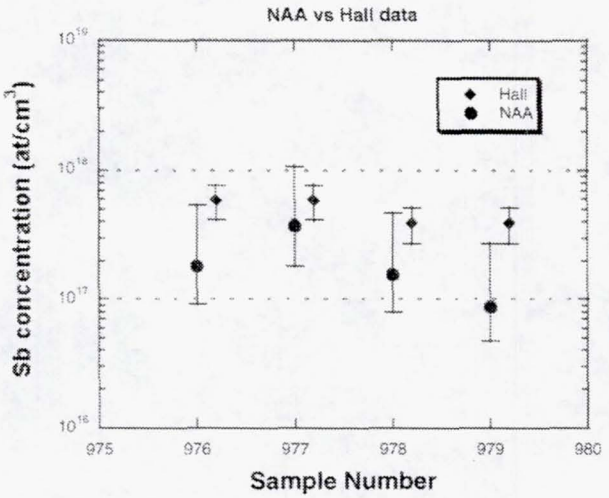

Figure 4. Predicted antimony content of Sb-doped Ge single crystal material using the activity measurements from Neutron Activation Analysis (NAA) and the calibration curve shown in Figure 3. The error bars are determined from the 95% confidence intervals. These measurements are compared with previous Hall effect measurements, which are shown with 30% error bars. The Hall effect data has been slightly offset in sample number to aid in comparison.

DEVELOPMENT OF A NEUTRON SPECTROMETER TO ASSESS BIOLOGICAL RADIATION DAMAGE BEHIND SPACECRAFT MATERIALS

R.H. Maurer[1], J.D. Kinnison[1], D.R. Roth[1], J. Miller[2],
L. Heilbronn[2], C. Zeitlin[2] and R. Singleterry[3]

[1]The Johns Hopkins University Applied Physics Laboratory
[2]Lawrence Berkeley National Laboratory
[3]NASA, Langley Research Center

Astronauts who spend months and years traveling long distances in spacecraft and working on other planets will be subjected to high energy radiation of galactic and solar origin without the protection of the Earth's thick (one writer has called it buff) atmosphere and magnetic field. The lack of natural protection will allow high energy cosmic ray particles and solar protons to crash directly into relatively thin spacecraft walls and planetary atmospheres producing energetic secondary particles in these collisions.

A substantial fraction of these secondaries will be neutrons that carry no electric charge and, consequently, are difficult to detect. At sea level on Earth the remaining neutrons are the result of many generations (approximately 10) of collisions, have very low energies (scientists call them thermal neutrons), and do not penetrate deeply into the human body. They do contribute to the natural background radiation seen by humans on Earth, but much of the dose is only at the surface or skin of the body.

In the International Space Station or on the surface of Mars, the secondary neutrons will be the result of only one or two generations of interaction due to the thinner (about a factor of 20 compared to the Earth's atmosphere) walls or atmosphere, have considerably more energy and penetrate deeply into the human body. In addition, neutrons are substantially moderated by hydrogenous material such as water. A significant fraction of the water exists in the astronaut's body. Therefore, the neutron can not only penetrate more deeply into the body, but also be stopped there and deposit all or most of its radiation dose in organs such as the liver, spleen, kidney, etc. We hypothesize that the risk of serious cancers will be increased for the exposed humans.

The portable, real time neutron spectrometer being developed by our team will monitor the environment inside spacecraft structures and on planetary surfaces. Activities supported by this grant will evaluate the neutron environment inside several candidate spacecraft materials at accelerator facilities. These experiments will enable engineers to choose the structure materials that minimize the production of secondary neutrons. With the information that the neutron energy spectrometer produces, scientists and doctors will be able to assess the increased risk of cancer and develop countermeasures. The instrument itself will include an alarm system to warn astronauts when high radiation fluxes are occurring so that they can seek shelter immediately.

The neutron spectrometer being developed at the Johns Hopkins Applied Physics Laboratory and School of Medicine has also been selected to fly on the Mars 2005 Lander. An engineering prototype spectrometer has been tested and calibrated with mono-energetic neutron beams at Columbia University. Detection efficiencies of 5% or more have been demonstrated in the 1-20 MeV neutron energy range. This prototype unit is flying at high altitudes in fighter aircraft out of NASA Dryden to verify its operating capability and obtain some atmospheric neutron data similar to the spectra to be experienced in the International Space Station or on the surface of Mars.

Our research program for this grant will have four components:

1) construction of an improved engineering model instrument dedicated to accelerator facility testing of spacecraft materials,
2) experimental characterization of the engineering model with respect to its neutron detection efficiency and ability to discriminate against charged particles including calibration of the instrument,
3) flight qualification of the engineering model,
4) measurement of neutron spectra produced by energetic proton and heavy ion beams colliding with candidate spacecraft structure and shield materials.

We will use the Loma Linda University Medical Center for proton beam testing and the Lawrence Berkeley Laboratory or Brookhaven National Laboratory for heavy ion beams to produce the collisions with the materials.

The instrument will consist of two sections. The front end section will contain the detector head and front end electronics as seen in Figure 1. Figure 2 shows the remaining instrument which consists of analog and digital pulse processing electronics. The primary purpose of the instrument is to yield the neutron spectrum produced behind shielding material due to nuclear reactions between the incident particle beam and the shielding material. This task is accomplished by recording neutron energy deposition events in a Lithium Drifted Silicon surface barrier detector (SiLi) and using a modeling approach to back out the most probable incident neutron spectrum.

The detector head will be placed behind the shielding material in an optimal position to record neutrons energy deposition events in the SiLi detector. The anti-coincidence shield allows us to discriminate charged particles events from neutron events in the SiLi detector. As an artifact of this measurement scheme it may be possible to do charged particle identification in the anti-coincidence shield which will be a scintillator. This is not a goal of the project but may be possible with a simple modification.

The remaining instrument (Figure 2) will process the analog pulses and prepare them for storage in a Multi-Channel Analyzer (MCA) which converts the analog pulse heights to digital values. A gate signal from the anti-coincidence channel will disable the first MCA when a charge particle is detected in the scintillator anti-coincidence shield. A second MCA can record the charged particle energy deposition events in the SiLi detector. The use of a second MCA to record charged particle events was not a original goal but is a simple addition that will be added in the second year of the project.

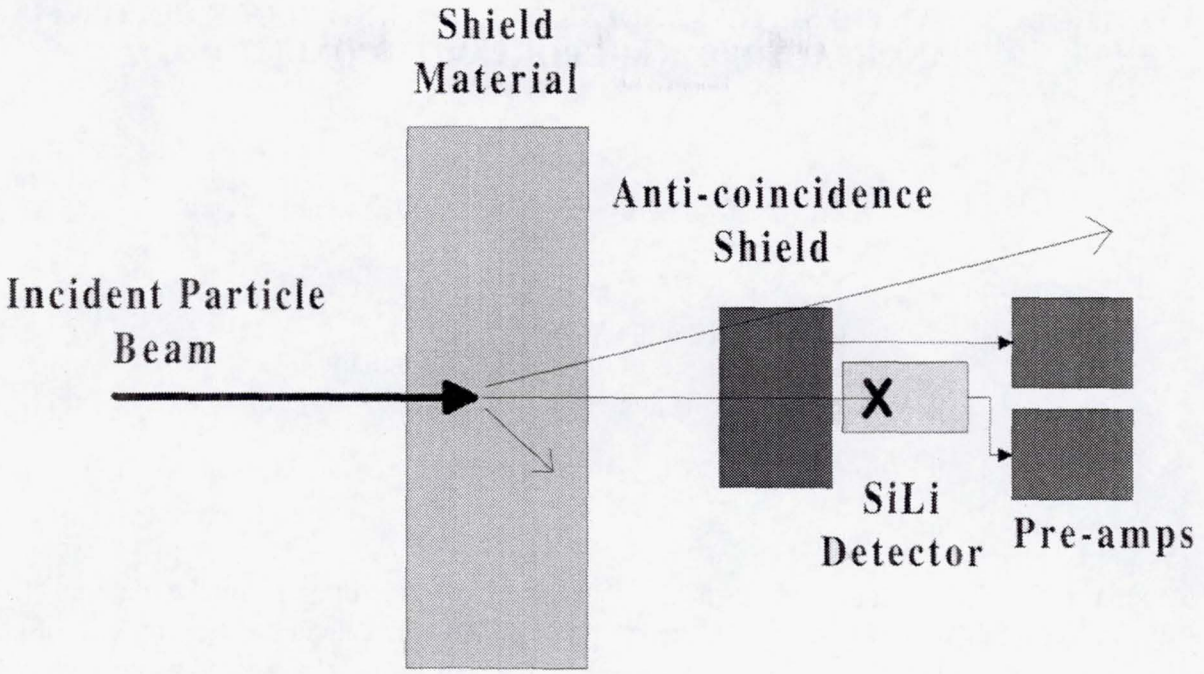

Figure 1. Detector head showing the major elements. The incident particle beam shown has a nuclear interaction in the shielding material resulting in three secondary particles. The top particle just clips the anti-coincidence shield, the middle particle (assumed a neutron) deposits energy in the SiLi detector, and the bottom recoil is absorbed in the shield material. The SiLi event is processed in the bottom pre-amp and sent to the remaining instrument for processing.

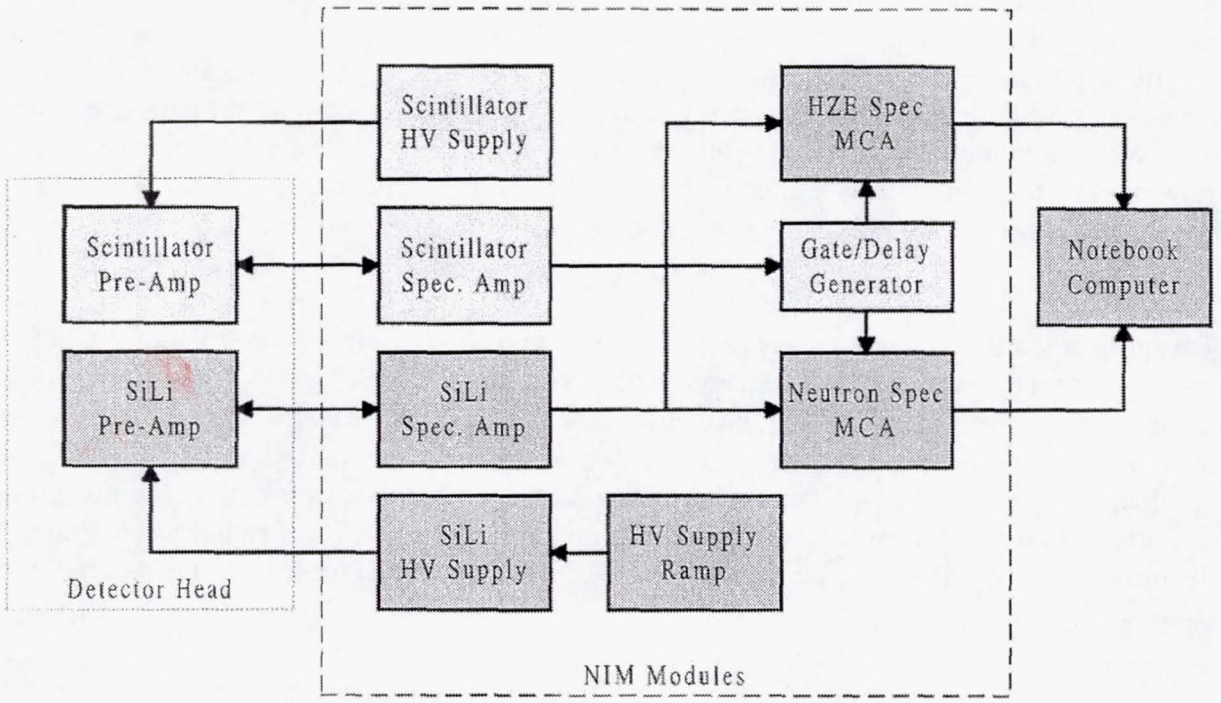

Figure 2. A block diagram of the major electronic subsystems are shown in this figure. The detector head sits in the primary beam path (detectors not shown). The NIM modules are 8 to 10 feet out of the primary beam path but still in the beam cave. The notebook computer and operator are located outside the beam cave and linked to the equipment via serial ports. The darker shaded areas indicated the SiLi detector channel while the lighter shaded areas indicate the anti-coincidence channel.

CONTROLLED SYNTHESIS OF NANOPARTICLES USING BLOCK COPOLYMERS: NANOREACTORS IN MICROGRAVITY CONDITIONS

Jimmy W. Mays*, Rigoberto Advincula, and Juan Pablo Claude

Department of Chemistry
University of Alabama at Birmingham
Birmingham, AL 35294

Nanoparticles (particles having sizes of 2-10 nm) of semiconductor and metallic materials (like CdS, ZnS, Cu2S, Au, and Co) are expected to play a significant role in the development of new microelectronic and electro-optical technologies in the near future. In order to achieve complete control over the nanoparticle's properties, as required for several important applications, it is necessary to produce samples that are as uniform in size and shape as possible. Despite much work by many research groups using different strategies for nanoparticle growth, the formation of monodisperse nanoparticles has not yet been achieved.

We are exploring strategies for nanoparticle growth within "nanoreactors" composed of various block copolymer assemblies. These assemblies include block copolymer micelles, star-block co-polymers, polymacromonomers, and bulk microphase separated block co-polymer films. The chemistries of these polymeric materials will be chosen so that one component will bind to, or react with, inorganic compounds (precursors to the semiconductors or metals), while the other component will be non-reactive and will provide stabilization. By confining particle growth to specific regions of the co-polymer vessels, control over nanoparticle size and shape may be achieved.

This project's official start date was April 11, 2000, so we have been working on this project for less than a month. A team of investigators having expertise in block co-polymer synthesis, polymer self-assembly, inorganic chemistry, and nanoparticle characterization has been assembled to conduct the various experimental tasks. A graduate student is synthesizing the initial styrene/2-vinylpyridine will block co-polymers. We have received applications from several postdoctoral candidates, and we soon hire one with prior expertise in nanoparticles. Instrumentation needed for the project will be ordered during the second week of May now that we have account numbers in hand.

* Corresponding author

EFFECTS OF TRAVELING MAGNETIC FIELD ON DYNAMICS OF SOLIDIFICATION

Dr. Konstantin Mazuruk*, Dr. Richard Grugel, Dr. Shariar Motakef

NASA Marshall Space Flight Center, Huntsville Al 35803, USA
e-mail: consty.mazuruk@msfc.nasa.gov

PROJECT OBJECTIVES

The objectives of this work are:

1) to develop theoretical and experimental fundamental features of the traveling magnetic field (TMF) technique, with the aim of identifying its benefits for microgravity research on solidification processing
2) to determine the influence of a traveling magnetic field on the following selected technologies:
   a) crystal growth of semiconductor materials by Bridgman and Float Zone techniques
   b) mixing of metal alloy melts prior to solidification

TMF is based on imposing a controlled phase-shift in a train of electromagnets, forming a stack. Thus, the induced magnetic field can be considered to be travelling along the axis of the stack. The coupling of this traveling wave with an electrically conducting fluid results in a basic flow in a form of a single axisymmetric roll. The magnitude and direction of this flow can be remotely controlled. Furthermore, it is possible to localize the effect of this force field though activating only a number of the magnets. This force field generated in the fluid can, in principle, be used to control and modify convection in the molten material. For example, it can be used to enhance convective mixing in the melt, and thereby modify the interface shape, and macrosegregation. Alternatively, it can be used to counteract thermal and/or solutal buoyancy forces. High frequency TMF can be used in containerless processing techniques, such as float zoning, to affect the very edge of the fluid so that Marangoni flow can be counter balanced.

The proposed program consists of basic fundamentals and applications. Our goal in conducting the following experiments and analyses is to establish the validity of TMF as a new tool for solidification processes. Due to its low power consumption and simplicity of design, this tool may find wide spread use in a variety of space experiments. The proposed ground based experiments are intended to establish the advantages and limitations of employing this technique.
In the fundamentals component of the proposed program, we will use theoretical tools and experiments with mercury to establish the fundamental aspects of TMF-induced convection through a detailed comparison of theoretical predictions and experimental measurements of flow field. In this work, we will conduct a detailed parametric study involving the effects of magnetic field strength, frequency, wave vector, and the fluid geometry.

*Principal Investigator

The applications component of this work will be focused on investigating the effect of TMF on the following solidification and pre-directional solidification processes:

1) Bridgman growth of Ga:Ge with the goal of counteracting the buoyancy-driven convection
2) Mixing of Pb-Ga and Pb-Sn alloys with the aim of initiating and maintaining a uniform melt prior to solidification processing
3) Float Zone growth with the aim of identifying, through simulations and model experiments, conditions needed to counteract Marangoni flow in a microgravity environment.

The proposed research has strong relevance to microgravity research and the objectives of the NRA. TMF can provide a unique and accurate mechanism for generation and control of desirable flow patterns for microgravity research. These attributes have significant relevance to 1) Alloy mixing prior to solidification in a microgravity environment. TMF can provide this mixing with a low level of power consumption. 2) TMF can offset the deleterious effects of Marangoni convection in microgravity containerless processing. Thus, TMF can be instrumental in further understanding this phenomena. 3) Generation of controlled flows will allow the investigation of the effect of these flows on growth morphology and growth kinetics. 4) On Earth, TMF has the potential to significantly counter-balance thermosolutal convection, thereby creating conditions similar to those obtained in microgravity.

Once demonstrated, this new tool for use in solidification has the strong potential to find applications in a host of microgravity material research projects.

I. Basics of Traveling Magnetic Field Technique

Externally imposed temperature and/or solutal gradients are inherent to crystal growth processes. On Earth, these gradients induce convection in the melt from which the crystal is grown. This buoyancy or solutal driven convection can degrade micro- and macroscopic homogeneity and increase the defect concentration in the grown materials. For these reasons, over the past twenty-five years or more, considerable research has been focused on controlling convection. One approach is to grow the material in a microgravity environment to reduce the primary driving force for convection. Another is to apply static magnetic fields to the electrically conductive melts to oppose convection by the induced Lorentz force. Recently, a new concept to control convection by utilizing magnetic fields that are variable in time and space has been put forward, *i.e.*, the rotational magnetic field (RMF). In electrically conducting melts enclosed in cylindrical containers RMF induces liquid motion consisting of a swirling basic flow and a meridional secondary flow. This flow has been found to be beneficial for several applications. It allows increase in crystal growth rate, and improves its homogeneity and quality [1,2]. RMF can also be used for mixing non-homogeneous melts in continuous metal castings [3]. These applied aspects have stimulated increasing research on RMF-induced fluid dynamics [10-23]. We have recently proposed yet another type of magnetic field configuration, that may find use in crystal growth techniques such as vertical Bridgman (VB), float zone (FZ), and the traveling heater method (THM) [4-9]. We termed it traveling magnetic field (TMF) as it consists of an axisymmetric magnetic wave. The frequency of this wave is sufficiently low, so that the variable in time magnetic field induces a negligible electric field in free space (no electromagnetic waves). Essentially, a controlled phase shift in a train of electromagnets induces a traveling magnetic wave. This wave, when coupled to an electrically conductive fluid, will result in a basic flow having the form of a single axisymmetric roll. The magnitude and direction of this flow can be remotely

controlled and used to control and modify convection in a molten semiconductor material. It can be used to either enhance or counteract existing convection, thereby influencing the solid/liquid interface morphology, as well as micro- and macro-segregation. TMF can be useful also in homogenizing melts prior to solidification, an especially useful feature when processing in a microgravity environment.

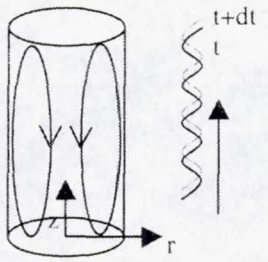

Figure 1. Schematic of TMF

Crystal growth techniques such as VB, FZ or THM utilize, as a rule, cylindrical ampoules. Mass transport is thus predominantly in the axial direction. In order to modify this process, a meridional flow can be used. Although RMF induces such a flow, it is not a basic flow but a secondary one due to nonlinear effects. Therefore, its properties are difficult to assess and its control is problematic, especially since a useful level of this flow will be close to the unstable time dependent region. Also, the direction of the meridional flow cannot be changed. It would be desirable to directly control meridional flow by a suitable body force as can be induced by TMF. This method consists of applying an axisymmetric magnetic wave along the axis of the ampoule containing the molten material. In order to accomplish this, a set of coils is wound around the ampoule. The coils are powered by ac current with predetermined phase offsets between sections. The geometry of this method is depicted in Figure1. In the low frequency approximation, the vector potential of the applied magnetic field can be expressed using a modified Bessel function as [4-9]:

$$\mathbf{A} = \mathbf{e}_{\varphi} \frac{B_0}{a} I_1(ar)\sin(\omega t - az). \tag{1}$$

Then the following set of equations in cylindrical coordinates is obtained:

$$\frac{\partial w}{\partial t} = \left[\frac{\partial^2}{\partial r^2} + \frac{1}{r}\frac{\partial}{\partial r} - \frac{1}{r^2} + \frac{\partial^2}{\partial z^2}\right]w + \frac{v_r w}{r} - \left(v_z \frac{\partial}{\partial z} + v_r \frac{\partial}{\partial r}\right)w - Ha^2 I_0^2(ar)\frac{\partial v_r}{\partial z}$$
$$+ \frac{\partial}{\partial r}\left(\left(Ha^2 v_z - \frac{Tm}{a}\right) I_1^2(ar) - Ra\theta\right) \tag{2a}$$

$$P\left(\frac{\partial \theta}{\partial t} + v_r \frac{\partial \theta}{\partial r} + v_z \frac{\partial \theta}{\partial z}\right) = \nabla^2 \theta \tag{2b}$$

Here vorticity is represented by the first equation with the second being the heat transport equation, needed later for demonstration of the effects of TMF on buoyancy convection. The equations are written in non-dimensional units (primes are dropped) and the adopted scaling is as follows: time $t = t' r_0^2/\nu$, velocity $v=v'\nu/r_0$, vorticity $w=w'\nu/r_0^2$, Rayleigh number $Ra = \frac{\beta g r_0^3 \Delta T}{\nu\kappa}$, Prandtl number $P = \frac{\nu}{\kappa}$, and Tm, Ha are defined by

$$Tm = \frac{B_0^2 \sigma \omega r_0^4}{2\rho\nu^2}, \quad Ha = \sqrt{\frac{B_0^2 \sigma r_0^2}{2\rho\nu}}.$$

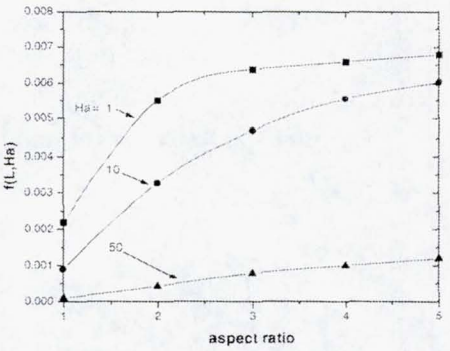

Figure 2. Plot of f as a function of aspect ratio for three values of Hartman number.

A steady state version of the set of equations (2) was numerically analyzed [7]. For small Hartmann numbers, $Ha<1$, and for small magnetic Taylor numbers, $Tm<1000$, a vector plot of the meridional flow is displayed in Figure 4 (left) and it represents a single axi-symmetric roll. With increasing Hartmann number (>10), the center of the roll is pushed towards the corner. For the linear regime (approximately $Tm<10^4$), the maximum value of the flow can be estimated as:

$$|V|_{\max} = Tm \frac{\nu}{r_0} f(L,Ha) \tag{3}$$

where $L=h/r_0$ is the aspect ratio. A plot of the function $f(L,Ha)$ is given in Figure 2. Consider, as an example, when a magnetic field of 5 gauss and 50 Hz is applied to the column of mercury having a 1cm radius and 10 cm length. Approximate values of $Ha=0.1$, $Tm=2000$, and $V_{\max}=0.2$mm/sec are obtained. Note that this is a significant velocity for crystal growth applications. Non-linearity in the transport equations (2) shows up for values of $Tm > 1000$. Essentially, it modifies the shape of the meridional roll. As Tm increases, the center of this roll drifts from the middle of the cylinder to the bottom, for the case of TMF propagating upwards. A contour plot of the stream function for the rather significant value of $Tm=10^5$ and for $Ha=1$ is displayed in Figure 3. The maximum of the stream function as a function of Tm, varies linearly for $Tm<1000$, after which a slight bowing effect is visible. Behavior then can be approximated by the power functional relation $Tm^{0.84}$.

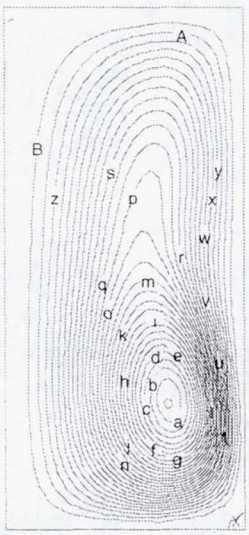

Figure 3. A contour plot of the stream function for TMF.

Now consider the possibility of reducing thermoconvective flow. The driving forces from TMF and buoyancy can be partially cancelled by appropriate selection of the Tm value. For illustration purposes,

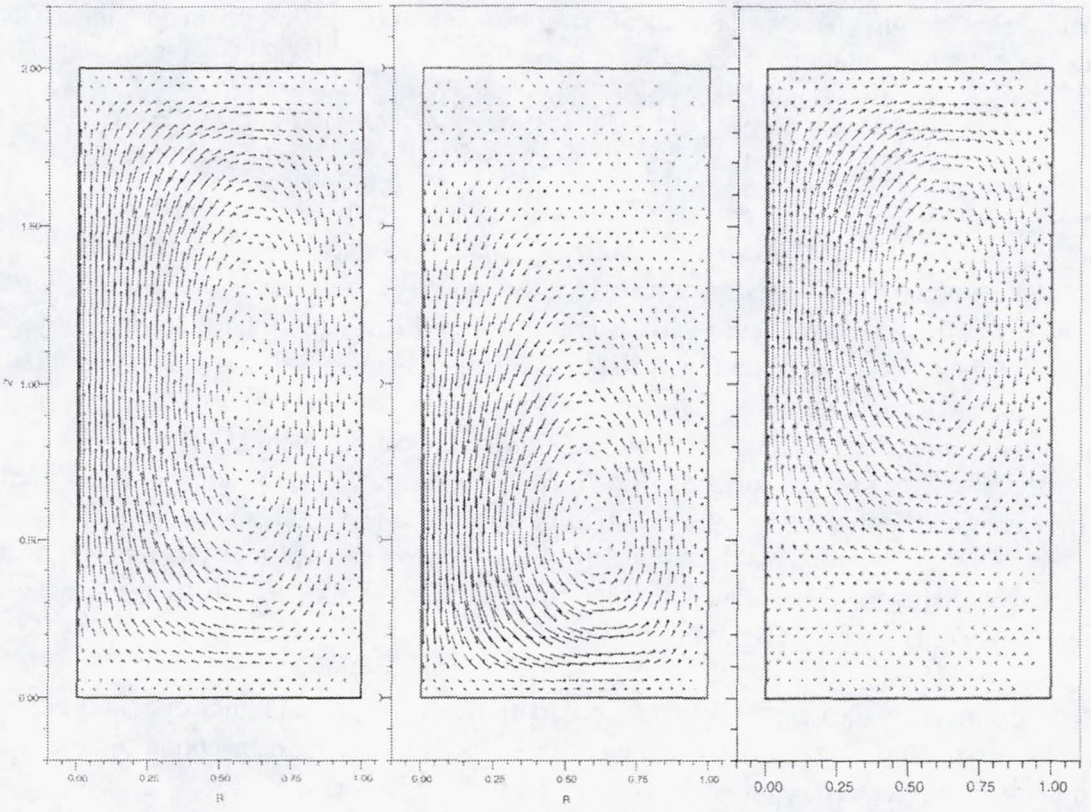

TMF Buoyancy TMF+Buoyancy

Figure 4. Flow patterns generated by a TMF, buoyancy, and a TMF and buoyancy combined.

we consider a thermal field with the following boundary conditions: linear variation of temperature along the side wall, quadratic in r at the bottom of the cylinder, and constant at the top. Without TMF, buoyancy resulting from the thermal field leads to the convective flow pattern depicted in Figure 4 (center) (*Ra*=10, *P*=1). When both TMF and buoyancy are included in the calculation, then for a certain *Tm,* the flow can be significantly reduced at the bottom of the cylinder as seen in Figure 4 (right). This type of flow circulation can be beneficial for crystal growth.

A simple prototype of the TMF generator has been recently constructed and test velocity measurements were performed [4]. The experimental setup consists of a cylindrical column of mercury, 3.17 cm in diameter and 12 cm in height, that is placed into the TMF set of coils. The anemometer response to the TMF for three values of applied power is presented in Figure 5. For the first 100 seconds there is no field (zero flow), for the next 5 minutes followed by a field of 3.5 gauss (rms). This is then followed by a 7 minute application of a 7.2 gauss field and, subsequently, to a 14 gauss field for 3.5 minutes The clear transition from quasi-steady flow (3.5 gauss) to oscillatory and subsequently chaotic flow as the

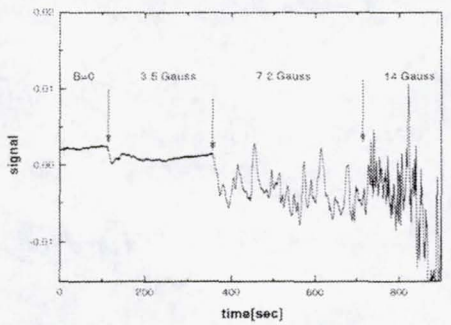

Figure 5. The anemometer response to the TMF for three values of applied power.

magnetic field strength is increased is evident. The observations of the flow character indicate that the transition to time-dependent flow occurs at approximately $Tm_{crit}=10^4$. Incidentally, this value is close to the one for the onset of oscillations in a rotational magnetic field geometry (aspect ratio 4:1).

II. Summary

A brief exposition of the TMF method has been presented. In essence, TMF induces a single axisymmetric vortex in circular cylinders filled with electrically conducting melts. The magnitude and direction of this flow can be remotely and easily controlled. When superimposed on the buoyancy force, the combined body force can be much smaller than the initial buoyancy force. This can result in substantially smaller and laminar steady-state flow. Such flow conditions in the vicinity of the growing crystal interface can be beneficial for its quality. Obvious TMF applications include VB and THM configurations. In the float zone method, surface tension driven convection can be modified by a suitable localized high frequency TMF. Alloy mixing prior to solidification can yet be another useful application of the TMF. Here flow along the axis of the ampoule induced by TMF can mix melts in a short time. RMF, as a competitive mixing method, is much less effective for long ampoules, as only two adjacent to the end cups vortices could promote axial mixing.

A theoretical model of the Lorentz force of arbitrary frequency induced in finite cylinders has been developed in [6]. Modeling of flow dynamics induced by this force has been conducted in [7], and preliminary experimental data on TMF can be found in [4,8,9].

REFERENCES

1. M. Salk, M.Fiederle, K.W.Benz, A.Senchenkov, A.Egerov, D.Matioukhin, "*CdTe and CdTeSe crystals grown by the travelling heater method using a rotating magnetic field,*" J. Crystal Growth 138 (1994) 161.
2. A.Senchenkov, I.Barmin, A.Tomson, V.Krapukhin, "*Seedless THM growth of $Cd_xHg_{1-x}Te(x=0.2)$ single crystals within rotating magnetic field,*" J. Crystal Growth 197 (1999) 552.
3. J.P. Birat, J. Chone, "*Electromagnetic stirring on billet, bloom, and slab continuous casters: state of the art in 1982,*" Ironmaking and Steelmaking, 10 (1983), 269.
4. K. Mazuruk, N. Ramachandran, M.P. Volz, "*Traveling Magnetic Field Induced Flow for Crystal Growth Applications,*" Proceedings of the 37th AIAA Aerospace Sciences Meeting, Reno, NV, AIAA paper 99-0941, (1999).
5. K. Mazuruk, "*Control of Convection by Dynamic Magnetic Fields for VB, FZ and THM Crystal Growth Applications,*" *Crystal Growth and Epitaxy-2000*, Ed. V. Stefan,subm.
6. K.Mazuruk, "*Lorentz Body Force Induced by Traveling Magnetic Fields,*" Magnetohydrodynamics, subm.
7. K. Mazuruk, "*Control of convection of electrically conducting melts by traveling magnetic fields,*" J. Crystal Growth, subm.
8. Ramachandran, N., Mazuruk, K., and Volz, M. P., 2000, "*Use of Traveling Magnetic Fields to Control Melt Convection,*" Journal of Japan Society of Microgravity Applications, Vol. 17, 98-103 (2000).
9. N.Ramachandran, K.Mazuruk, M.P.Volz, "*Use of Traveling Magnetic Fields to Control Melt Convection,*" *SPIE* Vol. 3792 (1999) 39.
10. E. Dahlberg, "*On the action of a rotating magnetic field on a conducting liquid,*" AB Atomenergi, Sweden, Rep. AE-447 (1972).

11. K.Mazuruk, M.P. Volz, *"Magnetic field effect on the stability of flow induced by a rotating magnetic field,"* Magnetohydrodynamics 35 (1999) 103.
12. K. Mazuruk, N. Ramachandran, M.P. Volz, D. Gillies, *"Frequency Effects of a Rotating Magnetic Field on Fluid Flow in Vertical Cylinders,"* SPIE Conference on Materials in Low Gravity, San Diego, 1997, SPIE Vol. 3123, pp. 262-271.
13. Ph. Marty, M.Witkowski, P.Trombetta, T.Tomasino, J.Garandet, *"On the stability of rotating MHD flows,"* Transfer Phenomena in Magnetohydrodynamics and Electroconducting Flows, 327-343 (1999), A.Alemany et al.(eds.), Kluwer Academic Publishers.
14. P. Dold, K.W. Benz, *"Modification of fluid flow and heat transport in vertical Bridgman configurations by rotating magnetic fields,"* Cryst. Res. Technol. 32 (1997) 51.
15. R.U. Barz, G.Gerbeth, U. Wunderwald, E. Buhrig, Yu. Gelfgat, *"Modeling of the isothermal melt flow due to rotating magnetic fields in crystal growth,"* J. Crystal Growth 180 (1997) 410.
16. Th. Kaiser, K.W. Benz, *"Taylor vortex instabilities induced by a rotating magnetic field: a numerical approach,"* Phys. Fluids, 10 (1998) 1104.
17. C. Ghaddar, C.Lee, S. Motakefr, D. Gillies, *"Numerical simulation of THM growth of CdTe in presence of rotating magnetic fields,"* J. Crystal Growth 205 (1999) 97.
18. M. Abricka, J. Krumins, Yu. Gelfgat, *"Numerical simulation of MHD rotator action on hydrodynamics and heat transfer in single crystal growth processes,"* J. Crystal Growth 180 (1997) 388.
19. Yu. Gelfgat, J.Priede, *"MHD flows in a rotating magnetic field (a review),"* Magnetohydrodynamics 31 (1995) 188.
20. Y. M. Gelfgat, L. A. Gorbunov, V.Kolevzon, *"Liquid metal flow in a finite length cylinder with a rotating magnetic field,"* Exp. Fluids 15 (1993) 411.
21. M.P. Volz, K.Mazuruk, *"Flow transitions in a rotating magnetic field,"* Experiments in Fluids 20 (1996) 454.
22. M.P.Volz, K.Mazuruk, D.Gillies, " *Dynamics of RMF Induced Flow* " J. Fluid Mechanics, subm.
23. M.P. Volz, K. Mazuruk, *"Thermoconvective instability in a rotating magnetic field,"* Int. J. Heat and Mass Transfer 42 (1999) 1037.

CONVECTIVE AND MORPHOLOGICAL INSTABILITIES DURING CRYSTAL GROWTH

S.R. Coriell[1], G.B. McFadden[1*], and B.T. Murray[2]

[1]National Institute of Standards and Technology, Gaithersburg, MD 20899
[2]Department of Mechanical Engineering, SUNY at Binghamton, Binghamton, NY 13902

During crystal growth or solidification of a binary alloy from a liquid phase, temperature and solute gradients are inherently present. In a gravitational field, these gradients can give rise to fluid flow in the melt. The interaction of fluid flow with the crystal-melt interface plays an important role in determining the properties of the solidified material. Convection in the melt and interface instability may both produce solute inhomogeneities [1]. In the absence of fluid flow, the conditions for the onset of morphological instability of isotropic materials are well established. However, the coupling between morphological instability and fluid flow can be complicated; interfacial instabilities depend on temperature and solute gradients that may be strongly influenced by the flow field. The flow field, in turn, may be influenced by the morphology of the interface.

There have been extensive measurements directed toward an understanding of dendritic growth from pure supercooled melts [2-6]. Of primary interest has been a comparison with theory of the dependence of the growth speed, V, and the tip radius, R, on the supercooling. One ingredient of the theoretical basis for this comparison is the Ivantsov solution [7], which is an exact solution for the steady-state growth of an isothermal semi-infinite paraboloid of revolution. This solution results in a relationship between the of Stefan number, S, (dimensionless supercooling) and the Peclet number, Pe, (dimensionless product of tip radius R and tip velocity V). For this solution the solid is isothermal and is assumed to have the same density as the liquid. The supercooling is the difference between the melting point of the material and the bath temperature. The second theoretical ingredient has been a value of the selection parameter, which is a dimensionless product of the tip velocity and the square of the tip radius; values of the selection parameter have been calculated from considerations of marginal stability [2,8] and from the theory of microscopic solvability [9-14].

Recently, Glicksman *et al.* [6] have performed very careful measurements of the dendritic growth of pure succinonitrile (SCN) in microgravity in order to reduce fluid convection and thus to conduct a stringent test of the above relationships. For measurements down to supercoolings of 0.05 K, reasonable agreement is obtained. Independent of selection, there appears to be a systematic discrepancy from the Ivantsov relationship. For supercoolings between 0.5 K and 1 K, the measured supercooling for a given Peclet number is about 10 % higher than would be predicted by the Ivantsov relationship (see Figure 10 of Reference [6]). Some possible reasons for this discrepancy are the effect of finite container size, thermal fields due to other dendrites, and deviations of shape from a paraboloid of revolution.

In previous work we have performed a number of investigations concerning the effect of fluid flow on dendritic growth. A closed form solution giving the effect of flow normal to the crystal-melt interface due to a density change upon solidification has been obtained [15]. This work extended the conduction solution of

*Corresponding author

Ivantsov to the case of convective transport of the thermal field. These results have recently been utilized by Chait *et al.* [16] to further analyse the dendritic growth experiments of Glicksman *et al.*

If there is natural convection in the melt, both the selection parameter and the relationship between undercooling and Peclet number might be expected to change. There is some evidence, however, that the selection parameter would be practically unchanged by natural convection. Experimental measurements for succinonitrile (SCN) dendrites by Lee, Ananth, and Gill [17] show that the selection parameter is practically constant for fluid flow velocities up to about ten times the dendrite growth speed. A selection parameter was previously reported by Huang and Glicksman [18] for measurements of SCN dendrites on Earth. This value was based on data for supercooling ranging from about 0.05 K to 2 K (see Figure 7 of Reference [18]). The influence of convection was apparent for supercoolings less than 1 K (see Figure 9 of Reference [18]).

We have also studied the effects of natural convection on the scale of the container size by using a simple stagnant film model of the flow near a sphere that represents the entire dendritic array issuing from a capillary tube into a supercooled liquid [19]. A related model has also been used to estimate the effects of the proximity of container walls to the growing dendrites [20]. Similar studies have also been performed by Pines *et al.* [21] and Schrage [22].

Previous studies in this area have all been based on a axisymmetric dendrite described by the Ivantsov solution. We have recently investigated the effect of a specific deviation of shape from a paraboloid of revolution, namely a paraboloid with a perturbation having n-fold symmetry about the growth axis. The possible importance of such a perturbation is suggested by the measurements of LaCombe et al. [3] of anisotropic tip shapes. A more general exact solution for steady-state solidification into a supercooled melt is that of Horvay and Cahn for an elliptical paraboloid [23]. For this solution the relationship between S and P depends on an additional shape parameter that characterizes the eccentricity of the elliptical cross-section. Such a body, however, has two-fold axial anisotropy. Nevertheless, this result suggests that a paraboloid having a perturbation with n-fold axial symmetry would also have a relationship between S and P that depends upon the amplitude of the perturbation. In collaboration with R. F. Sekerka (Carnegie Mellon University), we have obtained [24] such a solution for $n = 3$ and $n = 4$ by means of an expansion to second order in the perturbation amplitude, necessary because the first order correction vanishes by symmetry.

Dendrites with n-fold symmetry about a preferred growth direction generally occur because of the presence of anisotropy in surface tension or interface attachment kinetics. For a cubic material, dendritic growth in the [100] direction leads to shapes with four-fold symmetry [2]. Our solution technique is based on extending the known results for the two-fold Horvay-Cahn solution to the more difficult case of four-fold symmetry. In a parabolic coordinate system, self-consistent solutions for the thermal field and interface shape through second order in the interface amplitude can be obtained, together with a corresponding correction to the Ivantsov relation. The solution depends on a shape parameter that is proportional to the amplitude of the four-fold correction to the dendrite shape, as measured from the Ivantsov paraboloid of revolution. The shape parameter was measured experimentally for succinonitrile by LaCombe *et al.* for $Pe = 0.004$. Using this value in our model produces a predicted 9 % increase in S for this Peclet number, which is in good agreement with the deviation observed experimentally by Glicksman *et al.* In Figure 1 we show a three-dimensional view of the resulting dendrite tip shape.

Also in collaboration with R. F. Sekerka, we have estimated the shape parameter theoretically on the basis of a simple idea, namely, that the shape of the isothermal but anisotropic dendrite tip is approximately the same as a portion of the equilibrium shape of an isothermal body with anisotropic surface free energy [25]. We

recognize that the equilibrium shape is a closed convex body in a strictly isothermal environment, whereas our dendrite model [24] corresponds to a semi-infinite body with an isothermal surface that is growing from a non-isothermal melt. We note, however, that an *isothermal* body, either the Ivantsov paraboloid or a

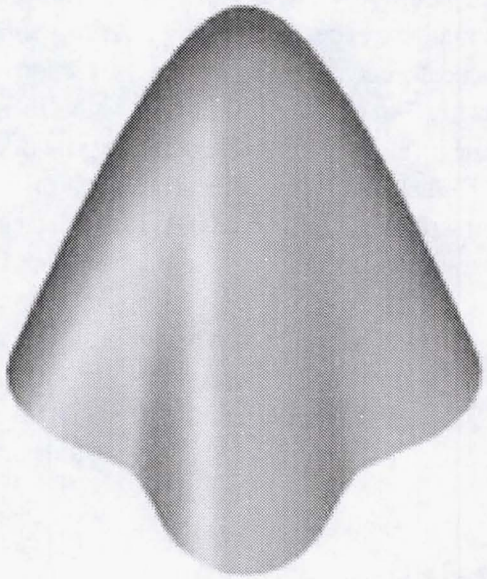

Figure 1. Calculated dendrite tip with 4-fold symmetry.

perturbed paraboloid with a four-fold axial symmetry, is used to determine the underlying relationship between the Peclet number and the supercooling for all existing theoretical analyses of dendritic growth. A non-isothermal dendrite surface is only taken into account, either by invoking a marginal stability hypothesis or by conducting a microscopic solvability analysis, in order to separate the product of tip radius and growth velocity that occurs in the Peclet number. In the present analysis, we do not attempt to calculate the tip radius and growth velocity separately, but only the relationship of the shape anisotropy to the anisotropy of the surface free energy.

We emphasize that a shape with variable curvature but with anisotropic surface free energy can still be isothermal; for example, the equilibrium shape itself is an example of an isothermal body for which the anisotropic Gibbs-Thomson equation is everywhere satisfied. It is not inconsistent to hypothesis that the dendrite tip *shape* is geometrically similar to the *portion* of the equilibrium shape near the growth direction, which is [001] for SCN. By comparing the anisotropic equilibrium shape near the [001] orientation with the isothermal solution with four-fold symmetry, we obtain a specific relation between the shape parameter of the four-fold solution and the cubic surface tension anisotropy.

The anisotropy of the surface free energy for SCN has been measured by Glicksman and Singh [26] and Muschol *et al.* [27]. Using their value for the anisotropy with our theory results in a shape parameter that compares favorably with the direct measurements of LaCombe *et al.* [3]. Note, however, that the experimental determination of the shape parameter is based on measurements of the dendrite shape for distances of up to ten tip radii from the tip, whereas our comparison to the equilibrium shape is only valid within a fraction of a tip radius from the tip. Another theoretical estimate of the shape parameter has been made by Brener *et al.* [11-14] based on microscopic solvability theory, and results in a value for the shape parameter that is about a factor of two larger than the experimental value. Their result is independent of the magnitude of the surface tension anisotropy. By means of numerical computations based on a phase-field model, Karma and Rappel [28] calculated a shape anisotropy close to the value of Brener *et al.*, and

therefore still somewhat larger than the experimental value, though these calculations are performed for larger undercoolings than are obtained experimentally. More recently, Karma *et al.* have performed phase-field simulations for dendritic growth at lower undercoolings, with special attention given to the computation of the tip radius of curvature and the shape parameter [29]. Computing the tip radius R using data very near the dendrite tip results in a computed value of R that is found to be sensitive to the level of anisotropy used in the model. Values of R and the four-fold shape parameter that are less sensitive to the anisotropy can be obtained from fits to the dendrite shape over an extended range that includes several tip radii away from the dendrite tip.

It appears that our simple assumption that the tip anisotropy can be calculated from an isothermal equilibrium shape is in somewhat better agreement with the experiment than that calculated from solvability theory, at least for the single data point for which both shape measurements and the surface energy anisotropy are so far available. On the other hand, the present theory does not include any assumption about the value of the actual tip temperature, so it leads only to a corrected value for the Peclet number *versus* supercooling. Unlike solvability theory, it makes no prediction about the separate values of tip radius and growth velocity.

REFERENCES

1. W.J. Boettinger, S.R. Coriell, A.L. Greer, A. Karma, W. Kurz, M. Rappaz, and R. Trivedi, Solidification microstructures: Recent developments, future directions, Acta Mater. 48 (2000) 43-70.
2. M. E. Glicksman and S. P. Marsh, The dendrite, in Handbook of Crystal Growth 1 Fundamentals, Part B: Transport and Stability, ed. D. T. J. Hurle (North-Holland, Amsterdam, 1993) p. 1075-1122.
3. J.C. LaCombe, M.B. Koss, V.E. Fradkov, and M.E. Glicksman, Three-dimensional dendrite tip morphology, Phys. Rev. E 52 (1995) 2778-2786.
4. M. E. Glicksman, M. B. Koss, L. T. Bushnell, Jeffrey C. LaCombe, and E. A. Winsa, Dendritic growth of succinonitrile in terrestrial and microgravity conditions as a test of theory, ISIJ Int. 35 (1995) 604-610.
5. J.C. LaCombe, M.B. Koss, and M.E. Glicksman, Nonconstant tip velocity in microgravity dendritic growth, Phys. Rev. Lett. 83 (1999) 2997-3000.
6. M.B. Koss, J.C. LaCombe, L.T. Bushnell, M.E. Glicksman, and E. A. Winsa, Dendritic growth tip velocities and radii of curvature, Met. Mat. Trans. 30A (1999) 3177-3190.
7. G. P. Ivantsov, Temperature field around spherical, cylindrical, and needleshape crystals which grow in supercooled melt, Dokl. Akad. Nauk SSSR 58 (1947) 567-569.
8. J. S. Langer, Instabilities and pattern formation in crystal growth, Rev. Mod. Phys. 52 (1980) 1-28.
9. J. S. Langer, Lectures in the theory of pattern formation, in Le hesard et la matiere/Chance and matter, Les Houches, Session XLVI, Course 10, (North Holland, Amsterdam, 1987) pp. 629-711.
10. David A. Kessler, Joel Koplik, and Herbert Levine, Pattern selection in fingered growth phenomena, Advances in Physics 37 (1988), 255-339.
11. E. A. Brener and V.I. Mel'nikov, Pattern selection in 2-dimensional dendritic growth,Advances in Physics 40 (1991) 53-97.
12. M. Ben Amar and E. Brener, Theory of pattern selection in three-dimensional nonaxisymmetric dendritic growth, Phys. Rev. Lett. 71 (1993) 589-592.
13. `E. Brener, Needle-crystal solution in three-dimensional dendritic growth, Phys. Rev. Lett. 71 (1993) 3653-3656.
14. E. Brener and V.I. Mel'nikov, Velocity selection and instability spectrum in 3D dendritic growth, JETP 80 (1995) 341-354.
15. G.B. McFadden and S.R. Coriell, The effect of fluid flow due to the crystal-melt density change on the growth of a parabolic isothermal dendrite, J. Crystal Growth 74 (1986) 507-512.

16. Vladimir Pines, Arnon Chait, and Marianne Zlatkowski, Anomaly in dendritic growth data - effect of density change upon solidification, J. Crystal Growth 169 (1996) 798-802.
17. Y. W. Lee, R. Ananth. and W. N. Gill, Selection of a length scale in unconstrained dendritic growth with convection in the melt, J. Crystal Growth 132 (1993) 226-230.
18. S.-C. Huang and M. E. Glicksman, Fundamentals of dendritic solidification—I. Steady-state tip growth, Acta Met. 29 (1981) 701-715.
19. R.F. Sekerka, S.R. Coriell, and G.B. McFadden, Stagnant film model of the effect of natural convection on the dendrite operating state, J. Crystal Growth 154 (1995) 370-376.
20. R.F. Sekerka, S.R. Coriell, and G.B. McFadden, The effect of container size on dendritic growth in microgravity, J. Crystal Growth 171 (1997) 303-306.
21. Vladimir Pines, Arnon Chait, and Marianne Zlatkowski, Thermal diffusion dominated dendritic growth - an analysis of the wall proximity effect, J. Crystal Growth 167 (1996) 383-386.
22. D. S. Schrage, A simplified model of dendritic growth in the presence of natural convection, J. Crystal Growth 205 (1999) 410-426.
23. G. Horvay and J. W. Cahn, Dendritic and spheroidal growth, Acta Met. 9 (1961) 695-705.
24. G. B. McFadden, S. R. Coriell, and R.F. Sekerka, Analytical solution for a non-axisymmetric isothermal dendrite, J. Crystal Growth 208 (2000) 726-745.
25. G. B. McFadden, S. R. Coriell, and R.F. Sekerka, Effect of Surface Free Energy Anisotropy on Dendrite Tip Shape, Acta Mater., in press.
26. M.E. Glicksman and N.B. Singh, in Rapidly Solidified Powder Aluminum Alloys, ed. M.E. Fine and E.A. Starke, Jr. (ASTM, Philadelphia, 1986), p. 44.
27. M. Muschol, D. Liu, and H.Z. Cummins, Surface-tension-anisotropy measurements of succinonitrile and pivalic acid – comparison with microscopic solvability theory, Phys. Rev. A 46 (1992) 1038-1050.
28. A. Karma and W.-J. Rappel, Quantitative phase-field modeling of dendritic growth in two and three dimensions, Phys. Rev. E 57 (1998) 4323-4349.
29. A. Karma, Youngyih H. Lee, and Mathis Plapp, Three-dimensional dendrite-tip morphology at low undercooling, Phys. Rev. E 61 (2000) 3996-4006.

A PHASE-FIELD/FLUID MOTION MODEL OF SOLIDIFICATION: INVESTIGATION OF FLOW EFFECTS DURING DIRECTIONAL SOLIDIFICATION AND DENDRITIC GROWTH

D.M. Anderson[1], W.J. Boettinger[2], G.B. McFadden[2]*, and A.A. Wheeler[3]

[1]Department of Mathematical Sciences, George Mason University; Fairfax, VA 27599
[2]National Institute of Standards and Technology; Gaithersburg, MD 20899
[3]University of Southampton; Highfield, Southampton, SO17 1BJ, UK

The phase-field model of diffusion-controlled solidification has recently been extended to include the effects of fluid flow in the melt [1-8]. The phase-field model is based on coupling the equations for heat flow in the liquid and solid phases with an auxiliary equation that describes the evolution of the phase-field variable, which is a non-conserved order parameter indicating the local phase, solid or liquid, at each point of the material. The solid-liquid interface is then represented by a diffuse transition layer in which the phase-field variable changes rapidly between its values in the bulk phases. The extended model includes fluid flow by a further coupling to the Navier-Stokes equations. In our work [1,2], the solid phase is treated as a fluid of high viscosity compared to the liquid phase. The main coupling in the Navier-Stokes equations is then through an additional term in the stress tensor that depends on the gradients of the phase-field variable, representing the effects of capillary forces within the diffuse interface [9]. This model is applied to solidification and crystal growth situations in order to investigate the effect of fluid motion in the melt on the growth characteristics.

In the original diffuse interface theory for a critical fluid, the density, which satisfies the continuity equation, is treated as the order parameter (see, *e.g.*, [10,11]). The momentum equation, modified to include the divergence of the capillary tensor, governs the flow while an equation of state relates the pressure, temperature, and density. This original theory for a critical fluid has been extended to investigate a range of hydrodynamic phenomena including capillary waves, moving contact lines, droplets and nucleation [9]. In the context of a binary fluid [12,13], composition may play the role of a conserved order parameter that satisfies a Cahn-Hilliard equation [14]. A variety of situations have been studied ranging from spinodal decomposition to thermocapillary flow; the review by Anderson *et al.* [9] and references therein provide further details. An early attempt to include fluid motion within a phase-field model is due to Caginalp and Jones [15,16]. They appended the inviscid momentum equation and the continuity equation to the phase-field model, but did not address the issues of momentum balance in the solid and capillary contributions to the stress tensor. Beckerman *et al.* [3-5] have employed the methodology of two-phase fluid flow, where the phase field parameter is interpreted as a solid fraction. Their model is used to study coarsening in a binary solid/liquid mixture with and without flow, as well as dendritic growth in a forced flow. Tonhardt and Amberg [6,7] have also performed two-dimensional numerical studies using adaptive finite elements to study the effects of a shear flow on dendritic growth morphology. In our work we bring together several ideas to develop a phase-field model which allows for

*Corresponding author

convection in the liquid phase [1,2]. Our model has two notable aspects: first, we represent both the solid and liquid phases as Newtonian fluids in which the viscosity of the putative solid phase is specified to be much larger than that of the liquid phase. Second, the interface is ascribed an anisotropic surface energy, which is non-standard for a model which treats the two phases as Newtonian fluids. These unconventional features are in keeping with our intention to model a solid-liquid system. In order to obtain the desired viscosity variation between the phases, the viscosity is assumed to depend on the phase field. The anisotropic surface energy is achieved by employing the generalized xi-vector formalism [17]. Unlike diffuse interface models which incorporate fluid motion coupled to a conserved order parameter description [9], we adopt a nonconserved order parameter in line with our aim of directly extending conventional phase field models of solidification to account for convection. This has the advantage that we may treat quasi-incompressible systems [18] in which the density of the solid and liquid bulk phases are each spatially uniform by allowing the density to be a prescribed function of the phase field.

With these assumptions we develop the irreversible thermodynamics [19] of the model from gradient functionals for both the entropy and internal energy. We identify governing equations that are consistent with the first and second laws of thermodynamics. The quasi-incompressibility assumption, which allows the density to depend solely on the phase field, and not the pressure, restricts the form of the thermodynamic potentials that may be employed [18]. The model comprises the compressible Navier-Stokes equations with a modified stress tensor that includes additional terms related to the capillarity tensor, an energy equation and a phase-field equation.

An important area of application is the study of flow effects on microstructure during solidification. For example, many experimental investigations, both in terrestrial and microgravity environments, have studied the selection of tip radius and velocity during dendritic growth. Phase-field models of solidification have been a useful tool in assessing the complicated morphologies associated with dendritic growth when diffusion (heat or solute) is the dominant growth mechanism. This research therefore aims to provide a theoretical model that will allow the modeling and computation of complex interfacial structures in realistic growth configurations. This will allow the assessment of flow effects on interfacial morphology in both terrestrial and microgravity environments. Numerical computations have been performed [2] on a simplified form of the model which represents the growth of a two-dimensional dendrite in a thin gap between two parallel thermally insulting plates. In these computations flow in the liquid arises because of the differing densities of the solid and liquid phases. An example is shown in the figure below. In the plot on the left, the phase field is shown in color, the pressure field is shown by contours, and the velocity field is shown by arrows. The calculation is performed using an adaptive finite difference scheme [20] with four levels of refinement; the different grid levels are shown in the plot on the right. In this calculation the solid is less dense than the liquid, generating an expansion flow away from the interface. For illustration purposes, the viscosities in the liquid and solid regions are taken to be equal, allowing a small residual flow in the solid region that can occur with this model.

We are currently examining the sharp interface limit of our convective phase-field model to assess the recovery of the standard interfacial boundary conditions. In addition to the usual stress conditions that correspond to conservation of momentum, we obtain the correct limiting form of the combined Laplace-Young, Gibbs-Thomson, and Classius-Clapeyron effects that relate the curvature, pressure jump, and temperature under equilibrium conditions at a phase boundary.

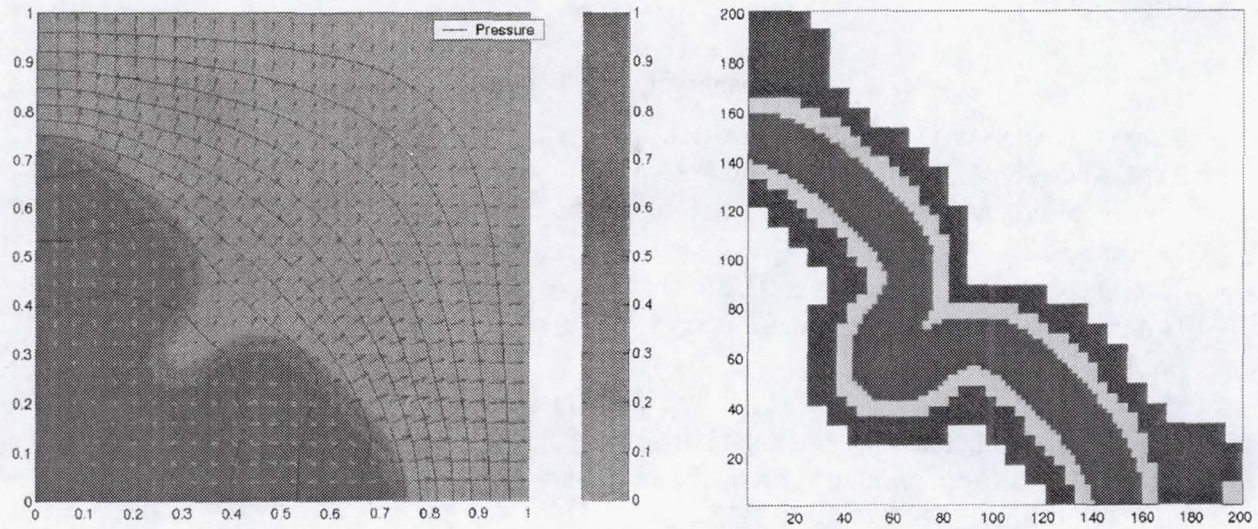

Figure 1. Expansion flow driven by a density change upon solidification (left), computed by using an adaptive finite difference scheme whose mesh levels (right) allow local refinement near the interface.

Karma and Rappel have recently developed a new sharp interface asymptotic analysis of the phase-field equations that is especially appropriate for modeling dendritic growth at low undercoolings [21]. Their approach relieves a stringent restriction on the interface thickness that applies in the conventional asymptotic analysis, and has the added advantage that interfacial kinetic effects can also be eliminated. However, their analysis focussed on the case of equal thermal conductivities in the solid and liquid phases; when applied to a standard phase-field model with unequal conductivities, anomalous terms arise in the limiting forms of the boundary conditions for the interfacial temperature that are not present in conventional sharp-interface solidification models, as discussed further by Almgren [22]. We have applied their asymptotic methodology to a generalized phase-field model which is derived using a thermodynamically consistent approach that is based on independent entropy and internal energy gradient functionals that include double wells in both the entropy and internal energy densities [23]. The additional degrees of freedom associated with the generalized phase-field equations can be used to eliminate the anomalous terms that arise for unequal conductivities. A similar approach may play a useful role in the more difficult case of alloy solidification, where the solid and liquid solute diffusivities differ by several orders of magnitude.

Diffuse interface models also arise in a natural way in mean field free energy models of ordering transitions in face-centered-cubic and hexagonal-close-packed binary alloys [24-26]. Such models are based on a Landau expansion of the free energy function in terms of three nonconserved order parameters that describe ordering on the underlying FCC lattice. The ordering models provide a natural description of surface energy anisotropy that is inherited automatically from the underlying crystal lattice. In recent work [27], we have extended our previous treatment to include sixth-order terms in the Landau expansion of the free energy that provides a more realistic treatment of first-order phase transitions for ordered states. In particular, this allows the computation of phase diagrams with realistic dependence on the composition and temperature fields. When combined with appropriate gradient energy terms, this model allows the self-consistent calculation of energetic and kinetic anisotropies of phase boundaries.

REFERENCES

1. D.M. Anderson, G.B. McFadden, and A.A. Wheeler, A phase-field model of solidification with convection, Physica D 135 (2000) 175-194.
2. D.M. Anderson, G.B. McFadden, and A.A. Wheeler, A phase-field model with convection: Numerical simulations, to appear in Interfaces for the Twenty-First Century (Imperial College Press, London, 2000).
3. H. J. Diepers, C. Beckermann, and I. Steinbach, in Solidification Processing 1997, ed. J. Beech and H. Jones, Proc. 4th Decennial Int. Conf. on Solid. Process. (University of Sheffield, Sheffield,1997) pp. 426-430.
4. C. Beckerman, H.-J. Diepers, I. Steinbach, A. Karma, and X. Tong, Modeling melt convection in phase-field simulations of solidification, J. Comp. Phys. 154 (1999) 468-496.
5. X. Tong, C. Beckerman, and A. Karma, Velocity and shape selection of dendrite crystals in a forced flow, Phys. Rev. E 61 (2000) R49-R52.
6. R. Tonhardt, Convective Effects on Dendritic Solidification, 1998 Ph. D. thesis, Department of Mechanics, Royal Institute of Technology, S-100 44 Stockholm, Sweden.
7. R. Tonhardt and G. Amberg, Phase-field simulation of dendritic growth in a shear flow, J. Crystal Growth 194 (1998) 406-425.
8. R. F. Sekerka and Zhiqiang Bi, Phase field model of multicomponent solidification with hydrodynamics, to appear in Interfaces for the Twenty-First Century (Imperial College Press, London, 2000).
9. D.M. Anderson, G.B. McFadden, and A.A. Wheeler, Diffuse-interface methods in fluid mechanics, Ann. Rev. Fluid Mech. 30 (1998) 139-165.
10. D.M. Anderson and G.B. McFadden, A diffuse-interface description of of internal waves in a near-critical fluid, Physics of Fluids 9 (1997) 1870-1879.
11. P. Papatzacos, Diffuse-interface models for two-phase flow, Physica Scripta 61 (2000) 349-360.
12. David Jacqmin, Calculation of two-phase Navier-Stokes flows using phase-field modeling, J. Comp. Phys. 155 (1999) 96-127.
13. David Jacqmin, Contact line dynamics of a diffuse fluid interface, J. Fluid Mech. 402 (2000) 57-88.
14. John W. Cahn and John E. Hilliard, Free energy of a nonuniform system. I. Interfacial free energy, J. Chem. Phys. 28 (1958) 258-267.
15. G. Caginalp and J. Jones, A derivation of a phase field model with fluid properties, Appl. Math. Lett. 4 (1991) 97-100.
16. G. Caginalp and J. Jones, in On the Evolution of Phase Boundaries, ed. M. E. Gurtin and G.B. McFadden, The IMA Series in Mathematics and Its Applications, Vol. 43 (Springer Verlag, New York, 1992) pp. 27-50.
17. A.A. Wheeler and G.B. McFadden, A xi-vector formulation of anisotropic phase-field models: 3-D asymptotics, Eur. J. Appl. Math. 7 (1996) 367-381.
18. J. Lowengrub and J. Truskinovsky, Cahn-Hilliard fluids and topological transitions. Proc. Roy. Soc. Ser. A 454 (1998) 2617.
19. S.R. de Groot and P. Mazur, Non-Equilibrium Thermodynamics (Dover, New York, 1984).
20. J.G. Blom, R.A. Trombert, and J.G. Verwer, Algorithm 758: VLUGR2: A vectorizable adaptive-grid solver for PDEs in 2D, ACM Trans. Math. Software 22 (1996) 302-328.
21. A. Karma and W.-J. Rappel, Quantitative phase-field modeling of dendritic growth in two and three dimensions, Phys. Rev. E 57 (1998) 4342-4349.
22. R.F. Almgren. Second-order phase field asymptotics for unequal conductivities, SIAM J. Appl. Math. 59 (1999) 2086-2107.

23. G.B. McFadden, A.A. Wheeler, and D.M. Anderson, Thin interface asymptotics for an energy/entropy approach to phase-field models with unequal conductivities, Physica D (in press).
24. R.J. Braun, J.W. Cahn, G.B. McFadden, and A.A. Wheeler, Anisotropy of interfaces in an ordered alloy: a multiple-order parameter model, Phil. Trans. Roy. Soc. (London) Series A 355 (1997) 1787-1833.
25. R.J. Braun, J. W. Cahn, G.B. McFadden, and A.A. Wheeler, Theory of anisotropic growth rates in the ordering of an FCC alloy, Acta Mater. 46 (1998) 1-12.
26. J.W. Cahn, S.C. Han, and G.B. McFadden, Anisotropy of interfaces in an ordered HCP binary alloy, Journal of Statistical Physics 95 (1999) 1337-1360.
27. R.J. Braun, J. Zhang, J.W. Cahn, G.B. McFadden, and A.A. Wheeler, Model Phase Diagrams for an FCC Alloy, to appear in Interfaces for the Twenty-First Century (Imperial College Press, London, 2000).

MICROGRAVITY INVESTIGATION OF DYNAMIC OXYGEN ADSORPTION IN MOLTEN SOLDER JETTING TECHNOLOGY

C.M. Megaridis[1] *, M. McNallan[1] , G. Bellizia[1] and D.B. Wallace[2]

[1]University of Illinois at Chicago
[2]MicroFab Technologies

INTRODUCTION

Surface tension forces play a critical role in fluid dynamical phenomena, which are important in materials processing. These forces can be more important in liquid-metal systems, than in their ceramic or polymer counterparts because of the high surface tensions of metal melts in comparison to other classes of materials. The surface tension of liquid metals has been found to be very susceptible to small amounts of adsorbed oxygen [1]. Consequently, the kinetics of oxygen adsorption can influence the capillary breakup of liquid-metal jets targeted for use in electronics assembly applications where low-melting-point metals (such as tin-containing solders) are utilized as an attachment and/or structural material for mounting of electronic components to substrates. By interpreting values of surface tension measured at various surface ages, adsorption and diffusion rates of oxygen on the surface of the melt can be estimated.

This research program investigates the adsorption kinetics of oxygen on the surface of tin-containing metal melts. Oxygen adsorption poses a severe impediment in processing technologies involving jetting of pure tin or tin-based alloys. While the problem of interest is one of fundamental fluid transport and surface science, it is also directly related to the novel technology of dispension (printing) of microscopic solder deposits for the surface mounting of microelectronic devices. This technology, known as solder jetting [2], features deposition of solder droplets in very fine, very accurate patterns using techniques analogous to those developed for the ink-jet printing industry. A major development challenge in the commercialization of solder jetting technology stems from the need to maintain adequate control of the local inert environment around the atomizing jet and the formed droplets for a wide variety of industrial applications. To this end, the limitations of solder jetting must be quantified as a function of oxygen content in the local inert environment. Alternatively, this requires the quantification of the influence of oxygen gaseous impurities in the ambient on the dynamic surface tension properties of the employed solder melts.

I. Oxygen Adsorption Considerations

When tin or solder droplets are produced in a jetting device, new gas-metal surfaces are created from the liquid melt. Initially, these surfaces are clean, and have high surface tensions characteristic of clean metals. With time, oxygen segregates to the surfaces, leading to a reduction in surface tension. The metal surface would be expected to be saturated with oxygen when the environment contains a partial pressure of oxygen at equilibrium between the metal and its oxide. Because both SnO_2 and PbO are very stable oxides at low temperature, the oxygen partial pressures necessary to saturate Sn/Pb molten surfaces at equilibrium are very low, approximately 8×10^{-50} atm for SnO_2 and $\sim 5 \times 10^{-39}$ atm for PbO

* Corresponding author

at 500 K. Therefore, oxygen saturation would be expected in nearly every gas environment after sufficiently long exposures.

Droplet formation during solder jetting takes place over time scales finer than one millisecond. If the time required for oxygen segregation is long in comparison to the time required for droplet formation, then the adsorption of oxygen is not expected to affect surface tension, and in turn, droplet formation. If the time for oxygen segregation is short in comparison to the time required for droplet formation, the surface will be saturated with oxygen before droplet formation. Finally, if the time required for oxygen segregation is of the same order of magnitude as the time required for droplet formation, then the surface tension of the metal may vary dynamically during the droplet formation stage. The time required for oxygen segregation to the surface depends on the source of the oxygen and the transport phenomena affecting its segregation.

There are two possible sources of oxygen that may affect droplet formation:

1. Some level of dissolved oxygen may be present in the metal in the melting vessel before droplet formation. This oxygen will diffuse to the newly formed surface and adsorb there. The rate of oxygen segregation from this source is controlled by the dissolved oxygen content of the solder and the diffusion coefficient of oxygen in the molten alloy. However, the maximum solubility of oxygen in liquid tin and tin-based alloys is very low. At 505K the atom fraction of dissolved oxygen in Sn saturated with pure O_2 is 1.35×10^{-8} [3]. This solubility is so low that a 100μm-diameter droplet of tin would not contain sufficient oxygen to fully saturate the surface even if all of the dissolved oxygen atoms were to segregate. Therefore, it is unlikely that sufficient oxygen can be present in the droplet bulk to saturate the surface, even after very long time periods.
2. Oxygen is likely to be present in the atmosphere into which the droplet is ejected. This oxygen will also be adsorbed on the metal surface given adequate time. The rate of oxygen segregation from this source is controlled by the pressure of oxygen in the atmosphere and the transport properties of the oxygen in the gas phase. The maximum possible rate of oxygen segregation is given by the Herz-Langmuir equation. Preliminary calculations indicated that oxygen saturation could occur in as little as 6×10^{-9}s, when the droplet is formed in pure oxygen at one atmosphere. This time is very short in comparison to the times required for droplet formation. As the oxygen partial pressure is reduced, the times required for saturation increase approaching 0.1 ms as the oxygen pressure approaches 10^{-5} atm. However, when the droplet is formed at atmospheric pressure in an environment consisting of a inert gas containing a small amount of oxygen, transport of oxygen to the surface is further limited by gas phase diffusion, and the conditions for application of the Herz-Langmuir equation are not satisfied. Under such conditions, oxygen transport to the surface is controlled by diffusion through a boundary layer of gas at the melt surface, and the oxygen transfer can be predicted more reliably by the Ranz-Marshall correlation [4] which expresses the mass transfer coefficient in terms of dimensionless parameters:

$$Sh = 2.0 + 0.6\, Re^{1/2} Sc^{1/3}.$$

In the above, Sh is the Sherwood number for oxygen transfer to the droplet (mass transfer analog to the Nusselt number), Re is the Reynolds number for flow past the droplet, and Sc is the Schmidt number of the gas (mass transfer analog to the Prandtl number).

II. Approach

Typical injection velocities in solder jetting are of the order of 1m/s, while the jet breakup lengths are of the order of 1mm. Thus, the capillary jet disintegrates into droplets under the action of surface tension in about a millisecond or less. Under these circumstances, the variation of surface tension with time must be resolved at temporal scales much finer than a millisecond. This severe requirement limits the choice of surface tension measurement techniques and points to a dynamic method of high accuracy under such extreme conditions. This method has been validated for non-metallic liquids of moderate viscosity [5], and is believed to have equally good potential to provide similar data for metal melts. However, the technique also requires a high degree of spatial resolution that can be afforded only at length scales larger than those encountered in solder jetting technology. In particular, the measurement of the contractions (necks) along an excited oscillating jet becomes increasingly more difficult as the length scales get smaller.

The need for reliable experimental data to guide process development, leads to scaled up jets (diameters near 0.5mm or better) to afford improved spatial resolution and flexibility in conducting such experiments. While the effect of gravity on the atomization behavior of 50-100μm-diameter jets is insignificant (breakup is completed very rapidly), gravity becomes increasingly more influential in the atomization of larger solder jets that are needed for the surface tension characterization experiments. As a result, the microgravity environment appears to be necessary to conduct the jet breakup experiments relevant to the solder microdroplet dispensing technology.

The microgravity experiments will be performed at the 2.2s drop tower of the NASA Glenn Research Center. The main elements of the experiment rig needed for the reduced-gravity tests have been constructed, and include an environmental chamber, a power distribution module (PDM), a computer-based data acquisition system, and a high-speed visualization system (Figure 1). At the center of the experimental apparatus is the molten solder droplet/jet generator, which provides the means of generating droplets or cylindrical jets on demand. Before ejection, the solder is heated to a temperature of 210°C (melting point is 183°C). The environmental chamber surrounding the generator is equipped with optical windows on the four vertical sides for viewing using an external light source, which provides back illumination. The rig dimensions are 0.97m x 0.41m x 0.91m; it is fully automated and has the durability to withstand 30-g deceleration levels experienced repeatedly on the airbag at the end of each drop experiment. All electronics on board the experiment rig are controlled by an on-board computer (DDACS). This programmable unit is loaded with an executable program just before each experiment to control the light, jet generation, and camera timing. All power for the electronics is delivered from on-board 24 V battery packs. Visualization is achieved through a high-speed digital camera (Kodak Ektapro RO). The operation of the camera is fully automated during each experiment sequence, recording up to a rate of 1000 frames per second. The camera is equipped with a lens allowing resolution of ~8 μm/pixel. The current version of the experiment can operate either in the drop-on-demand or the continuous jet mode. Current efforts concentrate on jets excited by a time periodic electric field, which is used as a means of providing a well-defined disturbance to the jet via a piezoelectric crystal. Resolving the spatial resolution of the capillary jet breakup geometry in a controlled ambient atmosphere allows the quantification of surface tension as a function of distance from the orifice (likewise, surface age) [5].

A second experimental setup (Figure 2), which is operated in normal gravity, targets the equilibrium surface tension of 63%Sn-37%Pb eutectic solder in oxygen-containing nitrogen atmospheres (in the range 100ppm-1% of O_2 in N_2). The operation of this apparatus is based on a variation of the maximum

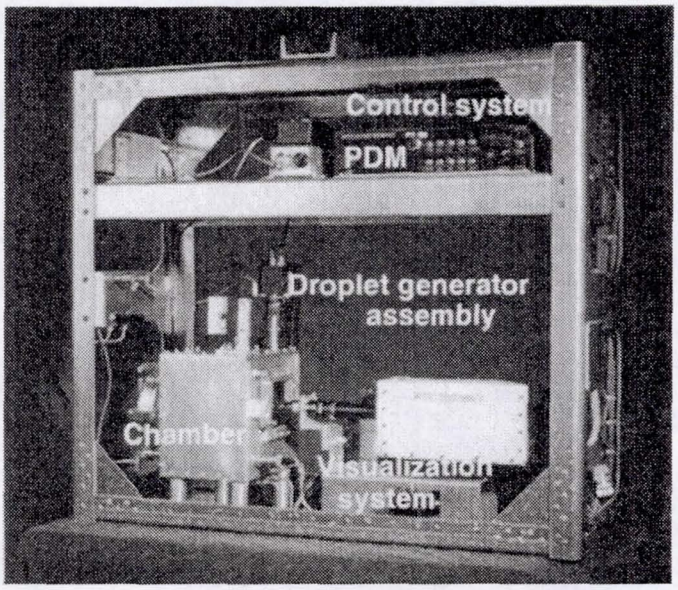

Figure 1: Photograph of the experiment rig planned for use in the reduced-gravity tests.

bubble pressure technique. In that, a gas of known composition is forced through capillary tubes at a bubbling rate of ~0.3Hz. A pressure transducer placed 2 feet upstream from the tip records the pressure continuously at a rate of 10Hz. Combining the maximum bubble pressures measured in two separate tubes allows the determination of the surface tension coefficient of the liquid metal in the flowing gas.

Preliminary experiments have been conducted with de-ionized water and other room temperature liquids with and without additions of surfactants. Measurements, such as the one shown in Figure 3, resulted in a value of surface tension within 1% of the value of 0.0728 N/m, as reported in the literature for water. These experiments showed that the setup provides measurements of surface tension coefficients within 5% of the literature values. Experiments in normal gravity are currently in progress to define the equilibrium value of surface tension of the solder melt as a function of ambient oxygen concentration and temperature. Comparisons between equilibrium and dynamic surface tension values are expected to provide fundamental information about the kinetics of surface adsorption of oxygen on lead-tin alloys.

III. Conclusion

The current program is in its third year of performance. Experiments are conducted in microgravity to determine the surface tension coefficient of 63%Sn-37%Pb solder as a function of molten-surface age and oxygen content in the atmosphere. In addition, experiments are performed in normal gravity to determine the corresponding surface tension values at equilibrium. The research is expected to provide a science base for the dynamic oxygen adsorption phenomena occurring in the novel solder dispensing technology. The study will allow the generation of designs and operating parameters for environmental control systems that are more efficient (in terms of nitrogen usage, space allocation, and energy usage) towards the production of solder deposits of highest quality; this, in turn, will aid the successful commercialization of this innovative technique in electronic component manufacturing or other relevant technologies.

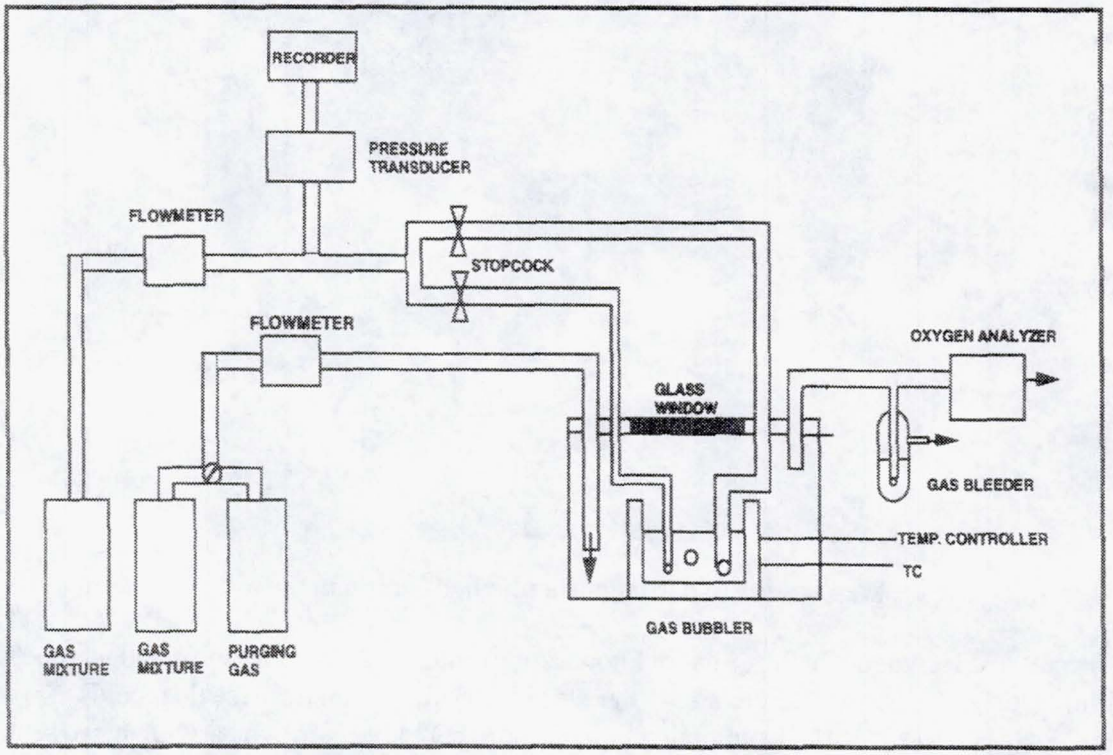

Figure 2. Schematic of maximum bubble pressure apparatus

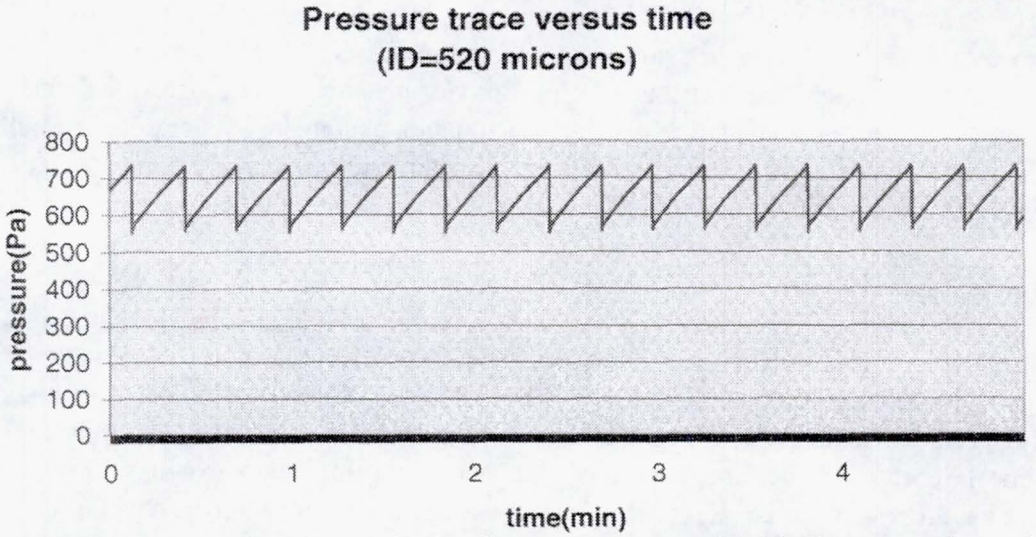

Figure 3. Typical temporal signal recorded by the pressure transducer in the set up shown in Figure 2. This particular trace was obtained when bubbling nitrogen gas through de-ionized water.

REFERENCES

1. Semenchenko, V. K., *Surface Phenomena in Metals and Alloys*, Pergamon Press (1962).
2. Hayes, D. J., Wallace, D. B., Boldman, M. T. and Marusak, R. E., "Picoliter Solder Droplet Dispensing," *Int. J. Microcircuits and Electronics Packaging*, 16:173 (1993).
3. Ramanarayanan, T. A. and Rapp, R. A. "The Diffusivity and Solubility of Oxygen in Liquid Tin and Solid Silver and the Diffusivity of Oxygen in Solid Nickel," *Metallurgical Transactions* 3:3239 (1972).
4. Geiger, G. A. and Poirier, D. R. *Transport Phenomena in Metallurgy*, Addison Wesley, 1973, pp 250, 539.
5. Ronay, M., "Determination of the dynamic surface tension of inks from the capillary instability of jets," *J. Colloid and Interface Sci.* 66:55 (1978).

RADIATION TRANSPORT PROPERTIES OF POTENTIAL *IN SITU*-DEVELOPED REGOLITH-EPOXY MATERIALS FOR MARTIAN HABITATS

J. Miller[1] *, L. Heilbronn[1], R.C. Singleterry Jr.[2], S.A. Thibeault[2], J.W. Wilson[2] and C.J. Zeitlin[1]

[1]Lawrence Berkeley National Laboratory
[2]NASA, Langley Research Center

We will evaluate the radiation transport properties of epoxy-martian regolith composites. Such composites, which would use both *in situ* materials and chemicals fabricated from elements found in the martian atmosphere, are candidates for use in habitats on Mars. The principal objective is to evaluate the transmission properties of these materials with respect to the protons and heavy charged particles in the galactic cosmic rays which bombard the martian surface. The secondary objective is to evaluate fabrication methods which could lead to technologies for *in situ* fabrication. The composites will be prepared by NASA Langley Research Center using simulated martian regolith. Initial evaluation of the radiation shielding properties will be made using transport models developed at NASA-LaRC and the results of these calculations will be used to select the composites with the most favorable radiation transmission properties. These candidates will then be empirically evaluated at particle accelerators which produce beams of protons and heavy charged particles comparable in energy to the radiation at the surface of Mars.

* Corresponding author

STATISTICAL STUDIES OF HETEROGENEOUS AND HOMOGENEOUS NUCLEATION

A.F. Izmailov[1*], J. Zaccaro[2] and A.S. Myerson[3]

[1]Polytechnic University, Six MetroTech Center, Brooklyn, NY 11201
[2]CNRS - Laboratoire de Cristallographie BP 166 38042 Grenoble cedex 09 - France
[3]Illinois Institute of Technology, 3301 South Dearborn St., Chicago, IL 60616

The objective of our study is to build experimental means as well as theoretical treatment allowing discrimination of heterogeneous and homogeneous, primary and secondary nucleation in solutions. Any success in this direction is of paramount importance in planning and controlling microgravity experiments in space.

Primary nucleation is a complex stochastic phenomenon. In the general case its stochastic nature is contributed by at least two independent stochastic sources:

1) Density fluctuations in a metastable (supersaturated) state. These fluctuations are intrinsic to the metastable state of matter and eventually lead to homogeneous nucleation given there are no heterogeneities present.
2) Presence of randomly distributed micro- and macro-heterogeneities in a supersaturated solution. Nucleation on these heterogeneities is known as heterogeneous nucleation.

Therefore, due to the stochastic nature of nucleation, the only way to study nucleation is to gather its sufficient statistics.

In the case of solutions both solute density fluctuations and heterogeneities contribute primary nucleation that results in the birth of solute nuclei. These nuclei themselves might serve as centers of another nucleation phenomenon - secondary nucleation. In order to discriminate all these different types of nucleation it is important to experimentally reproduce homogeneous nucleation and to have means to discriminate it from the heterogeneous nucleation. The heterogeneous nucleation alone has been intensively studied in bulk solutions for years.

The homogeneous nucleation in ground-based experiments can be achieved employing the Electrodynamic Levitator Trap (ELT) technique (see description of the technique in [1-4]). This unique technique allows containerless levitation of a solution microdrop in a chamber with controlled humidity of solvent (water) vapor. The graduate evaporation of water vapor brings the microdroplet through a sequence of states with increasing supersaturation. As it has been demonstrated in our numerous experiments, supersaturations achievable in solution inside of a levitated solution microdroplet are usually *30-100* times higher than the maximum supersaturations reported ever for the same solutes in bulk solutions [1-3]. This alone strongly indicates that nucleation observed in levitated solution microdroplets is homogeneous [see discussion in [1-4]).

In order to gather sufficient nucleation statistics it is required to repeat exactly the same nucleation experiment many times. The ELT technique provides this opportunity due to:

1) capability to produce *virtually identical* microdroplets (*1* part per 10^3 is size and *1* part per 10^4 in electric charge);
2) automation of the evaporation and deliquescence processes.

The quantity measured in these *virtually identical* experiments is induction (lag) time. This time is a stochastic quantity the probability density (distribution) of which is intrinsically related to and derived from the physics of underlying fluctuations of solute density.

In this study we report induction time statistics obtained with microdroplets of ammonium sulfate aqueous solution. We have measured *91* induction times obtained on the base of *16 virtually identical* microdroplets. Each microdroplet was processed through consecutive evaporation – deliquescence cycle at least five times. The relative humidity adopted in these experiments was kept constant as close as possible: it always was within the range of *38.5% - 40%* or better. The plot below represents the uncrystallized fraction of 91 runs versus time elapsed.

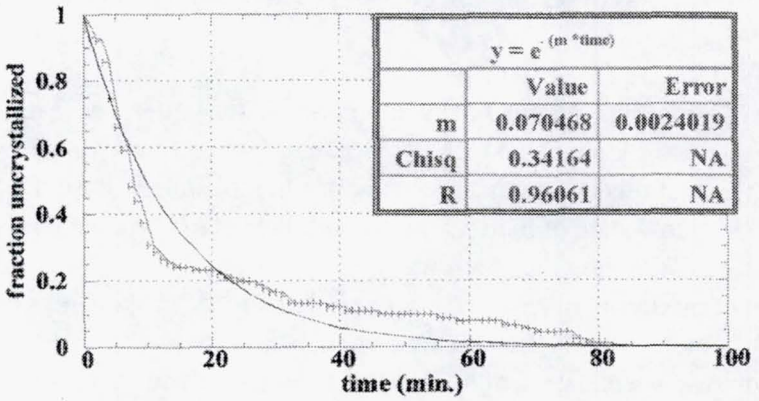

Figure 1. Plot of uncrystallized fraction of 91 runs versus time elapsed.

It is obvious that the experimental curve consists of at least two well distinguishable exponents with transition time at around *10 minutes*. It is natural to ascribe the first exponent, corresponding to shorter induction times, to heterogeneous nucleation, whereas the second one is most likely due to homogeneous nucleation.

REFERENCES

1. A.F. Izmailov and A.S. Myerson and H.S. Na, *Phys.Rev.*, 52E, 3923 (1996).
2. A.F. Izmailov and A.S. Myerson and H.S. Na, *J.Crystal Growth*, 166, 981 (1996).
3. A.F. Izmailov and A.S. Myerson and H.S. Na, *J.Crystal Growth*, 174, 369 (1997).
4. A.F. Izmailov, A.S. Myerson and S. Arnold, *J.Crystal Growth*, 196, 234 (1999).

REDUCTION OF CONVECTION IN CLOSED TUBE VAPOR GROWTH EXPERIMENTS

Robert J. Naumann * and In-Seok Shin

University of Alabama in Huntsville

The objective of this proposed effort is to test a novel method for suppressing convective flows during the growth of crystals by vapor transport in closed tubes to levels approaching those obtained in the microgravity environment. Since the Grashof number scales as the cube of the smallest dimension in the flow system, reduction of the size scale can be extremely effective in reducing unwanted convective flows. However, since materials of practical interest must be grown at least on the cm scale, reduction of the overall growth system is not feasible. But if the region just above the growing crystal could be restricted to a few mm, considerable reduction in flow velocity would result. By suspending an effusive barrier in the growth ampoule just above the growth interface, it should be possible to reduce the convective velocity in this vicinity to levels approaching flows in microgravity. If successful, this growth technique will offer a screening test for proposed space experiments that involve vapor transport to see if reduction of convection will result in improved material and will set a new standard against which the improvements obtained in microgravity may be judged. In addition, it may provide an improved method for preparing materials on Earth whose growth is affected adversely by convection.

The material we have chosen to work with is mercurous chloride. This choice was made for several reasons: 1. It is a technologically interesting acousto-optical material whose usefulness for device applications is still limited by structural defects that have been shown to be related to convection during the growth process by Singh and co-workers at the former Westinghouse Science and Technology Center (now Northrop-Grumman). 2. It is a relatively simple material to grow since it sublimes congruently and grows at low enough temperatures (~400°C) so that a transparent furnace may be employed to monitor the growth process. 3. The material is brightly colored and optically clear at the growth temperature so that the growth interface is easily visible and gross defects can be detected and possibly corrected during the growth process. 4. We, at the University of Alabama in Huntsville, Center for Materials Development in Space (UAH/CMDS), have had experience in growing this material though a previous cooperative agreement with the Westinghouse Science and Technology Center.

However, purification of the starting material has proven more difficult than anticipated. (Our previous experience in growing this system used purified material supplied by Westinghouse, which is no longer available. Commercially available Hg_2Cl_2 is only 95% pure.) Many attempts were made using the multiple stage sublimation purification method published by Singh and co-workers at Westinghouse. The purification apparatus consists of a line of 6 glass chambers connected by smaller diameter tubes. The initial charge is placed in the first chamber and heated to ~100°C while the system was pumped down to ~ 10^{-6} Torr using a turbomolecular pump with a

* Corresponding author

cold trap to remove water and the more volatile impurities. The system is then sealed and the charge is heated to ~250°C and allowed to sublime and condense in the second chamber leaving the less volatile impurities in the first chamber. The first chamber is then sealed off using a methane-oxygen torch and the process is repeated until the final purified material is collected in the sixth chamber.

Several difficulties were encountered. Flakes of the black oxychlorides from the first stage of purification were literally blown through several of the interconnected stages by the vapor pressure as the starting material was heated. This problem was solved by installing porous glass frit discs at the end of each purification stage. Next it was found that the material tended to condense completely around the circumference of the next purification stage. When this chamber is later heated, the large thermal expansion of the Hg_2Cl_2 causes the chamber to break. This problem was finally solved by placing the condensing chambers on a large Al heat sink and placing an infrared line heater above the chamber to drive the condensing material to the bottom of the chamber. After all of this, the final material has to be ground into a powder for loading into the growth ampoules. Even though this is carried out in a dry N_2 glovebox, black oxychlorides and metallic Hg were observed during the growth process, a result of the material's extreme sensitivity to trace quantities of water vapor. Several crystals have been grown using this preparation method, but their quality was poor due to the impurities in the material.

However, it was later found that one could start with commercially available material in a quartz growth ampoule that had been vacuum baked at >800°C, and grow a slug of polycrystalline material. This slug could then be placed in another growth ampoule and used to grow a fair quality crystal that was at least optically clear. The individual quartz growth ampoules are easier to clean and can be baked out at higher temperatures than the multi-stage purification apparatus. Also, the material is kept in the form of a compact slug, which eliminates the large surface area of a powder that can easily become re-contaminated. The process can be repeated until the desired purity is obtained. Crystals grown from materials purified by this technique are now being evaluated.

Because of the difficulties in obtaining highly purified starting materials, progress using the magnetically suspended effusive barrier has been slow. In one attempt to deploy such a baffle, the Fe-Nd magnets used to support the glass frit were apparently heated above their Curie temperature during the fabrication of the quartz growth ampoule and had lost their magnetism. Additional care to protect them during the fabrication process must be taken. Alternatively, a soft ferromagnetic material may be used in which magnetism can be induced after fabrication. This aspect will be addressed once we succeed in growing high quality material without the suspended effusive barrier.

SPACE- AND GROUND-BASED CRYSTAL GROWTH USING A BAFFLE (CGB)

A.G. Ostrogorsky[1], C. Marin[1], T. Peignier[1], T. Duffar[2], M. Volz[3], L. Jeter[3], P. Luz[3]

[1]Center for Microgravity and Materials Research, The University of Alabama in Huntsville, Huntsville, AL 35899
[2]Centre d'Etudes Nucleaires, Grenoble, France
[3]NASA, Marshall Space Flight Center

INTRODUCTION

The composition of semiconductor crystals produced in space by conventional melt-growth processes (directional solidification and zone melting) is affected by minute levels of residual micro-acceleration, which causes natural convection. The residual acceleration has random magnitude, direction and frequency. Therefore, the velocity field in the melt is apriori unpredictable. As a result, the composition of the crystals grown in space can not be predicted and reproduced.

The method for directional solidification with a submerged heater or a baffle was developed under NASA sponsorship [1-3]. The disk-shaped baffle acts as a partition, creating a small melt zone at the solid-liquid interface. As a result, in ground based experiment the level of buoyancy-driven convection at the interface is significantly reduced. In several experiments with Te-doped GaSb, nearly diffusion controlled segregation was achieved.

The investigation "Space- and Ground-Based Crystal Growth with a baffle (CGB)" is funded under NRA-94-OLMSA-06. The key goal of this investigation is to explore the use of the baffle in microgravity conditions. We anticipate that in space experiments, the baffle will reduce the level of natural convection in the melt driven by residual acceleration. The combined effect of microgravity (reduction of gravitational acceleration g by a factor of 10^6) and small zone melt (reduction of L and ΔT by a factor of 10^3) will generate the effective conditions of "nano-gravity" (the Rayleigh number is reduced by a factor of 10^9).

The investigation "Space- and Ground-Based Crystal Growth with a Baffle (CGB)" is funded under NRA-94-OLMSA-06. The investigation passed the Science Concept Review (SCR) on October 8, 1998. The main objective of the present investigation is to develop a method of directional solidification (Bridgman with baffle) which is less sensitive to residual acceleration than the conventional methods. The following systems will be studied:

a) GaSb doped with Te; the equilibrium segregation coefficient k = 0.35.
b) Ga-doped Ge; k = 0.087.
c) Pseudo-binary $(GaSb)_{1-x}(InSb)_x$ doped with Te; $0.001<x<0.01$; k = 0.1
d) Quasi binary $(GaSb)_{0.97}(InAs)_{0.03}$ doped with Te; k = 1.07 to 1.5.

The key goals of CGB are to:

1. Demonstrate a method of directional solidification (submerged baffle) which, in microgravity, yields crystals with *predictable* and *reproducible composition.*
2. Measure the exact shape of the initial transient in composition; the shape will provide the value of the diffusion coefficient of the dopant at the growth interface, D_i .
3. Test the Segregation number [4]
4. Determine if the ground-based experiments with the baffle and magnetic fields are nearly diffusion-controlled.

CGB is a parent investigation to the Materials Science Glovebox (MSG) investigation "Solidification Using the Baffle in Sealed Ampoules"(SUBSA). SUBSA is manifested for the First Utilization Flight 1 (UF1), August 2001, as one of the two first materials science experiments to be conducted at the International Space Station (ISS).

I. Ampoule Design

In the past two years, the ground-based research was focused on the Materials Science Glovebox (MSG) investigation. The flight hardware - furnace for directional solidification - was designed and built by Tech-Masters Inc.

In contrast to terrestrial experiments, space growth has to be conducted in sealed ampoules. Therefore, a key objective of this flight definition research is to design and test a simple and reliable baffle that can be used to grow the semiconductor crystals in sealed silica ampoules. We are currently developing and testing the ampoules with "Automatically Moving Baffles" for SUBSA. The schematic diagram of the ampoule is shown in Figure 1. The baffle is attached to a shaft and a

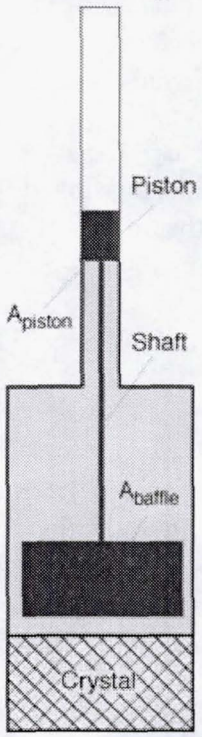

Figure 1. Schematic diagram of "automatic baffle."

piston covering the top surface of the melt. Due to the volumetric expansion during freezing, the melt is pushing on the piston which controls the axial position of the baffle. The ratio between the

cross-sectional area of the piston and the cross-sectional area of the baffle is set equal to the coefficient of volumetric expansion during freezing,

$$\frac{A_{piston}}{A_{baffle}} = \beta = \frac{\rho_l - \rho_s}{\rho_s} \qquad (1)$$

where ρ_l is density of the melt and ρ_s is density of solid at the melting point. During growth, the distance between the baffle and the crystal remains constant regardless of the growth rate or temperature distribution. There is no moving parts outside the ampoule. For MSG investigations we have chosen doped InSb and $InSb_{1-x}CdTe_x$ quasi-binary alloy because of the low melting point (512°C) , and high coefficient of volumetric expansion during freezing (β=12.5 %). The design of the ampoule with the automatic baffle, the parts and the motion of the baffle during a growth cycle is shown in Figure 2.

a) Beginning of Melting: The first spring extends until the piston touches the shoulder in the ampoule. Subsequently, the second spring will start extending.

b) End of Melting: The diameter of the baffle shaft is dimensioned to compensate for the reduction in volume during melting. Thus, the solid/liquid interface always stays 10 mm away from the baffle.

c) Growth: During freezing, because of the volumetric expansion, the baffle slowly returns in its original position, remaining always 10 mm from the interface.

d) End of Growth: The baffle is frozen in the crystal.

Figure 2. Motion of the automatic baffle during directional solidification.

Figure 3 shows a photograph of the ampoule with the automatic baffle developed at the Center for Microgravity and Materials Research, (CMMR). Figure 4 shows a photographs of the furnace for the Materials Science Glovebox investigation SUBSA developed by Tech-Masters Inc. Tech-Masters Inc. is testing and calibrating this furnace using ampoules with the baffle (such as the one in Figure 3) .

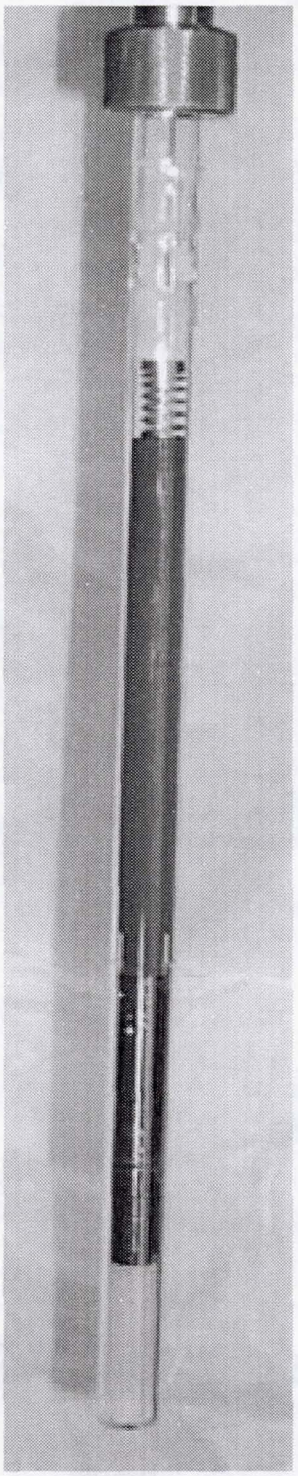

Figure 3. Sealed ampoule for SUBSA.

II. Ground Crystal Growth Experiments

Directional solidification as conducted in a low pressure Electro Dynamic Gradient (EDG) "Mellen" furnace with 18-heating elements (zones). The temperature of each control thermocouple was controlled by a computer, with 14 ½ bit resolution (corresponding to 0.03 °C resolution).

Numerous experiments were conducted with doped InSb. We focused on dopants having equilibrium segregation coefficient k $>$ 1, *e.g.*, Ca, Zn and Ga. Two growth experiments were conducted

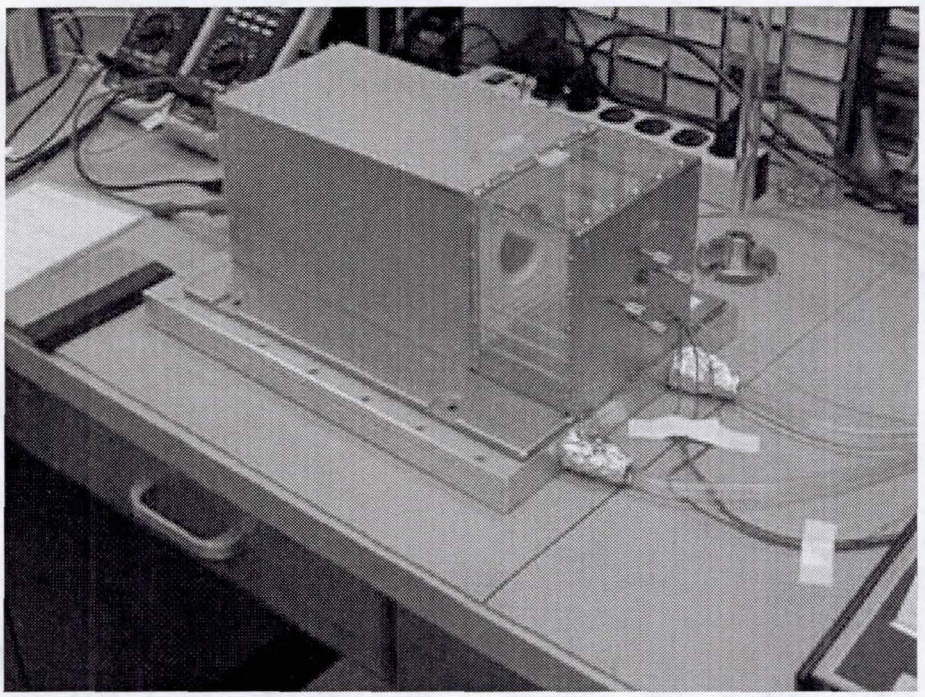

Figure 4. Furnace for MSG investigation developed by Tech-Masters Inc.

by melting together pre-synthesized InSb and CdTe, to form a melts having a composition $(InSb)_{1-x}(CdTe)_x$ [6]. Our goal was to determine whether in the grown crystals the concentration of Cd will remain equal to the concentration of Te. Note that the segregation coefficients of Cd and Te in InSb are different: k_{Cd}= 0.25 and k_{Te} = 0.6 respectively.

The charge was etched and rinsed. The 8 mm ID, sphere-shaped bottom, silica ampoule, was etched with HF, rinsed in DI water and methanol. The charge was kept at 250°C under vacuum for 15 hours and subsequently sealed in argon pressurized slightly below one atm. The temperature in the Mellen furnace was kept at 540°C for 25 hours, to allow dissolution of CdTe in InSb. Mechanical vibrations were imposed on the ampoule at irregular intervals (every 2-3 hours) to enhance the dissolution of CdTe and homogenize the melt. The melt was solidified by lowering the ampoule at 3.23 mm/h through the temperature gradient.

Figure 5 shows typical tip-nucleated crystals grown in the 8 mm ID silica ampoules. The grown crystals were free of cracks, which can be explained by the exceptionally low lattice mismatch.

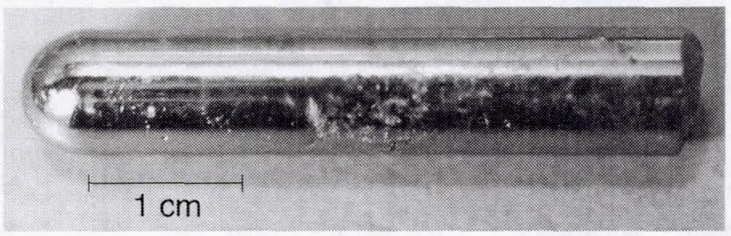

Figure 5. Tip-nucleated specimen *InSbCdTe#2*

Figure 6 shows the axial composition in the specimen *InSbCdTe#2* determined using the Electron Probe Micro-Analysis (EPMA). The concentration of Cd remained equal to the concentration of Te throughout the specimen. Since the equilibrium segregation coefficient of Cd (k=0.25) and Te (k=0.5 to 1) in InSb are notably different [7] our experiments seem to indicate that: (i) Cd and Te

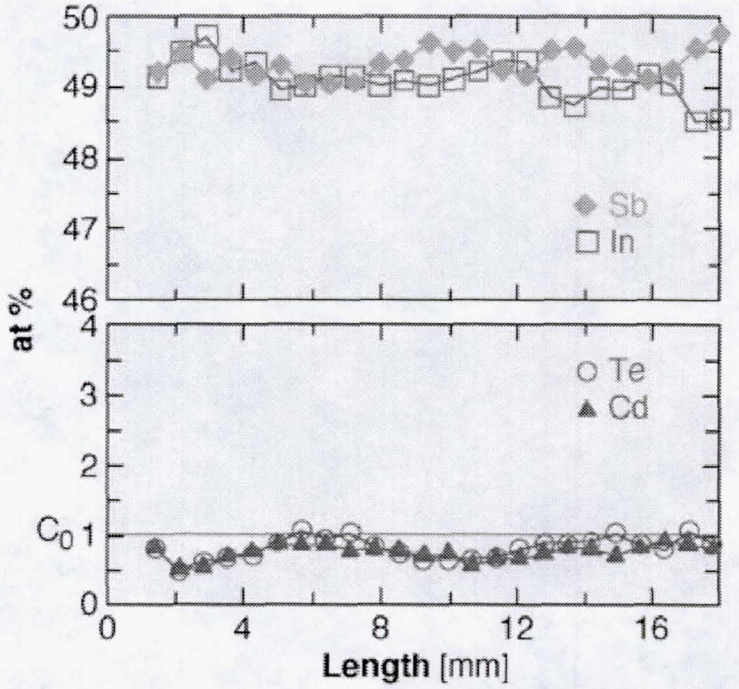

Figure 6. Axial composition of *InSbCdTe#2*; initial melt composition $C_0 = 2\%$ of CdTe, i.e., 1% Cd and 1% Te. Note $k_{Cd} = 0.25$ and $k_{Te} = 0.6$

remain associated in the InSb melt, and (ii) CdTe molecules are absorbed at the phase boundary. Therefore, the composition of these crystals is quasi-binary $(AB)_{1-x}(CD)_x$, not quaternary $A_xC_{1-x}B_yD_{1-y}$. The constraint x=y is held. Since the initial melt coposition is known) (2 % of CdTe, *i.e.*, 1% Cd and 1% Te), the effective segregation coefficient $k_{effective}$ of CdTe in InSb can estimated to be ~1. This favorable segregation coefficient may be related to the negligible lattice mismatch (0.0027 %).

III. Numerical Modeling

Numerical modeling is an integral part of our research in preparation for CBG and SUBSA. For modeling, we are using the finite code NEKTON [8], which is based on "macro" (spectral) finite elements. The numerical simulations are used:

- as a design tool, to optimize the geometry and the temperature field in the furnaces;
- as a research tool, to study the transport processes in different melt-dopant systems.

IV. Value to Scientific Field

If SUBSA and CGB yield the expected results, directional solidification with the baffle may become a preferred technique for directional solidification in space. The experiments will demonstrate that the baffle, without additional expense and drawbacks, will reduce the natural (*i.e.* free buoyancy-driven) convection in the melt to the point that it will not affect segregation. Furthermore, for the first time, we will measure precisely the diffusion coefficient at the growth interface, which is needed for interpretation of space experiments and modeling.

REFERENCES

1. A.G. Ostrogorsky, J. Crystal Growth 104 (1990) 233.
2. A.G. Ostrogorsky, F. Mosel and M.T. Schmidt, J. Crystal Growth 110 (1991) 950-954.
3. A.G. Ostrogorsky and G. Müller, J. Crystal Growth 137, (1994) 64-7
4. A.G. Ostrogorsky, Z. Dagojlovic, Proceedings of the International Aerospace Congress, Moscow (1994).
5. T. Duffar, A. Ostrogorsky and P. Dusserre Automatically Moving Baffle, Patent Number 98400833.4-2014, France, 1998.
6. C. Marin, A.G. Ostrogorsky, Bulk Growth of Quasi-binary Alloys,J.Crystal Growth 211 (2000) 194-201.
7. Handbook of Chemistry and Physics, CRS Press, 60th edition, 1980.
8. NEKTON 2.85 Users Manual, (1994).

ANALYSIS OF CONTAINERLESS SOLIDIFICATION MICROSTRUCTURES IN UNDERCOOLED MELTS AND COMPOSITE SYSTEMS

J.H. Perepezko

University of Wisconsin-Madison, 1509 University Avenue, Madison, WI 53706
phone: (608) 263-1678; perepezk@engr.wisc.edu

I. Objective and Application to Microgravity Knowledge Base

The main research objective is the evaluation and analysis of the undercooling and resultant solidification microstructures in containerless processing, including drop tube processing and levitation melt processing of selected alloys and composites. The results are intended for use as an experience base for the design of space-based microgravity experiments.

Containerless processing in ground-based drop tubes simulates microgravity conditions via solidification of liquid samples under free fall conditions. The containerless environment is also attained in levitation melt processing and removes a major source of impurities and heterogeneous nucleation sites, allowing for a large melt undercooling. This enhanced liquid undercooling exposes alternate solidification pathways, allowing for the formation of novel microstructures. Controlling the undercooling level provides some control of the operative solidification pathway and the resultant microstructure. The novel structures that may be produced in a ground-based containerless processing facility preview the wide range of possible materials processing experiments that may be conducted in a space-based laboratory. The results of the ground based study will be used to identify critical experimental variables in microgravity processing and the analysis can be used to design and define the science and hardware requirements for extended duration space experiments.

II. Research Task Description

The ground based program represents a balanced experimental and analysis effort directed toward the investigation of drop tube and levitation containerless processing methods. The investigation focus is on the understanding and analysis of microstructural evolution during solidification of undercooled melts. The liquid undercooling level in a laboratory scale (3 m) drop tube and levitation melting system can be altered through the variation of processing parameters such as alloy composition, melt superheat, sample size and gas environment. The solidification behavior is evaluated through metallography, thermal analysis and x-ray diffraction in conjunction with calorimetric measurements of falling droplets and a heat flow model of the processing conditions to judge the sample thermal history.

III. Solidification of Metal-Matrix-Composites

A central component of the proposed program addresses the use of containerless processing together with an undercooled melt containing incorporated particles to develop a critical evaluation of solidification front-particle interactions. In the solidification of composites the interaction be-

tween the solidification front and particles is central to effective processing. Undercooled liquid solidification simulates convection-free solidification conditions for such composites in a 1g environment. Numerous models for the interaction behavior have been proposed, but critical tests are lacking in many cases due to confounding gravitational effects. A common concept in the interaction models is the critical velocity for particle incorporation. Theoretical predictions of the behavior of the particles *i.e.* if they are either engulfed or pushed, as well as most of the experimental analyses [1-3] have been conducted under the constraint of planar interfaces. Such an idealized boundary condition is unlikely to be realized during application-relevant processes where dendritic patterns are common. The morphology of dendritic interfaces introduces a third mode for the resulting distribution of particles within the solidified sample. Besides engulfment and pushing an entrapment of particles in interdendritic or intercellular spaces is likely to occur and result in the confinement of the particles at the grain boundaries of the metallic matrix. It is intended to use a novel experimental design based upon an undercooled melt with particles to distinguish particle incorporation effectiveness as a function of undercooling in the presence of a distribution of particle sizes.

Powders of the pure metals Cu and Ni were mechanically blended with different nonmetallic powders and cold compacted in a hydraulic laboratory press. Levitation melting and differential thermal analysis provided the initial testing routine with respect to the compatibility of the different composite materials. It was found that the composite systems Cu/Al_2O_3, Cu/Ta_2O_5 and Ni/Ta_2O_5 are well suited for the experimental study of the incorporation behavior. In all three composite systems, oxide particles remained within the sample after melting the metallic matrix. Ta_2O_5 is of special relevance for this study, because it offers one of the highest densities of the stable oxides. Thus, the density driven buoyancy is minimized in the Cu/Ta_2O_5 and Ni/Ta_2O_5 composites thus simulating buoyancy-neutral experiment conditions in terrestrial settings.

In order to achieve variable undercooling levels before the onset of crystallization, DTA samples were encased in a flux of a borosilicate glass (Pyrex) to clean the surface from uncontrolled but potent nucleation sites such as *e.g.* the native oxides of the matrix metals. Figure 1 shows the DTA curves of Ni-Ta_2O_5 (a) and Cu-Ta_2O_5 (b) composite samples. For both composite samples, an undercooling, ΔT was observed during cooling. The Ni-Ta_2O_5 sample (Figure 1a) crystallized at 1260°C for a ΔT=195°C while the Cu-Ta_2O_5 composite (Figure 1b) crystallizes at 947°C for a ΔT=138°C [4]. The samples studied in this work contain dispersed, crystalline particles, but nevertheless undercool readily by more than 100°C and - as shown in Figure 1a for the case of Ni-Ta_2O_5 - even exceed a value of $\Delta T = 200°C$. Yet, these undercooling levels are less than the maximum values. This result emphasizes the small, but not negligible, heterogeneous nucleation potential of the oxide particles.

The effect of different levels of undercooling on the resulting microstructure is shown for the Ni/Ta_2O_5 composite system in Figure 2. The average particle diameter is 3μm. At low undercooling *i.e.* $\Delta T = 37$ K (Figure 2-a) the particles are confined in regions at the bottom of the sample. Microstructure analyses on splat-quenched samples have shown that the particles are distributed homogeneously inside the liquid sample. Thus, the microstructure shown in Figure 2a is a result of particle movement (pushing) produced by the moving solidification front. In contrast, Figure 2b shows an approximately homogeneous distribution of particles throughout the sample. A fraction of particles are confined at grain or cell boundaries, but many particles can also be found inside grains. This microstructure indicates that particle engulfment into the dendritic solidification front has occurred at the growth velocity that corresponds to an achieved undercooling of $\Delta T = 194$ K. The transition from particle pushing at lower undercooling *i.e.* the lower growth velocities to

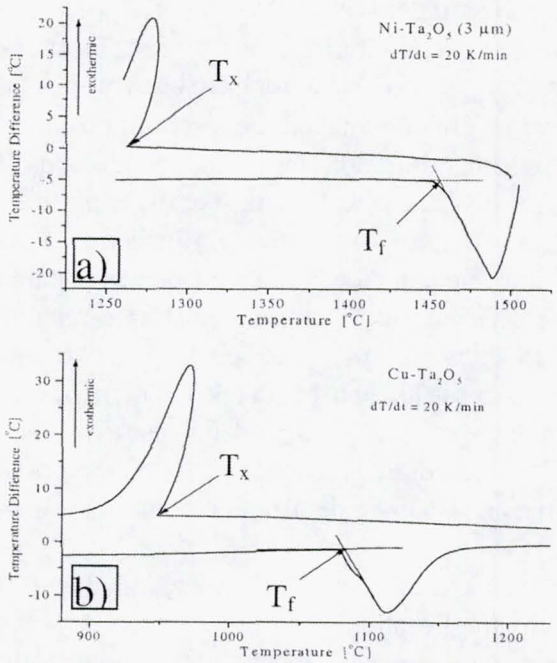

Figure 1. DTA-heating and cooling curves for glass encased (a) $Ni\text{-}Ta_2O_5$ and (b) $Cu\text{-}Ta_2O_5$. Heating and cooling rates were 20 K/min.

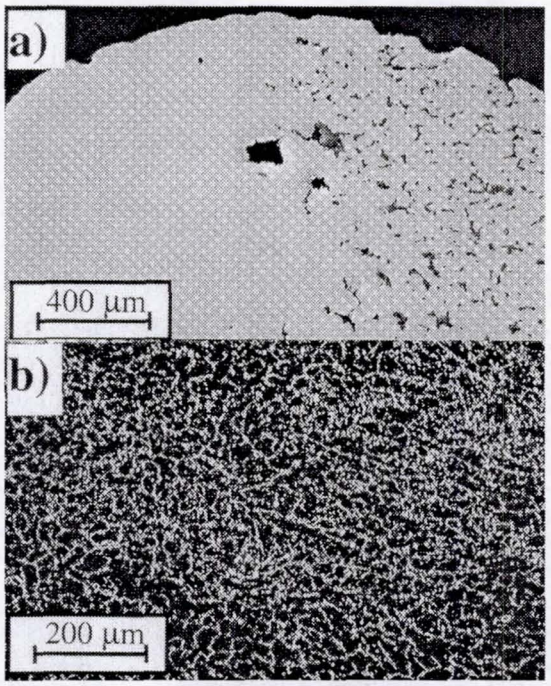

Figure 2. The polished cross-section of Ni/Ta_2O_5-composite samples which undercooled by (a) 37 C and (b) 194 C. Micrograph (b) was taken by using polarized light.

engulfment at larger rates of the interface movement (*i.e.* undercooling larger than $\Delta T \cong 90$ K) corresponds to the basic assumption of the kinetic models. The experiments on the Cu/Ta_2O_5 composite revealed qualitatively the same dependence: pushing at smaller undercooling and engulfment at $\Delta T \geq 60$ K of undercooling. The maximum critical velocities as functions of the particle radius were calculated for the Cu/Al_2O_3 composite system according to relations presented in references [5-7]. The calculated critical velocities for the particle sizes which were used for the

experiments (1.5 μm < R < 55 μm) are in the range of 10^{-3} to 10^{-5} m/s. Thus, the average critical velocities according to existing models are much less than 1 cm/s. Critical velocities of the same order of magnitude were calculated for the Ta_2O_5-containing composites. From given experimental data for the growth velocity of pure Ni [8] and pure Cu [9] as functions of undercooling, the critical undercooling, ΔT_c, which correspond to the calculated critical interface velocities for particle engulfment have been derived. The ΔT_c values are less than 5 K for all the composites studied. Thus, according to the kinetic models and in contradiction to the experimental results, engulfment should have taken place in all of the systems at the observed undercooling. The large difference between experimental and theoretical values cannot be explained by the uncertainty of the materials parameters. Experimental data for the growth velocity of undercooled metal-matrix composites does not exist. However, experience indicates that the growth velocity of the levitated sample at the undercooling observed is well in excess of 1 m/s. Quantitative measurements of the growth velocity in dependence of undercooling during containerless processing of composites are necessary for a complete evaluation.

The current studies have established that large undercooling levels in the presence of particles can be achieved and provide a suitable means to study the interaction of free dendrites with incorporated particles at variable growth velocities excluding the influence of thermal convection inside the liquid matrix. The interaction of a fast-moving, dendritic solidification front with dispersed particles during solidification processing of metal-matrix composites have revealed a new mode of the incorporation behavior that is not included in existing models and has not been experimentally accessed previously. Detailed studies of the effects of different experimental factors are now in progress to yield a clear understanding of the particle/solidification-front interaction that is needed to evaluate more complete analytical models. These studies will provide a database for future space experiments where the incorporation behavior can be analyzed under various conditions in the absence of the detrimental influence of convection. The combination of ground-based studies and experiments under microgravity conditions will provide an understanding of the key parameters of the particle incorporation process that can also lead to improved processing strategies.

IV. Duplex Partitionless Solidification

Lattice parameter measurements on splat-quenched Cobalt-Aluminum and Niobium-Palladium indicate that both systems solidify, similarly to Ni-V, as a two-phase structure consisting of supersaturated solid solution phases of different crystal structure. However, detailed SEM and TEM investigations of the solidification products as well as model calculations concerning the nucleation and growth kinetics during the present program show that the duplex structures discovered in Co-Al and Nb-Pd do not result from simultaneous nucleation of two phases [10]. Instead, both systems show a preferred nucleation and growth of the bcc-phase, followed by a solid-state transformation to form the fcc-phase. Further TEM-investigations will be used to characterize the transformation.

Completion of the nucleation kinetics analysis represents a main point of this part of the proposed program. The appearance of microstructural transitions affords valuable opportunities to examine competitive kinetic processes. At a kinetic transition the relative rates for competing processes approach a balance which in effect provides a useful constraint on the model based rate analysis calculations. Although a phase transition in the thermodynamic sense is a sharp change, a kinetic transition need not be sharp; especially for the processes involved in a nucleation reaction. Nucle-

ation transitions are probabilistic in nature so that a competition between one structure and another will occur over a range of processing conditions. The range of conditions over which a transition is observed can also offer a useful measure of the relative kinetic rates, J and the potency and concentration of nucleants.

The phase competition can be illustrated by Figure 3. In this simple eutectic system, a competition exists between the phases α and β. For simplicity the liquidus and T_0 temperatures for both phases have been assumed linear. Previous work [11] has found that the trend of the nucleation temperature often follows the trend of the alloy liquidus; thus the slopes of the T_n curves have been taken to be the same as those of the liquidus curves. Therefore the nucleation temperature of phase i (i = α or β) may be taken as

$$T^i_n(x) = T^c_n = m^i_L (x - x_c) \qquad (1)$$

where T^c_n and x_c represent the temperature and composition of the crossover of nucleation temperatures. The liquidus slopes have been defined with respect to the B component; thus in this diagram, $m^{\alpha}_L < 0$ and $m^{\beta}_L > 0$.

In this analysis, nucleation will be treated as steady state and the two phases are assumed to nucleate independently. The possibility of cooperative nucleation will be considered in later analysis. The nucleation frequency, J, at a given composition has been approximated over a small temperature and composition range by assuming that the nucleation barrier is constant [11]. This is a reasonable approach at relatively high undercooling levels, since the barrier (*i.e.*,$\Delta G^*/kT$) does not change as rapidly under these conditions. For the duplex partitionless reaction where both products develop by the same kinetic mechanism this condition yields a considerable simplification of the nucleation analysis to account for the composition range over which the reaction is observed. The basis for the rate analysis is illustrated in Figure 1a where the crossing point is at a temperature T_n. In order to express the change in J due to a change in temperature δT from T_n, a Taylor expansion is used. The derivative d *ln* J / dT evaluated at T_n is given by the symbol Φ ($\Phi<0$ above the maximum of the nucleation frequency curve). Note that since the nucleation barrier has been taken as constant, Φ is a constant.

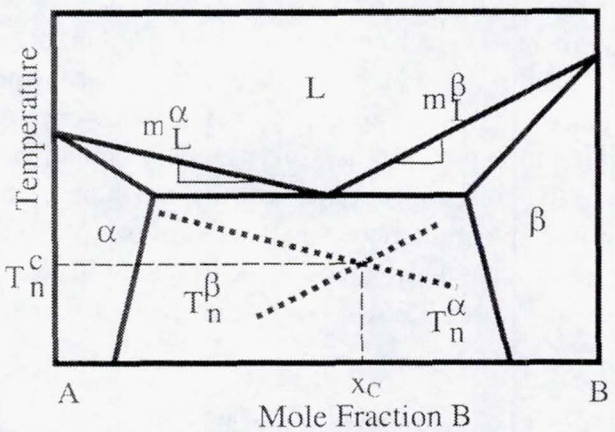

Figure 3. Schematic eutectic phase diagram showing α and β phase with liquidus slopes m^{α}_L and m^{β}_L. The $T_n{}^{\alpha}$ and $T_n{}^{\beta}$ curves cross at the temperature T^c_n and composition X_c.

The analysis requires an estimate of the temperature deviation, $\delta T'$, from T_n needed to change the nucleation frequency by a factor of K (K>1). The range of compositions for which the nucleation

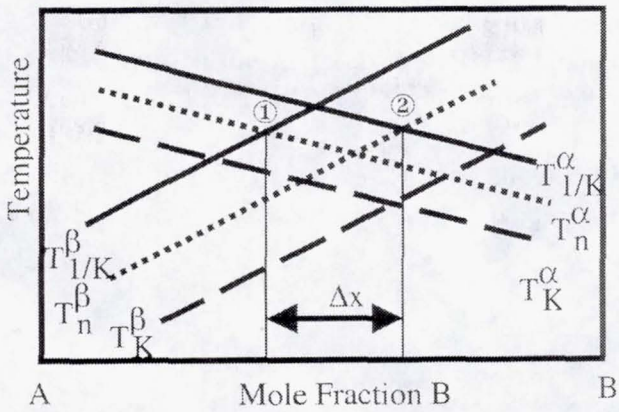

Figure 4. Expanded view of the nucleation temperature crossover region. The curves T^{α}_{n} and $T^{\beta}_{1/K}$ intersect at point 1, and T^{α}_{n} and T^{β}_{1K} intersect at point 2.

frequencies for α and β are within a factor K may be obtained by defining the compositions x_1 and x_2 (refer to Figure 4). The total range of duplex phase formation, Δx, may be obtained as

$$\Delta x = (x_2 - x_1) = \frac{\ln K}{(m_L^{\alpha} - m_L^{\beta})} \left[\frac{1}{\Phi^{\beta}} + \frac{1}{\Phi^{\alpha}} \right] \qquad (2)$$

Equation (2) may be used to describe the conditions for duplex phase formation in several different cases. For most metallic systems $|m_L| \approx$ 1-10 K/at.%. The parameter Φ strongly depends on the nucleation mechanism and the temperature. The heterogeneous nucleation kinetics of the Ni-V system has been modeled previously [12]. Based on [12], the heterogeneous nucleation frequencies for α-fcc and β-bcc in the composition range of interest showed that J changed by -8%/K for fcc and -9%/K for bcc near T_n; thus $\Phi^{\alpha} = -ln(1.08)$ and $\Phi^{\beta} = -ln(1.09)$. Thus, with $m^{\alpha}_{L} = -8.4$ K/at.% and $m^{\beta}_{L} = +5.5$ K/at.%, then the predicted range of duplex phase formation is about 4.1 at.%. This result compares well with the experimental observation that the structure develops over a range of about 5 at.%. Moreover, the duplex phase formation conditions that are incorporated in equation 8 reveal that useful guidance can be obtained from a simplified analysis. For example, the observation of the reaction over wide composition ranges is favored for alloy phase diagrams that display shallow liquidus curves for each of the competing phases. This feature is again in agreement with the reported examples. The analysis approach is being extended to allow for the construction of a processing map that will be essential in the design of a space experiment. This investigation contributes to the understanding of terrestrial solidification processing and demonstrates that microgravity processing methods can yield novel microstructures and phases that have not been observed with conventional processing approaches.

REFERENCES

1. S.N. Omenyi and A.W. Neumann, *J. Appl. Phys.*, 47, (1976) 3956.
2. J. Cissé and G.F. Bolling, *J. Cryst. Growth*, 10, (1971) 67.
3. D.M. Stefanescu, A. Moitra, A.S. Kacar and B.K. Dhindaw, *Metall. Trans. A*, 21A, (1990) 231.
4. G. Wilde, M. Byrnes and J.H. Perepezko, *J. Non-Cryst. Solids,* 250-252 (1999) 626.
5. J. Pötschke and V. Rogge, *J. Crystal Growth*, 94, (1989) 726.
6. D.M. Stefanescu and B.K. Dhindaw, "*Metals Handbook*", ASM, Vol. 15 (casting), (1988)142.
7. D. Shangguan, S. Ahuja and D.M. Stefanescu, *Metall. Trans A*, 23A, (1992) 669.
8. R. Willnecker, D.M. Herlach and B. Feuerbacher, *Phys. Rev. Lett.*, 62, (1989) 2702.

9. T. Suzuki, S. Toyoda, T. Umeda and Y. Kimura, *J. Crystal Growth*, 38, (1977) 123.
10. H. Sieber, D.R. Allen and J.H. Perepezko in *Solidification 1998*, eds. S.P. Marsh, J.A. Dantzig, R. Trivedi, W. Hofmeister, M.G. Chu, E.J. Lavernia and J.-H. Chun, TMS, 1998, p. 15.
11. J.H. Perepezko and J.S. Paik, Mat. Res. Soc. Symp.Proc., 8 , 49 (1982).
12. D.R. Allen and J.H. Perepezko, Mat. Sci. Res. Symp. Proc., 398, 57 (1995).

DEVELOPMENT OF A SPACE RADIATION MONTE-CARLO COMPUTER SIMULATION BASED ON THE FLUKA AND ROOT CODES

L.S. Pinsky[1], T.L. Wilson[2], A. Ferrari[3], Paola Sala[4], F. Carminati[5] and R. Brun[6]

[1] University of Houston
[2] NASA, Johnson Space Center
[3,4] INFI, Milan, Italy
[5,6]CERN, Geneva, Switzerland

INTRODUCTION

The radiation environment in space is a complex problem to model. Trying to extrapolate the projections of that environment into all areas of the internal spacecraft geometry is even more daunting. With the support of our CERN colleagues, our research group in Houston is embarking on a project to develop a radiation transport tool that is tailored to the problem of taking the external radiation flux incident on any particular spacecraft and simulating the evolution of that flux through a geometrically accurate model of the spacecraft material. The output will be a prediction of the detailed nature of the resulting internal radiation environment within the spacecraft as well as its secondary albedo. Beyond doing the physics transport of the incident flux, the software tool we are developing will provide a self-contained stand-alone object-oriented analysis and visualization infrastructure. It will also include a graphical user interface and a set of input tools to facilitate the simulation of space missions in terms of nominal radiation models and mission trajectory profiles.

The goal of this project is to produce a code that is considerably more accurate and user-friendly than existing Monte-Carlo-based tools for the evaluation of the space radiation environment. Furthermore, the code will be an essential complement to the currently existing analytic codes in the BRYNTRN/HZETRN family for the evaluation of radiation shielding [1]. The code will be directly applicable to the simulation of environments in low earth orbit, on the lunar surface, on planetary surfaces (including the Earth) and in the interplanetary medium such as on a transit to Mars (and even in the interstellar medium). The software will include modules whose underlying physics base can continue to be enhanced and updated for physics content, as future data become available beyond the timeframe of the initial development now foreseen. This future maintenance will be available from the authors of FLUKA as part of their continuing efforts to support the users of the FLUKA code within the particle physics community. In keeping with the spirit of developing an evolving physics code, we are planning as part of this project, to participate in the efforts to validate the core FLUKA physics in ground-based accelerator test runs. The emphasis of these test runs will be the physics of greatest interest in the simulation of the space radiation environment.

Such a tool will be of great value to planners, designers and operators of future space missions, as well as for the design of the vehicles and habitats to be used on such missions. It will also be of aid to future experiments of various kinds that may be affected at some level by the ambient radiation environment, or in the analysis of hybrid experiment designs that have been discussed for space-based astronomy and astrophysics. The tool will be of value to the Life Sciences personnel involved in the prediction and measurement of radiation doses experienced by the crewmembers on such missions. In addition, the tool will be of great use to the planners of experiments to measure and evaluate the space radiation environment itself. It can likewise be useful in the analysis of safe havens, hazard migration plans, and NASA's call for new research in composites and to NASA engineers modeling the radiation exposure of electronic circuits. This code will provide an important complimentary check on the predictions of analytic codes such as BRYNTRN/HZETRN that are presently used for many similar applications, and which have shortcomings that are more easily overcome with Monte Carlo type simulations. Finally, it is acknowledged that there are similar efforts based around the use of the GEANT4 Monte-Carlos transport code currently under development at CERN. It is our intention to make our software modular and sufficiently flexible to allow the parallel use of either FLUKA or GEANT4 as the physics transport engine.

I. Analytic and Monte Carlo-Based Codes

Since the 1960's many different radiation transport simulation codes have been developed [2-8]. The diversity in this development is the result of the wide variety of applications for which these codes are employed. These include uses as diverse as the estimation by NASA of flight crew radiation doses and the related problem in cancer treatment of estimating the delivered therapeutic radiation dose, to the use of these codes in the evaluation of data in accelerator-based elementary particle physics experiments. Indeed, the group at NASA/Langley under the able direction of Townsend and Wilson have played a lead role in the development of one of the most heavily used tools in routine use by NASA for this simulation problem [1]. Their work has pioneered what is termed the *analytic* method in contrast to the *Monte-Carlo* method. The Monte Carlo method has evolved in and become more widely used in the world of experimental particle physics. The present study is in the process of developing a new integrated Monte-Carlo software package, specifically tailored for use in the simulation of the space radiation environment, to address design problems, astronaut dosimetry calculations, and astrophysical payload design. The new code is to be based upon the melding together of two existing evolving codes, FLUKA [2-3, 5, 9-14], a Monte-Carlo radiation transport program, and the object-oriented physics analysis infrastructure known as ROOT [15-16].

In the early years of manned spaceflight the need existed then as now to predict and evaluate the effect of shielding on the radiation that flight crews are exposed to in space [17-20]. The choice of technique was driven in earlier times by the relatively modest capability of available computing power. Over the intervening years, with the exponential growth in both the hardware and software capability, the potential for extending the Monte-Carlo technique into applications that had once been impractical, has now become feasible. While there is still a clear need to pursue the development of both techniques, as recognized recently in the recommendations from the NASA sponsored Workshop on Predictions and Measurements of Secondary Neutrons in Space (NASA/JSC, 28-30 September, 1998) [21], the analysis discussed here is specifically directed towards the need to provide a state-of-the-art Monte-Carlo based code. The uses for the proposed radiation transport simulation that are of interest to the NASA community go well beyond just providing a complimentary technique for the evaluation of the radiation doses endured by

both crews and hardware (NASA's Code U). They also include the ability to provide detailed simulation of experiments such as the ACCESS (Advanced Cosmic Ray Composition Experiment for the Space Station) experiment that is currently being considered for deployment on the ISS (NASA's Code S). (The ACCESS Home Page may be viewed at http://www701.gsfc.nasa.gov/access/access.htm). This latter type of application is the sort for which the analytic type tools are least well suited, and for which the Monte-Carlo type are most beneficial.

II. FLUKA

FLUKA was originated by Professor Johannes Ranft beginning in 1970 for simulating particle cascades (FLUKA is acronym formed from the German for "Fluctuating Cascade") [22-25]. Professor Ranft has ceded control over the continued development of FLUKA to the INFN (Instituto Nazionale di Fisica Nucleare—the Italian National Nuclear Physics funding agency) group at the University of Milan. The individuals primarily responsible are a husband and wife team, Drs. Alfredo Ferrari and Paola Sala. Dr. Federico Carminati, who is currently the simulation coordinator for ALICE (the heavy-ion experiment being built for the Large Hadron Collider [LHC] project at CERN) is also a key person in the evolution of FLUKA. He was previously the manager for GEANT at CERN and he was responsible for porting FLUKA to the UNIX (including LINUX) operating system from VMS.

FLUKA is also a "biased" code. That is, FLUKA is designed to allow internally for the biasing in favor of the occurrence of rare events. This provides for their simulation at a higher than normal frequency. Such a feature allows the user to acquire statistics on rare events much faster than in linear codes. FLUKA automatically keeps track of this accounting and can do so for all of the internally simulated physics as well as for external packages. Thus, one does not have to play with the inputs and do off-line recombinations to assemble the outputs.

Further, FLUKA embeds the technology for simulating the transport of low-energy neutrons developed over 30 years by the nuclear reactor community. The cross-section libraries have been based upon the most recent data from JEF-1, JEF-2.2, ENDF/B-VI (the most recent compilations from Los Alamos), and JENDL-3. More than 60 different materials are included with temperature ranges extending down to cryogenic temperatures. This code has been used extensively to model the neutron environments near high energy physics experiment shielding and the associated databases, and can easily be updated when new compilations become available. FLUKA also embeds the well-known EGS code mentioned above to treat electromagnetic interactions. Ralph Nelson from SLAC, the principal party responsible for the EGS code, has publicly declared that FLUKA's implementation of EGS IV is "the best version of EGS IV on the market." FLUKA is arguably the most accurate integrated simulation available at the present time. Recently the ATLAS collaboration from the LHC project at CERN did a side-by-side comparison of all of the available Monte-Carlo codes and concluded at least for calorimetry applications that FLUKA is the best currently available code. Finally, FLUKA, is a maintained and updated code that can be expected to improve continuously over the foreseeable future. Information on FLUKA is also available at http://www.mi.infn.it/~battist/fluka.html.

Given FLUKA's comparative excellence as a radiation transport code, the question arises as to what modifications are required to make it useful for the routine simulation of the space radiation environment? First, although the FLUKA team is in the process of adding the complete range of heavy-

ion interactions needed to simulate the propagation of the heavy cosmic rays, it is not their highest priority, and assistance is needed to facilitate that implementation. Other physics improvements will be incorporated in the core physics code by the FLUKA team as they become available. Such enhancements will also continue to occur beyond the time of this proposed project's conclusion.

Secondly, since the FLUKA code was first designed, there has been substantial progress in the development of 3-D geometry software. Driven by computer graphics technology and ray-tracing applications, many new 3-D geometry packages are available. There is considerable room for improvement in the present geometry package used in FLUKA. The benefits of such an improvement would include an increase in the calculation speed during propagation simulations, and the additional bonus of easy access to industry-standard input and graphic display formats. The FLUKA team is interested in working with this proposed project to implement such an improvement.

However, beyond the need for some physics additions and internal geometry enhancements, the major reason that FLUKA is not more widely used is the awkward nature of the present interface to the code. Admittedly, the current input format is archaic and limited. Furthermore, the tools available to structure the form of the output are also limited and difficult to use. To address these limitations, the thrust of the project proposed here is to meld FLUKA together with the recently released physics analysis infrastructure known as ROOT. This task will require an intimate conversion of the FLUKA data structures as opposed to the simple serial attachment of one code to another.

III. ROOT

ROOT, which is rapidly becoming a major force in the world of particle physics analysis software, is the product of Dr. Rene Brun of CERN [15]. Dr. Brun is widely known in the particle physics software community. He is the original author of GEANT 3.21 and was the director of analysis software development at CERN for many years. In fact Tim Berners-Lee developed the World-Wide-Web while working under Dr. Brun at CERN. Dr. Brun also developed the widely used PAW (Physics Analysis Workstation) software tools.

Dr. Brun initially embarked on the project known as ROOT to address the specific limitations of PAW. However, during its development ROOT evolved into much more than a simple update of PAW. It has become not only an analysis and a visualization software program in one package, but a complete data handling infrastructure. At its heart, ROOT is based upon Object-Oriented (OO) data structures. This use of OO programming allows many difficult tasks with multiple uses to be done only once. For example, after the task of inputting the complex geometry of the ISS is done once, that same information can be used seamlessly as the input for the Monte- Carlo transport calculations. The same data structure can then be applied to visualizations of individual Monte Carlo events in a fly-through 3-D event viewer, or for choosing regions to provide plots of individual summed parameters. In fact, it can be employed for any analysis or display uses that need to specify or depict some portion of or indeed the entire structure in question. The best feature of ROOT is that much of the manipulation is provided via GUI (Graphical User Interface) menus and displays. Further, when special features need to be added, ROOT uses C++ as a scripting language. This implementation of the scripting language allows the user to create structures and functions that blend seamlessly into ROOT, providing a real user-extension of the system. Moreover an intelligent pre-

processor completely solves the problem of persistency of objects in disk storage. ROOT features and examples can be viewed on the Web at http://root.cern.ch. That site also contains the downloadable software with accompanying tutorials.

IV. Description of the Current Project

The goal of this study is to produce a well-documented code that can be widely distributed and employed by a variety of users. It is anticipated that the core project will be completed within three years.

In addition to the development of the code itself, databases will also be included to allow ease of simulation of the ambient radiation environment in space. Models of the trapped radiation, the galactic cosmic radiation, the modulation effects of the solar cycle, the albedo from the Earth's atmosphere, and a variety of solar flare examples will be included. Tools will be provided to allow users to tailor the inputs to specific mission profiles.

To accomplish our immediate task we would have liked to be able to modify the geometry package within FLUKA. However, a funding shortfall from our requested amount has lowered this task in priority. We are also limited due to the funding shortfall on the amount of FLUKA calibration we will be able to accomplish. We are proceeding to modify FLUKA to include heavy ion interactions and as needed for use with ROOT inputs. The result will be a combined package that will allow the use of the ROOT interface to input to and control FLUKA, and then seamlessly continue within ROOT to do the analysis of the output from FLUKA. Our approach will be generic and it will allow the developed infrastructure to be readily adapted to the use of any Monte Carlo transport code that allows independent subroutine calls for histogramming. Such a package will be useful not only for the final analysis of the eventual end product output, but it will be invaluable for iterative development of the simulation itself. Integrated single-event displays and the ability to examine the performance of the simulation in geometric as well as physics detail, will be of great benefit in providing rapid and efficient application of the code to the variety of tasks for which it is being developed. The analysis software can even be employed within the ROOT framework to create, fill and plot histograms during the actual data taking, allowing one to perform classical statistical analysis on them, including multi-parametric fits in real-time.

REFERENCES

1. Wilson, J. W., *et al.*, *Transport Methods and Interactions for Space Radiation*, J. W. NASA Ref. Pub. 1257, 1991.
2. Aarnio, P., *et al.*, *Proc. of the MC93 Int. Conf. on Monte Carlo Simulation in High-Energy and Nuclear Physics*, 22-26 Feb. 1993. P. Dragovitsch, S. Linn, and M. Burbank, eds. , World Scientific, Singapore, 88, 1994.
3. Ajaltouni, Z., *et al*, [ATLAS Collaboration], Results From a Combined Test of an Electromagnetic Liquid Argon Calorimeter with a Hadronic Scintillating-Tile Calorimeter, *CERN-PPE/96-178*, 8 Nov. 1996.
4. Bertini, H., *Oak Ridge Report ORNL-TM-1996*, 1967.
5. Ferrari, A., and P. Sala, GEANT Hadronic Event Generators: A Comparison at the Single Event Level, *ATLAS Note Phys-No-086, 6 June 1996, CERN, Geneva, Switzerland*, 1996.

6. MacFarlane, R., *et. al., Los Alamos Report LA-11904-MS*, 1991.
7. Paretzke, H., *et al.*, in *Atomic and Molecular Data for Radiotherapy and Radiation Research*, International Atomic Energy Commission, Vienna, IAEA-TECDOC-799, 1995.
8. Prael, R., "User Guide to HETC Code System", *Los Alamos Report*, 1985.
9. Battistoni, G., A Ferrari, C. Forti, E. Scapparone, Simulation of Muon Transport at High Energy: Comparison of a Few Different Codes, *Nucl. Inst. And Meth. A394*, 136, 1997.
10. Fasso, A., *et al., Proc. of the Workshop on Simulating Accelerator Radiation Environment*, Santa Fe, 11-15 Jan., 134, 1993, (Available as Los Alamos Report LA-12835-C, 1994).
11. Fasso, A., A. Ferrari, J. Ranft, and P. Sala, New Developments in FLUKA Modelling of Hadronic and EM Interactions, *Proc. 3rd Workshop on Simulating Accelerator Radiation Environment, KEK, Tsukuba, Japan, 7-9 May,* 1997.
12. Ferrari, A., T. Rancati, and P. Sala, *FLUKA* Applications in High Energy Problems: From LHC to ICARUS and Atmospheric Showers, *Proc. 3rd Workshop on Simulating Accelerator Radiation Environment, KEK, Tsukuba, Japan, 7-9 May,* 1997a.
13. Ferrari, A., and P. Sala, Intermediate and High Energy Models in FLUKA: Improvements, Benchmarks and Applications, *Prod. Int. Conf. On Nucl. Data for Science and Tech. [NDST-97], Trieste, Italy, 19-24 May,* 1997b
14. Sala, P., and A. Ferrari, *Proc. of the MC93 Int. Conf. on Monte Carlo Simulation in High-Energy and Nuclear Physics*, 22-26 Feb. 1993. P. Dragovitsch, S. Linn, and M. Burbank, eds., World Scientific, Singapore, 277, 1994.
15. Brun, R., *et al., Proc. of CHEP 97* (Computing in High Energy Physics), Berlin, 7-11 April 1997. (In press, Elsevier), 1997.
16. Brun, R., et. al., *ROOT Overview* and *ROOT Tutorials*, CERN, Geneva, Switzerland, Available directly from the ROOT web site at http:/hpsalo.cern.ch/root/Welcome.html, 1996.
17. NASA, *The Second Symposium on the Protection Against Radiation Hazards in Space*, NASA SP-71 (1965).
18. USAEC, *The First Symposium on the Protection Against Radiation Hazards in Space*, Gatlinburg, Tenn. (1962). U.S. Atomic Energy Commission, TID-7652, 1962.
19. Warman, E., ed., *Proc. of the Symposium on Natural and Manmade Radiation in Space*, Las Vegas, Nevada, 1971, NASA TM X–2440, 1972.
20. Grahm, D., ed., HZE-Particle Effects in Manned Spaceflight, *Nat. Acad. of Sciences*, 1973.
21. Badhwar, G. D., *Proc of the Workshop on Predictions and Measurements of Secondary Neutrons in Space* (NASA/JSC, 28-30 September, 1998), 1998.
22. Hanssgen, K., H.-J. Mohring and J. Ranft, *Nucl. Sci. Eng. 88*, 551, 1984.
23. Ranft, J., and S. Ritter, *Z. Phys. C20*, 347, 1983.
24. Ranft, J., and S. Ritter, *Z. Phys. C27*, 413, 1985.
25. Ritter, S., *Comp. Phys. Comm. 31*, 393, 1984.

COMPARISON OF STRUCTURE AND SEGREGATION IN ALLOYS DIRECTIONALLY SOLIDIFIED IN TERRESTRIAL AND MICROGRAVITY ENVIRONMENTS

D.R. Poirier[1], Principal Investigator; S.N. Tewari[2] and J.C. Heinrich[3], Co-Investigators

[1]The Department of Materials Science and Engineering, The University of Arizona, Tucson, AZ 85721. Phone: (520) 621-6072; Fax: (520) 621-8059; Poirier@u.arizona.edu
[2]Chemical Engineering Department, Cleveland State University
[3]The Department of Aerospace and Mechanical Engineering, The University of Arizona.

INTRODUCTION

The research is within a Flight definition Program, so our efforts have been directed to establishing the science base for directional solidification in low gravity environment. The primary purpose of this research is to compare the microstructure and segregation in a binary metallic alloy that is directionally solidified in terrestrial and low gravity environments. Models of dendritic solidification that are used to predict microstructural features upon solidification rely on the assumption of diffusional transports of both heat and solute. Important features of the models are the prediction of primary dendrite spacings and dendrite tip radii. However, the thermosolutal convection of liquid in, from, or close to the solid plus liquid region masks the diffusional processes at the dendrite tips and is also responsible for macrosegregation in directionally solidified castings. Availability of microgravity provides an opportunity to obtain experimental data, where thermosolutal convection and attendant macrosegregation are negligible. With terrestrial experiments, however, diffusive and convective phenomena occur simultaneously, which complicates the study of dendritic growth. Here we report some of the results from our terrestrial directional solidification experiments.

I. Objectives

Since thermosolutal convection strongly affects transport phenomena during solidification and leads to macrosegregates, known as freckles, our hypotheses are that the macrosegregation will be eliminated and the dendritic microstructure will be greatly altered in microgravity. This is a program to conduct experiments in long-duration microgravity environment, with the objective of studying dendritic microstructures and segregation in directionally solidified dendritic alloys in the absence of thermosloutal convection. The research is based on directionally solidified Pb-Sb alloys and simulations of solidification of alloys using continuum theory of porous media. Using space-grown samples of hypoeutectic Pb-Sb alloys, we will characterize dendrite arm spacing, dendrite tip radii, mushy zone morphology (volume fraction of interdendritic liquid), and both macrosegregation and microsegregation, and compare the results to the structures and segregation in terrestrially grown samples of the same alloy. The design of microgravity experiments is guided by our on-going terrestrial experiments and computer simulations, which are being done to identify suitable growth conditions and the effect of g-jitter in long duration microgravity experiments.

II. Experimental Results

The directional solidification experiments in hypoeutectic Al-Cu and Pb-Sb alloys have conclusively shown that convection affects interface morphology and segregation in terrestrial experiments. In Al-Cu, the rejected solute is heavier so that convection is not expected due to the axial gradients in temperature and composition. However, a radial gradient is always present in the directional solidification for which there is no threshold for convection. This causes the mushy zone length to become non-uniform across the sample cross-section and "steepling" of primary dendrites [1]. In the Pb-Sb alloy, there is significant convection because of the rejection of a lighter solute at the interface. Here we present results on the Pb-Sb alloys.

The solidifying alloys are quenched when steady growth conditions are attained, as indicated by thermocouples inserted into the samples; quenching reveals the dendritic structure. The quenched-liquid is distinguished from the dendritic solid growing during directional solidification because the quench causes the overlying liquid and the interdendritic liquid in the upper part of the mushy zone to solidify as very fine dendrites. By taking transverse sections, the primary dendrite spacing and several other metrics of the dendrites are measured.

Macrosegregation. The phase diagram for the Pb-Sb system has a eutectic at 251.1° C and 11.2 wt % Sb. Typical macrosegregation along the length of Pb-5.8 wt % Sb alloy ingots (0.7 cm diameter) that were directionally solidified at rates of 1 to 10 mm s^{-1} under a gradient of 140 K cm^{-1} is shown in Figure 1a. Fraction solidified (f_s) refers to the fractional length along the directionally solidified sample, C_s is the composition corresponding to f_s and C_o is the initial solute content of the melt. Thermosolutal convection has resulted in extensive transport of solute from the mushy zone into the overlying liquid; the extent of macrosegregation is exacerbated as solidification rate is decreased. Convection in the overlying liquid and in the vicinity of the dendrite tips still exists even at the higher growth rates. The longitudinal macrosegregation shows a good fit to the relationship, $C_s = k_e C_o (1-f_s)^{k_e^{-1}}$ [2,3], where k_e is an effective partition coefficient. Extent of macrosegregation can be quantitatively represented by k_e which is about unity in the absence of convection and decreases with increasing convection.

The more severe form of macrosegregation known as "channel segregates" has been observed in the Pb - 5.8 wt % Sb alloy only at lower thermal gradients (Figure 1b). The channel segregates

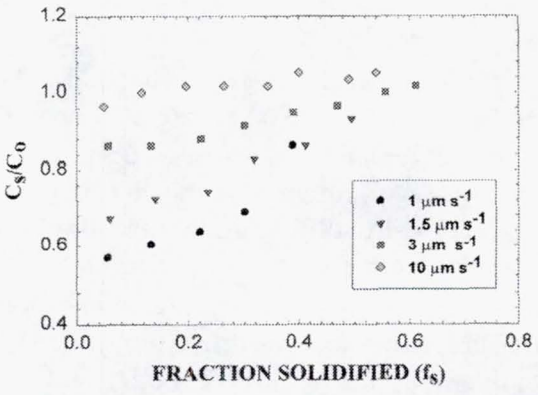

(a)

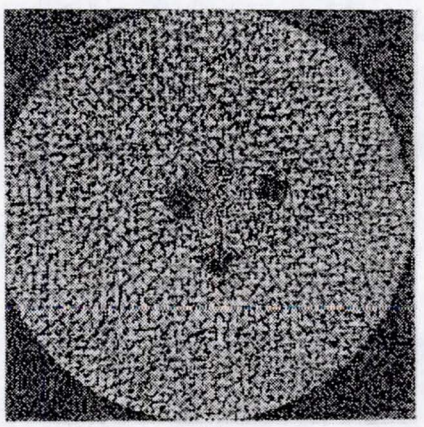

(b)

Figure 1. Macrosegregation in directionally solidified Pb-5.8 wt % Sb. (a) Longitudinal macrosegregation. Thermal gradient 140 K cm^{-1}. (b) Channel segregates in the interior. Thermal gradient 40 K cm^{-1}. Growth speed 3 μm s^{-1}.

always form in the sample interior for this alloy when it is solidified at 40 K cm^{-1} and 3 μm s^{-1}. Directional solidification experiments have been carried out where samples were initially grown at 10 or 30 μm s^{-1} at 40 K cm^{-1} and then the growth speed was decreased to 3 μm s^{-1}. Channel segregates did not form at 10 or 30 μm s^{-1}. However, after a growth of about 2 cm at 3 μm s^{-1} the segregates appeared in the sample interior. During the second series of experiments the sample was initially solidified at 3 mm s^{-1} and then the growth speed was increased to 10 or 30 μm s^{-1}. The channel segregates which formed during the initial solidification at 3 μm s^{-1} disappeared after the growth speed was stepped up to either 10 or 30 μm s^{-1}. Formation of channel segregates was associated with the most severe longitudinal macrosegregation.

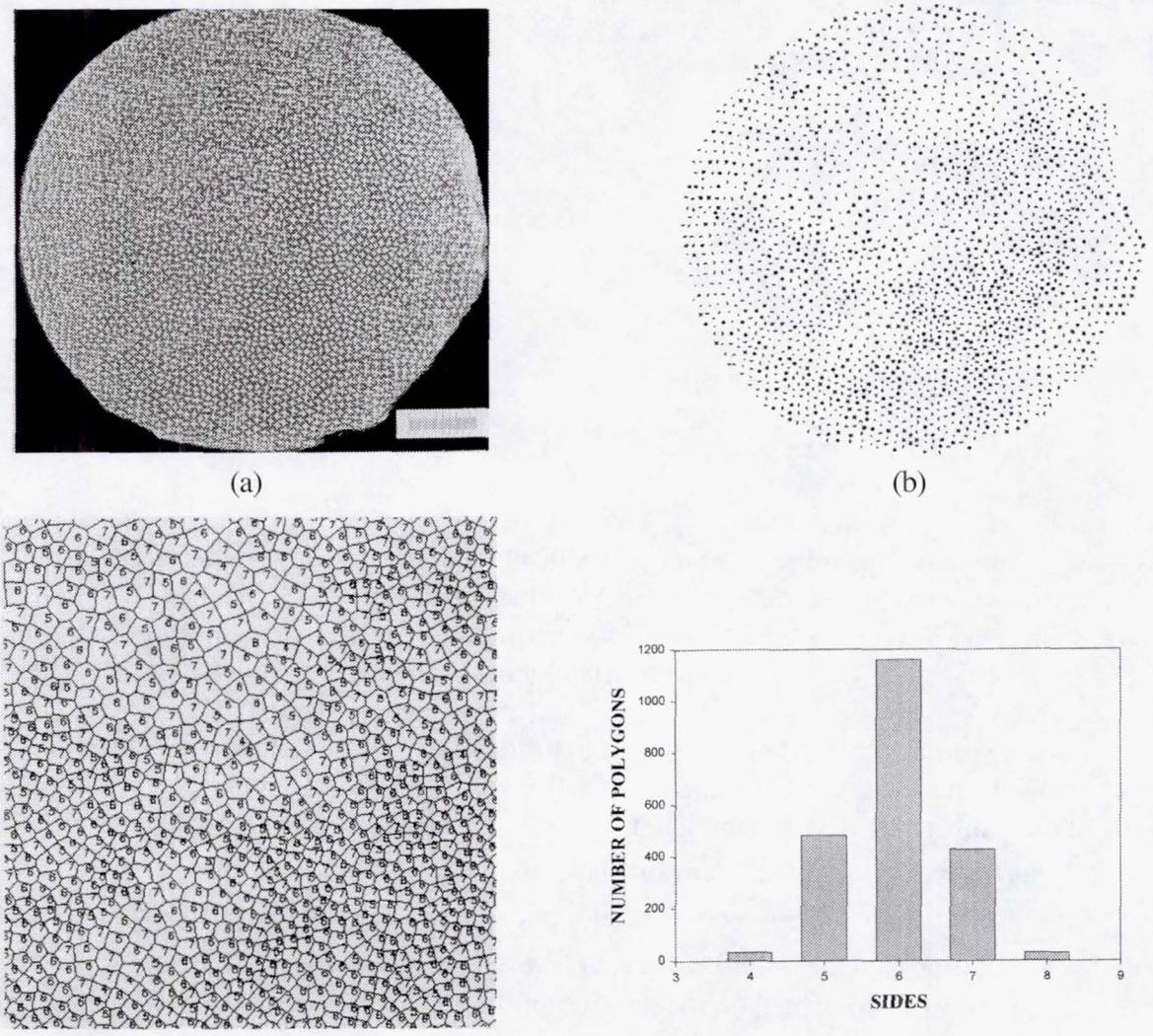

Figure 2. Primary dendrite distribution across the sample cross-section. (a) Pb- 2.2 wt % Sb. Thermal gradient 150 K cm^{-1}. Growth speed 30 mm s^{-1}. (b) Distribution of dendrite centers. (c) Voronoi polygons. (d) Frequency distribution of the number of nearest neighbors.

Primary Dendrite Distribution: Primary spacing is usually measured as $\sqrt{A/N}$, where N is the number of dendrites in a cross-sectional area, A. However, this procedure assumes a square distribution of primary dendrites. Experiments on Pb-Sb alloys have demonstrated that this assumption is not valid [4]. It is interesting to note that even when the channel-segregates do not form, the primary dendrite distribution across the entire sample cross-section is not uniform. This is shown in

Figure 2a for a Pb-2.2 wt % Sb sample grown at 30 $\mu m\ s^{-1}$ at 150 K cm^{-1}. There are regions of sparsely and densely distributed dendrites on the sample cross-section. This is more evident in Figure 2b which plots the points corresponding to the dendrite centers. Convection in the mushy region, close to the dendritic array tips, is responsible for this non-uniformity.

The number of nearest neighbors for each dendrite was determined by constructing Voronoi polygons (Figure 2c) for the points shown in Figure 2b. The frequency distribution of the number of neighboring polygons is shown in Figure 2d. There are very few polygons with four sides, whereas, there is a dominance of six-sided polygons. It suggests that dendritic distribution is not based on a square array. It is closer to a hexagonal arrangement.

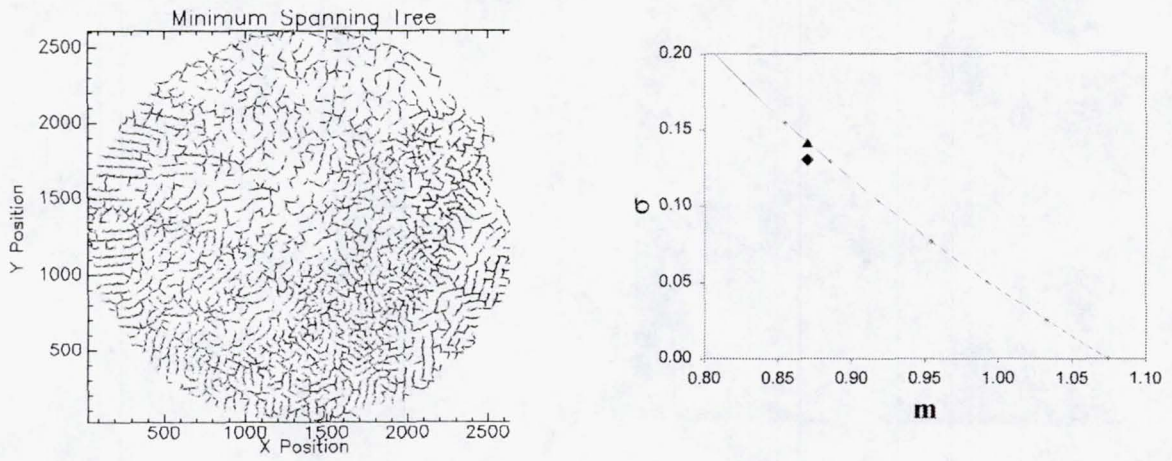

(a) (b)

Figure 3. Minimum Spanning Tree analysis of dendrite distribution. (a) Minimum Spanning Tree corresponding to Figure 2b. (b) The m- σ values obtained by MST analysis. The solid line corresponds to a hexagonal tessellation with superimposed random noise varying from 0 to 70% of nearest neighbor spacing.

A minimum spanning tree (MST) created from the dendrite centers is shown in Figure 3a. The mean branch length (m*) and its standard deviation (σ*) can be used to provide a statistical measure of the nearest neighbor distribution. It has been shown earlier [5] that the two parameters, m* and σ*, can be normalized by dividing them by the square root of the average cell surface <S> to yield *m* and σ, where, $m = \frac{m^*}{\sqrt{<S>}} \frac{N-1}{N}$, and $\sigma = \frac{\sigma^*}{\sqrt{<S>}} \frac{N-1}{N}$. The *m* versus σ plots can be used to compare arrangements with different nearest neighbor spacings. Figure 3b shows the typical m - σ values obtained for the Pb-Sb dendritic samples. The solid line in this figure is for a simulated hexagonal arrangement of points with increasing amount of superimposed random noise. The extent of random noise has been varied at 10% interval from zero to about 70% of the nearest neighbors in the hexagonal lattice. Increasing amount of noise increases σ and decreases m. The m-σ values for dendritic structures are same as those obtained from the simulated hexagonal lattice having about 50% superimposed random noise. It appears, therefore, that distribution of dendrites can also be visualized as a hexagonal tessellation with superimposed random noise, as was earlier proposed for cells [5].

Primary Dendrite Spacing: Figure 4 shows a typical frequency distribution of the number of nearest and higher order neighbors in a Pb-2.2 wt% Sb alloy solidified at 140 K cm^{-1} and 3 mm s^{-1}.

There is a distinct peak corresponding to the nearest neighbors. The second nearest peak is less distinct. Higher order peaks are masked by the large disorder in the spatial distribution of dendrites. The hidden peaks were deconvolutated by using Gaussian amplitude analysis after subtraction of the linear background to yield the mean nearest and higher order spacings. The ratio of the second to the first peak location was observed to be 1.85± 0.11, and that of the third to the first neighbor spacing to be 2.70± 0.25 [4]. For a square distribution these ratios would be 1.414 and 2, respectively. For a hexagonal distribution, the ratios would be 1.73 and 2.2. The experimentally observed ratio between the second and the first nearest neighbor spacing, 1.85, is closer to that for the hexagonal arrangement than to a square one.

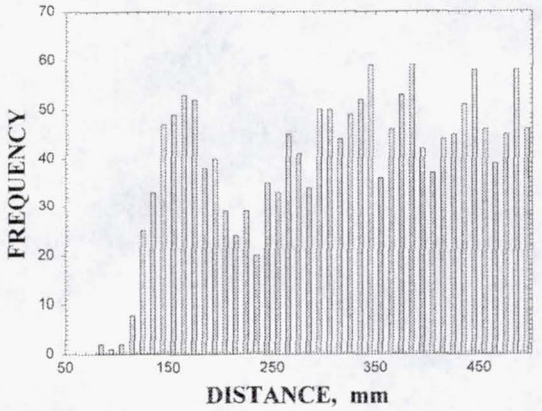

Figure 4. Frequency distribution of nearest and higher primary spacing in directionally solidified Pb-5.8 wt % Sb. Thermal gradient 140 K cm^{-1}. Growth speed 3 mm s^{-1}.

Figure 5 shows that the experimentally measured primary spacings are much smaller than the theoretical predictions based on the model due to Hunt and Lu [6]. The decrease in the primary spacing has been observed to show a good correlation with the degree of convection, as represented by the extent of longitudinal macrosegregation in Pb-Sn and Pb-Sb alloys [2, 7].

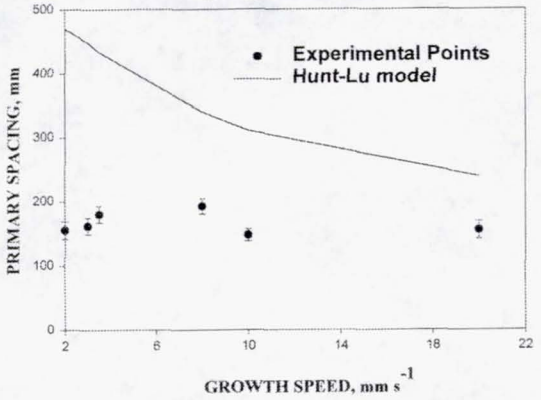

Figure 5. Growth speed dependence of primary spacings in directionally solidified Pb-5.8 wt % Sb. The curve is the minimum spacing calculated using model of Hunt and Lu [6].

III. Summary

During terrestrial solidification experiments on binary metallic alloys, solidification is always accompanied by convection. It has not been possible to eliminate the convective transport and the associated macrosegregation, in order to obtain the dendritie shapes and primary spacings, which

are determined only by the diffusive transports. Directional solidification experiments on Pb-Sb alloys are planned in the low gravity environment of space to obtain benchmark-data on dendritic morphology as a function of solidification parameters.

REFERENCES

1. M.H. Burden, D.J. Hebditch and J.D. Hunt: *J. Crystal Growth,* 1973, vol. 20, pp. 121-24.
2. S.N. Tewari and R. Shah: *Metall. Mater. Trans.*, 1996, vol. 27 A, pp.1353-1362.
3. S.N. Ojha, G. Ding, Y. Lu, J. Reye, and S.N. Tewari, *Metall. Mater. Trans.*, 1999, vol. 30A, pp. 2167-2171.
4. L.Yu, G.L. Ding, J. Reye, S.N. Ojha, and S.N. Tewari, *Metall. Mater. Trans.*, 1999, vol. 30A, pp. 2463-2472.
5. B.Billia, H. Jamgotchian, and H. Nguyan Thi: *Metall. Trans.*, 1991, vol 22A, pp. 3041-50,
6. J.D. Hunt and S.Z. Lu: *Metall. Mater. Trans.*, 1996, vol. 27A, pp. 611-623.
7. L.Yu, G.L. Ding, J. Reye, S.N. Ojha, and S.N. Tewari, "Mushy Zone Morphology during Directional Solidification of Pb-5.8 wt % Sb Alloy", (accepted for publication in *Metall. Mater. Trans.*).

FRONTAL POLYMERIZATION IN MICROGRAVITY: BUBBLE BEHAVIOR AND CONVECTION ON THE KC-135 AIRCRAFT

John A. Pojman[1] *, William Ainsworth[1], Yuri Chekanov[1], Jonathan Masere[1], Vitaly Volpert[2], Thierry Dumont[2], and Hermann Wilke[3]

[1]Department of Chemistry & Biochemistry
University of Southern Mississippi, Hattiesburg, MS 39406
www.pojman.com
[2]Laboratoire d'analyse numirique, Universite Lyon I, 69622
Villeurbanne Cedex, France
[3]Institute of Crystal Growth
Rudower Chaussee 6, D-12489 Berlin - Adlershof
GERMANY

Frontal polymerization is a mode of converting monomer into polymer via a localized exothermic reaction zone that propagates through the coupling of thermal diffusion and Arrhenius reaction kinetics. Frontal polymerization was discovered in Russia by Chechilo and Enikolopyan in 1972.[1] The macrokinetics and dynamics of frontal polymerization have been examined in detail[2] and applications for materials synthesis considered.[3]

Large temperature and concentration gradients that occur in the front lead to large density gradients. Figure 1 presents a schematic for a liquid monomer, usually a monoacrylate, being converted to a liquid (thermoplastic) polymer. The velocity can be controlled by the initiator concentration but is on the order of a cm/min.[2,4] If the liquid monomer is multifunctional, then a solid (thermoset) polymer is formed. Convection can occur with all types of monomers if the front propagates up a tube. Bowden *et al.* studied liquid/solid systems.[5] McCaughey *et al.* studied liquid polymer systems.[6] Descending fronts in thermoplastic systems are also susceptible to the Rayleigh-Taylor instability.[7]

I. Effective Interfacial Tension in Miscible Fluids

When two miscible fluids are placed in contact there exists a transient interfacial tension caused by differences in intermolecular forces. The theoretical basis goes back to an idea proposed in 1904, now called the Korteweg stress, in which a nonuniform concentration distribution can lead to stresses in a fluid.[8] Cahn and Hilliard developed the theory in 1958.[9] They proposed that the effective interfacial tension (EIT) should follow this relationship:

$$\sigma = k\int_{\Omega} |\nabla c|^2 d\xi$$

where C is the mole fraction of one component of a binary system, k is a constant with units of Newtons. If we consider a linear concentration gradient in one dimension, then we can write:

$$\sigma = k\frac{\Delta C^2}{\delta}$$

* Corresponding author

where δ is the length over which the concentration changes, and ΔC is the difference in composition.

Petitjeans measured the effective interfacial tension of glycerin and water, which are miscible in all proportions, using the spinning drop method and determined a value of 0.58 mN/m.[10] We have measured the dependence of the EIT and found it decreases with temperature. However, this is not true for hexyl acrylate/poly(hexyl acrylate), which increases with temperature.

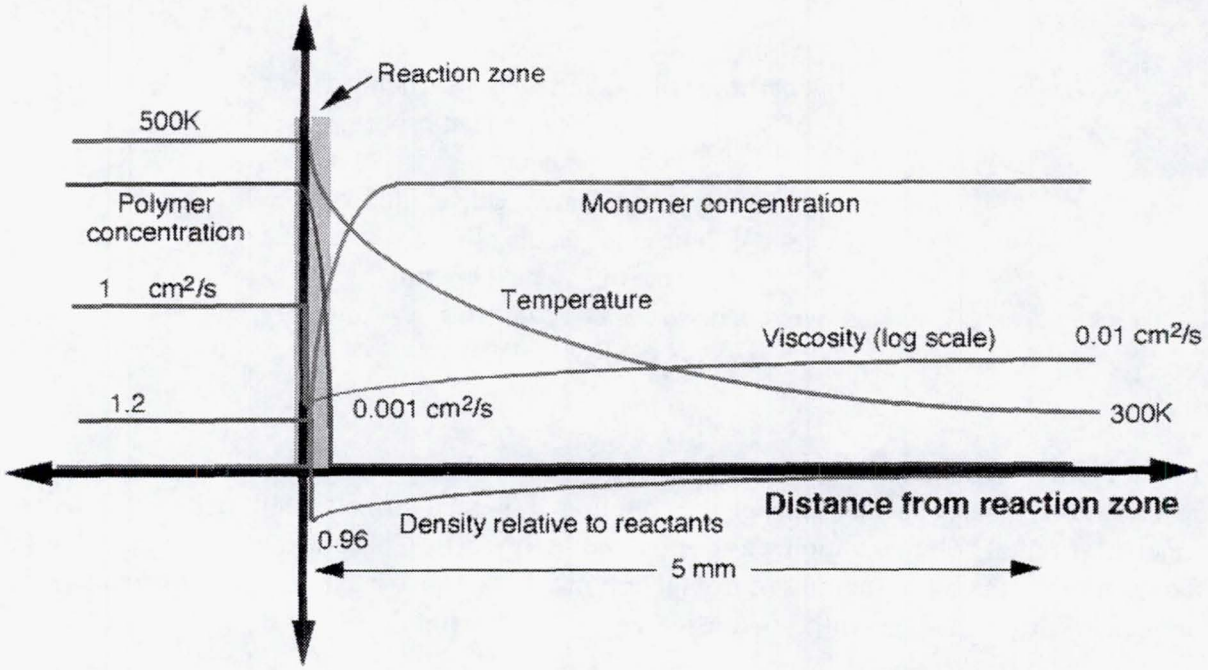

Figure 1. Schematic of a propagating polymerization front (liquid/liquid) showing approximate scales of variations in temperature, conversion, viscosity and density. Courtesy of Paul Ronney.

II. Effective-Interfacial-Tension Induced Convection (EITIC)

It is well known that temperature and/or concentration gradients perpendicular or parallel to a fluid/fluid interface can lead to convection.[11] Nonetheless, we know of no work on convection induced by effective interfacial tension gradients in miscible systems. Because of the large gradients produced in frontal polymerization, we propose that such convection could occur with a liquid monomer producing a liquid polymer. Specifically, measurements of the front width indicate that it decreases about 20% from the center of a 1.5 cm diameter tube to the walls, because of heat loss. We estimate the effective interfacial tension in the center of the tube to be 0.5 mN/m. At the wall it should be 0.4 mN/m.

Simulations for a model static system with the same gradient of interfacial tension with a single fluid indicates that flows would be has high as 20 cm/min for the monomer viscosity to 0.2 cm/min with 3 Stokes polymer.

We developed a numerical model based on Korteweg stresses induced by variations in the width of a sharp gradient and temperature gradients parallel to a uniform concentration gradient and demonstrated that convection can occur. The magnitude of the flow is comparable to that found in simulations with immiscible fluids but the flow exhibits a single vortex.

Tubular Reactors: Frontal polymerization of thermoplastics is an excellent model of adiabatic tubular reactor polymerizations without flow. Tubular reactors are prone to fouling because of radial gradients in conversion and molecular weight.[12-14] Such reactors are complex because there are instabilities from the flow and from buoyancy-driven convection. Frontal polymerization is the static analog of an adiabatic tubular reactor. Our analysis indicates that EITIC should occur in the frontal polymerization of thermoplastics. Such a fluid flow would affect the conversion and molecular weight distribution of the polymer produced.

Effects of Bubbles and Foam Formation: Polymeric foams are ideal construction materials in low earth orbit because of their rigidity. Because the foam structures need stiffness without having to support their own weight, very large scale structures could be assembled. Moreover, foams could be very useful construction materials on the moon or Mars because of their inherent insulating capabilities and their ability to shield against micrometeorites. Experiments on the *Conquest I* sounding rocket with butyl acrylate (thermoplastic) revealed an unusual bubble pattern in which nitrogen gas produced by the decomposition of the nitrile initiator formed a periodic structure.[7] For previous KC-135 experiments we reported that bubbles aggregated into large voids during weightlessness in the frontal polymerization of a thermoset.[15]

III. Experimental

Samples were flown aboard NASA's KC-135 aircraft. The parabolic flights afforded us approximately 20 seconds of low g (about 0.1 g) followed by a minute of 1 - 1.8 g. Tubes were 40 mm in diameter and equipped with a piston that moved in order to maintain isobaric conditions. _Hexyl acrylate and 1,6 hexane diol diacrylate were used as received from Aldrich. The initiator was a tricaprylmethyl ammonium persulfate (Aliquat 336 persulfate) that we synthesized.[16]

The thermoset foams consisted of 90% 1,6-hexane diol diacrylate (HDDA) with 10% 2-hydroxyethylmethacrylate (HEMA), which was added to slow the front velocity so that multiple parabolas could be seen in the same sample. A 10% Aliquat persulfate (tetraalkylammonium persulfate) solution was added to the monomer mixture as a bubble free initiator that will form free radicals. The blowing agent solution was made up of 5% Aliquat 336 and 95% distilled water. The Aliquat was added as a surfactant to allow the water to be dispersed in the organic monomer solution.

Reactions were initiated by heating the outside of the tube (for foam experiments) or by a nichrome wire directly in contact with the hexyl acrylate. Glycerin and water were studied by injecting one fluid (containing a dye) into the other in an apparatus that was free floated, allowing approximately 5 seconds of weightlessness.

IV. Results and Discussion

Attempts to observe convection in mg: With the frontal polymerization of hexyl acrylate we attempted to observe convection caused by the supposed gradient of effective interfacial tension. It was not possible to initiate the front and observe propagation in 20 seconds. Also, bubbles appeared from dissolved air. Figure 2 shows two images separated by a few seconds demonstrating how g jitter mixed the system. Even in high g the front sustained itself although the Rayleigh-Taylor instability was apparent (Figure 2). Molten polymer circulated above the front because of

heat loss, which caused a vertical gradient density. Polymer also sank from the front because it is more dense even when hot. Although the front would then propagate without any apparent convection during the next low g period, the convection reduced any radial gradient that would have been present and could have induced a fluid flow.

Thermoset Foams: As predicted, the bubble size did increase as the level of gravity decreased, but there was an overlap of the bubbles produced in microgravity into the region produced in 1.8 g. This overlap of regions eliminated our ability to measure the density of the foams produced.

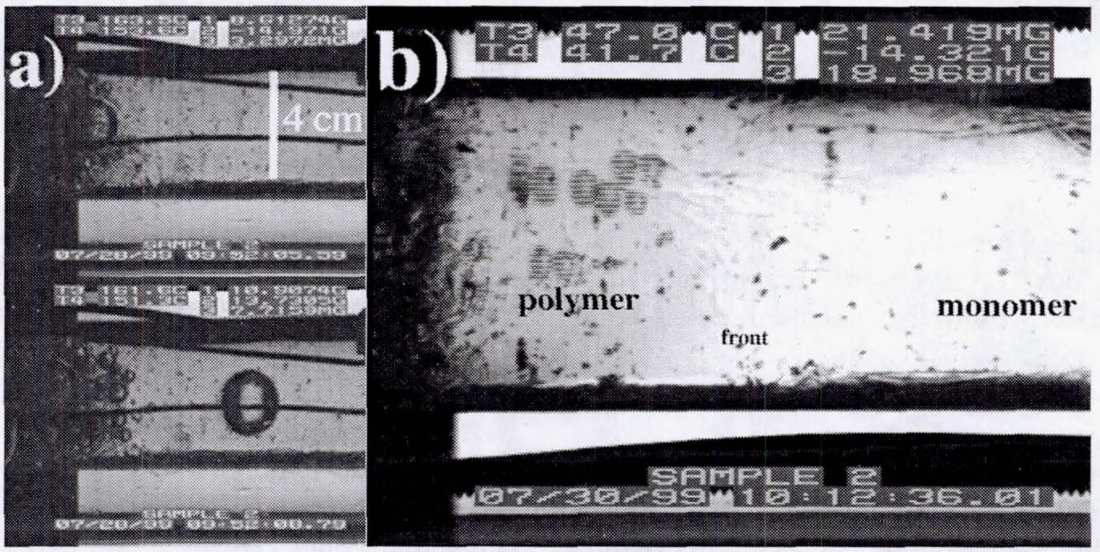

Figure 2. a) Two images of a hexyl acrylate polymerization front in the low g phase of the parabola. Notice how the bubble has moved to the right (down). b) The Rayleigh-Taylor instability in 2 g. "Down" is toward the right.

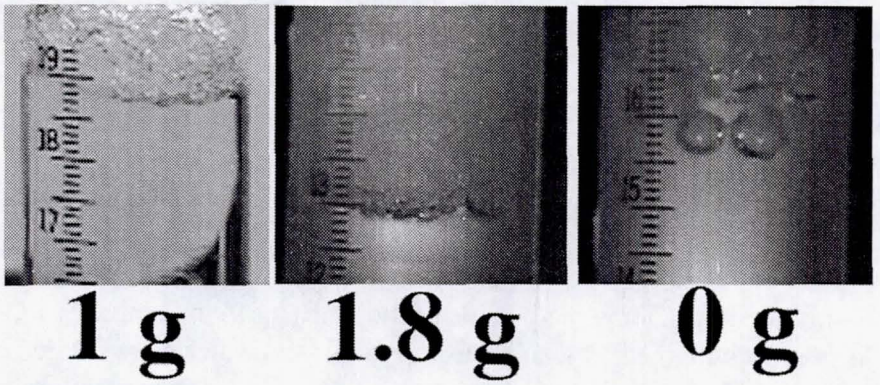

Figure 3. Bubbles in thermoset foams. Tubes are 2 cm in diameter.

V. Observations of Glycerin and Water in Low g

A question that arises if an effective interfacial tension exists is whether a drop of a miscible fluid spontaneously becomes spherical or if a jet spontaneously breaks into drops. We studied water injected into glycerin and glycerin injected into water in low g on the KC-135 aircraft. We free floated the apparatus to achieve quiescent conditions but only for a few seconds. Figure 4 shows how a drop of water does not become spherical during the short low g period. A stream of glycerin in water does not break into drops as could be expected from the Rayleigh instability for immiscible fluids. From Levich, we can estimate the time required for droplet breakup:[17]

$$\tau = \frac{5 * \text{radius} * \mu}{\sigma} = \frac{5(0.001m * 1Pa * s}{0.001mN/m} = 5s$$

The time scale is somewhat longer than the observation peroid allowed but no constriction of the stream was observed. It may be that the g jitter and fluid flow during injection perturbed the concentration gradient and reduced the EIT.

We performed another study to test if EITIC could be induced by a temperature gradient along a miscible interface. Water was carefully layered onto glcyerin. A light bulb was situated at the interface, which could heat the surrounding fluid 10°C in 2 seconds (Figure 5b). The experiment was free floated just after the heater was started. No fluid motion along the interface could be detected in the glycerin. Glycerin is so viscous that any flow would be very slow. Therefore, we diluted the glycerin with water, which would reduce the EIT but more rapidly decrease the viscosity. Unfortunately, the slightest bump to the apparatus in free float disrupted the interface.

VI. Conclusions

Experiments under weightlessness show clearly that frontal polymerization with bubbles produces foams with different bubble sizes in weightlessness. However, the bubbles produced during the high g phase affect the bubbles during the low g making it impossible to determine what the behavior would be if the front propagated only under low gravity.

Numerical simulations indicate that an effective-interfacial-tension induced convection can occur because of concentration and temperature gradients between a polymer and its miscible monomer. Because of g jitter, it was not possible to determine if the predicted effective interfacial tension gradient in a front causes convection in a front with a liquid monomer producing a liquid polymer. Model experiments with glycerin and water were inconclusive.

To determine how effective-interfacial-tension induced convection could affect polymer processing requires low periods of higher quality weightlessness.

VII. Acknowledgments

Support for this project was provided by NASA's Microgravity Materials Science Program (NAG8-973). We thank Steve Spearman, Doug Westra and Zena Hester of the Marshall Space Flight Center for developing hardware and flying experiments.

REFERENCES

1. Chechilo, N. M.; Khvilivitskii, R. J.; Enikolopyan, N. S. *Dokl. Akad. Nauk SSSR* 1972, *204*, 1180-1181.
2. Pojman, J. A.; Ilyashenko, V. M.; Khan, A. M. *J. Chem. Soc. Faraday Trans.* 1996, *92*, 2825-2837.
3. Khan, A. M.; Pojman, J. A. *Trends Polym. Sci. (Cambridge, U.K.)* 1996, *4*, 253-257.
4. Goldfeder, P. M.; Volpert, V. A.; Ilyashenko, V. M.; Khan, A. M.; Pojman, J. A.; Solovyov, S. E. *J. Phys. Chem. B* 1997, *101*, 3474-3482.
5. Bowden, G.; Garbey, M.; Ilyashenko, V. M.; Pojman, J. A.; Solovyov, S.; Taik, A.; Volpert, V. *J. Phys. Chem. B* 1997, *101*, 678-686.

6. McCaughey, B.; Pojman, J. A.; Simmons, C.; Volpert, V. A. *Chaos* 1998, *8*, 520-529.
7. Pojman, J. A.; Khan, A. M.; Mathias, L. J. *Microgravity Sci. Technol.* 1997, *X*, 36-40.
8. Korteweg, D. J. *Archives Neerl. Sci. Exacts. Nat.* 1904, *6*, 1.
9. Cahn, J. W.; Hilliard, J. E. *J. Chem. Phys.* 1958, *28*, 258-267.
10. Petitjeans, P. *C.R. Acad. Sci. Paris* 1996, *322*, 673-679.
11. Ostrach, S. *Annu. Rev. Fluid Mech.* 1982, *14*, 313-345.
12. Cunningham, M. F.; O'Driscoll, K. F.; Mahabadi, H. K. *Can. J. Chem. Eng.* 1991, *69*, 630-638.
13. Cunningham, M. F.; O'Driscoll, K. F.; Mahabadi, H. K. *Polym. Reaction Eng.*1992, *1*, 229-244.
14. Cunningham, M. F.; O'Driscoll, K. F.; Mahabadi, H. K. *Polym. Reaction Eng.*1992, *1*, 245-288.
15. Pojman, J. A. *Frontal Polymerization in Microgravity, AIAA 98-08113*; AIAA: Reno, NV, 1998.
16. Chekanov, Y.; Pojman, J. A.; Rasmussen, J. K. *Polym. Prepr. (Am Chem. Soc. Div. Polym. Chem.)* 1998, *39*, 465-467.
17. Levich, V. G. *Physicochemical Hydrodynamics*; Prentice Hall:, 1962.

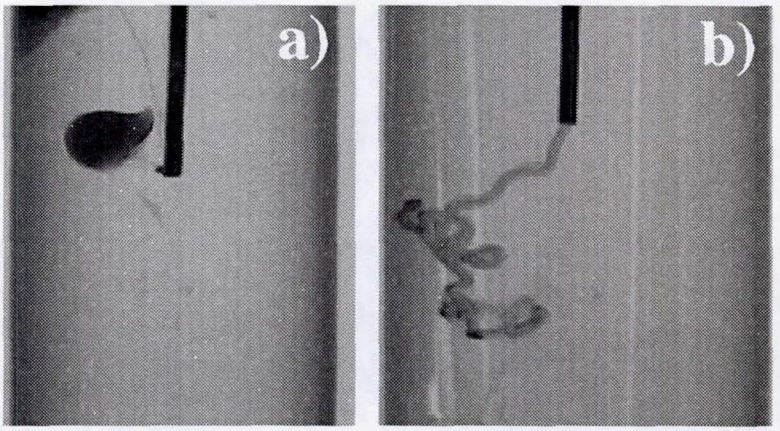

Figure 4. a) Water injected into glycerin in low g. b) Glycerin injected into water in low g. Tube diameter of 2.2 cm.

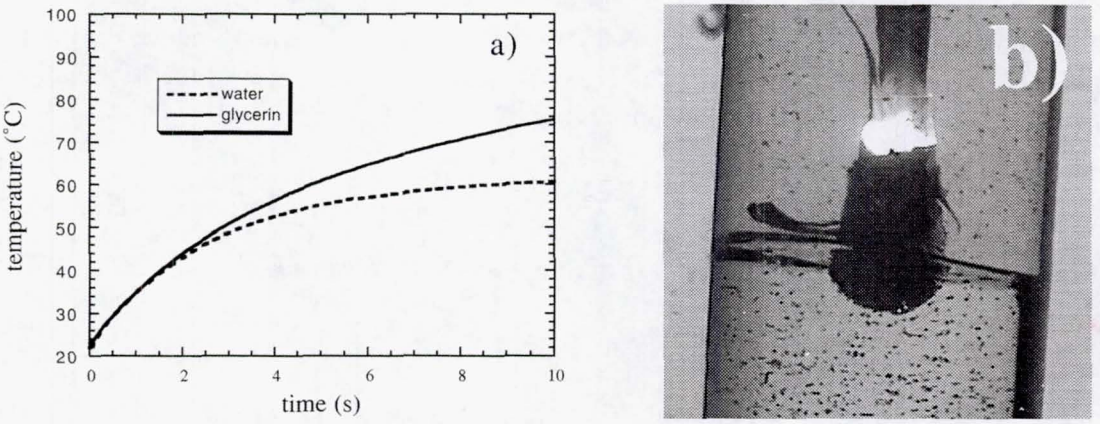

Figure 5. The time dependenceof the heater. Glycerin under water in a 2.2 cm diameter tube.

PRIMARY/CP/IN/23 2001 082 994

REPORT DOCUMENTATION PAGE

Form Approved
OMB No. 0704-0188

1. AGENCY USE ONLY *(Leave Blank)*	2. REPORT DATE	3. REPORT TYPE AND DATES COVERED
	March 2001	Conference Publication

4. TITLE AND SUBTITLE
Microgravity Materials Science Conference 2000

5. FUNDING NUMBERS

6. AUTHORS
N. Ramachandran,* N. Bennett,* D. McCauley,** K. Murphy,***
S. Poindexter,* Editors

7. PERFORMING ORGANIZATION NAMES(S) AND ADDRESS(ES)
George C. Marshall Space Flight Center
Marshall Space Flight Center, AL 35812

8. PERFORMING ORGANIZATION REPORT NUMBER
M–1003

9. SPONSORING/MONITORING AGENCY NAME(S) AND ADDRESS(ES)
National Aeronautics and Space Administration
Washington, DC 20546–0001

10. SPONSORING/MONITORING AGENCY REPORT NUMBER
NASA/CP—2001–210827

11. SUPPLEMENTARY NOTES
Proceedings of a conference held at Huntsville, AL, June 6–8, 2000. *Universities Space Research Association, **University of Alabama in Huntsville, ***Morgan Research Corporation (all Huntsville, AL)

12a. DISTRIBUTION/AVAILABILITY STATEMENT
Unclassified-Unlimited
Subject Category 23
Standard Distribution

12b. DISTRIBUTION CODE

13. ABSTRACT *(Maximum 200 words)*

The 2000 Microgravity Materials Science Conference was held June 6–8 at the Von Braun Center, Huntsville, Alabama. It was organized by the Microgravity Materials Science Discipline Working Group, sponsored by the Microgravity Research Division (MRD) at NASA Headquarters, and hosted by NASA Marshall Space Flight Center and the Alliance for Microgravity Materials Science and Applications (AMMSA). It was the fourth NASA conference of this type in the microgravity materials science discipline. The microgravity science program sponsored ≈200 investigators, all of whom made oral or poster presentations at this conference. In addition, posters and exhibits covering NASA microgravity facilities, advanced technology development projects sponsored by the NASA Microgravity Research Division at NASA Headquarters, and commercial interests were exhibited. The purpose of the conference was to inform the materials science community of research opportunities in reduced gravity and to highlight the Spring 2001 release of the NASA Research Announcement (NRA) to solicit proposals for future investigations. It also served to review the current research and activities in materials science, to discuss the envisioned long-term goals, and to highlight new crosscutting research areas of particular interest to MRD. The conference was aimed at materials science researchers from academia, industry, and government. A workshop on in situ resource utilization (ISRU) was held in conjunction with the conference with the goal of evaluating and prioritizing processing issues in Lunar and Martian type environments. The workshop participation included invited speakers and investigators currently funded in the material science program under the Human Exploration and Development of Space (HEDS) initiative. The conference featured a plenary session every day with an invited speaker that was followed by three parallel breakout sessions in subdisciplines. Attendance was close to 350 people. Posters were available for viewing during the conference and a dedicated poster session was held on the second day. Nanotechnology, radiation shielding materials, Space Station science opportunities, biomaterials research, and outreach and educational aspects of the program were featured in the plenary talks. This volume, the first to be released on CD-Rom for materials science, is comprised of the research reports submitted by the Principal Investigators at the conference.

14. SUBJECT TERMS	15. NUMBER OF PAGES
microgravity research, materials science, in situ resource utilization, new technology, biomaterials research, radiation shielding	719
	16. PRICE CODE A99

17. SECURITY CLASSIFICATION OF REPORT	18. SECURITY CLASSIFICATION OF THIS PAGE	19. SECURITY CLASSIFICATION OF ABSTRACT	20. LIMITATION OF ABSTRACT
Unclassified	Unclassified	Unclassified	Unlimited